INVESTIGATION ON SUPERSONIC HIGH-SPEED INTERNAL FLOWS AND THE TOOLS TO STUDY THEIR INTERACTIONS

SUBMITTED IN FULFILMENT OF THE REQUIREMENTS FOR THE
DEGREE OF DOCTOR OF PHILOSOPHY

January 2018

Francesca Gnani

School of Engineering
College of Science and Engineering
University of Glasgow

Contents

List of Tables

List of Figures

Abstract

AIR-BREATHING vehicles are characterised by a high level of integration between the propulsion system and the vehicle frame. Since the peculiarity of this type of aircraft is the absence of moving parts, before the air flow arrives at the combustion chamber, it must be slowed down to lower supersonic speeds, in scramjets, or to subsonic speeds, in ramjets, by means of a shock wave structure, called a shock train. The prediction and control of the shock train is important for the evaluation of the engine performance.

This work aims to improve the understanding of the flow mechanisms occurring in the shock train as a consequence of the interaction of shock waves with the boundary layer in long and narrow ducts. A full pressure sensitive paint system was developed. Polymer-based and ruthenium-based compounds were identified as suitable for the investigation of the shock train in the wind tunnel. Before being able to collect experimental data, the design and manufacture of an indraft supersonic wind tunnel able to operate at Mach numbers M= 2 and M= 4 was accomplished. The air at ambient conditions is drawn into the tunnel and then discharged into a vacuum tank with a volume of 34 m^3. Preliminary attempts to run the wind tunnel have identified the presence of leakages between the vacuum tank and the wind tunnel that prevented the establishment of the pressure difference required to obtain a supersonic flow in the test section.

In support of the experimental approach, different flow configurations are numerically studied using the RANS equations. The k-ω Wilcox model provided the most accurate results for such a complex flow field. Sensitivity studies are carried out since the characteristics of the shock train depend on several variables, including the duct geometry and the back pressure. The numerical findings revealed that the location of the shock train strongly varies with the grid size. Transient simulation is used to reproduce the shock train oscillation due to the pressure fluctuations that occur in the combustion chamber of an air-breathing aircraft. Under a sinusoidal forcing, the shock train executes a motion around its mean position that deviates from a perfect sinusoidal profile depending on the oscillation amplitude, frequency, and whether the pressure is first increased or decreased. With large oscillation amplitudes the shock train is greatly influenced by a pressure increase rather than a pressure drop, but the opposite is observed at small oscillation amplitudes. With varying forcing frequency, the shock displacement around its mean position decreases as the forcing frequency increases.

Author's Declaration

I declare that, except where explicit reference is made to the contribution of others, this dissertation is the result of my own work and has not been submitted for any other degree at the University of Glasgow or any other institution.

Signature .....

Printed name .....

Nomenclature

Roman Symbols

A	Area $[m^2]$
a	being the speed of sound $[m/s]$
C_n	Generic coefficient
C_f	Skin friction coefficient
C_P	Specific heat of air at constant pressure $[J/kgK]$
C_V	Specific heat of air at constant volume $[J/kgK]$
C_μ	Empirical constant
D	Duct diameter $[m]$, Drag $[N]$, Diffusion coefficient
D_{eq}	Equivalent duct diameter $[m]$
d_d	Diameter of particle $[m]$
d_{HC}	Cell size of the honeycomb $[m]$
d_M	Screen wire diameter $[m]$
$E(\kappa)$	Energy spectral density
$\boldsymbol{F}$	Vector of inviscid flux
f	Fuel-air ratio, Frequency $[Hz]$
$\boldsymbol{G}$	Vector of viscous flux
g	Acceleration of gravity at the standard sea level $[m/s^2]$
H	Test section height $[m]$
h	Enthalpy $[J/kg]$, Duct half height $[m]$
I	Luminescent intensity, current density $[A]$, Turbulence intensity
L	Honeycomb cells length $[m]$
L_{SC}	Settling chamber width $[m]$
$\mathcal{L}$	Characteristic length $[m]$
l_M	Screen mesh length $[m]$
ℓ	Characteristic length of the larger eddies $[m]$
k	Turbulence kinetic energy per unit mass $[m^2/s^2]$
K	Pressure drop coefficient
K_{sv}	Stern-Volmer constant
Kn	Knudsen number
L	Test section length $[m]$
M	Mach number
m	Mass $[kg]$
$\dot{m}$	Mass flow rate $[kg/s]$
n	Polytropic coefficient
P	Pressure $[Pa]$

Pr	Prandtl number
q	Heat flux
R	Universal gas constant [J/KgK]
Re	Reynolds number
S	Henry's solubility constant
S_M	Spacing between two screens [m]
S_P	Pressure sensitivity [$\%$100 kPa]
S_{PT}	Pressure sensitivity due to variation of temperature [Pa/K]
S_T	Temperature sensitivity [$\%/K$]
S_ϕ	Source term
s	Entropy [$J/molK$]
$\boldsymbol{T}$	Viscous stress tensor
t	Time [s]
T	Temperature [K], Thrust [N]
t	Time [s]
th	Paint thickness [μm]
TR	Turbulence reduction ratio
$\boldsymbol{U}$	Vector of velocity [m/s]
U	Characteristic velocity [m/s]
u	Velocity in x direction [m/s]
$\boldsymbol{U_g}$	Vector of grid velocity [m/s]
u_τ	Friction velocity [m/s]
u^+	Dimensionless velocity
x	Generic position, Component i of the position vector [m]
y^+	Dimensionless distance from the wall
v	Velocity in y direction [m/s]
V_{tank}	Vacuum tank volume [m^3]
$\boldsymbol{W}$	Vector of conserved variables
W	Test section width [m]
w	Velocity in z direction [m/s]

Greek Symbols

α	Empirical factor, Reynolds number exponent, Closure coefficient
β	Open-area ratio, Blending factor, Closure coefficient
β^*	Closure coefficient
γ	Ratio of specific heat capacity
Γ	Diffusion coefficient, Preconditioning matrix
δ	Boundary layer thickness [mm]
δ^*	Boundary layer displacement thickness [mm]
δ_{ij}	Kronecker delta
δ_ν	Viscous lengthscale [mm]
ε	Turbulent dissipation rate [m^2/s^3], Back pressure amplitude coefficient
ϵ	Relative error

θ	Boundary layer momentum thickness, Inflection angle
κ	Wavenumber
λ	Thermal conductivity, Wavelength $[nm]$
μ	Dynamic viscosity $[kg/ms]$
μ_τ	Eddy viscosity $[kg/ms]$
μ_{turb}	Turbulent viscosity $[kg/ms]$
ν	Kinematic viscosity $[m^2/s]$
π_c	Total pressure ratio
ρ	Density $[kg/m^3]$
σ_d	Closure coefficient
σ_k	Closure coefficient
σ_ω	Closure coefficient
τ	Lifetime, Shear stress $[kg/ms^2]$
$\tau_{relaxation}$	Time constant of paint response $[s]$
ϕ	Fluid property
ω	Rate of dissipation of energy per unit volume per unit time $[1/s]$

Superscripts

e	End of the run
i	Beginning of the run
$*$	Initial condition, Experimental condition, Throat condition
$+$	Maximum value
$-$	Minimum value

Subscripts

0	Total condition, Ambient condition
3	Condition in the combustion chamber entrance
4	Condition in the combustion chamber exit
e	Exit condition
f	Fuel
max	Maximum value
min	Minimum value
P	Pressure probe
R	Reference probe
ref	Reference condition
SL	Sea level
W	Wall condition
∞	Freestream condition
θ	Boundary layer momentum thickness

Acrynoms

CCD	Charge-coupled device
CFD	Computational fluid dynamics
CFL	Courant-Friedrichs-Lewy condition
DCR	Dual-combustor ramjets
DNS	Direct numerical simulation
DMR	Dual-mode ram-scramjets
GG	Green-Gauss
$HG\text{-}LSQ$	Hybrid Gauss-least squares method
LDV	Laser Doppler Velocimetry
LES	Large eddy simulation
MVG	Micro vortex generator
PSP	Pressure sensitive paint
$RANS$	Reynolds-averaged Navier-Stokes
RSM	Reynolds stress transport model
$SBVG$	Sub-boundary layer vortex generators
SCB	Shock control bumps
SNR	Signal-to-noise ratio
SST	Shear stress transport model
TVB	Total variation bounded gradient limiter
$URANS$	Unsteady Reynolds-averaged Navier-Stokes
VG	Vortex generator

1 | Introduction

THE desire of man to fly is as ancient as the world. In the 15th century Leonardo da Vinci studied the principle of the birds flight and designed some pioneering flight crafts which had the basic elements of the modern parachutes and helicopters [1].

The fascination for high speeds has inspired multiple generations of aerodynamicists and engineers to put great effort in developing high-speed aircraft. The 18th and 19th centuries became a period of intense study and several unsuccessful attempts led to the first sustained, controlled, powered flight, performed by the Wright brothers in 1903 [2]. From this point on, aviation has seen substantial improvements and the production of a wide range of different aircraft, playing a important role in making the world smaller [3].

Propeller-driven aircraft dominated the first 30 years of commercial aviation and, later, the introduction of the jet transport produced a dramatic increase of the aircraft range of speeds [4]. Up to Mach 3 the gas-turbine engine has an economic advantage but, to extend the range of engine operation to high altitudes and Mach numbers, the use of moving parts is no longer needed. A different approach, developed to achieve greater compression and heating of the air, compresses the air entering the engine by means of internal geometry changes.

1.1 Air-breathing propulsion

For high-speed vehicles travelling at high altitudes significant compression and heating of the air entering the combustion chamber are required. Air-breathing engines, such as ramjet and scramjets, have become particularly attractive due to their simplicity for the absence of rotating components, improved safety, mission flexibility, robustness, reduced operating costs, and capability of achieving higher combustion temperatures with the use of a fuel-injection pattern [5, 6]. On the other hand, since the thrust of an air-breathing engine is a function of flight Mach number and altitude, the drawback of this kind of systems emerges at subsonic speeds, when the low performance is due to the inability to achieve the efficient operational value of pressure rise [7]. Designing an engine able to operate over a wide range of Mach numbers is one of the key technological challenges in current times.

The mechanism of flow compression, which takes place in a ramjet or scramjet inlet, finds

other relevant applications characterised by the interaction of shock waves with the boundary layer such as supersonic compressors, ejectors, and wind-tunnel diffusers [8]. Therefore, the ability to accurately predict and control shock wave structures would provide a means to enhance the performance of flow devices operating at high speeds, the engine efficiency, or the mixing of fuel injected from the combustor walls [9].

The origins of ramjet technology were laid down around a century ago, in 1913, when a French engineer, René Lorin, published an article in the aviation magazine *L'Aérophile* expressing the idea to create jet propulsion by directing the exhaust gases from internal combustion engines into nozzles [10]. However, due to the lack of materials and technological limitations of the time, he could not have advanced this concept beyond the design stage [2].

Ramjet technology gained maturity after World War II. In 1947 the world's first aircraft powered exclusively by a ramjet, *Leduc 0.10*, illustrated in Figure 1.1, successfully performed the first powered flight [12]. Since it could not take off unassisted, the aircraft needed to be carried and then released by a mothership at the appropriate altitude. In a subsequent flight, in 1949, the *Leduc 0.10* was released by a *Languedoc S.O.161* at 36,000 ft achieving the necessary pressure conditions for the ramjet to sustain power [13]. Nine years later, in 1958, the *Nord 1500 Griffon*, shown in Figure 1.2, reached Mach 2.19, marking the first significant success in ramjet technology. A step further was made by Antonio Ferri [14], who revolutionised the design of high-speed vehicles proposing a new type of supersonic inlet, as illustrated in Figure 1.3. In this new configuration all the parts intended for the deceleration of the supersonic flow are placed outside of the diffuser. It was then recognised that an air-breathing propulsion vehicle could fulfil the possibility of hypersonic cruise and

Figure 1.1: The experimental ramjet aircraft Leduc 0.10 [11].

Figure 1.2: The Nord 1500 Griffon in 1955 [11].

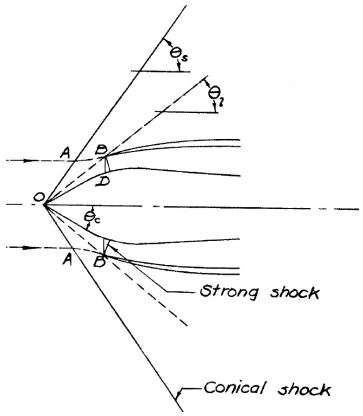

Figure 1.3: Schematic of the fixed geometry inlet proposed by Ferri [14].

recoverable space launchers, a feature not achievable with rocket engines [15].

For Mach numbers greater than 3, but below approximately 5, several configurations of air-breathing engines have been proposed depending on the mission requirements to provide sufficient mass flow, adequate lift and propulsion. In this flight regime the pure ramjet, illustrated in Figure 1.4, provides the most efficient thermodynamic cycle [17]. The flow is choked at the inlet, downstream of the isolator, causing a large back pressure at the combustor entrance and the formation of a sequence of shock waves inside the isolator which guarantees that the air enters the combustor at subsonic speeds ($M \sim 0.3$ to 0.4) [5]. The isolator is a nearly parallel duct placed between the inlet and the combustor with the purpose of containing the shock wave structures. It prevents the interaction of the flow at the inlet with that inside the combustion chamber [18], but has the drawback of added weight, internal drag and heat loads on the engine structure. A critical issue is the prediction of the minimal isolator length required by operability constraints. The presence of this component has been found effective in increasing the combustion heat release [19] and higher engine thrust can be achieved if the precombustion shock is confined into the isolator [20].

As the flight Mach number increases above 5, the deceleration of air to subsonic conditions introduces two problems. Firstly, the pressure rise to decelerate the flow to subsonic speed drastically increases the pressure losses associated with shock waves. The second issue is the increased gas temperature to very high values in the combustor [21]. This effect is not only responsible for structural problems, requiring an adequate selection of the wall

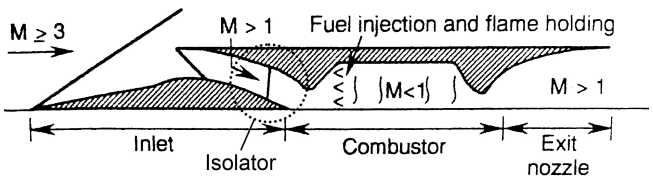

Figure 1.4: Schematic of a conventional ramjet engine [16].

material and cooling methods in the combustor, but also provokes chemical dissociation so that the combustion products might not be completely formed with consequent penalties in the engine cycle performance [22].

At flight speeds above Mach 8, the kinetic energy of the flow through the engine becomes high enough that the combustion pressure rise does not cause boundary layer separation. The flow is gradually decelerated at the inlet to a lower speed but remains supersonic in the combustor, where the fuel is injected and mixed with the flow. This configuration, called a pure scramjet, is illustrated in Figure 1.5. When the engine operates in scramjet mode, there is no shock train since the flow is supersonic through the entire engine and the isolator appears to be unnecessary. However, the area increase in the combustor is often not sufficient to mitigate the thermal choking caused by heat addition which enhances the adverse pressure gradient, favouring the unstart of the engine [17]. If a sudden pressure increase takes place, the wall boundary layer separates and the pressure rise propagates upstream. In this case the presence of the isolator helps to ensure that even though the boundary layer is separated over a large portion of the duct the core flow remains supersonic and forms an oblique shock train that contains the phenomenon of engine unstart.

The isolator plays a significant role on the flow transition from supersonic to subsonic conditions in dual-mode scramjet combustors [23]. Dual-mode ram-scramjets (*DMR*) or dual-combustor ramjets (*DCR*), illustrated in Figure 1.6, were introduced during the 1970s by the Applied Physics Laboratory (APL) and allow the engine to operate at both low and high supersonic Mach numbers [20], i.e. as a ramjet at a high Mach number but subsonic combustion or as a scramjet with supersonic combustion. The fuel is injected at either sonic or supersonic conditions and the combustion process occurs at subsonic conditions in a constant area duct which then becomes divergent. In this configuration the core flow is decelerated to subsonic conditions by the combined effect of the injection and heat release upstream of the fuel injector ports generating a shock train that extends into the combustion chamber [24].

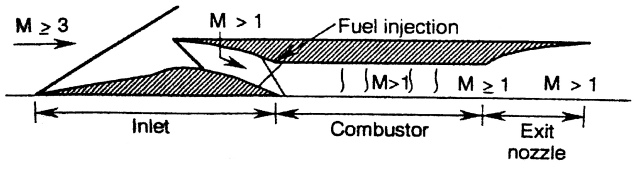

Figure 1.5: Schematic of a scramjet engine [16].

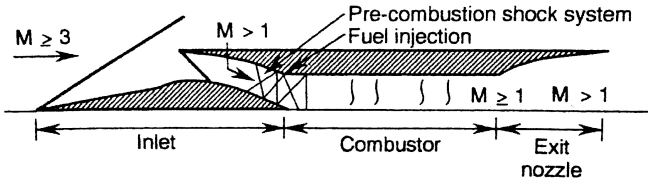

Figure 1.6: Schematic of a dual-mode ram-scramjet engine [16].

For Mach numbers from 8 to 18, the scramjet exhibits good performance. However, above Mach 18, friction losses increase considerably and scramjet operation becomes difficult. The performance gradually decreases, approaching that of a rocket engine [5]. The amount of available energy due to combustion is also a much smaller fraction of the incoming kinetic energy which leads to little gains. Figure 1.7 illustrates the flight corridor in which an air-breathing propelled vehicle can operate. The upper altitude limit is dictated by the need of the engine to maintain a relatively high dynamic pressure required for the maximum engine performance, namely the capture of sufficient air to enable the air-breather to operate efficiently [26]. The lower boundary is imposed by structural limitations since the aerodynamic forces are proportional to the air density [22].

1.1.1 High-speed intakes

The three main components of a scramjet/ramjet engine are: the supersonic air intake, the combustion chamber, and the jet nozzle, whose efficiency play an increasingly significant role as the flow Mach number increases [7]. Indeed, the most important parameters to evaluate the engine performance are the inlet pressure recovery, burner entrance Mach number, and nozzle efficiency. In an air-breathing device, the compatibility of these components with the vehicle is an important requirement to effectively control changes in speed, altitude, and airflow over the operational flight speeds [27,28]. The typical configuration places the engine on the lower surface of the vehicle. The external vehicle surfaces become components of the propulsion system, i.e. the vehicle forebody acts as the engine intake performing a large percentage of the inlet compression, whereas the vehicle aft becomes part of the nozzle.

A critical design question is the degree of compression the inlet is able to achieve relative to the freestream conditions. The optimal inlet compression is a function of several

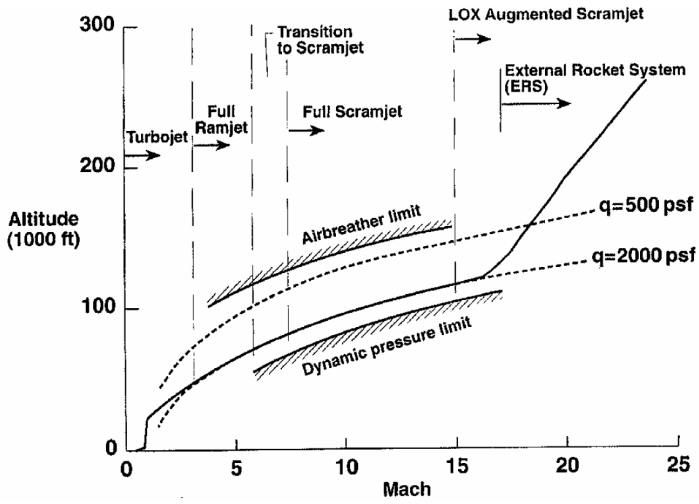

Figure 1.7: Hypersonic airbreathing flight corridor from Hunt [25].

conflicting factors which must be considered for each specific application. Too little compression may introduce difficulties in obtaining a stable combustion or lead to low efficiency of the engine cycle. Too high compression may not only dictate onerous constraints, such as the need for variable geometry to start the inlet or flow control to avoid boundary layer separation, but also leads to significant losses and high external drag.

A number of different forebody/inlet configurations with fixed and variable geometry have been designed since the 1960s to generate a specific level of compression over a wide range of flight Mach numbers [29, 30]. Three different types of hypersonic inlets can be employed to guarantee a certain compression ratio, namely: external, mixed, and internal compression [22]. In an external compression intake, the flow that enters the high-speed engine is compressed by means of shock waves located in front of the engine. This kind of compression allows the inlet to operate over a wide range of Mach numbers since it is self-starting and spills the flow at Mach numbers below the design point. The compression process in the internal compression inlet is performed by shock waves that are internal to the engine. As a consequence, this type of inlet can be shorter than the previous type, but difficulties arise in the integration with the vehicle structure and the need of an accurate variable geometry design. Taking into account these considerations, the majority of scramjet inlets have been developed to include both external and internal compression [31].

A high-speed inlet is designed to work at its optimal conditions, defined as the design point. In reality, during flight, an inlet works in the so-called off-design conditions when it experiences a variety of additional phenomena such as adverse flow conditions related to shock/shock interactions, viscous effects, and shock wave/boundary layer interactions. If these effects become too severe the inlet unstarts. The unstart of a hypersonic inlet is a phenomenon in which the shock wave structure, developed inside the inlet, is expelled outside. This produces an abrupt reduction in the captured mass flow and total pressure due to the spillage of air, and consequently a significant drop of engine thrust. The reasons that may cause an inlet to unstart are variations of flight Mach number, angle of attack, flight altitude, and back pressure. Unstart of hypersonic inlets has been widely studied [32, 33] in order to determine methods to predict this phenomenon allowing to widen the range of flight conditions [34–37]. As reported by Wagner et al. [38, 39], the unstart flow structure is highly three-dimensional and, since this phenomenon is remarkably violent and may cause catastrophic damages to the aircraft during flight, it must be avoided and controlled [40].

Possible ways to alleviate unstart include inlets of variable geometry or the control of flow spillage with a proper duct bleeding [7]. However, Emami et al. [41] showed that the shock wave/boundary layer interaction is the mechanism which causes inlet unstart independently of the inlet contraction ratio and mass capture. Che-Idris et al. [42], in agreement with Nair et al. [43], showed that even small changes in cowl height can effectively reduce the internal shock spillage and unstart despite the total drag increase due to a larger frontal

area. The detrimental effect of the impingement of the ramp shock on the internal duct walls can be mitigated with the inwards deflection of the cowl. This expedient, which has an impact comparable to the bleeding of the throat boundary layer, provides the largest pressure endurance with an optimal cowl convergence angle of 8 deg [44].

Raj & Venkatasubbaiah [31] developed a new methodology to design a mixed compression hypersonic inlet with the computational fluid dynamics analysis. It was found that the shock-on-lip condition, which is based on one-dimensional inviscid gas dynamic relations, does not occur in the viscous and two-dimensional models. Numerical simulations performed by Saha & Chakraborty [45] showed that adiabatic or isothermal wall boundaries have a pronounced effect in estimating the performance of the intake. Compared to the isothermal wall, an adiabatic wall provokes a greater flow spillage and the occurrence of a large separation bubble at the intake entrance. In disagreement, Wang & Guo [35] observed that during engine self-starting, the separation bubble at the inlet entrance remains until the freestream velocity is accelerated to the starting Mach number.

Previous studies on the unstart of high-speed engines were not able to properly describe the physics of the phenomenon because its oscillatory nature, experimentally observed by Tan and Guo [46], was not considered. The oscillations of the shock system at the exit of the inlet, known as buzz, is a complex phenomenon which causes variation of both inlet mass flow and pressure, and has detrimental effects on the stability of the engine that may lead to thrust loss, engine surge, or structural damages to the propulsion system [46]. The existence of "little buzz" and "big buzz" has recently been observed by Soltani & Farahani [47]. The mechanism of little buzz was thought to be due to an acoustic resonance phenomenon excited by the presence of a shear layer under the cowl lip whereas big buzz may exist before the buzz starts and is triggered by a boundary layer separation on the compression ramps. Boundary layer separation regions can be experimentally detected with several approaches. A well-established experimental method, pressure sensitive paint, is capable of providing a quantitative map of the pressure distribution over a surface, giving an accurate measurement of separation regions. Although pressure sensitive paint has been widely used for this purpose, its application to the study of shock train in internal flows has rarely been used [48].

The lack of a systematic investigation into the general characteristics of the inlet instability, at both on- and off-design conditions, is mainly caused by the lack of flow visualisation results, inaccuracy of the simulation tools, inconsistency between the flight and ground-simulated conditions, and the inability of the theoretical analysis to describe this complex phenomenon. Through the insight into the interactions of shock waves with the boundary layer that generate in long and narrow ducts, this work aims to provide qualitative and quantitative tools to improve the design of air-breathing inlets.

1.2 Aims and objectives

This project has the following main objectives:

- To design a wind tunnel that allows the study of the shock train in different flow and geometrical configurations.
- To implement a pressure sensitive paint system to measure transient shock wave phenomena at high speeds.
- To contribute to a better understanding of the complicated flow mechanisms involved in the shock train phenomena and to evaluate numerical techniques for such flows.
- To investigate the flow dynamics of the shock wave structure which develops inside a rectangular cross-sectional area duct at a flow Mach number of approximately 2.
- To analyse the sensitivity of the shock train to variations in the geometrical configuration and flow properties.
- To examine the effect of a back pressure periodical forcing on the flow behaviour with transient simulation.

1.3 Thesis structure

The structure of the dissertation is presented as follows.

Chapter 2 illustrates the state-of-the-art on high-speed engine intakes, and discusses the flow physics which develop inside. The purpose is to describe the physical mechanisms of shock trains occurring inside channels as well as the methodologies commonly employed to study this phenomenon.

Chapter 3 provides the theoretical background of the employed numerical method.

Chapter 4 introduces the experimental apparatus and methodologies employed in this project.

Chapter 5 describes the procedure and the choices adopted in designing the wind tunnel along with the theoretical background. A section is dedicated to the validation of the wind tunnel nozzles.

Chapter 6 discusses the numerical results of shock trains in rectangular ducts. The CFD methodology is firstly applied to two test cases available in the literature. The numerical results are compared with experimental data in order to validate the numerical solver and gain confidence in the numerical procedure that is applied to the current configuration.

Chapter 7 concludes with a summary of the main results achieved and recommendations for future investigations are described.

Appendix A provides the details about the theory behind the Method of Characteristics used to design the nozzle contours.

Appendix B includes the design of the Pitot rake for measuring the velocity profile in the test section of the wind tunnel.

Appendix C lists the author's publications.

2 | Literature survey

THE study of the physics of internal flows interacting with the boundary layer has received increasing interest with particular attention for the development of methodologies to enhance the performance of flow devices operating at high speeds, the combustion efficiency, or the mixing of fuel injected from the combustor walls. The actual knowledge of shock train and boundary layer development has been achieved with the contribution of different methodologies integrating experiments, numerical simulation and analytical analysis. The purpose of this chapter is to carry out a review covering the aspects that characterise the flow structures that develop inside the intakes of air-breathing vehicles.

2.1 Shock train

During flight at altitude, low density air enters the engine inlet, where it is compressed before reaching the combustor. In the majority of high-speed inlets the flow compression is achieved using both external and internal processes by means of shock waves. Internal compression is achieved inside the isolator through an extremely complex mechanism characterised by a shock wave structure that spreads over a long distance in the flow passage [18]. The combustion of fuel causes a rapid pressure rise in the combustion chamber and the formation of a shock wave structure inside the isolator results in different conditions upstream and downstream of the flow passage.

For a supersonic flow in a duct, Crocco [49] highlighted that the deceleration from supersonic to subsonic velocity does not occur through a normal shock, but with a more complicated and gradual transition, also confirmed by Matsuo et al. [50]. In the inviscid limit, in the absence of a boundary layer, the shock structure would be a single normal shock wave [51]. However, due to the existence of a viscous boundary layer, this simple pattern rarely occurs and the shock structure is spread into a series of oblique or lambda shock waves [16].

The fundamental characteristics of the interaction between a shock wave and the boundary layer with the creation of a series of shocks was initially described by Crocco [49] in 1958. The shock wave/boundary layer interaction creates a local thickening of the boundary layer and leads to the formation of a virtual nozzle throat. As Figure 2.1 shows, a throat-like

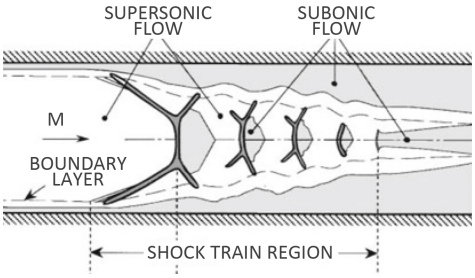

Figure 2.1: Two-dimensional sketch of the shock wave/boundary layer interaction [52].

geometry is generated between two consecutive shocks with a resulting change in the duct cross-section. Therefore, immediately downstream of the main shock, the flow is accelerated again to supersonic speeds through this virtual nozzle until the next shock recompresses the flow again [52, 53]. The shock system is referred to as a shock train or pseudo-shock, however some researchers have made a distinction using the term shock train to mean a series of shocks and the term pseudo-shock to refer to the entire region of pressure rise [50, 54].

The shock train system depends on the passage geometry, wall friction, Mach number, Reynolds number based on the tube height, boundary layer thickness, and pressure conditions at the two extremities of the duct [17]. As the flow Mach number increases, the effect of increased blockage becomes more relevant with the consequent promotion of multiple shock interactions, production of lower pressure recovery, and extension of the wave structure along the duct [55].

Lustwerk [56] observed that the shock wave structure changes depending on the variation of the boundary layer thickness upstream of the shock train, also referred to as flow confinement [50]. The flow confinement is defined as the ratio of the undisturbed boundary layer thickness, δ, to the duct half height, h. This is in agreement with Babinsky & Harvey [57], who reported that multiple shocks are more likely when the ratio of boundary layer displacement thickness to duct height is greater than a few percent. Morgan et al. [54] found that the flow confinement is more important than total pressure loss in locating the initial shock within an isolator. Weiss et al. [58] confirmed that the confinement level and Mach number are the dominant variables which characterise the position and length of the shock train, whereas the Reynolds number has a much smaller effect, and therefore different experiments can be easily compared [59]. On the other hand, it was reported by Neumann & Lustwerk [60] that the length of the shock region is affected by scale effects since it depends on the equivalent length-to-diameter ratio.

Fischer & Olivier [61] have more recently demonstrated that the shock train length is dependent on the ratio of the wall temperature to that of the free stream flow. Adiabatic or hot-wall boundary layers are less resistant to adverse pressure gradients than cold-wall boundary layers because cold-wall boundary layers are thinner and have higher skin friction.

2.1.1 Shock train structure

As illustrated in Figure 2.2(a), with shock Mach numbers up to 1.2, a very weak interaction takes place: the shock wave is close to an inviscid normal shock and no separation occurs at the wall [50]. Ikui et al. [62] reported that with a low Mach number the shock wave/boundary layer interaction is weak (see Figure 2.2(b)), the shock is nearly normal and changes inclination continuously with increasing distance from the wall [63]. The boundary layer on the walls is thin with an adverse pressure gradient with possible separation, which tends to reattach immediately [54].

As the Mach number increases up to approximately 1.5, as shown in Figure 2.2(c), a stronger interaction takes place and the foot of the shock bifurcates near the wall surface, gradually forming a λ shape. The boundary layer at the shock becomes thicker and the pressure rise is sufficient to generate separated regions. Above Mach 1.5 the compression downstream of the shock becomes stronger and forms successive shock waves with regular or Mach-type reflections, as in Figure 2.2(d) [64]. At the point of bifurcation, a secondary shear layer in the form of slip lines may be observed. At a Mach number of 1.86, the λ shape changes into a χ shape, and at a Mach number of 2.42, the shock structure becomes a series of weak oblique shocks. Sugiyama et al. [65] observed the λ-shape structure up to Mach 2, but at a Mach number of 4 a dramatic change of the separation mechanism takes place, in agreement with Hataue, [66] who faced some difficulties in observing a clear shock train at Mach 3. Sullins [16] was able to observe the formation of the precombustion shock system at a Mach number of 5.7, but above Mach 5.95 the pressure in the combustor reaches a value below the separation pressure and the shock system is eliminated. The flow remains supersonic through the entire engine and the isolator is used as a constant area combustor with fuel injectors installed upstream of the isolator, as illustrated in Figure 2.3.

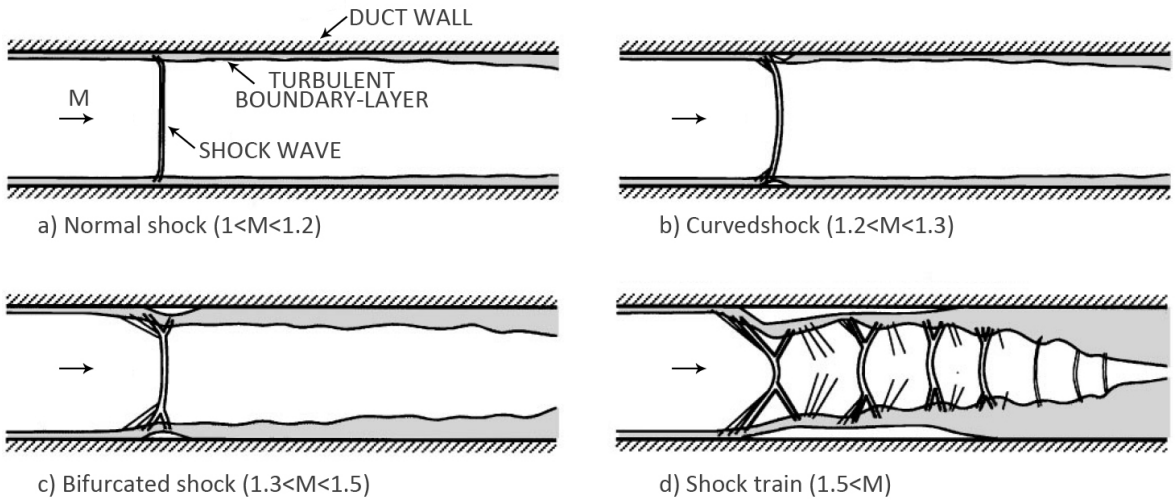

Figure 2.2: Schematic of shock wave/boundary layer interaction in a constant area duct [50].

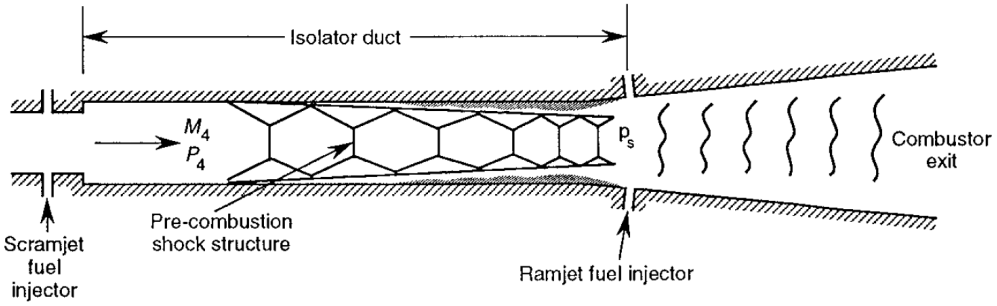

Figure 2.3: Schematic of a scramjet combustor utilised as an isolator duct in the ramjet mode of operation [18].

Figure 2.4 shows the typical configurations experimentally observed with two values of inflow Mach number: the λ shock train or normal shock train, in Figure 2.4(a), and the χ shock train or oblique shock train, in Figure 2.4(b). The Mach number at which this distinction takes place is in the range between M= 2 and M=3 [29]. The schematic of these shock train configurations is illustrated in Figure 2.5. The series of normal shock waves, characteristic of flows with thin inlet boundary layers and low Mach numbers, in Figure 2.5(a), is comprised of successively decreasing strength and distance between succeeding shocks up to the point where a terminal shock occurs [53]. The major portion of the compression takes place at the first normal shock which splits into two different parts as it interacts with the boundary layer. After the first shock, the boundary layer reattaches and grows generating successive shock waves that are normal at the centre of the duct. With higher inflow

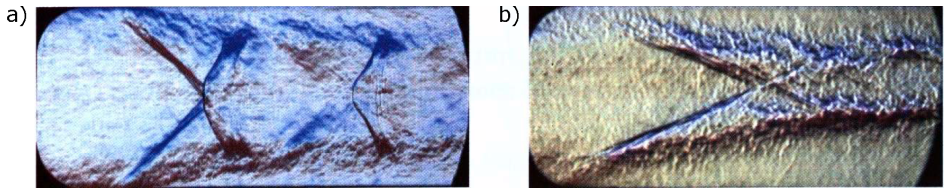

Figure 2.4: Schlieren photographs of: a) λ shock train at M= 2; b) χ shock train at M= 4 [67].

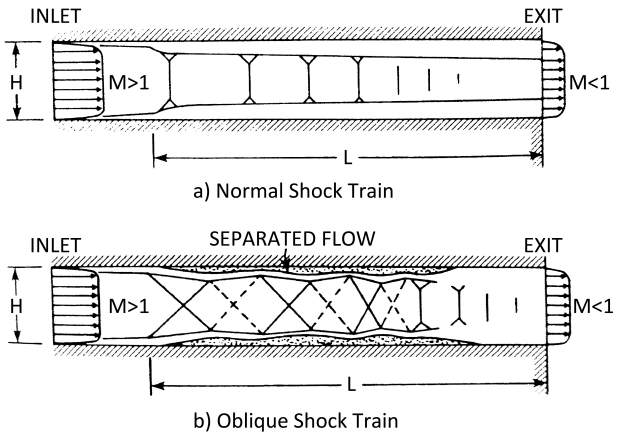

Figure 2.5: Schematic of the flow pattern of: a) Normal shock train; b) Oblique shock train [29].

Mach numbers (M> 3) and a larger flow confinement, the normal portion of the first shock gradually reduces and the λ shocks at the opposite walls grow until they combine into an oblique shock wave. Carroll et al. [68] observed that the same behaviour extends also to the subsequent shock waves, and the flow pattern, called oblique shock train, is similar to the schematic depicted in Figure 2.5(b). In this case, the initial oblique shock separates the boundary layer, reflects from the opposite walls of the duct, and propagates downstream alternating between compression and expansion. The boundary layer remains separated for long distances.

When the interaction of the shock wave with the boundary layer is particularly strong, the shock train is followed by a mixing region, after which the flow is fully subsonic and uniform. The entire structure, schematically shown in Figure 2.6, is called a pseudo-shock wave [62]. According to Ostras & Penzin [69], the pseudo-shock is composed of a dissipation layer at the walls, and a central almost isentropic layer. The mixing region, called supersonic tongue by Om et al. [55], consists of a double-tongue-shaped supersonic flow, which passes through a system of compression waves near the centreline of the duct, bounded by a subsonic outer region [58]. This region changes its shape and extension with changing Mach number due to the boundary layer thickening and its occurrence depends on the duct length [68]. Nagai [70] observed that the radial distribution of the total and static pressure across the shock train is subject to changes due to the presence of shock waves and viscous diffusion. As illustrated in Figure 2.7, at the beginning of the shock train the static pressure distribution exhibits a complicated pattern whereas towards the end of the shock train the pressure presents a more gentle profile. Nevertheless, discrepancies with the computed prediction of the mixing region are present, since compared to experimental observations, a smaller embedded supersonic region behind the shock is obtained [55].

A typical wall pressure variation through a pseudo-shock is illustrated in Figure 2.8. In the initial portion of the shock train, the pressure increases rapidly because of the oblique or bifurcated normal shock waves. At the centre of the duct the flow undergoes successive local changes from supersonic to subsonic through multiple normal shocks, which are not detected by wall pressure measurements because the surface pressures tend to be smeared out due to the dissipative behaviour of the boundary layer. In the mixing region, for x= 5 to x=11 in Figure 2.8, the pressure continues to rise with a lower rate until it reaches a maximum

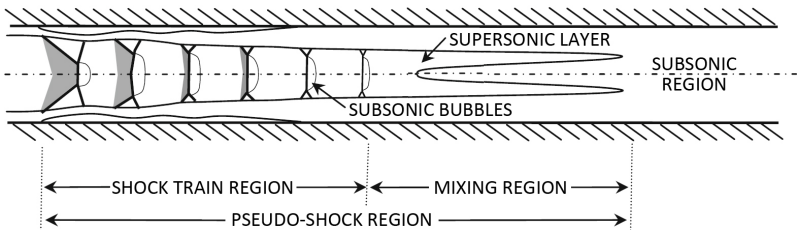

Figure 2.6: Sketch of a pseudo-shock system [58].

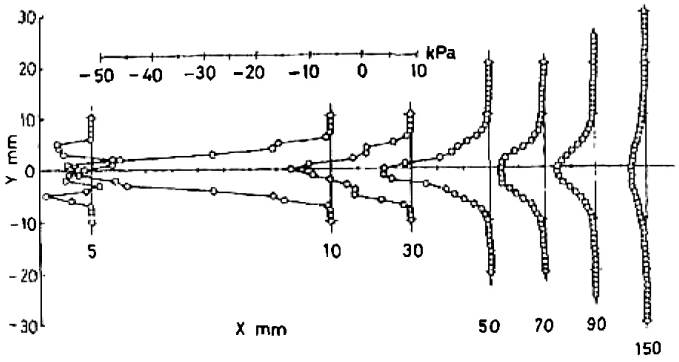

Figure 2.7: Radial distribution of static pressure across the shock train system [70].

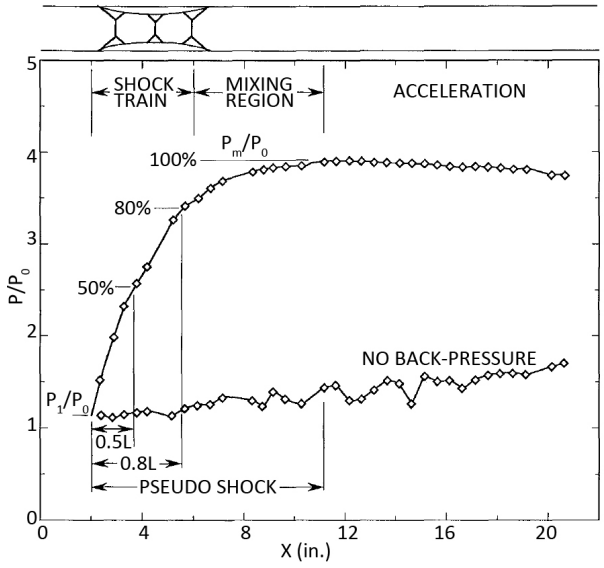

Figure 2.8: Wall pressure variation through the shock train at Mach number of 2 [18].

where the flow is decelerated to subsonic speeds, after which the flow is accelerated again, and the pseudo-shock region terminates [50]. The actual separation of the shock train and the mixing region is not clearly defined because the pressure measurements are not able to significantly show changes between the two regions [58]. It can be observed that the pressure increases rapidly through the shock train and more moderately in the mixing region: 50% of the maximum pressure rise is achieved in approximately 1/4 of the length of the shock train, and 80% in approximately 1/2.

For each Mach number, the pressure recovery along the shock train is smaller compared to that through an inviscid normal shock wave since each shock causes a significant total pressure loss [64] and viscous effects in the mixing region [58]. The static pressure ratio across the shock train reduces as the boundary layer displacement thickness increases. This trend becomes more evident for higher Mach numbers [71]. As the experimental data in Figure 2.9 show, the maximum isolator exit pressure is achieved when the pseudo-shock and the isolator are of the same length. The length of the pseudo-shock is defined as the

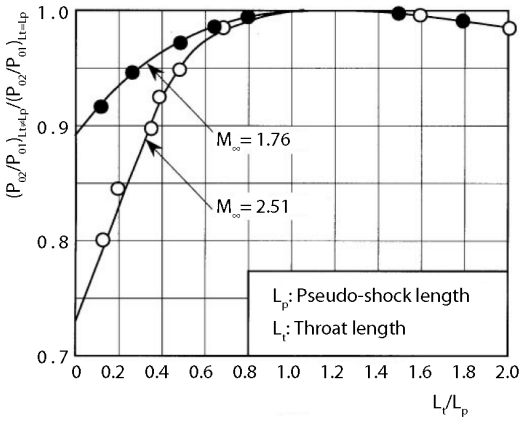

Figure 2.9: Total pressure recovery as a function of isolator and pseudo-shock lengths [72].

region from the head of the shock train to the end of the static pressure recovery region. It increases with both the boundary layer thickness relative to the duct diameter and the Mach number upstream of the shock train, and has been found to vary in the range of 4 to 15 tube diameters [73]. Therefore, the isolator must be designed to be of sufficient length to prevent inlet unstart, but not overly long to avoid excessive weight and additional shear losses [20]. As Reinartz et al. [74] experimentally observed, the growth of the boundary layer introduces viscous losses which cancel out the advantage of an additional length. On the other hand, the magnitude of the pressure profile decreases with decreasing isolator length, and this trend becomes more evident for higher Mach numbers [72, 75].

The optimum length of a constant area passage has been found to lay between 8 to 12 tube diameters for Mach numbers in the range 1.8 to 4.2 [60]. According to Sullins [18], with a duct length of 10 to 20 duct heights, the shock train pressure rise can reach up to 95% of the normal shock strength but, as pointed out by Emami et al. [41], the optimal isolator length must be designed as a trade-off of all the component requirements over the flight envelope.

2.1.2 Shock train oscillations

The description of the shock train is further complicated by the presence of a violent and irregular oscillating behaviour, which was initially investigated by Ikui et al. [76] and confirmed by further studies [77–79]. High-speed schlieren, obtained by Gawehn et al. [52] and illustrated in Figure 2.10, shows that the shock waves of the shock train are not located at a fixed point but oscillate with time about the time-mean position even when the upstream and downstream pressures remain constant. Yamauchi et al. [80] encountered difficulties in visualising the shock train in their PIV mean streamwise velocity measurements because of the shock wave fluctuations. The time history of the wall pressure measured upstream and downstream of the shock train front position, in Figure 2.11, demonstrates the unsteady nature of the shock train.

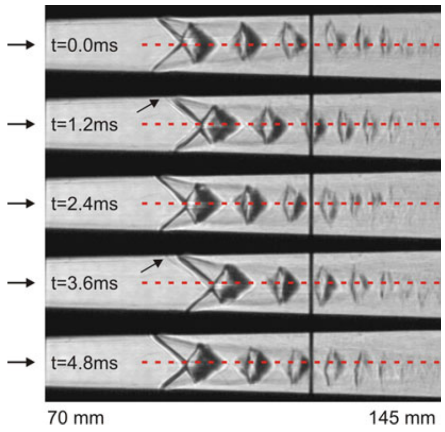

Figure 2.10: Schlieren image of the oscillating and asymmetric shock train system [52].

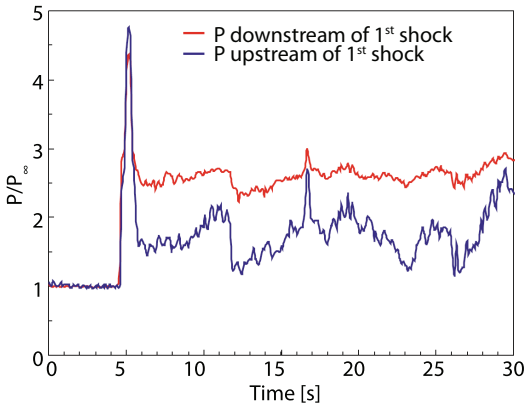

Figure 2.11: Wall pressure change distribution around shock train [80].

Experimental data from Ikui et al. [76] showed that the oscillation amplitude of the first shock in the shock train is smaller than those of the subsequent shock waves, leading the authors to conclude that the oscillation of the first shock influences the oscillation of the entire flow structure. The mechanism of the shock train oscillation was described by Yamane et al. [81, 82] to be caused by the interaction of two frequencies which travel in the opposite direction and excite each other. The pressure fluctuation due to the oscillation of the air in the divergent passage downstream of a straight duct travels upstream through the shock train and excites the first shock oscillation. This generates a strong pressure fluctuation which propagates downstream and, in turn, maintains the oscillation in the channel.

Gawehn et al. [52] hypothesised that the axial movement of the shock train oscillation is caused by the boundary layer oscillations in the shock train. Sugiyama [83] conjectured that the oscillation mechanism of the shock train is caused by the thickening of the boundary layer in the proximity of the first shock wave of the shock train. A throat-like shape is generated between the first and the second shocks, changing the actual throat cross-section. Since the boundary layer thickness changes along the duct, the throat cross-section also changes and induces the first shock to oscillate with a frequency that depends on the basic oscillation of

the air column between the first shock and the duct exit. Similarly, the computed results in the core flow obtained by Robinet & Casalis [84] showed an increase of the longitudinal mean velocity behind the shock due to the expansion caused by the separation bubble in the boundary layer. However, the authors demonstrated that the self-sustained oscillation can be predicted with the inviscid quasi-one-dimensional stability theory and, therefore, this phenomenon is not caused by the transverse waves carried by the boundary layer.

According to Sajben et al. [63], the characteristics of the fluctuations are dependent on the cause of separation, i.e. pressure-gradient or shock-induced separated flows. Su & Zhang [85] identified the back pressure as an important variable on the shock train unsteadiness. The entire shock train oscillates with a frequency which increases with the pressure ratio. Hsieh & Coakley [86] found the oscillation frequency dependent on the duct length-to-height ratio. Bogar et al. [87, 88] observed downstream-travelling counter-rotating vortices originating near the upstream edge of the separation bubble, but no information has been deduced to relate the vortices' characteristics with the oscillation frequency.

Gawehn et al. [52] also observed that, while oscillating, the shock structure changes between symmetric and asymmetric, but this behaviour was not captured by numerical simulation even when using the three-dimensional unsteady Reynolds-averaged Navier-Stokes (URANS) equations. Similar results were obtained by Sun et al. [67] who observed that the shock system randomly attached to the bottom or top wall in the experiments, but the computations were not able to reproduce these asymmetric characteristics. Sugiyama [83] reported that λ- and χ-type shock waves are characterised by different acoustic properties and, as the location of the pseudo-shock wave moves downstream, the shock is transformed from λ to χ type. Xiao et al. [89] observed that, for a supersonic flow in a convergent-divergent nozzle with a moderate expansion ratio, the flow asymmetry does not switch side during a given run. However, for the same level of perturbation, from one experimental run to another, the asymmetry could change side, in agreement with Papamoschou et al. [90,91]. The numerical investigation of diverging isolators with a rectangular cross-section performed by Kawatsu et al. [92] led to the conclusions that a large separation region appeared at only one corner of the test section. Additionally, once the separation is formed, it remains in the same position and does not move to another corner. This asymmetry generates a violent noise and fluctuating wall load which, if strong enough, may provoke fatigue failure [50].

In contrast to attached flows, the acoustic characteristics in the presence of flow separation have been found to be more complicated and not predictable with acoustic theory [87]. Hsieh et al. [93] imposed a sinusoidal pressure fluctuation at the exit plane of the diffuser to simulate the response of a ramjet inlet to the unsteadiness of the combustion chamber using two-dimensional URANS equations. The computed solution showed a non-sinusoidal variation of velocity at the exit plane, in contrast with both the acoustic theory and small-perturbation models. According to these two models the velocity is described by a sinusoidal

function of the same frequency with altered phase angle and amplitude.

The investigation carried out by Oh et al. [94] reproduced the movement of the terminal shock in response to an externally imposed pressure oscillation in the diffuser. This produced large vorticity fluctuations in the radial direction, as well as variations of the size of the boundary layer separation and the terminal shock configuration. The authors concluded that a supersonic inlet under supercritical operation acts as an effective acoustic damper, absorbing disturbances arising downstream. A more recent study by Klomparens et al. [95] analysed the response of a shock train due to a downstream pressure force reporting that the oscillatory motion of the shock train speed is decomposed into low frequency and high frequency components. The magnitude of the high frequency component is larger but does not show the oscillatory motion of the shock train.

2.1.3 Isolator duct geometry

The structure of a shock train is significantly affected by a change in the area because it extends over a great distance along the passage, and even in a straight channel the analytical calculation of the shock train length is very complicated [96].

A small divergence angle or constant area ducts produce higher efficiencies of shock compression. In this condition, a positive velocity gradient exists in the subsonic flow downstream of the shock compression region which stabilises the boundary layer and reduces separation [56, 97]. According to Walther et al. [98] the use of divergence angles of 1 to 2 degrees on both the duct walls of the combustor inlet is effective in mitigating the steep static pressure rise downstream of the fuel supply point and counteracts the thermal blockage by heat addition. The small level of divergence is meant to counteract the boundary layer growth so that the effective fluidic cross-section remains constant. Huang et al. [23] found that small divergence angles of the isolator may have a significant impact on the shock structure in scramjet isolators. Figure 2.12 shows the effect of divergent angle on the shock train with a constant back pressure. As the divergence angle increases from 0 to 1 degrees, the front of the shock wave moves towards the entrance of the duct, and the shock train changes from an oblique to a normal shock configuration. However, for duct angles greater than 1.5 deg, the flow expansion at the entrance of the isolator causes a larger separation of the boundary layer on the walls. The front of the shock train is pushed downstream with a zone of negative pressure ahead of the shock train and the shock train exhibits again the oblique shock characteristics. This is due to the fact that small expansion angles can reduce the effect of the boundary layer separation and decrease the intensity of the first shock wave. When the expansion angle is sufficiently increased, the boundary layer separation becomes so strong that it cannot be counteracted by the beneficial effect of the expansion angle. This behaviour is illustrated in Figure 2.13.

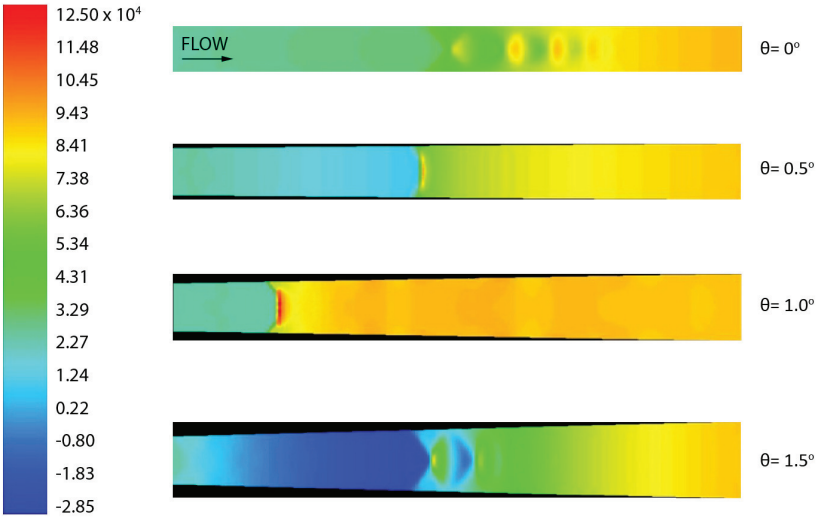

Figure 2.12: Numerical static pressure contours in Mach 2 scramjet isolators with different divergence angles [23].

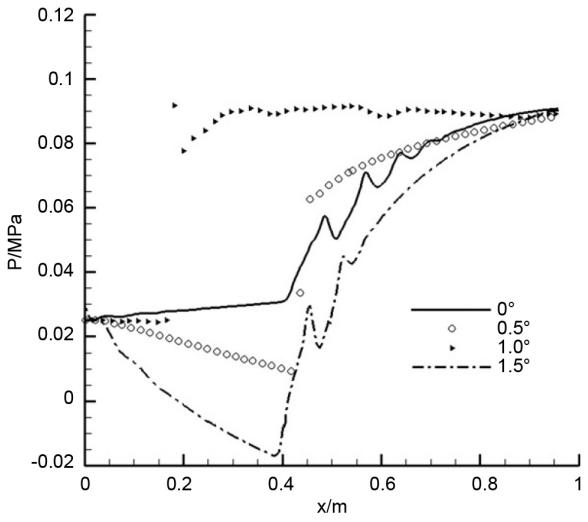

Figure 2.13: Static pressure distribution along the centreline of the duct in Mach 2 scramjet isolators with different divergent angles and constant back-pressure of 90 kPa [23].

The majority of research on high-speed isolators has focused on cylindrical ducts, and only recently on rectangular cross-sections. This choice is due to the fact that the axisymmetric configuration minimises the three-dimensional effects from the shock wave/boundary layer interactions encountered in rectangular channels [53]. Kawatsu et al. [92] reported that in diverging rectangular ducts a large separation of the boundary layer, caused by the first shock of the shock train, occurs only at one corner of the upper wall of the test section whereas in a constant area duct the separated region was observed near all the corners. Additionally, in a constant area duct, from both numerical and experimental results shown in Figure 2.14, the boundary layer separation occurs only near the corners of the duct but not at the centre plane of the test section as it is perceived with schlieren photography. The circular

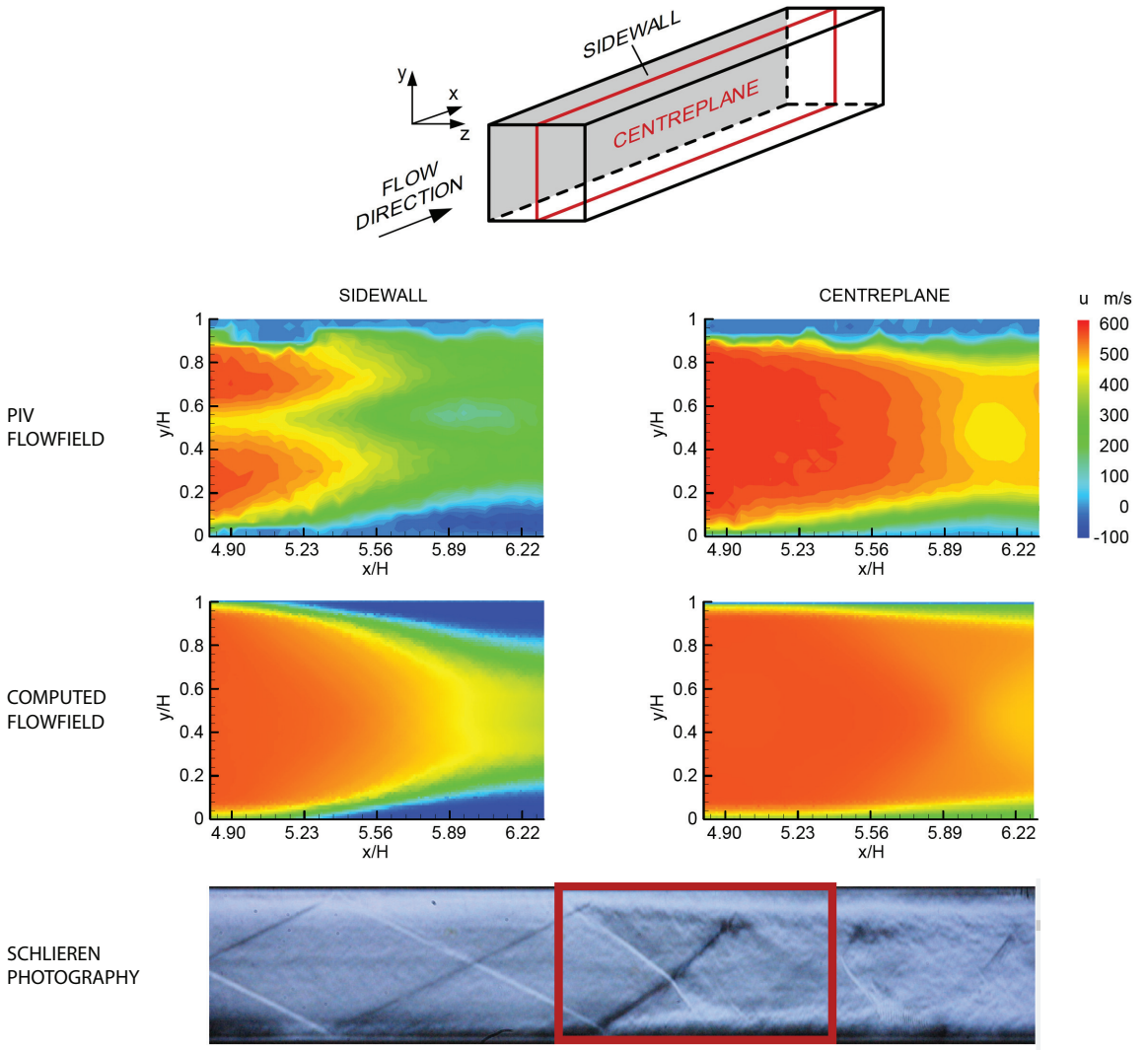

Figure 2.14: Contours of the streawise component of the velocity vector on x-y plane and schlieren photograph in a constant area duct at flow Mach number of 2.3 [92].

duct has the strongest capability for supporting the combustion backpressure compared with other shapes [99].

Billig et al. [20] stated that the trend of the pressure rise for cylindrical and rectangular cross-sections is quite similar, suggesting that the shock train characteristics may also be similar. As reported by Bement et al. [19], no similarity law linking the various geometries and the applicability of correlations to the design of rectangular isolators have been reported. Lin et al. [99] showed that, compared to rounded cross-sectional area ducts, in the rectangular configuration the pressure profile of the shock train initially rises steeply, reaches a maximum value early, and drops quickly at the isolator exit. Also, the maximum pressure rise is smaller, independent of the Mach number. These differences were attributed to the fact that in the rectangular duct, the larger cross-sectional perimeter and the presence of the four corners lead to an increased cross-sectional area of the duct covered by the boundary

layer, thus reducing the effective free-stream area. On the other hand, for the same Mach number, the leading edge of the shock train was detected to be roughly at the same axial position inside the isolator for both circular and rectangular cross-sections. Sridhar et al. [100] numerically obtained almost the same total pressure recovery for isolators of square and square-to-circular shapes. However, as illustrated in Figure 2.15, the two geometries led to different flow characteristics, i.e. the square isolator is characterised by a longer shock structure with the shock train front placed more upstream, and with thinner and longer separated regions due to the influence of corner vortices.

The macroscopic structures and characteristics of shock train forming in rectangular ducts have mostly been investigated for Mach numbers up to M= 2. Few studies have covered higher Mach numbers and Sugiyama [65] was one of the first to extend the range up to M= 4. It was highlighted that a Mach 4 shock train is characterised by large pressure fluctuations and presents an asymmetric flow configuration that greatly deviates from the top to bottom walls. Sullins [18] noticed that the back pressure can be controlled without moving the shock train, using a step in the duct, as schematically illustrated in Figure 2.16. When the shock train starts downstream of the step, the maximum pressure is less than that in a constant area duct and a significantly longer duct is required to reach the same pressure. When the shock train starts upstream of the step, the area expansion caused by the step yields a slightly higher pressure due to subsonic diffusion across the step.

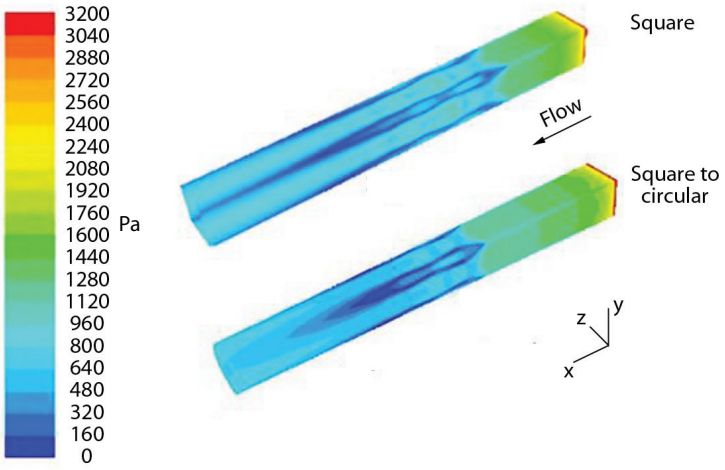

Figure 2.15: Wall shear stress contour in a square duct and a square-to-circular isolators [100].

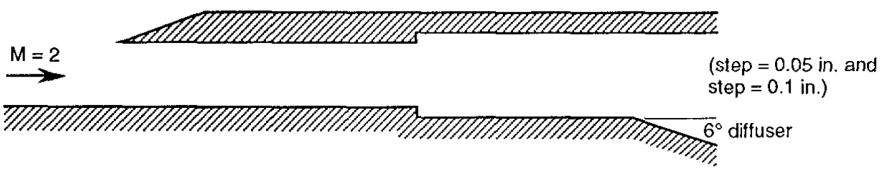

Figure 2.16: Schematic of a rectangular isolator with a step [18].

2.2 Analytical and numerical modelling of shock trains

An extensive investigation on pseudo-shock waves was carried out by Matsuo et al. [50] in 1999 and other experimental studies with the aim of validating the various analytical models used [58]. The numerous variables which contribute to generating a complicated interaction between the shocks and the boundary layer make the analysis of the flow field extremely challenging. For this reason, simplified analytical formulations have been developed to estimate the pressure distribution and the length required to achieve the necessary pressure rise in the isolator. The advantage of this conservative approach is that it allows the parametrisation of the static pressure using only the conditions ahead of the shock train as well as avoiding to solve the full Navier-Stokes equations [101]. The majority of the models assume the absence of heat transfer, however if surface heat transfer is included, the local and global effects of a shock wave/boundary layer interaction will be altered [102]. As stated by Inger et al. [103], even a small variation of the surface temperature above the adiabatic value significantly influences the global aerodynamics and therefore the solution of the governing equations.

The flow in a shock train is far from one-dimensional [50, 52], but the mechanism of formation of multiple shock waves can be explained through an equivalent one-dimensional model, as outlined by Om & Childs [53] and shown in Figure 2.17. The first shock wave causes an increase of the boundary layer thickness large enough to choke the flow. Therefore, the subsonic flow immediately behind the first shock wave is accelerated through the converging channel between sections AA and BB, where it reaches sonic conditions. After section BB, the divergent duct causes the supersonic flow to expand and form a second normal shock wave. At this point, the increased thickness of the boundary layer starts the same process described for the first normal shock. The second normal shock in turn produces another normal shock wave, and the mechanism is repeated until the normal shock wave becomes weak enough so that the flow is no longer choked.

The theoretical total pressure recovery through a normal shock in a duct, having an initial boundary layer, was originally calculated by McLafferty [8] using Equation 2.1 on the basis

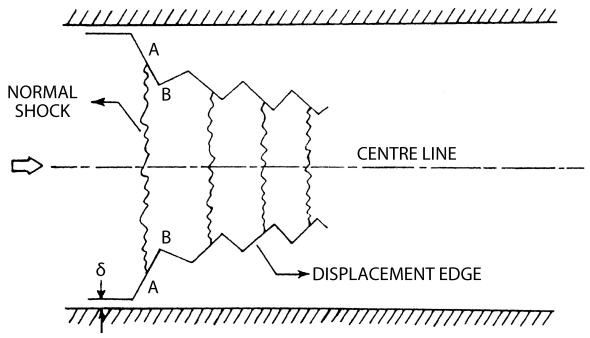

Figure 2.17: One-dimensional flow model of the formation of multiple shock waves in a duct [53].

of two-dimensional equations of continuity, conservation of momentum, and conservation of energy,

$$\frac{P_{02}}{P_{01}} = \left(\frac{P_1}{P_{01}}\right)\left(\frac{P_{02}}{P_2}\right)\frac{K_{W1}}{K_{W2}}\left(1 - \frac{2\delta^*}{H}\right) \tag{2.1}$$

where δ^* is the boundary layer displacement thickness, H is the height passage and K_W is an airflow parameter defined as:

$$K_W = \frac{2}{H}\int_0^{H/2} \frac{1}{(P/P_0)\,(A/A_*)} dy \tag{2.2}$$

with A/A_* being the isentropic area ratio.

With the assumptions of the formation of a normal shock wave and negligible viscous effects, the calculated total pressure recovery through a normal shock is reduced by an amount proportional to the displacement thickness of the boundary layer approaching the shock. In reality, shock compression in divergent ducts exhibits a gradual increase in pressure at the wall, confirmed by the pressure measurements obtained by Castagna [104]. Although this discrepancy illustrated the inadequacy of the normal shock theory, the accuracy was found to increase with smaller duct divergence angles and higher Mach numbers.

Crocco [49] and Tamaki et al. [105, 106] proposed two analytical models assuming that the overall pressure ratio across the shock train equals that of a normal shock and neglecting the effect of the upstream boundary layer and wall friction in the pseudo-shock region. With its simplicity, Crocco's *shockless model*, schematically illustrated in Figure 2.18 and expressed by Equation 2.3, reveals the essential characteristics of the pseudo-shock,

$$\frac{P}{P_1} = \left(\frac{1 - w'^2}{1 - {w_1}^2}\right)^{\frac{\gamma}{\gamma-1}} \tag{2.3}$$

where γ is the ratio of specific heat capacity and w is the Crocco number or non-dimensional velocity defined as:

$$w = \frac{u}{\sqrt{2C_P T_0}} \tag{2.4}$$

The symbols in Equation 2.4 are defined as follows: u is the axial component of the velocity vector, C_P is the specific heat of air at constant pressure, and T_0 is the total temperature.

The model developed by Tamaki et al. [105,106] referred to as the *shock reflection model*, states that not only the wall but also the main flow is affected by pressure changes. The description of the variation of static pressure occurs across successive oblique shock waves and, therefore, the shock angles of the series of shock waves in the shock train are needed in advance. Even though the mathematical formulation was different, the results of both the

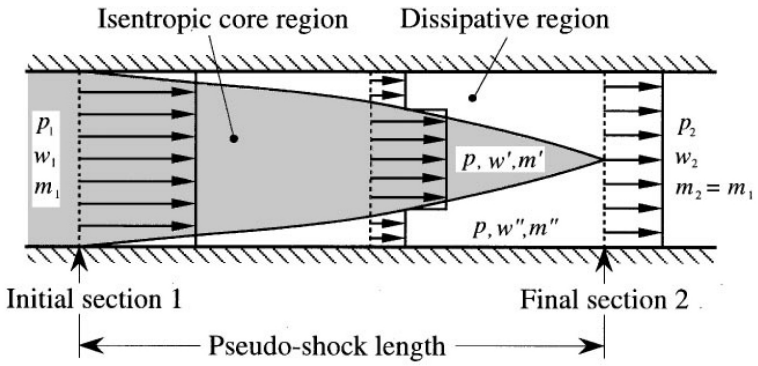

Figure 2.18: Crocco's shockless model [49].

models led to the same flow properties, which strongly diverged from the experimental data.

The assumptions which the *shockless model* relies on, have been found to be the source of the discrepancy with experimental investigations and an improved model, called the *diffusion model*, was proposed by Ikui et al. [62]. The model is illustrated in Figure 2.19 and the analytical form is defined by Equation 2.5,

$$\frac{P - P_1}{P_2 - P_1} = \frac{\left[{w_1}^2 \left({w_1}^2 - 2{w^*}^2\right) + {w_1}^2 {w^*}^2 E\right](1 - E)}{\left({w_1}^2 - {w^*}^2\right)^2 - {w_1}^2 \left({w_1}^2 - {w^*}^2\right) E\,(1 - E)} \tag{2.5}$$

where w^* is the Crocco number at sonic conditions, $E = e^{-c(x/D_{eq})}$, x is the axial coordinate, D_{eq} is the equivalent duct diameter, and c is a coefficient experimentally determined for the deceleration of velocity in high-speed regions of the pseudo-shock:

$$\frac{dw'}{dx} = -cw' \tag{2.6}$$

This model removes the assumption of Crocco's *shockless model* of isentropic flow in the centre of the duct, and is able to determine the length of the shock train, defined as the distance where the velocity in the central core region becomes equal to that in the outer

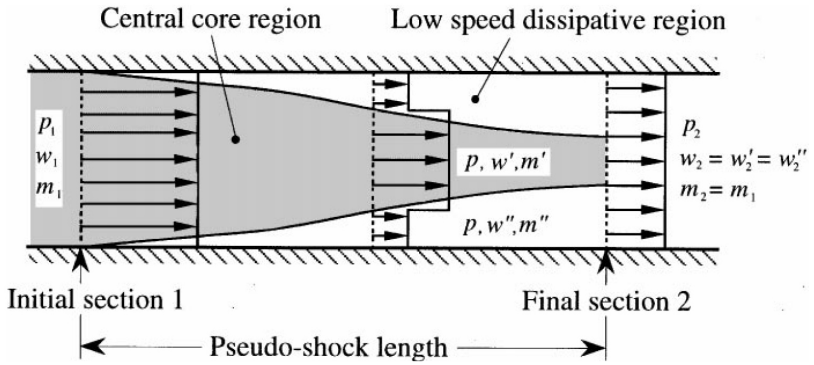

Figure 2.19: Diffusion model proposed by Ikui et al. [62].

dissipative region. In spite of the closer agreement with experimental data, discrepancies remained, particularly for low Mach numbers due to the fact that a low supersonic flow is not fully diffused within the distance, leading to a significant deviation from the assumptions of the uniform flows both upstream and downstream of the pseudo-shock.

More accurate agreement with empirical data was obtained with further improvements by Ikui et al. [73] if the effect of the upstream boundary layer and wall friction losses is included in the model schematically illustrated in Figure 2.20 and defined by Equation 2.7,

$$\frac{P}{P_1} = \frac{1}{\xi}\left[\frac{(1-\mu)}{M'}\left(1+\frac{\gamma-1}{2}M'^2\right)^{-1/2} + \frac{\mu}{M''}\left(1+\frac{\gamma-1}{2}M''^2\right)^{-1/2}\right] \tag{2.7}$$

where μ denotes the mass flow ratio m''/m and ξ is defined as follows:

$$\xi = \frac{(1-\mu_1)}{M_1'}\left(1+\frac{\gamma-1}{2}M_1'^2\right)^{-1/2} + \frac{\mu}{M_1''}\left(1+\frac{\gamma-1}{2}M_1''^2\right)^{-1/2} \tag{2.8}$$

All the aforementioned models have the limitation that only the pressure rise through the shock train region can be determined. Based on empirical results, a quadratic correlation method for cylindrical ducts, expressed by Equation 2.9, was proposed in the 1970s by Waltrup et al. [107–109] to relate the distance over which the shock structure is spread with the flow parameters,

$$\frac{x\left({M_1}^2-1\right)Re_\theta{}^\alpha}{D^{1/2}{\theta_1}^{1/2}} = 50\left(\frac{P}{P_1}-1\right) + 170\left(\frac{P}{P_1}-1\right)^2 \tag{2.9}$$

where D is duct diameter, M_1 is the Mach number, θ_1 is the boundary layer momentum thickness, Re_θ is the Reynolds number based on the boundary layer momentum thickness, and P/P_1 is the pressure rise across the shock train. This equation requires the determination of the boundary layer momentum thickness along the isolator wall, which depends on the surface roughness and the Mach number upstream of the shock train. This method

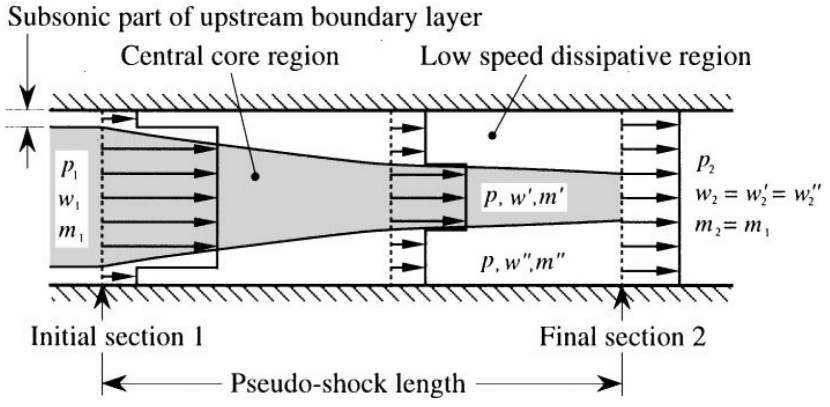

Figure 2.20: Modified diffusion model [73].

was corrected by Billig [110] for its applicability to two-dimensional rectangular ducts by substituting the duct diameter D with the duct height H, as Equation 2.10 illustrates.

$$\frac{x\left({M_1}^2-1\right){Re_\theta}^\alpha}{H^{1/2}{\theta_1}^{1/2}}=50\left(\frac{P}{P_1}-1\right)+170\left(\frac{P}{P_1}-1\right)^2 \tag{2.10}$$

Weiss et al. [58] analysed the different shock train models with different pressure levels and Mach numbers up to M= 2. They concluded that the model developed by Billig [110] in Equation 2.10 accurately reproduced the pressure gradient for the shock train in a rectangular duct at low Mach numbers, in particular in the shock train region. However, a better agreement between the measured and predicted values of the shock train length in the Mach number range from 1.33 to 1.85 was obtained by Wang et al. [111] with an additional correction including the degree of flow asymmetry, D_θ:

$$\frac{x\left({M_1}^2-1\right){Re_\theta}^\alpha}{\left(1+D_\theta\right)^\beta H^{1/2}{\theta_1}^{1/2}}=50\left(\frac{P}{P_1}-1\right)+170\left(\frac{P}{P_1}-1\right)^2 \tag{2.11}$$

where the factor β assumes values based on the actual measured data. The parameter D_θ is defined as:

$$D_\theta=\frac{\theta_{max}-\theta_{min}}{\theta_{max}}\times 100 \tag{2.12}$$

with θ_{max} and θ_{min} being the boundary layer momentum thickness corresponding to different values of boundary layer thickness at the two walls of the duct, as Figure 2.21 illustrates.

It can be observed that when D_θ is zero the flow is completely symmetric at the isolator entrance and Equation 2.11 reduces to Equation 2.10. This experimental correlation was introduced because, in reality, the flow field inside the isolator is asymmetric, even though researchers have put a great deal of effort in studying symmetric conditions [111]. It was also observed that, for a given pressure ratio, the length of the shock train becomes larger as the asymmetry of the flow grows.

In Equations 2.9 to 2.11, the Reynolds number exponent α assumes the value of 0.25, obtained from a regression analysis of the data [110]. However, a recent paper by Sridhar et al. [100] achieved α= 0.225 by averaging the values of square and circular ducts.

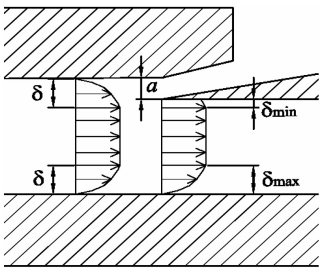

Figure 2.21: Boundary layer asymmetry at the isolator entrance [111].

Zimont & Ostras [112] studied the shock train in the presence of a thick boundary layer and formulated the *jet-flow model* assuming a supersonic jet-like nature of the dissipation zone development. Although the static pressure rise agreed well with the experimental results, the model is quite complex due to the presence of the Bessel function in the integral equations.

If the Mach number and the static pressure inside the shock train are known, the *separation model* proposed by Shchetinkov [113] approximately predicts the configuration of the separation region. The model assumes a negligible flow velocity in the separation region, the transverse pressure gradient at any cross-section and the variation of the total temperature through the shock train region.

Neglecting the wall friction and heat transfer inside the shock train, Nagai & Yaga [114] formulated a relationship through Equation 2.13, in which the ratio of the total pressure at the final and initial sections of the pseudo-shock increases as the boundary layer thickness at the initial section increases,

$$\frac{P_2}{P_1} = \frac{\zeta_1 w_1}{1 - \eta_1 {w_1}^2} \frac{1 - \eta_2 {w_2}^2}{\zeta_2 w_2} \tag{2.13}$$

where ζ and η are the correction factors for the mass flux and energy respectively in the integral equations of continuity and conservation of energy.

Matsuo et al. [115] proposed a *mass averaging pseudo-shock model* for a constant area duct with a fully turbulent boundary layer. This model, expressed by Equation 2.14, is able to explicitly obtain the flow properties across the shock train and predicts the static pressure rise and total pressure loss with good accuracy, particularly for high Mach numbers,

$$\frac{P_2}{P_1} = \frac{\bar{M}_1}{\sigma_1 M_2} \left[\frac{2 + (\gamma - 1)\, \bar{M}_1^2}{2 + (\gamma - 1)\, \bar{M}_2^2} \right]^{1/2} \tag{2.14}$$

with:

$$\sigma_1 = \frac{\bar{\rho}_1 \bar{u}_1 A_1}{\int_{A_1} \rho u \, dA} \tag{2.15}$$

The only analytical expression which relates the pressure gradient experienced by the flow along a duct in the presence of separated regions and the length required to achieve the full pressure rise was proposed by Ortwerth [116]. Referring to Figure 2.22, the core flow in region I, subject to a pressure gradient due to the area restriction caused by the separated flow (region III), passes through the shock train and expands through an area increase after being decelerated to subsonic conditions. The formula, given by Equation 2.16, was determined by Ortwerth [116] from a comprehensive experimental campaign at different Mach numbers, Reynolds numbers and duct geometries, and hence is applicable to a wide range of flow

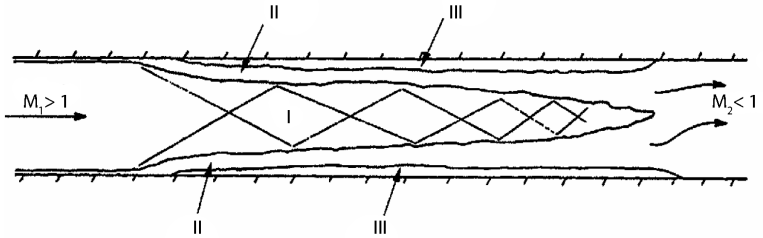

Figure 2.22: Flow model for separation in a duct developed by Ortwerth [116].

conditions and geometries,

$$\frac{d\,(P/P_1)}{dx} = 4K\ \gamma\ P/P_1\ M^2 \tag{2.16}$$

where $4K$= 44.5 C_{f0}, in which C_{f0} is the friction coefficient at the location where the flow initially separates. This equation can be used to close the system of differential equations of mass, momentum, and energy in the presence of flow separation to predict the pressure distribution through the entire duct. Equation 2.16 was used by Tu & Segal [117] with two values for the wall friction coefficient, C_{f0}= 0.01 and C_{f0}=0.005, finding a strong dependence of the model accuracy on the selection of the friction coefficient. As Figure 2.23 illustrates, the value of 0.005 underpredicts the pressure rise, and even though the 0.01 value initially matches the experimental data, it gradually diverges later.

A *non-optimal ramjet-diffuser model* proposed by Auslender [118], consistent with the experimental data obtained by Emami et al. [41], improved the estimation of the static pressure distribution throughout the diffuser and the maximum-obtainable values.

Lin et al. [99] obtained a linear relationship between the centreline Mach number, M_{CL}, at the isolator exit with the pressure ratio downstream and upstream of the isolator, P_2/P_1. Although two different correlations were developed for rectangular and circular isolators in

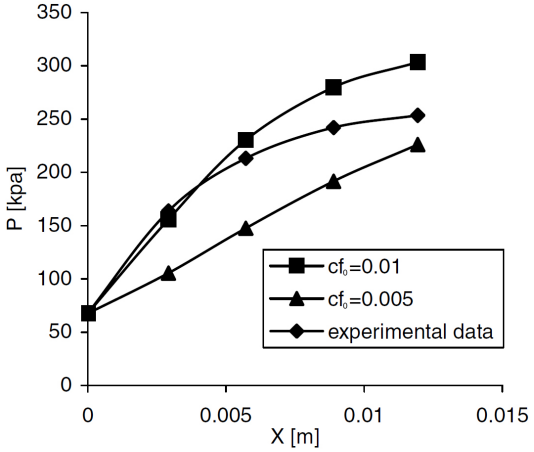

Figure 2.23: Influence of the wall friction coefficient on the isolator pressure rise [117].

Equation 2.17 and Equation 2.18 respectively, the centreline Mach number is a function of the facility nozzle Mach number, M_0, and linearly decreases with back pressure. Additionally, for a given value of the back pressure, the circular geometry provides higher centreline Mach numbers, as Figure 2.24 illustrates.

$$\frac{M_{CL}}{M_0} = -1.17\ {M_0}^{-2.40} \left(\frac{P_2}{P_1}\right) + 1.78\ {M_0}^{-0.64} \tag{2.17}$$

$$\frac{M_{CL}}{M_0} = -0.94\ {M_0}^{-2.20} \left(\frac{P_2}{P_1}\right) + 1.60\ {M_0}^{-0.48} \tag{2.18}$$

The majority of investigations of shock trains have been performed neglecting the wall temperature effects. A recent study carried out by Fischer & Olivier [119] showed that in cases with low total temperature or high isolator entrance Mach number, the shock train is made of several weak shocks and the pressure rise exhibits a linear trend. On the other hand, for high total temperature or low isolator entrance Mach number conditions, a well-defined first shock is observed in front of the shock train. In this case, due to the steeper pressure gradient at the beginning of the shock train, the pressure rises with a quadratic correlation. This shows the inadequacy of the models that do not include wall temperature effects in cases when the isolator wall is heated. However, the authors stated that the validity of the suggested modification was demonstrated only for a limited range of flow condition and geometry.

The current understanding on the mechanisms of the shock train phenomenon is not sufficient and an accurate estimation of the pressure distribution across the isolator needs to be formulated to obtain a reliable prediction of shock trains in internal flow systems. More accurate two- or three-dimensional flow description, including transverse pressure gradients,

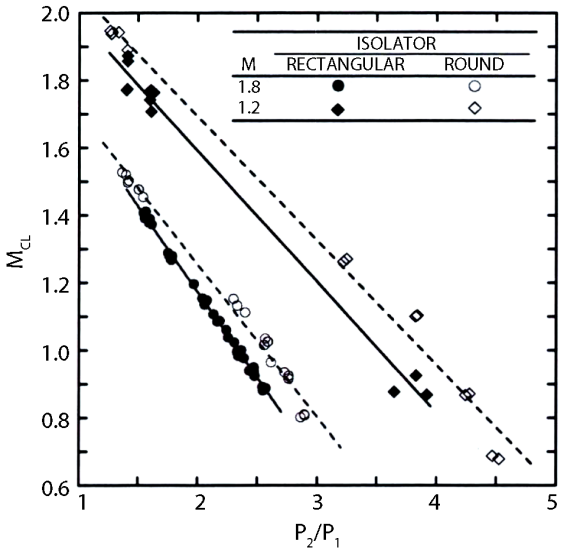

Figure 2.24: Relationship between the centreline Mach number M_{CL} at the isolator exit with the pressure ratio P_2/P_1 [99].

heat transfer, and flow unsteadiness, can be achieved with numerical simulation. From the 1980s, the growth in computer speed and storage capabilities combined with the development of sophisticated algorithms has allowed the use of numerical codes as a valuable tool for analysing the structure of internal flows [120].

Numerical codes have shown to be promising and satisfactory results have been obtained. As an example, Mousavi and Roohi [121] were able to well predict the shape of the first shock wave. However, differences with experimental data are still encountered as demonstrated by the numerical pressure distribution inside a scramjet isolator obtained by Baurle et al. [122]. While the experimental pressure distribution monotonically increases through the shock train, the computed data exhibited an oscillatory behaviour. Several numerical approaches have been implemented to analyse shock trains because of the challenging behaviour that characterises supersonic internal flows. A detailed review of the numerical achievements and status will be provided in Section 3.1.

2.3 Shock wave/boundary layer interaction control

As already explained, in an high-speed inlet velocity reduction from the freestream value is obtained through an efficient sequence of shock waves which impinge on the walls of the inlet frame interacting with the boundary layer. Excessive blockage or an asymmetric entrance condition can aggravate the diffuser flow and boundary layer separation, which often causes a decrease of the inlet performance and flow stability [123]. The unstart process is associated with a pressure rise due to combustor heat release that is too high for the boundary layer to withstand. As observed by Im et al. [124], the boundary layer characteristics and separation strongly affect the unstart process. To counteract the negative effects of shock wave/boundary layer interactions, adequate manipulation of the boundary layer development and separation is necessary [57, 125]. This section provides an overview of the main techniques to control the development of the boundary layer.

Several flow control techniques have been successfully applied to low-speed flows, but the use in the high-speed regime is still limited [126]. Flow control techniques make use of different physical principles and are generally classified as passive and active control. In passive control techniques, one or more sections of the surface structure is used to modify the flow and thus control boundary layer separation. On the contrary, active control techniques employ a powered device which adds energy to the flow and can be switch on and off depending on the need [123].

One possibility to control the behaviour of the boundary layer is the use of passive bleeding. This method was firstly applied by Prandtl [127] in 1904 to prevent separation in a

channel with a large angle of divergence, and since then many bleeding configurations for supersonic inlets have been developed and optimised [128]. In general, bleeding is effective in reducing boundary layer separation at the shock impingement location, improving shock stability, and increasing the pressure recovery [129, 130]. By using a bleeding device Weise [131] was able to remove the boundary layer separation, observing the flow pattern changing from a shock train into a single normal shock configuration, as Figure 2.25 illustrates. Cohen and Valerino [132] demonstrated that boundary layer suction upstream of the normal shock in a constant area duct reduces the oscillation amplitude.

In a bleeding system, such as a double-cone supersonic inlet in Figure 2.26, a bleed slot is located between the start and end points of a shock wave, with a bleed plenum installed under the bleed slot. Compared to a supersonic inlet without bleeding, a more uniform flow is supplied to the engine by removing the low energy flow from the boundary layer near the throat. By changing the cross-sectional area of the sonic throat the critical mass flow rate of the bleeding system can be effectively controlled.

The drawback of bleeding is that a significant fraction of the ingested inlet mass flow is removed [134] and, as reported by Harloff & Smith [135], the flow removal increases with the Mach number. For high-speed systems, another problem that affects structural integrity is the temperature of the flow being bled due to extreme viscous heating in hypersonic boundary layers [136, 137]. Paynter et al. [138] found that the boundary layer growth rate in the bleed region is influenced by the combined effect of the surface roughness and the mixing of high- and low-energy air in the boundary layer. Additionally, the bleeding system significantly

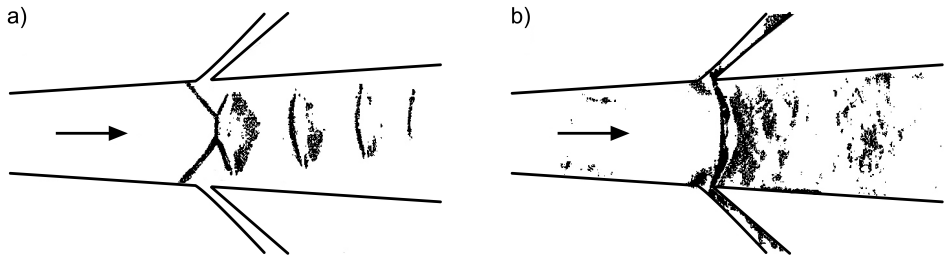

Figure 2.25: Boundary layer control in diverging channel: a) No control; b) Boundary layer suction [131].

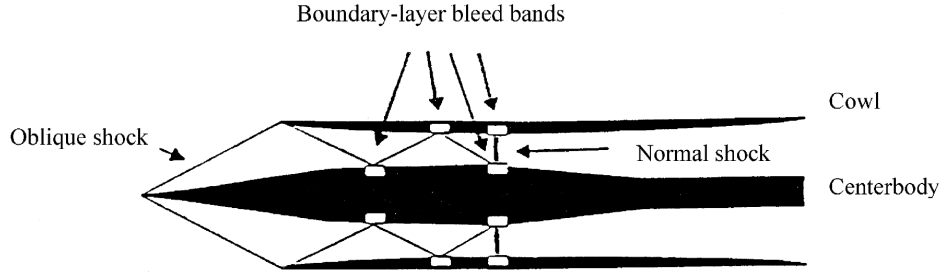

Figure 2.26: Boundary layer bleed in a mixed-compression supersonic inlet [133].

increases the complications in the inlet design due to movable compression ramps and slots controlled by sophisticated software or mechanical systems.

Similar to bleeding, porous walls located at the location of shock impingement can be used for flow control [123]. The main advantage of this approach is the reduction of design complexity and volume penalties, since no mass removal and bleed ducting is required [139]. At the interaction region, the flow is injected upstream of the shock and sucked downstream, establishing a natural circulation within the enclosed cavity [133]. The pressure difference across the shock is thus spread more uniformly and the flow is compressed in a more isentropic manner [140].

The use of streamwise slots placed at the position where a normal shock wave interacts with the boundary layer appears to be effective for a range of shock locations compared to the aforementioned methods which exhibit decreasing benefits in off-design conditions [141]. Since the effect of slots on the boundary layer is localised to the region behind the slots, lower viscous penalties and total pressure loss are observed compared to flow control devices with wall transpiration. On the other hand, the boundary layer displacement and momentum thickness are subject to detrimental effects, which then increase the viscous drag [142].

Gefroh et al. [133] combined this concept with aeroelastic flaps to balance the two opposing tendencies of recirculating transpiration. The system, called mesoflaps for aeroelastic recirculating transpiration (MART), consists of small flaps with a scale length of the order of few boundary layer thicknesses to passively control injection and bleeding. As illustrated in Figure 2.27, the flaps are rigidly fixed at their upstream end but free to deform at the downstream end in response to a pressure difference which establishes between the supersonic flow and the subsonic cavity flow. Since at subsonic conditions the pressure above and below the mesoflaps is nearly the same, no deflection occurs. Therefore, no transpiration is induced from the slots to the surface, which means that surface roughness present in conventional passive control techniques at off-design conditions is minimised at this location. This

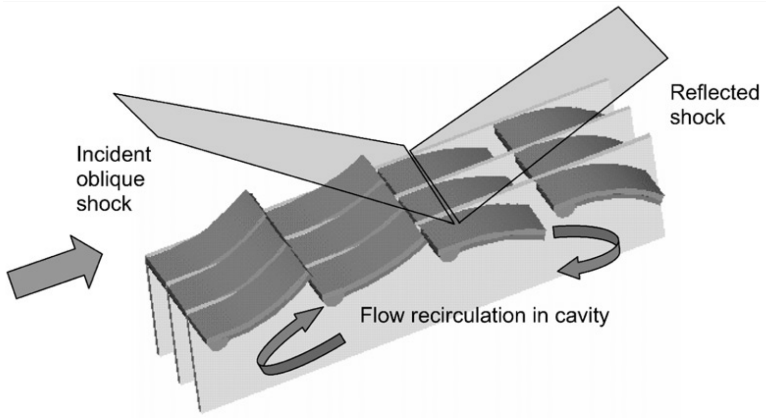

Figure 2.27: Schematic of aeroelastic mesoflaps [133].

device reduces the boundary layer thickness downstream of the shock and the efficiency increases with flap deflection due to the larger flow recirculation rate. Hafenrichter et al. [143] studied different configurations of flap arrays as well as various mesoflap thicknesses finding that the thickness, and consequently the deflection and the transpiration rate, affect the boundary layer properties, and the static and total pressure recovery.

Another mechanism to manipulate boundary layer separation due to adverse pressure gradients is the use of boundary layer trips to promote turbulence [15]. Vortex generators (VGs) have been used in a wide range of aviation applications spanning from the wings of civil aircraft to the intakes of supersonic jet engines, to reduce fluctuating pressure loads for buffet control [144] or delay flow separation [145]. Micro Vortex Generators (MVGs), also referred to as sub-boundary layer vortex generators (SBVGs), are characterised by having a height smaller than the boundary layer thickness (10% to 90% of δ [123]). Although MVGs cannot completely eliminate flow separation, they are particularly effective in controlling flow separation because of a lower drag penalty than conventional vortex generators [146].

VGs act during all phases of the flight envelope by energising the boundary layer. The mixing process between the high-momentum external flow and the low-momentum near-wall flow is enhanced and the shock interaction is alleviated [140]. These devices, initially introduced in the 1940s, work by developing counter-rotating longitudinal vortices in the near-wall region [147]. These vortices remain in the boundary layer for a significant streamwise distance, so that higher pressure gradients can be tolerated before separation and, if separation occurs, the vortices accelerate reattachment [129]. On the other hand, this method presents the disadvantage to increase parasitic drag, which increases with the device size. The flow development behind VGs scales with their height, i.e. larger microramps lead to a greater low-momentum wake, and larger and stronger vortices [148]. Holden & Babinsky [144] found that different levels of control of the shock-induced separation and total pressure loss depend on the spatial arrangement of VGs. Although an optimum spanwise spacing has not yet been established [148], an array of microramps along the spanwise direction demonstrated higher performance compared to the single configuration, as shown in Figure 2.28.

A promising passive method for shock control is the so-called shock control bump (SCB) [149], firstly investigated by Ashill et al. [150]. It consists of placing a ramp in proximity of the location where the shock wave impinges on the wall but, due to the presence of the boundary layer, a λ shock structure takes place, as Figure 2.29(a) illustrates. As shown in Figures 2.29(b) and 2.29(c), this device has the effect to split the normal shock wave into a number of weaker oblique or compression waves ahead of the shock, followed by a tail which is necessary to bring the flow downstream of the shock parallel to the surface [152]. The premise of this strategy relies on the fact that the total pressure loss across multiple oblique shock waves is smaller than that across a normal shock with the same pressure jump, with the consequent achievement of an overall mitigated effect.

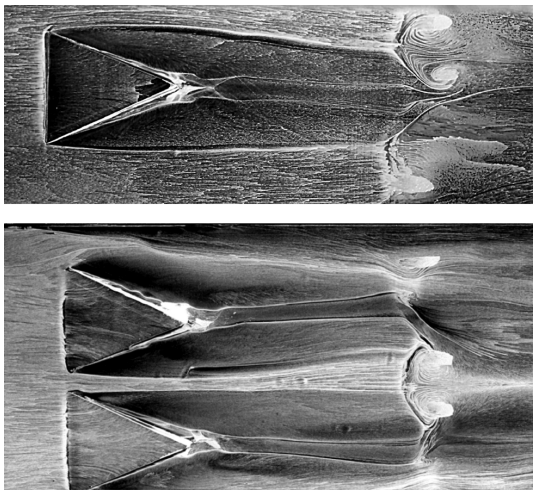

Figure 2.28: Microramp flow visualisation in single and array configuration [148].

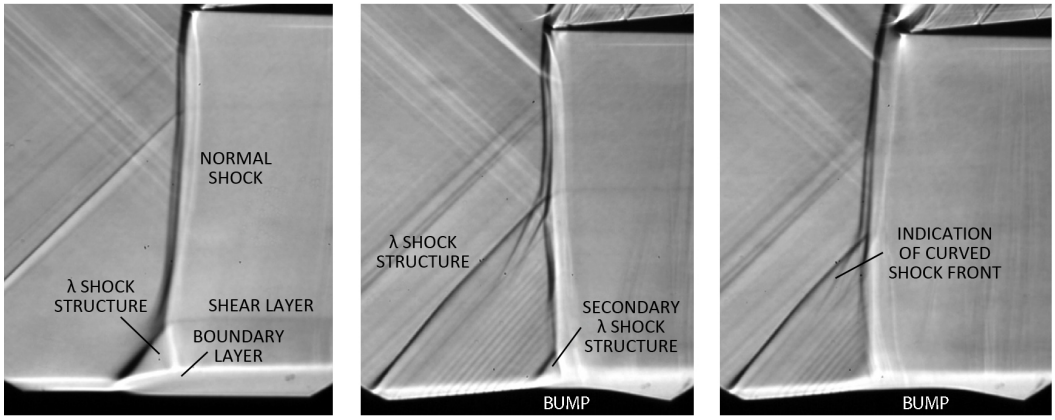

Figure 2.29: Effect of two-dimensional bumps on shock wave/boundary layer interactions [151].

Although the use of SCBs has demonstrated a significant reduction in drag at design conditions, considerable penalties in performance have been reported when the shock position varies. Figure 2.30(b) shows the optimal configuration characterised by a large λ shock without additional total pressure losses which occur when the shock structure is positioned too far upstream, causing secondary shock systems, or too far downstream, causing boundary layer thickening, in Figures 2.30(a) and 2.30(c), respectively.

Lim et al. [153] enhanced the control of the shock wave/boundary layer interaction by replacing the compression ramp used in conventional supersonic inlets with a three-dimensional bump. Similar results were reported by Ogawa & Babinsky [151], who investigated several bump configurations, as shown in Figure 2.31. Zhang et al. [154] recently studied a deformable two-dimensional bump which appears only when the supersonic/hypersonic inlet operates at a high Mach number, but disappears at low Mach number so that the duct height is increased for the inlet starting. However, since the effects of this device deteriorate at off-design conditions the use of such a control method during flight is questionable.

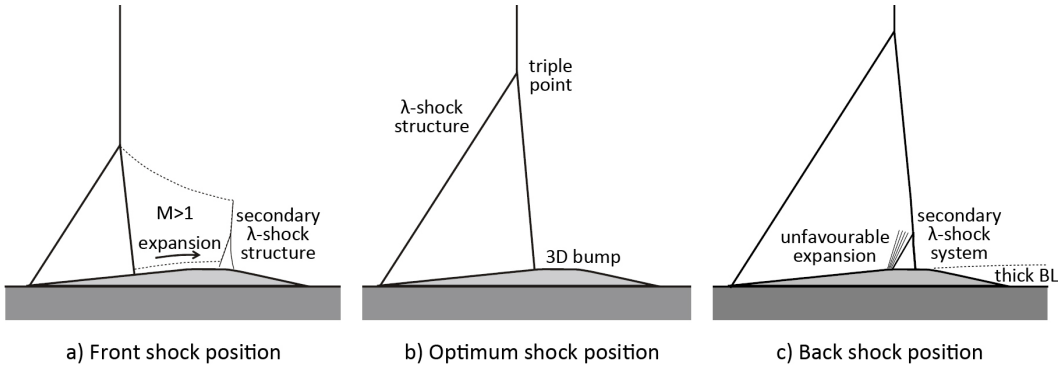

Figure 2.30: Schematic of λ shock configuration at various shock positions [151].

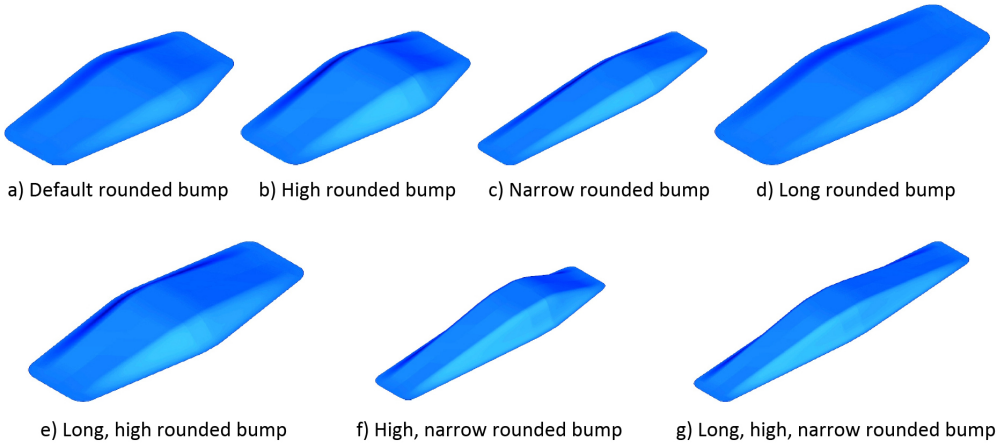

Figure 2.31: Schematic of different three-dimensional bumps [151].

The sensitiveness of fluids to musical tones has been detected since the middle of the 19th century when it was observed that regular aerial pulsations generated by musical notes are sufficient to develop synchronised fluctuations in a candle flame [155]. It has more recently recognised that the combustor performance in aircraft engines is influenced by the fuel injection mode. The introduction of air or fuel along the walls has been used to reduce the low-momentum flow in the boundary layer, thus alleviating separation and heat transfer problems inside the isolator. Qin et al. [32] numerically investigated the effect of fuel injection on the pseudo-shock finding that the variations of shock structure, strength and leading edge position depend on the way the fuel is injected. Also, if the level of asymmetric fuel injection is too high, the isolator unstarts. Steady microjets have experimentally been shown to be effective on flow control, particularly in reattaching large separated regions [156, 157]. Resonance enhanced microjets (REM) produce large amplitude oscillations and operate over a wide bandwidth, even with slight geometry and pressure changes [158, 159].

It is worth mentioning that the pseudo-shock wave characteristics and control have been used to enhance the fuel/air mixing and increase the combustion efficiency when the fuel is perpendicularly injected into the freestream [160–162]. When subjected to a back pressure,

the isolator flow is characterised by an increase in temperature and decrease in gas velocity, providing a highly non-uniform favourable environment for the fuel/air mixing and flame ignition inside the combustor [99].

Surface electrical discharges, with a plasma filament placed between the anode and the cathode located upstream of a shock interacting with a boundary layer, called localised arc filament plasma actuators (LAFPAs), can also be employed for manipulating the flow [163]. The arc discharge which occurs between the two electrodes gives rise to the formation of plasma in the arc channel within the gas. Across this gap the electrons are accelerated by the electric field, gaining the energy to collide with the gas molecules thus enhancing the ionization and producing more electrons. According to Samimy et al. [164], localised arc-generated pressure/temperature flow perturbations can be efficiently employed not only to low-speed or low-pressure flows but also in high Reynolds number and high-speed flows with low energy consumption, large amplitude and high bandwidth. Caraballo [147] observed that the unsteady nature of the leading leg of the λ shock wave, which forms as a consequence of the shock wave/boundary layer interaction, can be controlled by forcing the flow with LAFPAs, as Figure 2.32 illustrates.

Mechanisms of plasma flow control include electrohydrodynamic (EHD) and magneto-hydrodynamic (MHD) interactions, and thermal heating [165, 166]. The first two methods rely on the Lorentz force generated by an adjustable magnet located at the inlet in the presence of plasma to change the flow direction and control the boundary layer [164]. The heated region creates local thermal and pressure perturbations which act as a bump in the flow, thus generating streamwise vortices which transfer the high-energy freestream flow into the boundary layer.

Roupassov et al. [167] reported that, to control boundary layer separation at low Mach numbers, a nanosecond pulsed voltage is more efficient compared to sinusoidal excitations. This is in agreement with Ali et al. [159], who observed that high-amplitude pulsed actuators are more efficient than the same kind of actuator operating in steady mode, and Adelgren et al. [168], who demonstrated that the frequency control of the electrical arc perturbation enhances the mixing of a supersonic jet within the shear layer and induces the formation

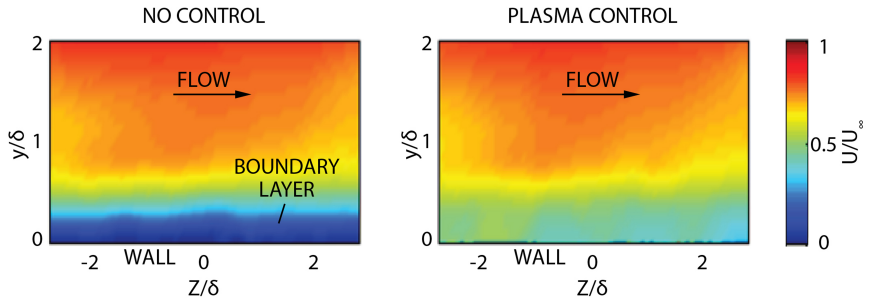

Figure 2.32: PIV streamwise velocity map in a Mach 2 inlet flow [147].

of large-scale structures. Pulse plasma jets, also called spark jets, are a mix between arc filament plasma actuators and air jets, and effectively control the shock wave/boundary layer interaction if the coupling with the structural resonance frequencies is avoided [169, 170].

Plasma flow control technology is currently one of the most advanced approaches to control a wide range of flows, from stationary to separated and turbulent, with a fast reaction time, and low weight and size [167]. The majority of experiments have demonstrated a high efficiency in controlling shock wave patterns, separated regions, and laminar to turbulent transitions [171–173]. However, the prohibitively high energy storage unit required by a plasma-exciting device, the limitation due to ionization instabilities, and the problems related to the interference on the radio communication and flight guidance, are aspects that need to be addressed before the application of this technology to real flow devices [174].

Since the 1950s it was recognised that the location of the shock train leading-edge in the isolator can be used as an input variable in an automatic feedback controller [175]. Initial methodologies to detect the shock train leading edge relied on the increase of the wall pressure. The approach was then developed further introducing statistical parameters including the pressure ratio, pressure root mean square intensity, pressure signal spectral analysis, static pressure summation model, and back pressure static model [63, 175]. Among several methods, Le et al. [176] found the standard deviation of wall pressure to be the best way of determining the shock train leading-edge location in the isolator for operational applications. Chang et al. [177] developed a detection algorithm based on the pressure signal profile given by a large number of sensor probes, which is compared with a reference value, to design the optimal pressure sensor array capable to detect the shock train leading-edge location. Although this principle appears simple, the reference value needs to be constantly modified depending on flight conditions, inlet geometry, angle of attack, and yaw. Additionally, the accuracy of the measured data may be perturbed by the noise introduced by shock reflections as well as the limitation due to the discrete sensor distribution, which requires polynomial interpolation to obtain the signal where no sensors are available.

The various methods developed to control the interaction of the boundary layer with a shock wave have attempted to achieve suppression of boundary layer separation or reduction of total pressure losses with simple and robust actuator systems, easily integrated with the geometry. All the discussed techniques offer advantages and disadvantages and, even though some are more suitable for high-speed inlet applications, none are able to fulfil the goal without incurring installation or operating penalties [159]. Since vortex generators improve the boundary layer downstream of the shock and suppress the separation region, these devices are particularly suitable for supersonic intake applications, in spite of the fact that a lower mass-averaged total pressure is obtained downstream of the shock [140].

2.4 Conclusions

The shock system inside a high-speed engine is typically made of a series of shock waves, known as a shock train, which performs a gradual pressure rise between the inlet and the combustion chamber. Depending on the isolator entrance conditions it assumes different configurations containing a series of bifurcated normal shocks or crossing oblique shocks. The reason a single normal shock wave does not occur is due to the interaction with the viscous boundary layer that spreads the shock structure along the flow passage.

In spite of the technological advances in the last fifty years, the shock train structures are extremely complex and still not well understood. Simplifications in describing the flow structure have been introduced to reduce the difficulties encountered in the flow description. The reduced complexity not only has been identified as the source of inconsistency between experimental and analytical results but also limited a complete description of the flow.

The majority of the analytical formulations have focused on the prediction of the maximum static pressure recovery. Empirical expressions have been introduced to relate the distance over which the shock structure is spread with the flow parameters. For an accurate estimation, the dependence of these expressions on the flow characteristics such as the boundary layer momentum thickness requires a great amount of experimental data. Additionally, the inadequacy of the analytical models becomes significant if the isolator wall is heated because the shock train changes its behaviour.

Some analytical expressions can be applied only to cylindrical ducts, and experimental data have been mostly limited to constant area ducts and symmetric conditions. The validation of models applicable to rectangular geometry has been particularly challenging and gaps in the current knowledge about rectangular cross-sections are still present. More accurate models applicable to a wider range of flow and geometry conditions are necessary.

Simulations have become an important tool in the design of high-speed vehicles, since above Mach 12 the reproduction of the flow conditions in ground test facilities is challenging. However, numerical codes still present limitation in describing the shock trains. Experimental results remain an invaluable resource not only for validating numerical simulation, but also for the understanding of the physical flow behaviour. It is clear that, to achieve an in-depth understanding of shock trains, experimental and numerical tools need to advance together in an interacting manner.

Ultimately, several flow control techniques have been proposed to manipulate the shock wave/boundary layer behaviour, but none have been found suitable for high-speed inlets without drawbacks and, therefore, further investigations are needed.

3 | Numerical methodologies

As the flow speed increases in the supersonic regime, additional challenges arise in estimating the accuracy of analytical models and in reproducing the thermochemistry of the flow in ground-testing facilities for long test duration [124]. Expensive wind tunnel testing as well as limitations in instrumenting the flow field in high-speed inlets have led industry towards an increasing use of computational analysis to estimate the flow physics and to design flow devices with adequate performance [178, 179]. Also, as pointed out by Sun et al. [67], some flow measurements in shock trains cannot be experimentally obtained. Quaatz et al. [180] stated that key mechanisms, such as the interaction between three-dimensional shock waves and recirculation zones, are too complex to be analysed by experiments alone.

The accurate replication of the severe flight conditions requires testing of full-scale models, which move at the same velocity in a fluid having the same static pressure, temperature, and chemical composition as that in flight [122]. On the other hand, when the chemical processes are in equilibrium and the flow properties depend only on the local conditions, a scaled model can be employed [181]. In this case it is necessary to describe the physics making the correct assumptions since, as stated by Krishnan et al. [182], laminar-to-turbulent transitions which are relevant at small scale may not be so important at the full scale. Experiments on hypersonic inlet unstart in ground facilities are performed with temperatures considerably lower than in real flight conditions, where for a vehicle flying at a Mach number of 6 and an altitude of 25 km the total temperature can reach up to 1800 K.

Computational fluid dynamics (CFD) is a numerical tool that allows to solve the partial differential equations governing the physics of flow around or within designed objects [183]. This includes the replication of phenomena such as shock waves, boundary layers, dissipation, diffusion, convection, and turbulence. In the aerodynamics field, gas flows can be described by the compressible Navier-Stokes equations, i.e. the conservation of mass, momentum, and energy. The intrinsic problem of numerical methods is that, to solve differential equations, the domain of interest must be divided into cells, known as a grid or mesh. The simulation of the physical phenomena with a chosen numerical method introduces an approximation that differs from the exact solution. This chapter describes the main numerical findings on shock trains and provides the description of the numerical approach used for the current study.

3.1 Numerical modelling of shock trains

For analysing the structure of internal flows, numerical codes have shown to be promising and satisfactory results have been obtained [66], although differences with experimental data are still encountered [50]. Simulation makes use of existing and validated codes where possible, and applies improvements of numerical and physical models where the geometry and flow regime under consideration cannot be described with the current knowledge. Nonetheless, experimental results remain an invaluable resource not only for validating numerical simulation, but also for the understanding of the physical flow behaviour [184].

The computational modelling of compressible flows is quite difficult because of the challenging behaviour of the shock train and shock wave/boundary layer interactions. Numerical results obtained by Boon & Hillier [185] showed good agreement with experimental data for Mach numbers in the range 5 to 7, but for Mach 6 the solution depends on the initial conditions. Koo & Raman [186] used a variety of numerical schemes, subfilter models, and computational grids to validate experimental studies of isolator unstart showing that grid resolution and suitable numerical schemes are important to accurately resolve the boundary layer and flow separation. Various numerical techniques have been developed to analyse air-breathing propulsion [120, 179, 182, 187, 188] and only the main findings are reported here.

The choice of the appropriate turbulence closure model and the inability to reproduce the shock train oscillating behaviour are common problems in the literature and still require further investigation [122]. Mousavi & Roohi [121] were able to predict the shape of the first shock wave by closing the Reynolds-averaged Navier-Stokes (RANS) equations with the Reynolds stress transport model (RSM), as illustrated in Figure 3.1. With the same turbulence model, Gawehn et al. [52] also satisfactorily predicted the overall shock train structure, but a strong deviation from experiments was obtained with the shear stress transport model (SST). Conversely, the SST model applied by Saha & Chakraborty [45] in a hypersonic intake for freestream Mach numbers from 3 to 8 led to a good agreement of the wall pressure distribution between the predicted and measured values.

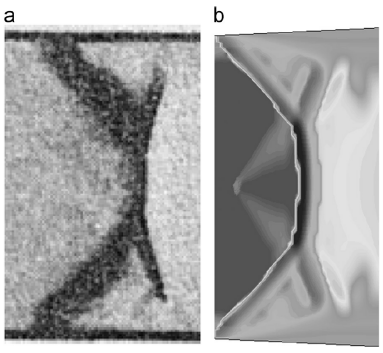

Figure 3.1: Comparison of a λ shock a) Experimental; b) Numerical [121].

At the NASA Langley Research Center, Baurle et al. [122] carried out a computational campaign on the flow inside a scramjet isolator using several turbulence closure models. All the models failed to accurately predict the shape and the extent of the separated flow region caused by the shock wave/boundary layer interactions. As Figure 3.2 illustrates, the experimental wall pressure distribution monotonically increases through the shock train while the computed profile shows an oscillatory behaviour. The pressure distribution illustrates also the dependence of the shock train to the grid resolution. The numerical errors result in a delayed initiation of the shock train and a small alteration of the shock structure details.

The Baldwin-Lomax algebraic turbulence model was a popular choice in the 1980s. Good agreement with experimental data was achieved by Kumar [189] in a Mach 5 two-dimensional scramjet/ramjet inlet and by Sun et al. [67, 71] in a square duct at Mach 2 and 4. However, Dutton & Carroll [68, 190] preferred the two-equation Wilcox-Rubesin model over the Baldwin-Lomax model since it has been shown to be more effective in flows with shock wave/boundary layer interactions. Since three-dimensional boundary layers present the possibility of anisotropic shear, the effective eddy diffusivity may be different depending on the direction. Consequently, any turbulence model which avoids using the Boussinesq approximation has the potential for a more accurate prediction [191].

RANS equations that are based on the ω-formulation generally are in good agreement with experimental data as the anisotropic behaviour of turbulence is specified. Chan et al. [179] demonstrated that the k-ω Wilcox model is suitable for supersonic and hypersonic aerothermodynamic applications. Om et al. [55] reproduced the experimental observations in an axisymmetric duct for Mach numbers between 1.28 and 1.48 and a Reynolds number equal to 4.92×10^6 using the Wilcox-Rubesin turbulence model. In the case of an attached boundary layer, the details of a normal shock wave interacting with the boundary layer were well predicted. On the other hand, in case of flow separation, the discrepancies of the simulated results with the experiments increased as the separation becomes larger.

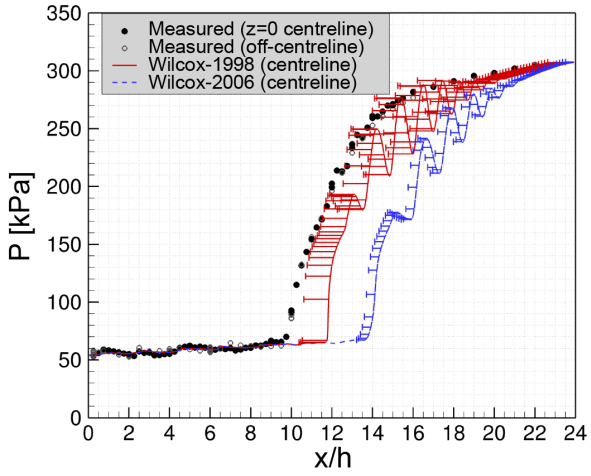

Figure 3.2: Comparison of wall pressure measurement with computed results [122].

Most studies have concentrated on two-dimensional simulations [32, 67] even though an adequate description of a three-dimensional flow with a two-dimensional model is unreasonable [192]. Three-dimensional investigations are becoming increasingly more common to study the effect of the four walls surrounding rectangular ducts on the characteristics of the shock train system [79]. As often happens to reduce computational time, Sridhar et al. [100] used as computational domain only one-quarter of the actual duct. As a consequence, the results led to a symmetrical flow field, in contrast with the experimental findings discussed in Section 2.1.2. Kawatsu et al. [92] used the full geometry as a computational domain in rectangular ducts with both constant and diverging cross-sectional areas. While in the case of a constant area duct separated flow regions were observed near all the corners of the duct, in a diverging duct a large separation of the boundary layer caused by the first shock occurs only at one corner of the test section, as illustrated by the dotted circles in Figure 3.3. Additionally, once the separation is formed, it remains in the same position and does not move to another corner.

Compared with the RANS equations, Krishnan [182] demonstrated the feasibility of LES on scaled intake models at Mach 8, obtaining a more realistic result in capturing the boundary layer separation bubble. Figure 3.4 illustrates the comparison between the computed density gradients and the experimental schlieren photography performed by Quaatz et al. [180]. The LES computation was capable of well resolving the shock train system in a divergent duct with rectangular cross section at a Mach number of 1.91. The behaviour of the shock train structure and the position of the first shock are accurately predicted, in agreement with Kamali et al. [193]. However, even though the authors stated that the LES results agreed with the wall pressure measurements, the results reported in Figure 3.5 show that the RANS approach better matches the experimental findings.

The RANS equations have demonstrated to adequately resolve the characteristics of shock wave/boundary layer interactions in supersonic internal flows. On the other hand,

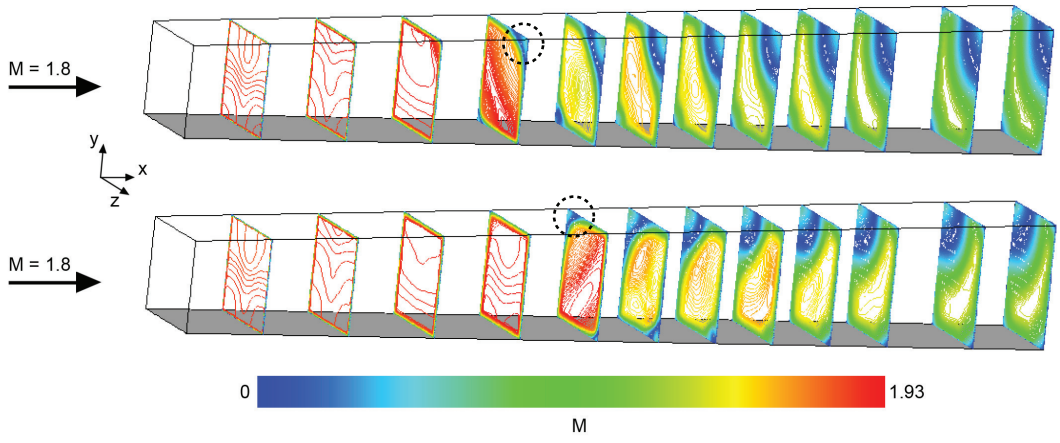

Figure 3.3: Numerical Mach number contours in diverging duct at flow mach number of 1.8 [92].

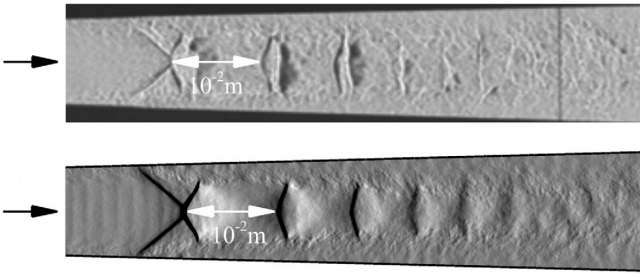

Figure 3.4: a) Schlieren photography; b) LES density gradients spatially averaged along the z-direction [180].

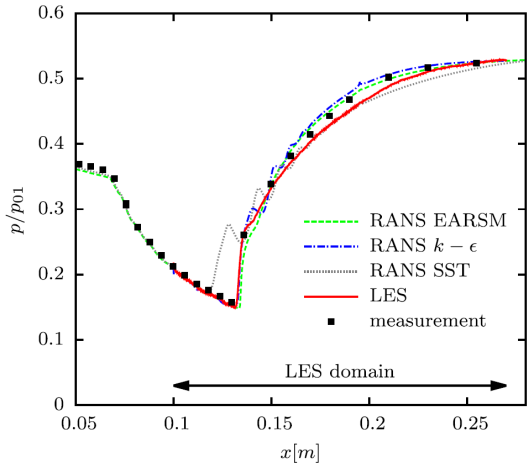

Figure 3.5: Comparison of different numerical simulations in a divergent duct at Mach 1.91 [180].

the shape and axial location of the shock train may change depending on the various turbulence models that limit a reliable prediction of the shock train. The current knowledge on a suitable numerical approach to analyse the shock train characteristics and quantify the pressure distribution across the isolator is not sufficient and further research is needed.

3.2 Grid structure

The grid generation for the discretisation of the flow domain is one of the most important aspects to successfully replicate the real flow behaviour. This is an intrinsic problem of simulation as the flow domain is replaced with a discrete number of elements over which the governing equations describing the problem are resolved. As a consequence, the size and quality of the generated grid strongly influence the time of the simulation and the accuracy of the final result. As an example, Figure 3.6 illustrates that a finer grid allows to capture the structures of the shock wave/boundary layer interaction of a shock train in more details. In Figure 3.6(b) the shape of first shock is better resolved, as well as the second shock wave, which is barely visible in Figure 3.6(a).

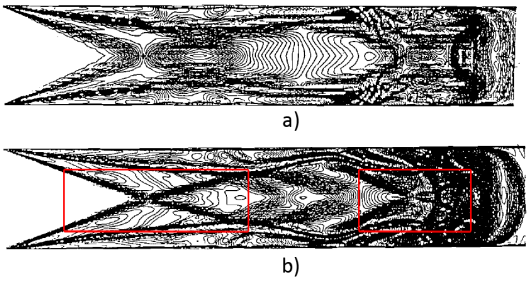

Figure 3.6: Density contours at M= 3: a) 350 $\times$ 77 grid points; b) 350 $\times$ 153 grid points [66].

The grid can be of different types and grid refinements are often locally applied in order to increase the number of cells in regions of particular interest. In general, an unstructured grid faithfully represent the geometry since cells are randomly distributed throughout the domain. This is particularly convenient when the geometrical contour of the computational domain has complex shapes. However, in some situations when there is a prevalent direction of the flow, a structured grid is more appropriate. In this case the grid elements are organised and arranged about the flow main direction.

Different cell shape can be used depending on the purpose [194]. As an example, polyhedral elements easily adapt to any surface and geometry so that even very complex geometries can be spatially discretised with a good balance between grid quality (including aspect ratio, skewness, orthogonality, and smoothness), ease, and accuracy of the results. However, polyhedral elements are directly dependent on the quality of the starting surface triangulation meaning that a starting surface of bad quality will affect the quality of the final volume grid.

The choice of the numerical method and grid strategy are strongly related [183], so that the dimensionless wall distance, y^+, has been introduced as an indicator of the grid capability to properly resolve the boundary layer. In internal flows, such as flows in channels, ducts, or pipes, an accurate treatment of the boundary layer is of imperative importance. The boundary layer has the effect to slow down the fluid near the wall and, at the same time, to accelerate the flow near the centre of the duct. An approximated value of y^+ can be estimated, however the exact value can only be determined at the end of the simulation once the actual boundary layer profile is resolved. In general, a sufficient resolution of the profile across the boundary layer implies the use of a minimum of 10 to 20 cells within the boundary layer. For simulating shock-separated hypersonic flows, using a y^+ less than 0.3 is recommended [179].

To estimate the wall distance it is necessary to firstly compute the Reynolds number given by Equation 3.1:

$$Re_x = \frac{\rho U_\infty x}{\mu} \tag{3.1}$$

In order to calculate the wall shear stress, τ_w, the skin friction coefficient must be determined.

For a turbulent boundary layer several formulas evaluate the local skin friction coefficient, C_f, over a flat plate. With the the $1/7^{th}$ power law for $5 \times 10^5 < Re_x < 10^7$:

$$C_f = 0.027 {Re_x}^{-1/7} \tag{3.2}$$

The wall shear stress, τ_w, the friction velocity, u_τ, and the viscous lengthscale, δ_ν, are defined as follows:

$$\tau_w = 0.5 C_f \rho u^2 \tag{3.3}$$

$$u_\tau = \sqrt{\frac{\tau_w}{\rho}} \tag{3.4}$$

$$\delta_\nu = \frac{\nu}{u_\tau} \tag{3.5}$$

For high Reynolds numbers, the flow consists of a large core layer where the molecular momentum transfer can be neglected compared to the turbulent momentum transfer, and a thin wall layer where both molecular and turbulent momentum transfer act [195]. The two layer thicknesses are of different orders of magnitude: the thickness of the core layer is approximately half the duct height, whereas the wall layer thickness, δ_ν, is defined by Equation 3.5.

The non-dimensional distance, y^+, and velocity, u^+, are defined by Equations 3.6 and 3.7, respectively. It has been experimentally observed that the dependence of u^+ on x is very small and is a function of y^+ only [196]. This leads to the so-called the law of the wall $y^+ = y^+(u^+)$.

$$y^+ = \frac{y u_\tau}{\nu} = \frac{y}{\delta_\nu} \tag{3.6}$$

$$u^+ = \frac{u}{u_\tau} \tag{3.7}$$

Figure 3.7 illustrates that different regions in the near-wall flow are defined on the basis of y^+. The region where $y^+ > 50$, where the direct effect of viscosity is negligible, is referred as outer layer and is composed of the log layer and the defect layer. Measurements have shown that both in internal and external flows, the streamwise velocity varies logarithmically with distance from the surface with Equation 3.8 [197]. In supersonic flows, the values of the von Karman constant κ= 0.41 and the log law offset C= 5.0 are recommended [198].

$$u^+ = \frac{1}{\kappa} ln y^+ + C \tag{3.8}$$

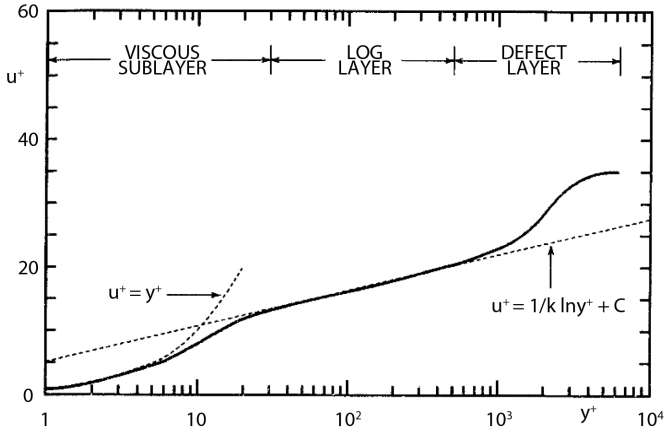

Figure 3.7: Velocity profile for a turbulent boundary layer [197].

In the portion of the flow where $y^+ < 50$, the fluid inertia is small whereas the effect of molecular viscosity on the shear layer becomes more important. In this region, called the viscous sublayer, there are two primary mechanisms that govern a turbulent boundary layer. The molecular diffusion of momentum and the rate at which momentum per unit area per unit time is transferred to the surface, which is equal to the local shear stress τ. Additionally, for values $y^+ < 5$, the turbulent shear stress is negligible compared to the viscous stress [199].

The velocity profile through the boundary layer can be approximated with either empirical or semi-empirical laws. For high-speed flows, the boundary layer becomes turbulent, the gradient at the wall becomes smaller, and the wall shear stress is higher. For turbulent boundary layers the velocity profile is normally approximated by a power-law relationship, in Equation 3.9, based on empirical observation.

$$u = U_\infty \left(\frac{y}{\delta}\right)^{1/n} \tag{3.9}$$

The exponent n is a function of the Reynolds number and usually varies between 6 and 8 [197]. For Reynolds numbers smaller than 10^7, the value of n= 7 suggested by Prandtl is applicable to a wide range of pipe flows and known as the $1/7^{th}$ power law. According to this formula at y= 0 the gradient is horizontal, thus infinite. In reality, a laminar sublayer exists next to the wall, where the velocity grows very quickly from zero and merges with the boundary layer.

3.3 Governing equations

The inviscid Euler equations are a useful preliminary design tool to capture the main flow features and save computer time since a reduced number of computations and grid points are needed. However, a more accurate analysis of inlet flows requires the inclusion of viscosity.

In practical applications which involve gases or liquids, viscosity is usually ignored because tangential forces are very small compared to the other forces, allowing convenient simplifications in the equations of motion. This assumption is accurately applicable everywhere except near the wall, where the boundary layer is responsible of problems related to friction and heat transfer [195]. While for low Mach number non-reacting flows, calorically perfect isentropic gas relations can be used with sufficient accuracy, in the hypersonic speed range, real-gas effects, large thermal variations, strong viscous/inviscid interactions of laminar and turbulent flows must be included [200]. The Navier-Stokes equations are widely employed because they allow the simultaneous solving of the viscous and inviscid flow fields. However, computations which include the interaction between shock waves and turbulence are highly sensitive to the turbulence closure model [43, 55].

Compressible turbulent fluid flows are described by the Favre mass-averaged equations [201] that consist of the instantaneous conservation law for mass, momentum, and energy.

$$\frac{\partial \rho}{\partial t} + \frac{\partial}{\partial x_j}\left(\rho U_j\right) = 0 \tag{3.10}$$

$$\frac{\partial}{\partial t}\left(\rho U_i\right) + \frac{\partial}{\partial x_j}\left(\rho U_i U_j\right) = -\frac{\partial P}{\partial x_i} + \frac{\partial \tau_{ji}}{\partial x_j} \tag{3.11}$$

$$\frac{\partial}{\partial t}\left[\rho\left(e + \frac{1}{2}U_i U_i\right)\right] + \frac{\partial}{\partial x_j}\left[\rho U_j\left(h + \frac{1}{2}U_i U_i\right)\right] = \frac{\partial}{\partial x_j}\left(U_i \tau_{ij}\right) - \frac{\partial q_j}{\partial x_j} \tag{3.12}$$

The symbols U_j and x_j are the j-th component of the velocity and position vectors, e is the specific internal energy, h= $e + P/\rho$ is the specific enthalpy, t is the time, P is the pressure, ρ is the density, q_j is the heat flux, and τ_{ji} is the viscous stress tensors defined as:

$$\tau_{ij} = 2\mu S_{ij} \tag{3.13}$$

The mean strain-rate tensor, S_{ij}, is specified as follows:

$$S_{ij} = \frac{1}{2}\left(\frac{\partial U_i}{\partial x_j} + \frac{\partial U_j}{\partial x_i}\right) - \frac{1}{3}\frac{\partial U_k}{\partial x_k}\delta_{ij} \tag{3.14}$$

where δ_{ij} is the Kronecker delta. The heat flux, q_j, is defined by Equation 3.15 in which λ is the thermal conductivity and Pr is the laminar Prandtl number. The Prandtl number depends on the properties of the fluid only, and is governed by the ratio of the dynamic viscosity and heat conductivity, therefore Pr= 1 implies a perfect balance between viscous dissipation and heat conduction, and hence the wall is adiabatic [198].

$$q_j = -\lambda\frac{\partial T}{\partial x_j} = -C_P\frac{\mu}{Pr}\frac{\partial T}{\partial x_j} \tag{3.15}$$

To close Equations 3.10 to 3.12 an equation of state needs to specified, i.e. the perfect gas law, in Equation 3.16, with R= 287.058 J/kgK being the specific gas constant.

$$P = \rho RT \tag{3.16}$$

Additionally, the gas is assumed calorically perfect so that Equations 3.17 and 3.18 are valid, where C_V and C_P being the specific heat of air at constant volume and pressure, and are a function of temperature. The viscosity is calculated with the Sutherland's law, in Equation 3.19, with the reference viscosity μ_{ref}= 1.716 $\cdot 10^{-5}$ kg/ms, the reference temperature T_{ref}= 273.15 K, and Sutherland temperature T_S= 110.4 K.

$$e = C_V T \tag{3.17}$$

$$h = C_P T \tag{3.18}$$

$$\mu = \mu_{ref} \left(\frac{T}{T_{ref}} \right)^{\frac{3}{2}} \frac{T_{ref} + T_S}{T + T_S} \tag{3.19}$$

3.3.1 Vector form of the conservation laws

The three laws of conservation in Equations 3.10 to 3.12 can be combined and written in the equation shown below, which is referred to as the Navier-Stokes equation for viscous flow. In Cartesian integral form for an arbitrary control volume, V, with differential surface area, $d\boldsymbol{a}$, the equations are:

$$\frac{\partial}{\partial t} \int_V \boldsymbol{W} dV + \oint \left[\boldsymbol{F} - \boldsymbol{G} \right] \cdot d\boldsymbol{a} = \int_V \boldsymbol{H} dV \tag{3.20}$$

where $\boldsymbol{W}$ is the vector of conserved variables, $\boldsymbol{F}$ and $\boldsymbol{G}$ are the vectors of inviscid and viscous fluxes, which contain terms for the heat flux and viscous forces exerted on the body, and $\boldsymbol{H}$ is the source term set to 0. The vectors are defined as:

$$\boldsymbol{W} = \begin{bmatrix} \rho \\ \rho \boldsymbol{U} \\ \rho E \end{bmatrix}, \quad \boldsymbol{F} = \begin{bmatrix} \rho \left(\boldsymbol{U} - \boldsymbol{U_g} \right) \\ \rho \left(\boldsymbol{U} - \boldsymbol{U_g} \right) \times \boldsymbol{U} + P \boldsymbol{I} \\ \rho \left(\boldsymbol{U} - \boldsymbol{U_g} \right) H + P \boldsymbol{U_g} \end{bmatrix}, \quad \boldsymbol{G} = \begin{bmatrix} 0 \\ \boldsymbol{T} \\ \boldsymbol{T} \cdot \boldsymbol{U} + \boldsymbol{q} \end{bmatrix} \tag{3.21}$$

with the variables ρ, $\boldsymbol{U}$, E, $\boldsymbol{U_g}$, P, H, $\boldsymbol{T}$ and q having their meaning of density, velocity vector, total energy, grid velocity vector, pressure, total enthalpy, viscous stress tensor, and heat flux vector, respectively. The total enthalpy is defined as H= $h + |\boldsymbol{U}|^2/2$.

3.4 Numerical method

The Navier-Stokes equations are discretised using the cell-centred finite volume method in STAR-CCM+ 11.02.010. The full system of the governing equations of continuity, momentum, and energy are simultaneously solved at once in a coupled double precision manner.

The computational domain is divided into a finite number of small control volumes and a discrete versions of the integral form of the continuum transport equations are applied to each control volume. The integral equation of the general transport quantity ϕ, in Equation 3.22, is discretised in the form expressed by Equation 3.23. The terms in these equation are the transient term, the convective flux, the diffusive flux, and the volumetric source term, respectively.

$$\frac{\partial}{\partial t}\int_V \rho\phi dV + \int_A \rho\phi\left(\boldsymbol{U}-\boldsymbol{U_g}\right)\cdot d\boldsymbol{a} = \int_A \Gamma\nabla\phi\cdot d\boldsymbol{a} + \int_V S_\phi dV \tag{3.22}$$

$$\frac{\partial}{\partial t}(\rho\phi V)_0 + \sum_f \left[\rho\phi\left(\boldsymbol{U}\cdot\boldsymbol{a}-G\right)\right]_f = \sum_f \left(\Gamma\nabla\phi\cdot\boldsymbol{a}\right)_f + \left(S_\phi V\right)_0 \tag{3.23}$$

With S_ϕ being the source term and Γ the diffusion coefficient.

Inviscid fluxes are evaluated using Liou's AUSM+ flux-vector splitting scheme based on the upwind concept. This scheme is the more appropriate choice for solving flows involving Mach numbers equal or greater than approximately 3 [194].

Convection flux at a face is discretized with a second-order upwind scheme. Therefore the face value of a flow variable, ϕ_f, is computed using the following equations:

$$\left[\rho\phi\left(\boldsymbol{U}\cdot\boldsymbol{a}-G\right)\right]_f = \dot{m}_f\phi_f \tag{3.24}$$

$$\dot{m}_f\phi_f = \begin{cases} \dot{m}_f\phi_{f,0} & for \quad \dot{m}_f \geqslant 0 \\ \dot{m}_f\phi_{f,1} & for \quad \dot{m}_f < 0 \end{cases} \tag{3.25}$$

with $\phi_{f,n}$, for n= 0 and n= 1, linearly interpolated from the cell values on either side of the face as:

$$\phi_{f,n} = \phi_n + \left(x_f - x_n\right)\cdot\left(\nabla\phi\right)_{r,n} \tag{3.26}$$

This formulation requires the determination of the gradient in each cell with the subscript r meaning the reconstructed value. For this purpose, the computation of the gradients is done using the Hybrid Gauss-Least Squares (HG-LSQ) gradient method, in Equation 3.27, that uses a blending factor, β, to determine the method used in calculating the gradient. When the blending factor is equal to 1 the Least Squares (LSQ) method is used whereas the

Green-Gauss (GG) method is employed when β= 0.

$$(\nabla\phi)_r^u = \sum_f (\phi_n - \phi_0)\, {w_f}^0 \tag{3.27}$$

$$w_f^0 = \beta {w_f}^{LSQ} + (1-\beta)\, w_f^{GG} \tag{3.28}$$

The superscript u denotes the unlimited value, whereas the variables w_f^{LSQ} and w_f^{GG} are the computed gradient with the LSQ and the GG method, respectively.

The problem in the simple reconstruction of the face values from the unlimited reconstruction gradients is that this value can be outside the range of cell values found in neighboring cells. Consequently, the gradient reconstruction needs to be limited with the use of a scale factor, α, expressing the ratio of the limited and unlimited values:

$$(\nabla\phi)_{r,n} = \alpha(\nabla\phi)_{r,n}^u \tag{3.29}$$

with $\alpha = min\,(\alpha_f)$ and α_f defined by the Minmod limiter as:

$$\alpha_f = min\,(1, 1/r_f) \tag{3.30}$$

where

$$r_f = \begin{cases} \frac{\Delta_f}{\Delta_{max}} & for \quad \Delta_f > 0 \\ \frac{\Delta_f}{\Delta_{min}} & for \quad \Delta_f \leq 0 \end{cases} \tag{3.31}$$

$$\Delta_f = (x_{f,n} - x_n) \cdot (\nabla\phi)_{r,n}^u \tag{3.32}$$

$$\Delta_{max} = \phi_0^{max} - \phi_0 \tag{3.33}$$

$$\Delta_{min} = \phi_0^{min} - \phi_0 \tag{3.34}$$

However, it might happen that gradients are excessively limited, causing convergence to slow or stall. To avoid this problem, STAR-CCM+ [194] allows the activation of the model property total variation bounded gradient limiting (TVB). This property lets reconstructed values to vary by an additional difference, δ, defined as:

$$\delta = \Psi \cdot max\,(\Delta_{max} - \Delta_{min}) \tag{3.35}$$

where $(\Delta_{max} - \Delta_{min})$ is the largest difference between local maximum and local minimum anywhere in the simulation and Ψ varies between 0 and 1.

A grid initialization technique that solves inviscid equations at a series of grids starting from coarse to fine is employed. The finest grid level solution is then set as an initial solution to start simulation. The advantage of this technique is the acceleration and achievement of a more robust convergence. The Courant-Friedrichs-Lewy (CFL) condition is set at 0.5.

3.5 Turbulence modelling

There are three common approaches for solving turbulent flows, i.e. direct numerical simulation (DNS), large eddy simulation (LES), and Reynolds-averaged Navier-Stokes (RANS). DNS solves the full unsteady Navier-Stokes equations for all turbulence scales and thus this approach remains limited to simple geometries since it is extremely computationally expensive. LES also solves the full unsteady Navier-Stokes equations for motion scales of the order of the grid size and uses a turbulence model for smaller sub-grid scale motions. It is more cost-effective than DNS although the accuracy is depending of the grid resolution. However, both these approaches are limited to low-turbulent Reynolds numbers [198]. The RANS equations are an approximation of the Navier-Stokes equations obtained by a time averaging process. This approach is acknowledged as the most computationally efficient to model realistic aerospace systems [179], although unsteady small-scale phenomena cannot be recovered [180].

The RANS equations are written by substituting each instantaneous transport property, ϕ, with a mean value, $\bar{\phi}$, and a fluctuating component, ϕ', [198].

$$\phi = \bar{\phi} + \phi' \tag{3.36}$$

$$\bar{\phi}\left(x\right) = \lim_{T \to +\infty} \frac{1}{T} \int_{t_0}^{t_0+T} \phi\left(x,t\right)\, dt \tag{3.37}$$

The resulting equations for the mean quantities are similar to those used for steady-state situations, but differ from the original equations by the presence of an additional term in the momentum transport equation. This term is a tensor quantity, $\overline{u_i u_j}$, known as the Reynolds stress tensor. Depending on the algebraic relationships used to relate this term to the mean flow different turbulence models have been proposed.

Turbulence consists of random fluctuations in velocity and pressure, in both space and time. These fluctuations arise from instabilities, patches of swirling fluid, that grow around the mean direction of fluid motion until the action of viscosity dissipates them into finer whirls. This unsteady state of fluid motion is generated when the inertia of the fluid exceeds the threshold below which viscous forces gradually stop the chaotic behaviour. Figure 3.8(a)

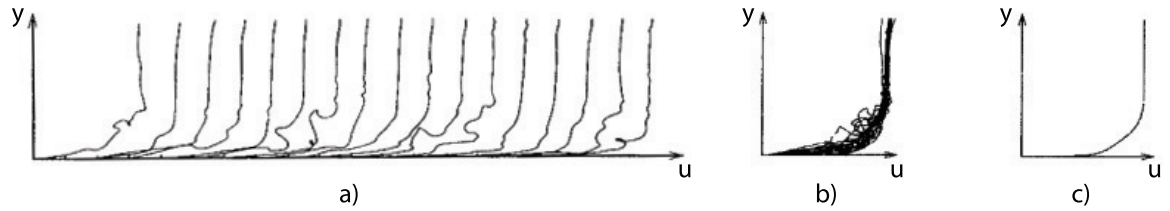

Figure 3.8: a) Boundary layer velocity profiles at the same location from the leading edge of a flat plate at different time instants; b) All profiles; c) Averaged profile [197].

illustrates the velocity profiles $u\,(y)$ at the same location on a flat plate at different time instants. To mathematically describe turbulence, a statistical approach has been introduced [197]. Figure 3.8(b) shows that all the profiles can be averaged obtaining a mean velocity profile in time, in Figure 3.8(c).

In 1941 Kolmogorov proposed the universal equilibrium theory to describe turbulence, stating that the smallest scales depend on the rate at which the larger eddies supply energy, $\varepsilon = -dk/dt$, and the kinematic viscosity, ν. The kinetic energy of the turbulent fluctuation per unit mass, k, is defined by Equation 3.38:

$$k = \int_0^\infty E\,(\kappa)\ \kappa \tag{3.38}$$

where $E\,(\kappa)$ is the energy spectral density. For high Reynolds numbers, k can be related to the supply energy, ε, and the characteristic length, ℓ, of the larger eddies by:

$$k \sim (\varepsilon \ell)^{2/3} \tag{3.39}$$

Therefore, the turbulent dissipation rate, ε, as well as the specific dissipation rate, ω, can be estimated by Equations 3.40 and 3.41, where C_μ represents an empirical constant equal to approximately 0.09.

$$\varepsilon = C_\mu^{3/4} \frac{k^{3/2}}{\ell} \tag{3.40}$$

$$\omega = \frac{k^{1/2}}{C_\mu^{1/4} \ell} \tag{3.41}$$

The turbulence length scale, ℓ, is a physical quantity related to the size of the large eddies that contain energy in turbulent flows. In fully-developed duct flows, the size of ℓ is restricted by the size of the duct because turbulent eddies cannot be larger than the duct diameter. An approximate estimation of ℓ can be obtained with the relation $\ell = 0.07\ D_{eq}$, where D_{eq} is the duct equivalent diameter [202]. However, for wall-bounded flows that involve a turbulent boundary layer, the turbulence length scale is calculated from the boundary layer thickness as $\ell = 0.4\ \delta$.

The flow field in internal flows is composed of a turbulent boundary layer close to the wall and an inviscid free stream. Therefore, to close the RANS equations, it is necessary to include an appropriate model that relates the thermodynamic properties and the Reynolds stress tensor. Since the 1960s the choice of a suitable turbulence model has led to a substantial amount of unsuccessful results [101]. The reason of this has been attributed to the inability of simulations to predict the skin friction and velocity profiles close to the wall, as well as the behaviour of the shock train, including separation, reattachment, turbulence intensity, and flow unsteadiness.

The choice of the model depends on the flow regime under investigation and is sometimes guided by conflicting issues, i.e the need for an accurate and detailed design which opposes low costs and fastness requirements [203]. Depending on how many partial differential transport equations are solved in addition to the time-mean relations, the model is referred as a *n*-equation model [195]. When the relation between the turbulence shear stress and the mean motion is given by an algebraic relation, the model is called an algebraic or a zero-equation turbulence model. This type of model uses the Boussinesq hypothesis to relate the Reynolds stress tensor with the gradient of the mean velocity so that the eddy viscosity, μ_t, is assumed as an isotropic scalar quantity. The eddy viscosity is an apparent viscosity that, in contrast to the molecular viscosity, μ, which is an intrinsic property of the fluid, depends on the local flow conditions [198]. The advantage of this approach is the relatively low computational cost associated with the computation of the turbulent viscosity. The disadvantage of the Boussinesq hypothesis is that it assumes μ_t to be an isotropic scalar quantity, which is not strictly true. However, the assumption of an isotropic turbulent viscosity typically works well for shear flows dominated by only one component of the turbulent shear stresses such as wall boundary layers, mixing layers, and jets [202].

The algebraic turbulence model proposed by Baldwin & Lomax [204] was formulated for computations where the boundary layer properties, such as boundary layer thickness or the displacement thickness, are difficult to be determined [197]. It eliminates one of the sources of arbitrariness since the model does not require the definition of the boundary layer thickness [205]. To characterise the scale of turbulence, the vorticity at each point in the flow field is used. The model applies an inner law from the wall up to the location where the eddy viscosity in the inner law is equal to that of the outer law, which is applicable for the rest of the flow field [189].

The Baldwin-Lomax turbulence model has been applied to a variety of two- and three-dimensional flow fields and is suitable for high-speed flows with attached thin boundary layers. The use of such a closure model appears to give satisfactory results as long as the flow is unseparated, but when the flow is separated, discrepancies with experiments have been reported [206]. On the other hand, according to the authors, the model works also in separated flows since the prediction of the points of boundary layer separation and reat-

tachment agreed well with experiments [204]. Usually, this model is used in quick design iterations where robustness is more important than capturing all details of the flow physics.

In general, algebraic models are not very accurate and reliable for separated flows [197]. In fact, when the boundary layer separates, the streamlines are not parallel to the surface as they are for attached boundary layers, therefore a turbulence model that includes all the components of the Reynolds-stress tensor is more appropriate. Knight [207] reported that the algebraic Baldwin-Lomax model does not precisely predict the recovery of a turbulent boundary layer downstream of a strong two-dimensional shock interaction. Although great care must be used in cases with large separations and significant curvature/rotation effects, Hsia [208] applied the Baldwin-Lomax model in the parts of two-dimensional scramjet inlet where turbulent flow were expected to occur. Additionally, it has been reported that the value of the constants C_{cp} and C_{Kleb} which define the model are dependent on the flow Mach number [190, 209].

In 1945, Prandtl postulated a mathematical description of the turbulent stresses in which the eddy viscosity depends on the kinetic energy of the turbulent fluctuation, k. By proposing a partial differential equation for approximating the exact equation of k, he developed the concept of the one-equation turbulence model. Among the various models proposed, the Spalart-Allmaras model is a relatively simple one-equation model that solves a transport equation for the turbulent viscosity. It was designed specifically for aeronautics and aerospace applications involving wall-bounded flows and has shown to give good results for boundary layers subjected to adverse pressure gradients [202]. Typically, the model is suitable for applications in which the boundary layer remains mostly attached and no large separated regions occur, from incompressible to transonic speeds [197].

Models that solve two partial differential equations belong to the family of the two-equation models. Many two-equation models have been proposed, for instance for k and ε or for k and ω. The standard k-ε is a semi-empirical model that relies on the assumption that the flow is fully turbulent and the effects of molecular viscosity are negligible. It provides a good compromise between robustness, computational cost and accuracy, but it is very difficult to integrate though the viscous sublayer [194]. The parameter ω, which defines the rate of dissipation of energy per unit volume per unit time, was introduced in 1942 by Kolmogorov. The k-ω model is less complicated and requires less computational time than the k-ε model. It is also capable to reproduce subtle features close to the solid boundary and is more accurate for two-dimensional boundary layers with both favourable and adverse pressure gradients, and in the presence of separation induced by the interaction with a shock wave [191, 197]. One of the weak points of the Wilcox model is the sensitivity of the solutions to values for k and ω outside the shear layer [202].

In 1994 Menter proposed a two-equation model which combines both the k-ε and the k-ω models [199]. The approach consists in using the k-ω model near the wall multiplied

by a blending function. In this way, the blending function is zero close to the wall, which corresponds to the standard k-ω equation. On the contrary, in the far-field the blending function is unity, corresponding then to the k-ε model. The shear stress transport model (SST) was a modification developed by the introduction of a limiter placed on the eddy viscosity to make the shear stress proportional to the kinetic energy in the boundary layer [198]. This model has demonstrated to perform well in a variety of flows, especially for boundary layer flows.

Another category is the Reynolds stress transport models (RSM), also referred to as second-moment closure models [198], that allow to include non-local and history effects. This approach, initially proposed by Rotta in 1951 [197], is the most complex and computationally expensive. It requires the solution of six transport equations for each component of the Reynolds stress and an extra equation to obtain the length scale of the local turbulence. Thus, it is recommended for situations in which the turbulence is strongly anisotropic to accurately account for the effects of separation, recirculation, curvature and swirl.

As previously mentioned, the k-ω Wilcox turbulence model has demonstrated to be the most appropriate choice to close the RANS equations for supersonic internal flows. Therefore, it will be used to numerically study the shock train behaviour in Chapter 6 with equations defined by Equations 3.42 and 3.43 [210].

$$\frac{\partial}{\partial t}\left(\rho k\right) + \frac{\partial}{\partial x_j}\left(\rho U_j k\right) = \frac{\partial}{\partial x_j}\left[\left(\mu + \sigma_k \mu_t\right)\frac{\partial k}{\partial x_j}\right] + \rho\tau_{ij}\frac{\partial U_i}{\partial x_j} - \beta^*\rho\omega k \tag{3.42}$$

$$\begin{aligned}\frac{\partial}{\partial t}\left(\rho\omega\right) + \frac{\partial}{\partial x_j}\left(\rho U_j \omega\right) = \frac{\partial}{\partial x_j}\left[\left(\mu + \sigma_\omega \mu_t\right)\frac{\partial \omega}{\partial x_j}\right] \\ + \alpha\frac{\omega}{k}\rho\tau_{ij}\frac{\partial U_i}{\partial x_j} - \beta\rho\omega^2 + \sigma_d\frac{\rho}{\omega}\frac{\partial k}{\partial x_j}\frac{\partial \omega}{\partial x_j}\end{aligned} \tag{3.43}$$

The variables σ_k, σ_ω, σ_d, α, β, and β^* are closure coefficients.

3.6 Conclusions

Most numerical studies on shock trains attempted to match the computed results with experimental variables often located at the duct centreline that are difficult to be acquired with non-intrusive methodologies. Even though the agreement between computations and experimental data are increasingly improving, numerical flow field describing shock trains are limited by the choice of the numerical algorithms employed.

None of the numerical techniques developed so far has reached a satisfactory level of agreement with measured data. More accurate flow models must be employed, including the application of transverse pressure gradients, heat transfer and flow unsteadiness. Furthermore, two-dimensional simulations are largely used because of the limited computational resources required. Three-dimensional simulations would be valuable since a two-dimensional description has demonstrated the inability to reproduce the flow field.

RANS equations are the most used approach to study internal flows. In particular, the k-ω turbulence model have demonstrated to provide the most accurate results in a wide range of flow configurations. This indicates that RANS equations closed by the k-ω model can be used to provide a deeper insight of the shock train flow field in the current study.

4 | Experimental methodologies

COMPRESSIBLE flows are extensively studied due to their wide applications in the scientific and industrial fields. To completely define the flow characteristics the knowledge of density, pressure, temperature and velocity is necessary. High-speed flows are challenging to be measured, and both qualitative and quantitative methodologies employed to study the flow properties in this project will be illustrated in this chapter. The importance of collecting data of flow field with the highest resolution achievable in time and space is crucial to resolve both large and small scale flow structures. The availability of a huge amount of high-quality experimental data guarantees to satisfy the requirements to obtain a better observation of the physics of the flow as well as to have a meaningful comparison with numerical simulation. The experimental aims of this thesis are to identify and set up the experimental methodologies suitable to collect data for the study of shock trains in the current wind tunnel.

4.1 Schlieren photography

Schlieren photography is a method to visualise compressible flows that relates the refractive index of the light passing through a transparent medium with the medium density. Although the results are limited to a qualitative observation, it is an important tool that gives immediate accessibility of the flow field and allows the insight of many flow features.

The occurrence of atmospheric refraction was known since the time of the Ancient Greeks and Romans [211]. Kleomedes reported that the sun is visible when already hidden under the horizon because of the refraction of light rays. However, the laws describing this phenomenon were unknown until the XVII century when the first reported experiment on the refraction of light was performed by Robert Hooke [212], laying the foundation of the schlieren technique. In his book, *Micrographia*, Hooke introduced a new point of view, stating that the light rays pass through an infinite amount of thin layers which have a slightly different density, and thus refractive index. Hooke's experiment consisted in simply observing the thermal disturbance of air due to the presence of a candle, employing another candle as a light source. The reenactment of Hooke's original experiment is illustrated in Figure 4.1.

Other scientists contributed to the enhancement of this technique and one of the main

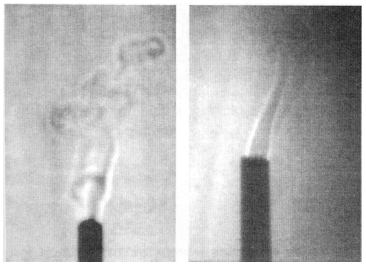

Figure 4.1: Image from a reenactment of Hooke's original schlieren [213].

participation was given by the physicist Jean-Paul Marat in the XVIII century who invented the helioscope. With this device, Marat observed that the projected shadows of a candle show luminescent moving halos. The uneven optical density, responsible of the unequal refraction, is hardly visible with naked eye. To enhance the visibility of such variations, optical devices have been improved based on the peculiarity that the ray path of a light beam through an inhomogeneous medium is not rectilinear but follows a curved trajectory. The physicist Leon Foucault invented the knife-edge test, a cut-off device which allows the discrimination of regular and irregular rays [213]. Another physicist, August Töepler, is recognised as the inventor of the schlieren methodology. Referring to density gradients in inhomogeneous transparent media, Töepler called his experimental apparatus, composed of a lantern as a light source, a knife-edge cut-off device and a telescope for viewing the shock wave motion, with the German word *Schliere* which means streak, striation.

Being an optical method, schlieren photography has the characteristic to not disturb the flow and is one of the most important and powerful approaches to visualise high-speed flow features such as shock waves, shear layers and turbulence. However, since the basic equations describing the variation of the refractive index assumes negligible changes along the optical axis, schlieren images provide only a two-dimensional description of the flow.

4.1.1 Theory of Schlieren photography

While in a homogeneous medium the refractive index of the light is the same everywhere, an inhomogeneous optical medium exhibits a spatial variation of the refractive index. These gradients can be static, like irregularities in glass, or dynamic such as variations in pressure, density, composition, or temperature in fluids.

In the case of gases the physical principle is expressed in Equation 4.1, through the linear relation between the gas density, ρ, and the refractive index, n, which is defined as the ratio between the light speed in vacuum, c_o, and the light speed in the medium, c.

$$n - 1 = k\rho \tag{4.1}$$

The Gladstone-Dale coefficient, k, for air in standard conditions is about 0.23 cm^3/g, whereas for other gases it may vary from 0.1 to 1.5. The refractivity of a gas, $(n-1)$, depends on its composition, temperature, density, and the wavelength of light.

The atmosphere is an inhomogeneous media due to the presence of turbulence, weather phenomena, thermal convection, etc. All these effects change the atmospheric density and make starlight to twinkle due to a distortion of the light rays. This principle is applied to high-speed flows where the sharp density change across the shock wave front is used to detect the refracting or reflecting action of the steep density gradient of the light beam. The part of light beam that is deflected is separated from the collimated beam, which passes through the knife-edge and is focused in the camera. The intensity variations are then recorded in an image made of brighter or darker points with respect to the background, corresponding to the shape and density of the refractive object.

The sensitivity of the schlieren system, S, is defined as the rate of change of the image contrast with respect to the refraction angle [214]. The sensitivity can be written in terms of the focal length of the second mirror, f_2, which focuses the light beam into the plane of the knife-edge, and the portion of the light source image passing through the cut-off device, h, with Equation 4.2.

$$S = \frac{f_2}{h} \tag{4.2}$$

From this equation it is clear that the sensitivity can be enhanced both increasing the focal length of the second parabolic mirror or reducing the amount of light which passes through the knife-edge [213]. Since a smaller gradient of the refractive index leads to a smaller light ray deflection, when a greater amount of light is cut off by the knife-edge the schlieren system becomes more sensitive and tiny disturbances are visible. However, small values of h require the use of a powerful light source to avoid insufficient illumination, and high-pressure xenon lamps are commonly employed. The continuous light source guarantees that a sufficient amount of light is captured by the high-speed cameras even for a short exposure time to acquire data of fast processes such as transient phenomena.

Additionally, another limit of sensitivity is due to the diffraction effects at the knife-edge. As the uncovered part of the knife-edge, h, is made narrower, the knife-edge begins to behave as a slit, and thus the image appears less discernible and the inaccuracy increases.

4.1.2 Setup of Schlieren photography

Schlieren can be set up with different configurations. Töepler's z-type two-mirror schlieren system, illustrated in Figure 4.2, is the most commonly employed and its name derives directly from the arrangement of the equipment. Two identical mirrors are placed tilted in the

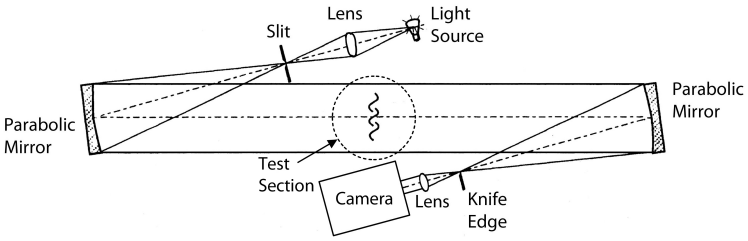

Figure 4.2: Schematic of the schlieren setup.

way to make the horizontal light beam to follow a z-shaped path with the light source and the recording unit placed at two ends of the optical path.

This configuration is widely used since it allows to minimise the space employed for the setup still locating each component at the optimal distance in the light path. On the other hand, the incident and reflected rays from the mirrors are off-axis introducing optical aberrations, i.e. comma and astigmatism [213]. Comma arises when the direction of the light reflected from a mirror depends on the point of reflection and has the effect to spread a point into a line. The image suffers from astigmatism as a consequence of the off-axis tilt of the mirror and from differences in the path length along the optical centreline leading to a non-uniform background when a high sensitivity is used. Optical aberrations are minimised using small off-axis angles. The z-type configuration has the peculiarity to further reduce the aberrations of the mirrors, which have the same off-axis angle. According to Vasil'ev [215], astigmatism can be eliminated by placing correcting lenses near the focal point.

The schlieren images from the study of diamond airfoils used a light beam obtained from a synchronized pulse diode laser with 640 nm wavelength and pulse duration set to 10 ns to better visualise shock waves. As illustrated in Figure 4.3, the light beam is then collimated with a parabolic mirror of 200 mm diameter and 1000 mm focal length. The light beam then

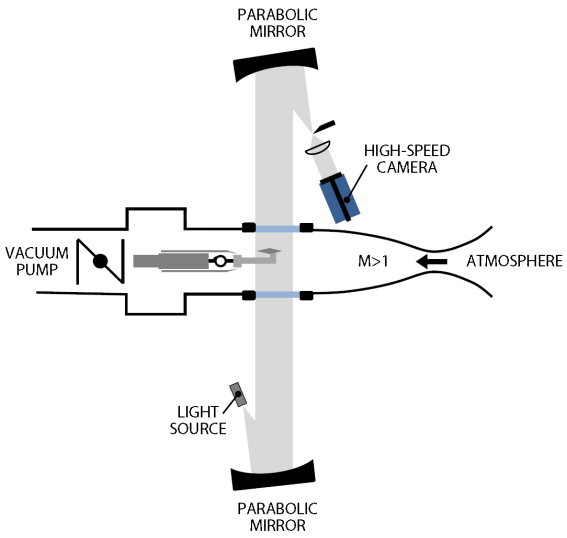

Figure 4.3: Optical arrangement of the experimental schlieren setup used in the wind tunnel at Nagoya University.

illuminates the test section before being focused by another parabolic mirror identical to the previous one. A knife-edge is placed at the focal length of the second mirror, after which a focusing lens of 100 mm diameter is placed before the high-speed framing Phantom camera with a maximum of 1280 $\times$ 800 pixels and 8.2 $\times$ 10^6 fps. Images of size 256 $\times$ 128 pixels were recorded with a frame rate of 200000 fps.

4.2 Development of pressure sensitive paint (PSP)

The traditional way to measure pressure over a surface consists in the use of pressure transducers at specific locations on the surface. However, this method has several disadvantages. As Bell et al. [216] reported, the main drawback of pressure transducers is due to the fact that pressure is measured in predetermined points giving a discrete pressure distribution. A large number of transducers would lead to a high-resolution distribution of the surface pressure, but the high cost and complexity of the experimental apparatus might be impractical. Furthermore, the orifices affect the collected data introducing a disturbance in the flow due to cavity effects.

A different approach, called pressure sensitive paint (PSP), has been developed in the aerodynamic field and extended to other applications, such as medicine and chemistry, to measure the blood oxygen content [217, 218]. The working principle of oxygen quenching of luminescence was discovered in 1935 by Kautsky & Hirsch [219], but PSP began to be studied for aerodynamic applications from the 1980s [220]. However, the first successful result in aerodynamics was obtained in the 1990s with the pressure mapping on a NACA airfoil in an indraft wind tunnel at a Mach number of 0.66 [221].

PSP is now a well-established method for surface pressure measurements employed to a wide range of wind tunnel experiments. It not only solves the intrusiveness downside of the pressure transducers but also provides a global and quantitative map of the pressure distribution over a surface. The limitation in spatial resolution is due to the pixel resolution of the imaging device [222] meaning that very small flow structures, including boundary layer separation, can be detected [223]. Klein et al. [224] calculated the two-dimensional forces and momentum distributions on the surface of an aircraft model from the static pressure obtained with PSP without the use of complex instrumentation like load cells. Although the experimental rig is quite expensive compared to pressure tapping, the costs are amortized as the number of experiments increases and the benefits are well rewarded with reliability and fast response characteristics [217].

Most PSP have a response time of the order of several millisecond so that the application of PSP to unsteady flows is still difficult. In the last few years the paint formulation has been

improved considerably with the achievement of coatings characterized by a step time close to 1 μs [222]. However, in flow fields characterised by large temperature gradients the use of such technique presents challenges.

For the current investigation, PSP would provide valuable information about the boundary layer development on the walls. The pressure distribution over a surface is capable to identify with accuracy boundary layer separations, which in turn provide the exact axial coordinate of the leading shock in the shock train. Knowing with precision the location where the shock train establishes in the wind tunnel test section would allow the validation of the numerical results. In this section the behaviour of different pressure sensitive paints is examined in order to select the optimal paint to be applied in the experimental facility.

4.2.1 Theory of PSP

PSP relies on the oxygen quenching of luminescent molecules. This happens when a light source at a specific wavelength irradiates the luminescent molecules of the coating which are excited to a higher level of energy. In returning to their unexcited ground state, these molecules lose energy both emitting luminescence and colliding with oxygen molecules through a process called oxygen quenching [217], as Figure 4.4 illustrates.

The collision process between luminophores and oxygen molecules leads to an inversely proportional relation between the rate of quenching and the oxygen concentration described by the Stern-Volmer equation:

$$\frac{I_0}{I} = 1 + K_{sv}\left(T\right)\left[O_2\right] \tag{4.3}$$

where I_0 is the luminescent intensity when the oxygen concentration is zero (vacuum condi-

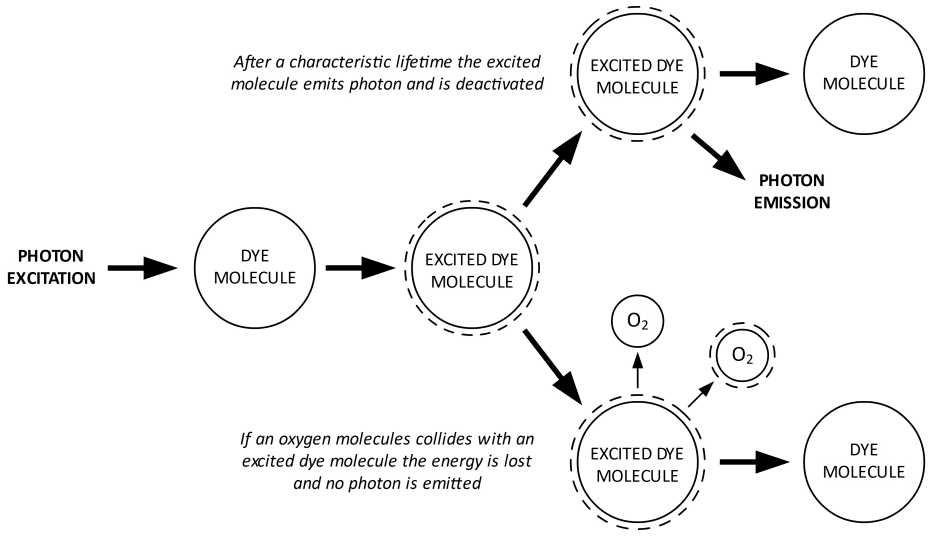

Figure 4.4: Schematic of oxygen quenching.

tions), K_{sv} is called Stern-Volmer constant and $[O_2]$ is the oxygen concentration. P_0 and T_0 are the pressure and temperature which correspond to the reference intensity I_0. Equation 4.3 is commonly expressed in terms of non-dimensional intensity and pressure by Equation 4.4, where the reference conditions I_{ref} and P_{ref} are usually assumed as those when the wind tunnel is not running (wind-off condition) [220].

$$\frac{I_{ref}}{I} = A\left(T\right) + B\left(T\right)\left(\frac{P}{P_{ref}}\right) \tag{4.4}$$

Equation 4.4 assumes that the relation between the oxygen concentration and the partial pressure is linear. This approximation is valid only in a limited interval of pressures but, in general, is sufficiently accurate [217]. However, to extend its validity to a wider range of pressures, the non-linear phenomena that take place between the luminescent intensity and the pressure caused, for instance, by the presence of imperfections in the coating are included in Equation 4.5. In this equation the pressure ratio terms, $(P/P_{ref})^n$, are multiplied by temperature-dependent coefficients, $C_n\left(T\right)$, that differ from one luminophore to another and are determined with static calibration [48, 225].

$$\frac{I_{ref}}{I} = C_0\left(T\right) + C_1\left(T\right)\left(\frac{P}{P_{ref}}\right) + C_2(T)\left(\frac{P}{P_{ref}}\right)^2 + ... \tag{4.5}$$

The pressure sensitivity S_P, expressed in $\%\,/kPa$ in Equation 4.8, is non-dimensionalised at reference condition and describes the change in luminescence signal over a given pressure change [226]. The temperature sensitivity S_T, expressed in %/K Equation 4.7, describes the change in luminescence signal over a given temperature change at reference condition.

$$S_P = \frac{\Delta\left(I_{ref}/I\right)}{\Delta\left(P/P_{ref}\right)} \tag{4.6}$$

$$S_T = \frac{\Delta\left(I/I_{ref}\right)}{\Delta T} \tag{4.7}$$

The parameter S_{PT}= S_T/S_P, is then defined as the pressure sensitivity because of a variation of temperature. Higher pressure sensitivity corresponds to lower S_{PT} [227].

4.2.2 Temperature sensitive paint (TSP)

A similar photo-physical process is the one used by the temperature sensitive paint (TSP) which provides an accurate quantitative measurement of surface temperature. The heat flux to the surface, and therefore the surface temperature, is a function of the local heat transfer coefficient. As the heat transfer coefficient is substantially larger for a turbulent boundary layer compared to a laminar boundary layer, TSP is very useful for the detection of the transition from laminar to turbulent from a sharp increment in the surface temperature.

Compared to PSP, TSP molecules that are in the excited state release energy through thermal quenching, a non-radiative decay mechanism. As the temperature increases, the probability that the molecules return to the ground state by a radiationless process also increases. The luminescent intensity from the molecule in this case is a function of the temperature to which the molecule is exposed and therefore is non-sensitive to pressure. The relationship between intensity and temperature is expressed by the Arrhenius law [228], where E is the activation energy for the non-radiative process and R the universal gas constant.

$$ln\frac{I\left(T\right)}{I\left(T_{ref}\right)} = \frac{E}{R}\left(\frac{1}{T} - \frac{1}{T_{ref}}\right) \tag{4.8}$$

4.2.3 Coating properties

As illustrated in Figure 4.5, the pressure sensitive paint usually consists of a multilayer coating structure applied to the model surface composed of the screen layer, the contact layer, and the active layer [224]. The screen layer is composed of a special white paint that creates optical uniformity on the model surface, increases the reflection of light, and amplifies the emission signal [217]. The contact layer is applied to ensure a better adherence between the screen layer and the active layer, so that the coating can withstand both normal and tangential loads of airflow. The active layer consists of a polymer highly permeable to oxygen with pressure sensitive luminescent luminophores dispersed within it. To correct non-homogeneous illumination, intensity sensitive luminophores are included in the mixture.

Due to the variety of luminescent molecules and oxygen-permeable matrices, PSP can be used in different aerodynamics testing scenarios [229, 230]. Experiments are affected by the formulation of the coating which determines the value of Stern-Volmer coefficients. Depending on the flow field, research groups usually develop a suitable coating. In general, the desirable characteristics of paint combine both photophysical and mechanical properties. The main physical property required is the application of a coating with a thickness that does not modify the flow characteristics. Additional desirable properties are adhesion, hardness, smoothness, ease to be sprayed on the surface. Non-toxic solvent with fast evaporation

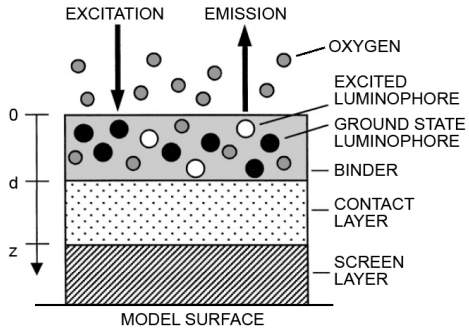

Figure 4.5: Pressure sensitive paint structure [217].

should be selected as chemical composition. The performance required are primarily small temperature sensitivity, high luminescence and paint stability. Moreover, a desirable characteristic of the coating is that the difference between the emitted and the absorbed wavelengths is large enough to easily separate the two signals. The detection of light from sources other than the PSP coating would lead to errors in the measurement and reduction in accuracy. The use of optical filters in front of the detector and excitation sources ensures that the wavelength of the illumination source does not overlap with that of the paint luminescence emission.

The binder enhances the molecules collisions and partially inhibits the interaction of atmospheric oxygen with the embedded luminophore molecules [222]. The desirable characteristic of the binder is to be sufficiently permeable to oxygen but not too much in order to avoid that the luminophores are burnt. The binder can dramatically alter the properties of the PSP coating reducing the probability of oxygen-dye collisions, changing the luminescence characteristics of the molecules, and affecting the time response of PSP to pressure changes. Figure 4.6 illustrates the difference between two coatings, PSP1 and PSP2, where only the binder is changed.

The temporal response time, $\tau_{relaxation}$, of PSP depends on the paint thickness, th, and the oxygen diffusion coefficient of the binder, D, with the following proportion:

$$\tau_{relaxation} \propto \frac{th^2}{D} \tag{4.9}$$

As reported by Kameda [231], the typical diffusion coefficient for oxygen in polymer is less than $10^{-9}\ m^2 s^{-1}$ and the thickness of the polymer layer is approximately 10-40 μm, meaning that the characteristic time is greater than 0.1 ms. The slow response to rapid pressure change makes polymer based PSP unsuitable to measure unsteady flow phenomena [232].

From Equation 4.9, the attempt to reduce the response time can be done either decreasing the paint thickness or increasing the diffusivity coefficient. The reduction of the paint thickness degrades the signal to noise ratio (SNR), thus a trade off between the two requirements is necessary. Schairer [233] proposed an analytical formula to determine the optimum paint

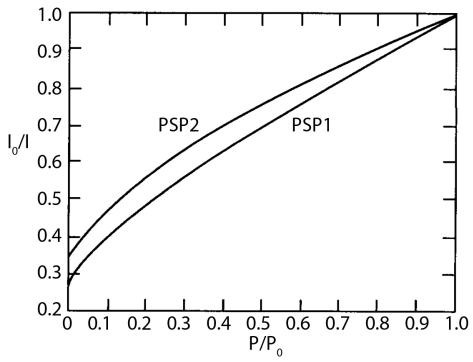

Figure 4.6: Pressure calibration curves of two coatings, PSP1 and PSP2, with the same active molecule but different binder [217].

thickness. The other way to improve the temporal response characteristics of PSP is to increase the diffusivity of gas within the paint binder. This approach was introduced by Baron et al. [234] by having the luminophores absorbed in a porous silica gel plate. Although this PSP formulation is very fragile for wind tunnel application, a time response of the order of submilliseconds was demonstrated to be achievable. Several types of porous binders have been formulated to enhance energy transfer with oxygen molecules increasing the interaction surface and maintaining a good luminescence intensity [222]. The different processes of oxygen permeation between conventional and porous PSP coatings is illustrated in Figure 4.7. With a porous substrate, the area available to oxygen to permeate is considerably larger. Hybrid formulations such as the combination of a high-concentration of ceramic particles with a small amount of polymeric binder or the removal of the binder and application of the luminophore directly on a micro-porous surface have also been proposed [229,232,235,236].

4.2.4 Anodized-aluminium PSP (AA-PSP)

Application of PSP to high-speed tests is not easy since high-enthalpy flows may present large temperature variations on a test model. In shock tube applications the duration of the experiment is of the order of milliseconds so that the temperature effects of PSP are usually negligible. However, in blow-down hypersonic wind tunnels the temperature effect can become comparable to the pressure effect making it difficult the compensation for temperature.

Anodized-aluminium PSP (AA-PSP) makes use of an electro-chemical process to increase the surface porosity before the application of the luminophores. A test model requires a long time to be anodized since it undergoes careful pre-treatment, anodization, and a final post-treatment [237]. The luminophores are absorbed into the microscopic pores by dipping the model in a solution containing dye [238].

In porous anodized aluminium, Knudsen number, Kn, is greater than unity, therefore the gas diffusion is dominated by the Knudsen diffusion [231]. The effective diffusion coefficient, in Equation 4.10, with R the universal gas constant, M the molecular weight of the gas, T the temperature, and d the diameter of the micropores, is approximately $5 \times 10^{-6}\ m^2 s^{-1}$

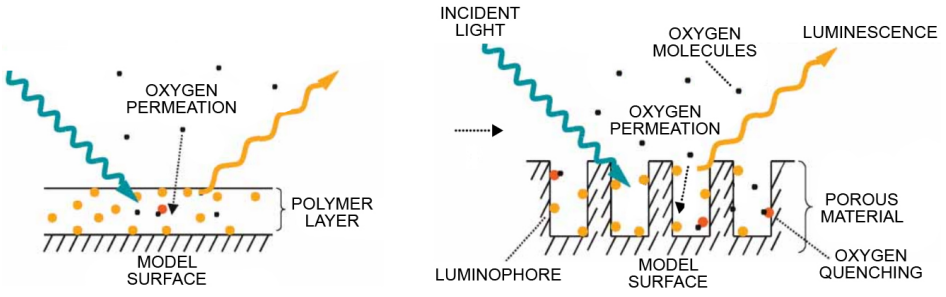

Figure 4.7: Oxygen permeation process in: a) Conventional PSP; b) Porous PSP [222].

in the case where the micropores have diameter in the range $10\ nm < d < 100\ nm$. The response time for AA-PSP is of the order of microseconds [239], however the pore diameter and depth affect the response time and values of approximately 0.1 μs can be achieved [222].

$$D = d\sqrt{\frac{8RT}{9\pi M}} \tag{4.10}$$

AA-PSP has the drawback to be highly sensitive to humidity and the possibility to apply a hydrophobic layer has been explored. It has been shown that the application of an hydrophobic layer reduces the paint aging and the hysteresis effect is less pronounced [238]. Nakakita [240] adopted a series of measures to eliminate humidity effects including heating the model after the application of the dye and keeping the model in a vacuum environment with dry air during the tests. By calibrating the paint more than once a day, the authors noticed small changes in the pressure sensitivity but after 10 days no further change in the paint characteristics was observed.

Several kinds of luminophores can be used and are divided into three main families: ruthenium polypyridyls, platinum/palladium porphyrins, and pyrene derivatives. Ruthenium-based and platinum-based paints hold the desirable characteristics to be easily employed in aerodynamic testing since they show excellent properties in terms of pressure and temperature sensitivity. Although ruthenium-based coats are difficult to be incorporated into polymer systems and have low sensitivity to oxygen, are a popular choice in AA-PSP. Koike et al. [48] successfully applied AA-PSP with ruthenium luminophores to study the unsteady behaviour of shock trains inside a constant area duct. Porphyrins compounds have long luminescent lifetimes, good sensitivity to oxygen, but low signal at atmospheric pressure. Platinum tetra(pentafluorophenyl)porphine (PtTFPP) is largely used in PSP experiments because of its high photostability although the lifetime spans from 10 μs at ambient conditions to 85 μs at vacuum conditions [241]. Pyrene derivatives, which belong to the group of aromatic hydrocarbons, are characterised by low temperature sensitivity and long fluorescence lifetime of the order of 200 ns, but suffer of high photo-degradation [222]. In Figure 4.8 a pyrene-based and a ruthenium-based paint are compared: pyrene has a more linear behaviour

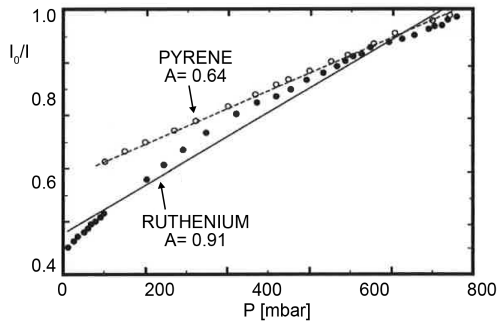

Figure 4.8: Calibration curves for ruthenium and pyrene at 20^{o}C [224].

but lower pressure sensitivity. As reported by Egami et al. [241], the AA-PSP tends to have a non-linear relationship between luminescence intensity and pressure, so that a polynomial of the second order in the Stern-Volmer equation needs to be used.

4.2.4.1 AA-PSP preparation

The procedure to make the coating has been described in detail by various authors but some differences have been identified. After several attempts, the procedure to correctly anodize aluminium surfaces is summarised below. It is of fundamental importance that the test model is made of an aluminium alloy otherwise the thin anodized aluminium layer would not form onto the surface during the electro-chemical process.

- Firstly, the aluminium model is degreased by wiping with ethanol (C_2H_5OH) and chemically polished by immersion in a 2 wt% (or 3 wt%) sodium hydroxide (NaOH) solution for 5 min. Sakaue [242] dipped aluminium sheets in a 2% NaOH solution for 2 min whereas Kameda et al. [231] used a 3% NaOH solution for 3 min.
- The aluminium model is then washed with distilled water and left to dry.
- Sulfuric acid (H_2SO_4) is diluted with water with 1 mol/l [231].
- The anodization is achieved by immersing the model in the electrolytic solution and connecting it to the anode of a DC power supply whereas a pure aluminium sheet is used as cathode. Power is supplied with a constant current density of 10 mA/cm^2 [242] or 12.5 mA/cm^2 [231] and voltage of 20-25 V. A continuous stirring is necessary to keep the solution with uniform concentration and temperature. Sakaue [242] used a temperature of 0^{o}C, Gregory et al. [222] recommended a low temperature of 5-10^{o}C, whereas Yang et al. [237] left the solution at room temperature.

  The thickness of the anodized layer is almost linear to the anodization time. Kameda et al. [231] obtained a uniform porous surface with micropore diameter in the range 20 to 100 nm and thickness increasing from 6.1 μm in 15 min to 27.5 μm in 60 min.
- A post-treatment process that removes hydrates or oxidation layer from the surface is obtained by immersing the model in 3 wt% phosphoric acid (H_3PO_4) solution for 20 min at constant temperature of 20-30^{o}C [227]. To remove the alumina layer Sakaue [242] dipped the anodized sheet in a 5 wt% phosphoric acid for 20 min at 30^{o}C.
- The aluminium model is then rinsed with distilled water and left to dry.
- The dye molecules are applied via adsorption by dipping the model into a solution in which the luminophores are dissolved.

The relative concentration of the solution, the type of solvent and the dipping duration depend on the luminophores and can lead to different paint characteristics. Sakaue et al. [242] investigated the effect of eight solvents with different polarity index on ruthenium since the solubility of the luminophore depends on the polarity of the solvent [226]. The optimum luminophore concentration for a ruthenium-based dye in dichloromethane solvent (CH_2Cl_2) is of the order of $0.3 \times 10^{-3}\ mol/l$ for 1 min at 298 K [241, 243]. Merienne et al. [227] dissolved a ruthenium complex in CH_2Cl_2 with 0.54 mM for 1.5 min. Kameda [231] applied several combinations of luminophores and solvents with a proportion of 28 mg of luminophore in 40 ml of solvent but different dipping times. For example, 10 s was used for the ruthenium in CH_2Cl_2 and 5 s for PtTFPP in C_2H_5OH.

4.2.5 Binary formulation

The thermal quenching inherent in PSP paints ensures that a temperature rise alters the probability that the molecule return to the ground state through a non-radiative process [244]. Another source of temperature sensitivity occurs in polymer binders since the oxygen permeability is a function of temperature. Regardless of the paint formulation, an effective implementation of a PSP requires that temperature effects are characterised and corrected. Compensation of temperature effects for PSP data collected in wind tunnels are beneficial since wind-off and wind-on images are not acquired at the same model temperature [245].

Binary pressure sensitive paints have been developed to accomplish the needs to minimise temperature dependence as well as to correct model movements and non-homogeneous illumination. In binary paints a reference probe is incorporated within the paint. It holds the characteristics of: being excited by the same illumination wavelengths as the pressure probe; having the emission spectra that does not overlap with that of the pressure probe; having not the same temperature dependence as pressure sensor; must not interact with the pressure sensor; must have similar solubility properties [246–248].

A successful application of binary paint was achieved by Goss et al. [249] by adding to the UniFIB paint from ISSI another signal. UniFIB has already a low temperature sensitivity of $0.5\%/K$, but with the addition of pyridine, temperature sensitivity was reduced to $0.0\%/K$. Khalil et al. [248] concluded that the temperature dependence with the addition of a porphine-based as a reference luminphore was substantially reduced compared to that of the pressure sensitive luminophore alone. Rare-earth complex are often used as temperature sensitive dye since the excitation band is usually in the UV range and the emission spectra does not interfere with that of the pressure probe [250–252]. Mochizuki et al. [253] reported that europium in combination with palladium complexes are the most prospective candidates for PSP/TSP paints. However, it seems that europium complexes could be degraded under continuous irradiation of excitation light in the co-presence of palladium complexes. Klein

et al. [224] were able to detect vortex interactions and fine flow structures instabilities with a pyrene derivative as a pressure sensitive probe and a europium complex as a reference dye. Egami et al. [241] recently applied a fast response bi-luminophore pressure sensitive paint on an anodized aluminium substrate with a inkjet printing of sensor-dot arrays. It was reported that the interference between the PSP and TSP luminophores in conventional bi-luminophore AA-PSP prepared with the dipping method degrades the sensitivity or the luminescence intensity. This new method appears promising since it would solve the need to dissolve PSP and TSP dyes in a cosolvent. Indeed a suitable solvent for each dye is selected to achieve high luminescence intensity and high sensitivity.

4.2.6 Coating calibration

Ideally, the Stern-Volmer coefficients would not have a temperature dependence, leading to a perfect inversely proportional relation between the luminescent intensity and pressure. However, in reality this is not the case and the application of some corrections to the calibration equation are necessary for reconstructing quantitative information from the pressure distribution over a surface of the model.

There are three types of calibration: *a priori* methods, *in-situ* calibrations, and *direct* calibration of the entire model in the wind tunnel test sections (only in pressurised wind tunnels). The a priori calibration, called also static calibration, consists in collecting data by varying both pressure and temperature when the sample is excited by a light source in an external calibration chamber giving the Stern-Volmer coefficients prior to testing in a wind tunnel. The values of pressure and temperature in the calibration chamber are continuously monitored using a pressure transducer and a thermocouple, respectively. The advantage of calibrating a sample is that a full-scale test is not necessary and potential paints can be evaluated at the same time. However, the absolute level of pressure can be difficult to be computed due to the many bias errors that affect the measurement. This type of calibration is very sensitive to temperature and humidity changes between the static calibration performed under controlled conditions and the physical test. Additionally, Klein et al. [224] reported that the sample does not have the same optical properties as the model since usually the thickness of the paint is not the same. To correct these systematic errors in a priori calibration, the in-situ, or dynamic, calibration has been developed [222].

In in-situ calibration, the paint is calibrated in the wind tunnel with the assumption that the model is isothermal. This approach uses the value of pressure transducers on the actual test model to relate the luminescent signal of PSP to the corresponding locations of pressure taps. Systematic errors are reduced since the overall changes in incident light intensity are absorbed by the calibration coefficients and spatial variations in temperature are averaged among all points included in the calibration [217, 237].

There is also a hybrid technique that combines the in-situ and a priori calibrations, called the k-fit method [254]. This method is particularly useful in situations where the range of measured pressures does not cover the range encountered in the experiments [216]. Pressure sensitivity of the paint at a single temperature is determined a priori in a calibration chamber and expressed with a second-order polynomial in I_{ref}/I in Equation 4.11. The factor K, which accounts for the differences in temperature between the wind-off and wind-on conditions, is adjusted in situ to provide the best fit of the data from pressure tapping.

$$\frac{P}{P_{ref}} = C_1 + C_2\left(\frac{KI_{ref}}{I}\right) + C_3\left(\frac{KI_{ref}}{I}\right)^2 \tag{4.11}$$

To perform static calibration, an in-house PSP calibration system was designed by using a calibration chamber co-operating with a measuring system controlled in the LabView environment. The setup system used in this research is illustrated in Figure 4.9. The calibration chamber, made of aluminium, allows the visualisation of an area with diameter of 100 mm through a 20 mm thick quartz glass. The components of the chamber include a Peltier thermoelectric plate, pressure and temperature sensors, a pressurising inlet, and a valve to evacuate pressure. On the rear cover, a heat sink attached to a small fan ensure that heat is released outside of the chamber. The PSP sample was held on the Peltier plate with a thermal glue to create good contact between the calibration sample and the heat exchanger. The Peltier plate, with dimensions of 55 $mm \times 55$ mm and maximum temperature difference of 74^{o}C, allowed to control temperature in the chamber by regulating the power. The temperature was measured with a thermocouple and monitored with a thermocouple meter display with accuracy of $\pm 0.5^o$C. The pressure inside the calibration chamber was controlled with a Kulite pressure transducer.

A 400 nm LM2X-DMHP LED was used as illumination source to excite the PSP samples. LEDs are excellent light sources for PSP since the light is fairly uniform, stable and

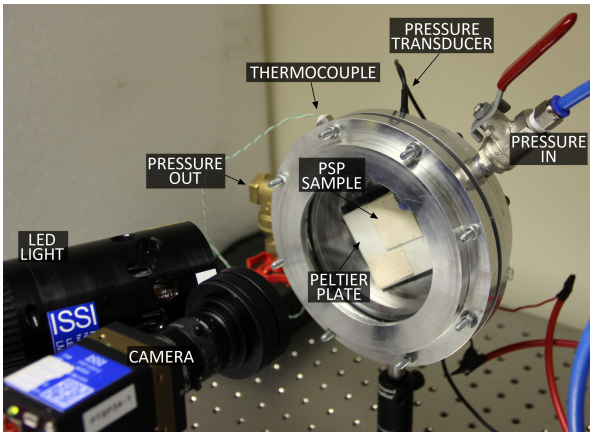

Figure 4.9: Setup used for static calibration.

produces little heat, but have the drawback to change wavelengths when temperature heats them up [246]. In this configuration, the camera was located normal to the test section minimising errors due to internal reflections and the LED on its side. Moreover, to avoid the effects of non-uniform illumination and obtain a stable amount of light, the LED was switched on around 5 min before the data acquisition.

A series of optical filters were placed in front of the optical detector with the purpose to eliminate light from sources whose wavelengths could contaminate the coating emissions [217]. If external wavelengths are not eliminated, measurement errors occur reducing the result accuracy. The whole calibration procedure requires to be carried out in the dark in order to minimise the contamination from external light sources. The filtered signal was recorded with a 2-megapixel CCD camera with 12-bit dynamic range. In all cases, 40 sequential shots were collected with a frame rate of 35 fps and later averaged into one image. The averaging procedure increases the signal-to-noise ratio (SNR) and thus reduces the random noise of the PSP which affects each single image [225].

The data gained from PSP tests are in the form of intensity maps that need to be converted into pressure maps. At this stage, any misalignment between the wind-on and wind-off images can be corrected by determining and applying a transformation to the model coordinates [217]. The raw images show a gradient in colour due to variations in paint thickness, excitation light intensity on the sample surface and non-uniform luminophore concentration [218]. These effects are eliminated by taking the ratio with respect to the reference condition. The resulting variables, I_{ref}/I and P/P_{ref}, are plotted in the so-called Stern-Volmer graph and the coefficients of the Stern-Volmer equation can be determined.

In binary pressure sensitive paints, each signal can be collected separately using two cameras fitted with a set of optical filters to selectively capture the emission wavelengths [241, 248, 252]. Rather than using optical filters in front of the camera lens and complicated DAQ systems, the filtering can be applied on the chip using a Bayer filter that separates the two spectrally different signals emitted by the binary pressure sensitive paint. The raw output of Bayer-filter cameras is referred to as a Bayer pattern image where each pixel is filtered to record only one of three colors. Therefore, the three images are split depending on the wavelengths as approximately 390 nm to 475 nm for blue, 475 nm to 600 nm for green, and 600 nm to 750 nm for red. This means that the temperature and pressure sensitive dyes need to be carefully selected with emission spectra in a specific range of wavelengths to be detected by separate channels. In the current setup, the red and green channels are recorded simultaneously using one camera. For the binary paints, the output displayed in the Stern-Volmer plot is achieved by taking the ratio of the luminescent intensity of the pressure probe signal, f_S, and the reference signal, f_R, in Eqaution 4.12. The ratio of the images, R, is then divided by the ratio of the reference images, R_0, to generate a ratio-of-ratios, expressed by Eqaution 4.13, that compensates for temperature and illumination errors.

$$R = \frac{f_S(P,I)}{f_R(P,I)} \tag{4.12}$$

$$\frac{f_S(P,I)/f_R(P,I)}{f_S(P_0,I_0)/f_R(P_0,I_0)} \tag{4.13}$$

If the temperature sensitivity of the pressure and reference signals are identical, then the ratio pressure signal over reference signal is temperature insensitive [246].

4.2.7 Calibration results

In this section several paints have been investigated in order to find the optimal paint to be applied to the wind tunnel tests. The calibration procedure consisted of recording the luminescent intensity for each temperature at different pressures from vacuum to ambient.

4.2.7.1 Polymer-based paint

Four polymer-based paints from Innovative Scientific Solutions (ISSI) have been tested and the characteristics are reported in Table 4.1. The formulation of the paints adopts PtTFPP as active luminophore in a polymer matrix. Titanium molecules are included to enlarge the porosity of the polymer and to increase the SNR [255]. An additional fluorescent probe is added in the binary formulations. The type of the second probe is not provided by ISSI, but they state that it was chosen in order to closely match the temperature sensitivity of the pressure sensitive probe. 7 to 9 layers of cross coats were applied to a metal sample and a Dektac II profilometer was used to measure the thickness of the polymer compounds. All filters were mounted in front of the camera in conjunction with an additional reflective filter which blocks specular reflections from contacting the filter glass.

The samples were calibrated separately therefore an exact use of the same temperature and pressure values for all cases was not possible. However, Figure 4.10 illustrates that all

Name	$\boldsymbol{\lambda_P[nm]}$	$\boldsymbol{\lambda_R[nm]}$	**Filter**	$\boldsymbol{S_P[\%/kPa]}$	$\boldsymbol{S_T[\%/K]}$	$\boldsymbol{th[\mu m]}$
UniCoat	650	-	610 longpass	1.1	0.8	36
Binary UniCoat	650	525	530 longpass	0.7	0.7	30
UniFIB	650	-	610 longpass	1.9	0.6	29
Binary FIB	650	550	530 longpass	1.4	0.4	17

Table 4.1: Polymer-based paints from ISSI. The subscript of the peak of the emission wavelength is P for the pressure probe and R for the reference probe, respectively.

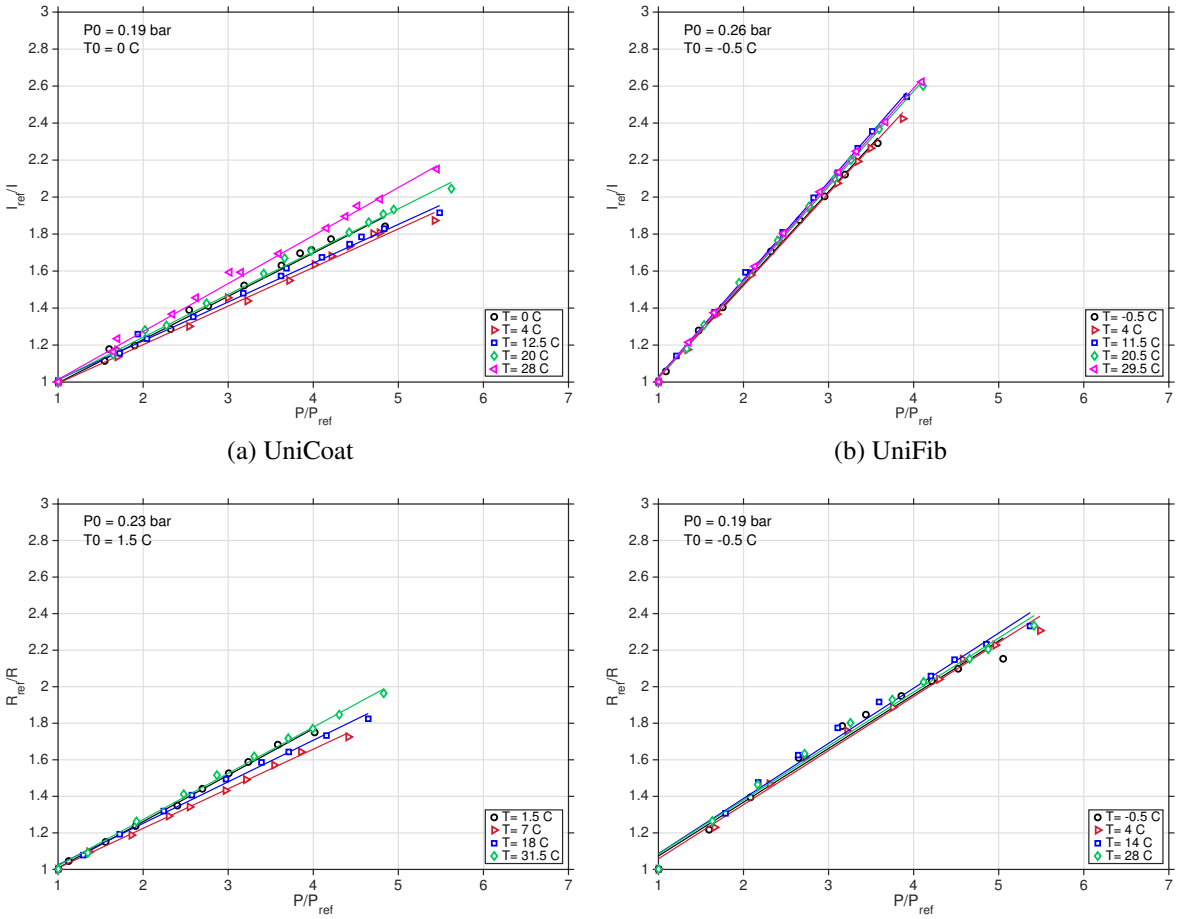

(a) UniCoat

(b) UniFib

(c) Binary UniCoat

(d) Binary UniFib

Figure 4.10: Stern-Volmer plot for different polymer-based paints.

the paints fit well with a first-order polynomial. All paints exhibit a small temperature dependence which is reduced further in binary paints. Additionally, compared to the UniCoat, the temperature dependence of UniFib compounds is significantly attenuated. In particular, Binary UniFib not only shows good characteristics as a PSP paint but also has the smallest thickness so it is particularly indicated for being applied to the internal high-speed flows where even a small change in the boundary layer could led to a considerably different result.

4.2.7.2 Ruthenium-based paint

The combination of voltage, current intensity, and time influence the outcome of the anodization process. Several attempts have been performed with small aluminium samples to determine the porosity of the surface and therefore the way the luminophores are absorbed. The effect of the current density, I, used during the anodization process on the aluminium surface is illustrated in Figure 4.11. Three samples were anodized for 30 minutes with voltage of 25 V and a current density I= 1, 2, and 3 A. The sulfuric acid was kept at a low

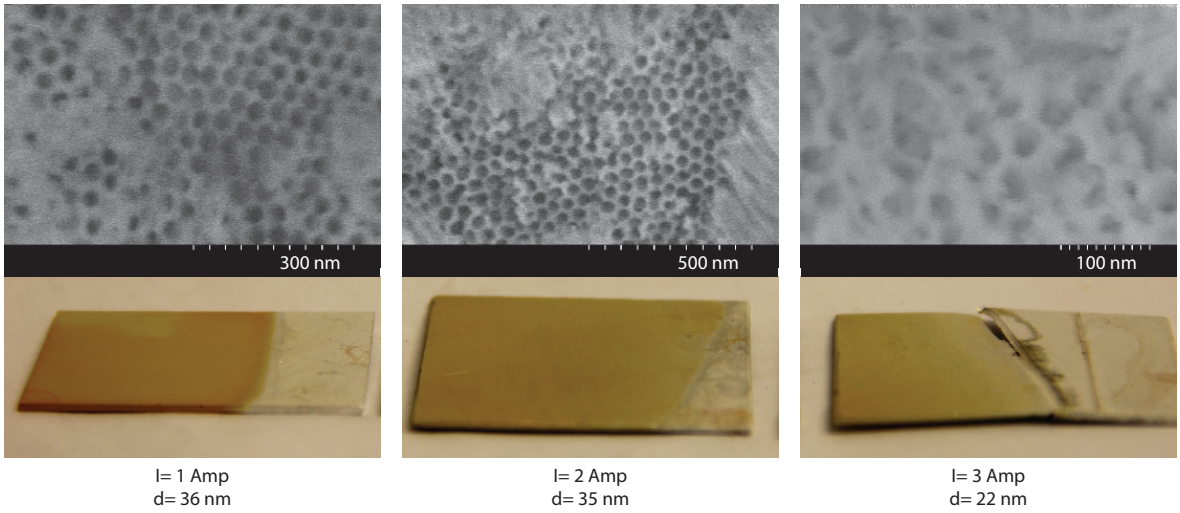

Figure 4.11: Effect of different currents intensity on surface details from scanning electron microscope (top) and alluminium alloy samples (bottom). From left to right I= 1, 2, and 3 A.

temperature by immersing the beaker into a bowl with cool water. The pores size were determined from the scanning electron microscope (SEM) images and are consistent with the literature. It has been observed that a high current intensity generates smaller pores size but also visibly reduces the thickness of the sample causing a change in the shape of the surface.

Static calibration of two ruthenium complex paints, $Ru(phen)_3^{2+}$, developed in-house have been examined. Tris(1,10-phenanthroline) ruthenium (II) chloride ($Ru(phen)_3Cl_2$) and tris-(bathophenanthroline) ruthenium (II) perchlorate ($Ru(phen)_3(ClO_4)_2$) were solved in dichloromethane (CH_2Cl_2) with concentration of $0.3 \times 10^{-3}\ mol/l$ for 5 min. The emission spectra of both the paints is in the range of $550 < \lambda < 650\ nm$ [225]. Figures 4.12 and 4.13 illustrate the Stern-Volmer plot of the two paints anodized for 30 minutes with

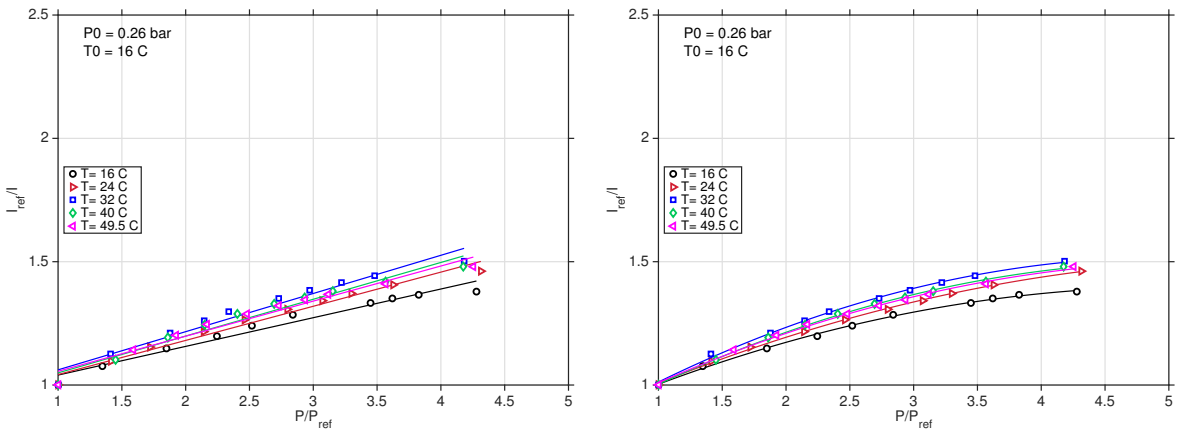

Figure 4.12: Stern-Volmer plot of $Ru(phen)_3Cl_2$ with: a) First-order polynomial; b) Second-order polynomial.

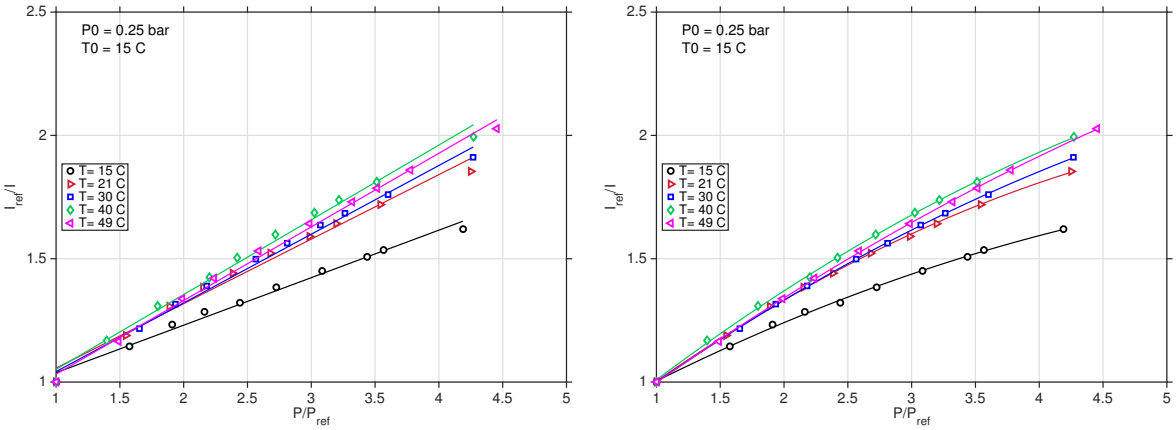

(a) (b)

Figure 4.13: Stern-Volmer plot of $Ru(phen)_3(ClO_4)_2$ with: a) First-order polynomial; b) Second-order polynomial.

voltage of 25 V and a current density I= 1.5 A. $Ru(phen)_3Cl_2$ exhibits a pressure sensitivity of 0.45%/kPa, whilst $Ru(phen)_3(ClO_4)_2$ shows a pressure sensitivity of 0.74%/kPa. In terms of temperature sensitivity, $Ru(phen)_3Cl_2$ exhibits a maximum temperature sensitivity of 0.14%/K in comparison to the 0.3%/K of $Ru(phen)_3(ClO_4)_2$. The average error between the experimental data and the corresponding value from the polynomial was estimated to be respectively less than 2% for $Ru(phen)_3Cl_2$ and 1.8% for $Ru(phen)_3(ClO_4)_2$ with a first-order polynomial curve. The data are better represented by a second-order polynomial due the effect non-linear terms. In this case, the error is dropped to less than 0.5% for $Ru(phen)_3Cl_2$ and 0.4% for $Ru(phen)_3(ClO_4)_2$.

The effects of non-linearity were investigated further in Figure 4.14. Two consecutive tests were performed for three temperatures. After the tests at constant temperature, the tem-

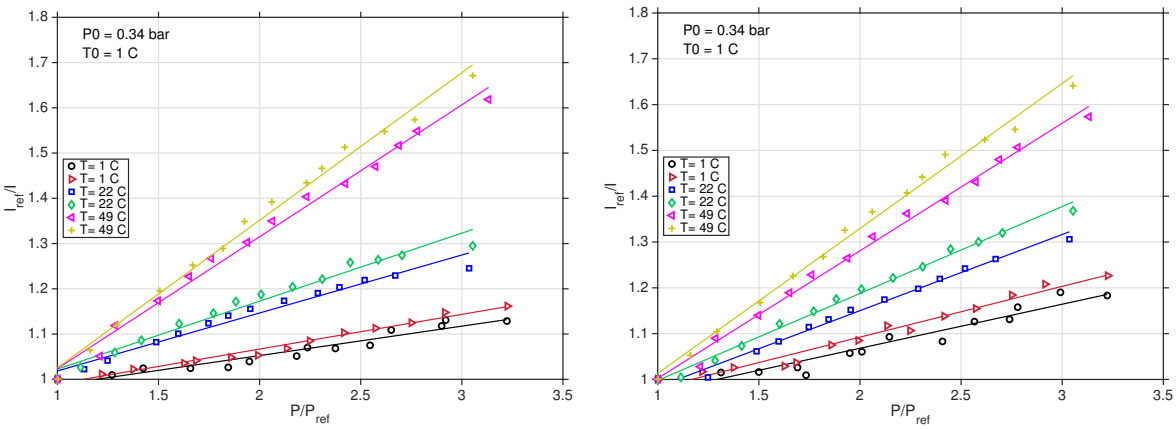

(a) $Ru(phen)_3Cl_2$ (b) $Ru(phen)_3(ClO_4)_2$

Figure 4.14: Stern-Volmer plot with a first-order polynomial for different AA-PSP paints.

perature was changed acting on the Peltier plate which required a time interval of 30 minutes to settle. It can be been observed that both the paints exhibit the same behaviour. For each temperature, the second test showed an increased intensity ratio, I_{ref}/I. The difference in the Stern-Volmer plots for constant temperature is due to the photo-degradation of the paint during time. Intensity signal was recorded every minute for 30 minutes. The variation of intensity with time is illustrated in Figures 4.15 and 4.16. An interesting feature is the change in the slope after 7-8 min. In the first few minutes the decrease in intensity is more pronounced and this tends to be more evident at high temperature and low pressure. At 1 bar this behaviour is observed only in $Ru(phen)_3Cl_2$ whereas the signal of $Ru(phen)_3(ClO_4)_2$ decreases with an almost constant rate independently of the temperature and time. It might be concluded that, when subject to a uniform light source, the paints are likely to loose part of their luminescent properties in the initial moments. After that, the photo-degradation continues at a lower rate.

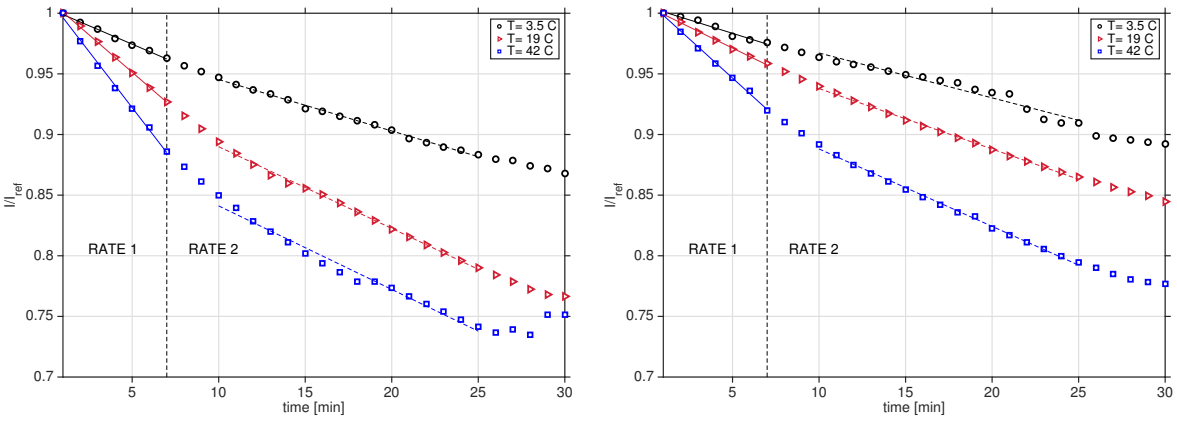

(a) 0.3 bar (b) 1 bar

Figure 4.15: Photodegradation of $Ru(phen)_3Cl_2$ with time.

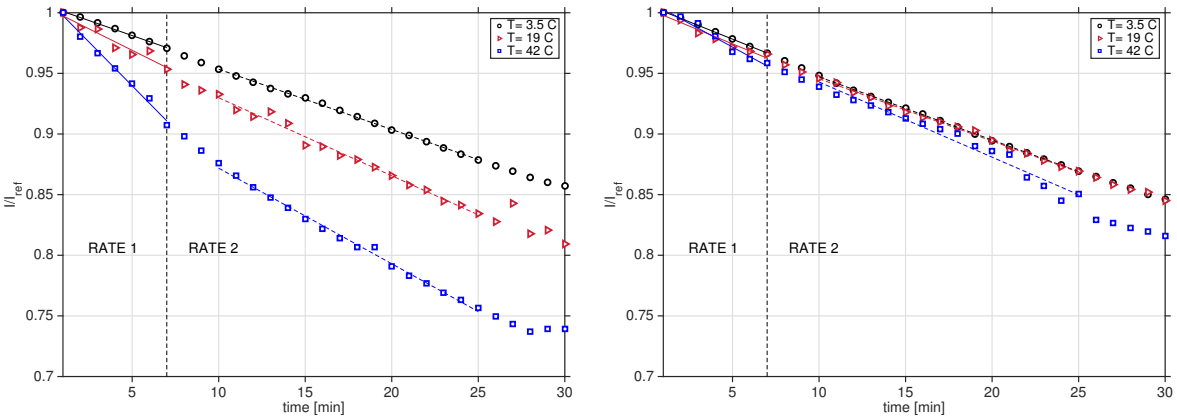

(a) 0.3 bar (b) 1 bar

Figure 4.16: Photodegradation of $Ru(phen)_3(ClO_4)_2$ with time.

4.2.8 PSP sources of uncertainty

Due to the large number of variables inherent to this technique, an accurate estimation of the overall measurement uncertainty is difficult. The sources of uncertainty can be divided in three main categories: calibration errors dependent on the response of the paint, uncertainties introduced by the measurement system, and uncertainties in the signal analysis.

The main undesirable characteristics of PSP coating is the photo-degradation of luminescent molecules so that the response to excitation decreases with time of exposure, producing a calculated pressure higher than the actual value [225]. The strong illumination of the test model contributes to the coating degradation during long experiments. Aerodynamic loading induces motion and deformation of the test model with the consequent non-perfect matching of all the point and illumination distribution between the wind-on and wind-off images [217]. The correction is done through a process of spatial alignment by knowing the location of uniformly distributed markers over the model surface.

Although Bell et al. [216] extensively explained the limitation of the detector identifying three different sources of error (shot noise, dark current shot noise, and read noise), the main source of luminescent intensity error is the photon shot noise, a random error that reduces the SNR. PSP measurements depends on how accurately the detector can measure small changes in light intensity during image acquisition [216]. If the light intensity is too low, the collection and averaging of several images improves the SNR. On the other hand, if light is too bright, images saturate and the luminophores are degraded [225]. The employment of different filters and the width of the wavelengths range also affect the results [256]. Self-illumination effects occur when the camera collects the light that reflects on the model and can successfully be removed by painting the test section with absorbing paint [246].

In addition, the temperature used for each calibration curve is an averaged value due to small temperature variations caused by the heat produced from the light source. Nonetheless, in static calibration the temperature is well controlled and thus the error is contained. This does not happen in wind tunnel testing where the temperature surface distribution is unknown and uncertainty is introduced.

It is worth to mention that although PSP has the advantage to be a non-intrusive technique compared to conventional pressure tapping, it still affects the flow field. The surface finish of the coating influences the boundary layer and the finite thickness of the paint alters the model geometry causing a change in the pressure distribution and thus the aerodynamic drag [217]. Also, in in-situ calibration, pressure tappings are still necessary and the shape of the paint in the proximity of the orifices might influence the flow. The orifices can be covered before PSP application with small pieces of adhesive tape, or by inserting wire pieces of appropriate diameter, or by blowing air through the taps if the second end of the taps is accessible. However, after removing these precautions, in the vicinity of pressure tap

orifices the shape of the paint might have changed with the creation of sharp edges, bumps or craters, as shown in Figure 4.17. Therefore, often no protection is used since experience of numerous experiments has shown that by spraying a thin polymer layer of PSP does not significantly change the shape of the pressure taps.

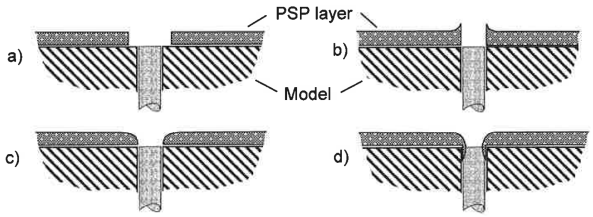

Figure 4.17: Effect of orifice deformation by paint application with different means of taps covering.

4.3 Conclusions

The setup of density-based diagnostics used in the wind tunnel at Nagoya University was provided here. The same configuration has also been implemented for the current experimental facility. Schlieren is a technique commonly employed for a qualitative evaluation of the flows field since its optical sensitivity is crucial to resolving some flow features. However, only an effective combination of different experimental techniques would allow the insight of the shock train characteristics. Other flow diagnostics are more suited to capturing boundary layer instabilities. Several pressure sensitive paints have been calibrated to identify the paint that holds the optimal properties for the application to shock train studies.

Four polymer-based paints with PtTFPP as active luminophore have shown to hold good physical, chemical and photoluminescent properties for the use in unsteady high-speed flows. Binary paints are particularly indicated because temperature effects are characterised and corrected. Among the polymer-based paints, Binary UniFib showed the best characteristic for being applied to internal flows since it has the smallest temperature dependence and the smallest paint thickness. On the other hand, polymer-based paints may be inadequate to capture high-speed flow phenomena and anodized-aluminium PSP is more indicated. Two ruthenium-based AA-PSP formulations have been successfully developed. The static calibration of both the compounds showed similar behaviour with a temperature sensitivity lower that 1%/K even though $Ru(phen)_3(ClO_4)_2$ has a higher pressure sensitivity.

The main drawbacks of AA-PSP are the non-linearity behaviour of the paint and the high sensitivity to temperature, humidity and light. The investigation of the effects of photodegradation with a uniform light source revealed that the intensity signal varies with time. The paints loose the luminescent properties at a high rate in the first few minutes and then continue to degrade at a lower rate.

5 | Design of an indraft supersonic wind tunnel

THE collection of experimental data is necessary to understand the fundamental flow physics to study aircraft aerodynamic behaviour and performance. Employing a scaled model allows the determination of the influence of design variables in a faster, easier, and cheaper manner compared to building full-scale prototypes. The model needs to be geometrically similar to the prototype, including the scaled reproduction of design details and surface roughness. This condition is satisfied when the Reynolds numbers approaches as closely as possible the full-scale value. In the fluid dynamics experiments driven by boundary layer effects, a change in the Reynolds number leads to changes in the stability of the boundary layer and surface friction, which, in turn, affect the nature of separation.

5.1 Overview of the experimental facility

Since the first wind tunnel, built in the 1920s and showed in Figure 5.1, valuable information have been collected to analyse the behaviour of flows subject to varying conditions, within channels and over solid surfaces. It is important to understand the properties of the flow through these tunnels to design a device capable of obtaining the desired flow speed as well as to ensure uniform, steady, and low-turbulence flow in the test section [258]. The achievement of these requirements becomes more challenging as the flow Mach number increases.

Figure 5.1: Langley Laboratory's first wind tunnel in 1921 [257].

Wind tunnels are firstly classified in function of the flow speed in the test section, i.e. low-speed and high-speed tunnels. Another distinction is whether or not the tunnel is an open-circuit or a closed-circuit. Intermittent open-circuit wind tunnels have been preferred to continuous ones because of the reduced power required and, as Figure 5.2 shows, are classified into blowdown and indraft tunnels depending on the condition the power is supplied [259]. In a blowdown facility, high-pressure air is stored in reservoirs and discharged to atmosphere. An indraft tunnel, like the one used for this project, draws atmospheric air across the tunnel and then discharges it into a vessel at a pressure lower than atmospheric.

As illustrated in the schematic in Figure 5.3 and with more details in the CAD assembly in Figure 5.4, to be fully functional the indraft supersonic wind tunnel designed for this project is made of several components:

- Drier mechanism
- Settling chamber equipped with honeycomb and mesh screens
- Converging-diverging de Laval nozzle
- Test section
- Diffuser
- Isolation valve placed between the test section and the vacuum tank
- Vacuum chamber
- A vacuum pump

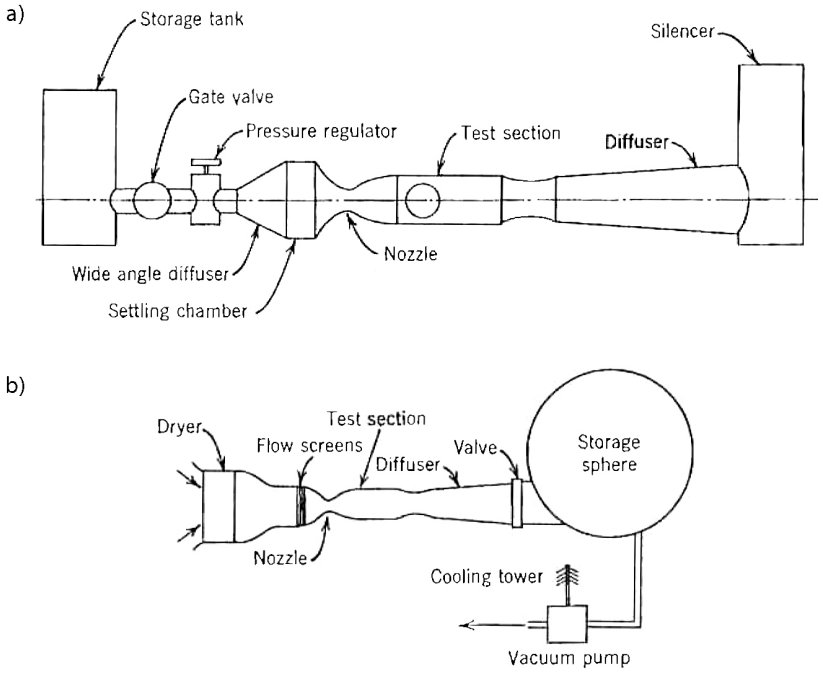

Figure 5.2: Schematic of: a) Blowdown wind tunnel; b) Indraft wind tunnel [259].

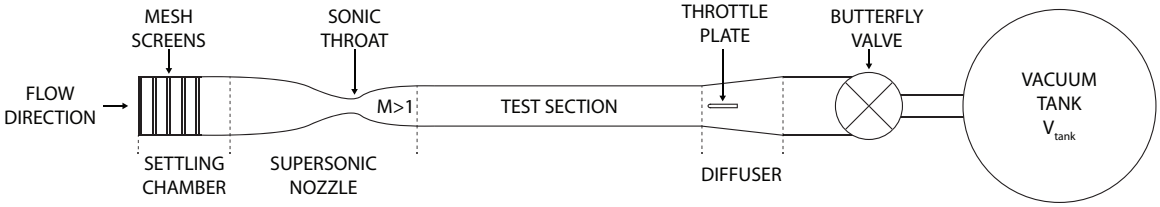

Figure 5.3: Schematic of the indraft supersonic wind tunnel used in this project.

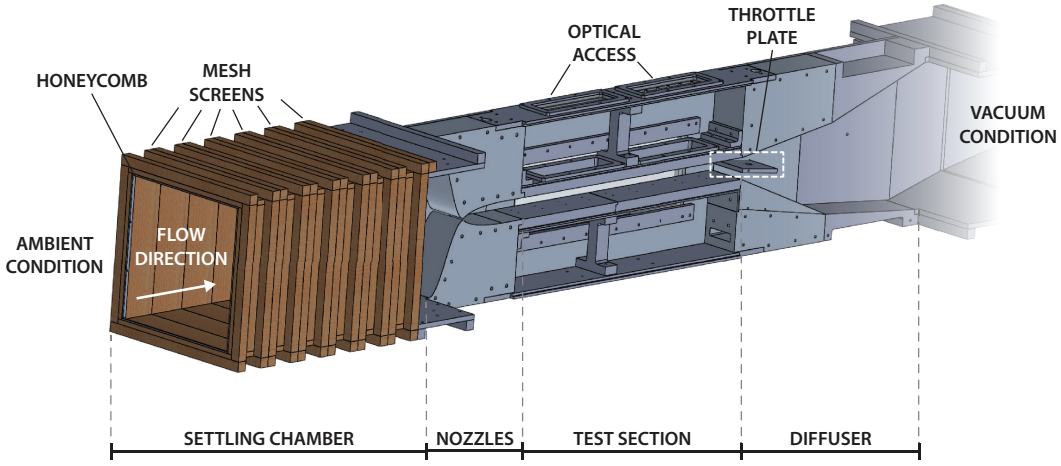

Figure 5.4: CAD assembly of the specifically designed wind tunnel.

As soon as a downstream control valve is opened, air at ambient pressure is drawn into the tunnel, passing through the inlet and the nozzle, where it is accelerated up to the sonic condition at the point of minimum area, i.e. the throat. A uniform and supersonic flow establishes inside the test section and is discharged into a vacuum tank.

5.1.1 Wind tunnel run time

Intermittent tunnels are characterised by the fact that the time available for each run is dependent on the volume and pressure of the low-pressure tank, varying from millisecond to minutes. The run terminates when the pressure difference between the two ends of the tunnel is no longer sufficient to drive the flow at the nozzle Mach number.

Following the procedure by Pope & Goin [259], the run time, t, for an indraft wind tunnel is given by:

$$t = \frac{V_{tank} P_e}{\dot{m} R T_e} \left[1 - \left(\frac{P_i}{P_e} \right)^{1/n} \right] \tag{5.1}$$

where V_{tank} is the vessel volume, R is the universal gas constant. The subscripts e and i indicate the end and the beginning of the run, respectively. The value of the polytropic coefficient, n, varies between 1.4 for an adiabatic process and 1.0 for an isothermal process,

but for a new wind tunnel a value of 1.15 is recommended [259]. The mass flow rate, $\dot{m}$, set by the throat, is defined by Equation 5.2.

$$\dot{m} = P_0 A^* \sqrt{\frac{\gamma}{RT_0}\left(\frac{2}{\gamma+1}\right)^{\frac{\gamma+1}{(\gamma-1)}}} \tag{5.2}$$

with the symbol A^* is the area of the nozzle throat, γ is the specific heat capacity, and the subscript 0 indicates the total conditions.

For the calculation of the run time in the wind tunnel with test section area of 101.60 $mm \times$ 54.42 mm, the initial conditions of the existing vacuum tank are: a volume V_{tank}= 34 m^3, an ideal pressure of P_i= 0.001 $mbar$, and a temperature of T_i= 300 K considering the temperature rise due to the drier particles. The final temperature is taken as ambient T_e= 288 K, whereas the final pressure is calculated for each Mach number by extrapolating the data from the book by Pope & Goin [259].

As reported in Table 5.1, this facility has a running time of around 59 s, 93 s, and 124 s, and mass flow rate $\dot{m}$ of 0.27 kg/s, 0.11 kg/s, and 0.04 kg/s for Mach number of 2, 3, and 4, respectively. Comparing similar experimental facilities, Sun et al. [67] used a pressure-vacuum 80 mm square test section supersonic wind tunnel with run times of 15 s and 20 s for Mach 2 and 4, respectively. Wang et al. [260] tested a Mach 2 wind tunnel with the run time of approximately 10.5 s in absence of pseudo-shock.

M	$time$ $[s]$	$\dot{m}$ $[kg/s]$
2	59	0.27
3	93	0.11
4	124	0.04

Table 5.1: Wind tunnel running time.

5.1.2 Design philosophy

The current design has been carried out following the key concepts summarised below:

- Simplicity: the operation relies on a quick opening of a valve.
- Flexibility: a modular design is preferred to easily change components as well as reduce manufacturing costs and time. Additionally, a wide range of experimental techniques can be applied with optical access from several points.
- Safety: the wind tunnel is safe as it is run by a vacuum tank with the only risk of implosion.

- Cost: the entire designed has been adapted to an existing wind tunnel built for a subsonic project by Giuni [261], and modifications have been manufactured with a trade-off between the optimal choice and costs.
- Duration: a long run time allows the collection of a large amount of data per run.

5.2 Settling chamber

The free-stream air entering the wind tunnel is initially forced to pass through a settling chamber, a large-area low-velocity section, placed upstream of the nozzle. Common values of the flow velocity in the settling chamber are in the range between 3 and 30 m/s. The section area of the settling chamber was designed by Giuni [261] with a contraction ratio of 13 which provides a flow velocity of 15 m/s.

The efficiency of supersonic wind tunnels largely relies on the control of the amount of vapour due to temperature and pressure gradients caused by the geometrical variation which occur when the flow passes through the nozzle. If the moisture percentage becomes sufficiently high to cause air condensation, a dense fog appears in the tunnel with consequent irregularities in the flow characteristics such as unwanted shock waves, changes in the local Mach number and other flow properties, compromising the data collected [262]. This phenomenon is particularly important in hypersonic wind tunnels due to the great expansion, unless the air is supplied at extremely low temperature [263]. In supersonic facilities, the moisture can be easily absorbed by desiccant particles with a porous surface that works by capillary action. According to Pope & Goin [259], the particles efficiently trap the moisture when are heated up to around 138^oC and their effectiveness depends only on the material properties and not on the size or shape of the particles. Also, once the desiccant has saturated, it can be heated up regenerating itself. Schmitz & Bissinger [264] reported that for Mach numbers lower than 5 there is no need to heat up the air and a freestream total temperature of 280 K was used for their experiment. This is confirmed also by Kawatsu et al. [92], who studied the shock train in an indraft tunnel at a flow Mach number of 2.3. The air entering the wind tunnel was discharged to a vacuum tank in an arrangement similar to that used in the current project. For the design of the current wind tunnel a vertically-oriented tray was rigidly mounted at the entrance of the wind tunnel, before the honeycomb and mesh screens, enclosing activated alumina desiccant particles which act as the drier.

During the design of a wind tunnel, a consistent amount of work is devoted to ensure the flow in the test section holds a high level of uniformity and steadiness. Even small imperfections in the settling chamber flow greatly affect the characteristics of the flow dynamic

within the test section such as: turbulence intensity, noise level, and mean velocity non-uniformities [265]. To reduce flow disturbances and inhomogeneities, it is essential to obtain a uniform flow over the entire inlet area before being accelerated through the nozzle. To do so, most high-speed wind tunnels are designed with a combination of honeycombs and screens that promote the breakage of turbulent eddies in front of the nozzle [266]. Mesh screen have been found to be the most effective methods for the reduction of the longitudinal component of turbulence whereas honeycombs suppress the lateral velocity components produced by the swirling motion of the airflow [267, 268].

5.2.1 Honeycombs

Honeycomb cells work by eliminating the lateral components of turbulence. Several studies have been performed to optimise the configuration and the length-to-diameter ratio of the cells, L/D. According to Li et al. [269], if this ratio is greater than 10, the turbulence generated by honeycombs begins to decay. Kulkarni et al. [267] found a value between 8 and 12 to be the most effective in suppressing the free-stream turbulence. Additionally, in this range the flow quality at the exit of the settling chamber is independent of the honeycomb cell shape. Mehta & Bradshaw [270] reported that an almost complete turbulence suppression is achievable in a length equivalent to 5 to 10 cell diameters, and an optimal cell size of 6 to 8 times the diameter guarantees the maximum overall benefit. In any case, the cell size should be smaller than the smallest lateral wavelength of the velocity variation, and a mesh screen with around 150 cells per settling chamber diameter can be used. For Bradshaw & Pankhurst [271] 50 cells per settling chamber diameter were adequate for close-circuit tunnels, but a smaller cell size must be used if small-scale turbulence is required. For the choice of cell size, since the settling chamber has a square sectional-area with a side length of L_{SC}= 366.4 mm, the equivalent diameter D_{eq} has been calculated:

$$D_{eq} = \sqrt{\frac{4{L_{SC}}^2}{\pi}} = 413.44\ mm \tag{5.3}$$

And thus the cell size d_{HC} is:

$$d_{HC} \simeq \frac{D_{eq}}{150} = 2.76\ mm \tag{5.4}$$

Several geometrical shapes may be used for the cross-sectional cell shape of the honeycomb, such as square, circular, or regular hexagonal, but the choice depends on the ease in construction. Regarding the material, aluminium honeycombs are preferred than paper ones in high-performance tunnels because of their ability to tolerate higher loads [270]. For the current wind tunnel, honeycombs with regular hexagonal cells with an ideal cell length of L= 20 mm based on the cell size have been chosen.

5.2.2 Mesh screens

The purpose of the mesh screens is to make the flow velocity profiles uniform by imposing a static pressure drop that effectively reduces the boundary layer thickness [270]. To be effective, the screens have to be placed upstream of the working section so that large-scale eddies are removed, producing eddies of a smaller scale which then rapidly decay.

The selection of the mesh size and diameter is important to obtain good performance of the screen, i.e. efficiently attenuate both the turbulence intensity of the incoming flow and that generated by the mesh itself. In fact, although honeycomb and mesh screens are effective in reducing the turbulence level of the incoming flow, they also create additional turbulence [269, 272]. The scale of the eddies introduced by the screen depends on the Reynolds number based on the diameter of the wires, d_M. According to Bradshaw & Pankhurst [271], a local Reynolds number $Re_\beta = U d_M / \beta\nu$, with β being the screens open-area ratio and ν the kinematic viscosity, lower than 80 avoids wire turbulence generation. Kulkarni et al. [267] restricted the range to 40 to 50, in agreement with Groth & Johansson [273] who stated that the vortices are shed if the Reynolds number based on wire diameter is greater than 40.

In order to achieve the necessary low Reynolds number, a screen with wires of small diameter are preferred. However, if the screen wires are too fine, they will not be effective in removing swirl or large eddy motions [272]. For wind tunnel applications, an open-area ratio, β, defined by Equation 5.5, where l_M is the screen mesh length, greater than 0.57 has been found effective in reducing the directional instabilities [270]. If β is smaller than 0.57 the flow passing through the cells produces instabilities with spanwise variations in the boundary layer thickness and surface shear stress [271].

$$\beta = \left[1 - \frac{d_M}{l_M}\right]^2 \tag{5.5}$$

The reduction of turbulent fluctuations is measured through the pressure drop coefficient K. It has been reported that a screen able to guarantee a pressure drop coefficient of approximately 2 removes almost all the variation in the longitudinal mean velocity [270]. Several relationships have been proposed to define K even though the accuracy is questionable [274, 275], but the Wieghardt's formula [276], in Equation 5.6, has been proven to be the most satisfactory expression for free-stream flow speed U in the range 0 to 20 m/s.

$$K = \frac{\Delta P}{0.5\rho U^2} = 6.5 \left[\frac{1-\beta}{\beta^2}\right] \left[\frac{U d_M}{\beta\nu}\right]^{-1/3} \tag{5.6}$$

The use of more than one screen has been found effective in reducing the turbulence, as long as they are placed sufficiently apart [277]. Bradshaw & Pankhurst [271] reported that a minimum of 4 to 5 screens are needed for nearly all purposes. If the distance between two

screens is too short, the distortion of the flow through the last screen may be significant. The minimum spacing to effectively reduce turbulence should be of the order of the larger energy containing eddies, i.e. the static pressure must fully recover from the perturbation before reaching the subsequent screen. On the contrary, if the distance is too far a boundary layer growth occurs. It has been found that a screen spacing, S_M, equivalent to about 0.2 times the settling chamber diameter performs successfully [270]. Bradshaw & Pankhurst [271] suggested a distance between two screens equal to $500d_M$ whereas previous experiments demonstrated that this distance can be reduced till 0.02 chamber heights without adverse effects [277].

The turbulence reduction, TR, is dependent on the pressure drop coefficient, K, which in turn depends on the properties and number of the screens, n. In general, the turbulence reduction is estimated with Equation 5.7 given by Dryden & Schubauer [278].

$$TR_1 = \frac{1}{(1+K)^{n/2}} \tag{5.7}$$

According to Tan-Atichat et al. [279] this equation underpredicts the measured values and thus Equation 5.8 was introduced to improve the accuracy.

$$TR_2 = \frac{1}{(1+K)^{n/2.7}} \tag{5.8}$$

In order to determine the ideal mesh size with a settling chamber equivalent diameter D_{eq} of 413.44 mm, the distance between two mesh screens S_M is taken as $0.2D_{eq}$, the wire diameter d_M= $S_M/500$, and the mesh aperture l_M= $S_M/100$. With an initial flow speed U= 5 m/s [266, 273] and dynamic viscosity μ= 1.983 $\times 10^{-5}$ kg/ms at ambient conditions with temperature of 300 K, the ideal screen mesh properties are determined, as reported in Table 5.2. However, due to the adaptation of the wind tunnel to an existing facility, the distance between two mesh screens S_M was constrained to a value of 101.6 mm. Based on this, the optimal mesh screen number has been determined. Additionally, the final choice was a trade-off between optimal design condition and practicality of finding the meshes. Table 5.2 summarises the mesh characteristics for the 6 aluminium screens used.

	d_M $[mm]$	l_M $[mm]$	S_M $[mm]$	β	K	Re_β	TR_1	TR_2
Ideal	0.17	0.83	82.69	0.64	1.26	92.29	8.62	16.27
Optimal adaptation	0.20	1.02	101.6	0.64	1.18	113.39	9.65	17.69
Actual	0.28	1.31	101.6	0.62	1.19	161.76	9.50	17.49

Table 5.2: Mesh screen.

5.3 Supersonic nozzle

At the exit of the settling chamber, the flow, still subsonic, needs to be accelerated to the desired test section Mach number through a specially designed cross-sectional area change, as Figure 5.5 illustrates. When the speed of the flow approaches the speed of sound, compressibility effects become important so that an area decrease causes a compression in the flow whereas the flow expands when forced to pass through an area increase. In order to accelerate the flow from subsonic to sonic speeds, a decreasing area from the supply section to the throat is necessary. Once the flow has reached the sonic condition a further acceleration is obtained by expanding the flow through an area increase. Therefore, the design of a supersonic nozzle needs to accomplish the requirement of accelerating the flow to supersonic speed through a smooth convergent-divergent contour that provides the flow in the working section uniform, parallel, and free from shock waves.

The area ratio between the nozzle throat and test section is one of the most important part of the entire wind tunnel since a good design translates into a good quality flow, which is a fundamental characteristic of a wind tunnel. Since the maximum flow rate at the throat cannot be exceeded, a single nozzle enables the achievement of only one Mach number and Reynolds number in the working section. A wind tunnel able to operate in a range of discrete test section Mach numbers can be designed with replaceable nozzle contours or by the employment of a device which provides an adjustable geometry, such as the plug-type and flexible nozzles. As illustrated in Figure 5.6, the most versatile method of obtaining variable nozzles is to utilise flexible walls with a single or multiple jacks to control the shape. Even though this approach allows a high degree of flexibility, the use of adjustable plates arises uncertainties about the flow uniformity in the test section and problems related to proper sealing in addition to higher costs for construction and maintenance [262]. Therefore, usually a pair of semi-permanently symmetrical contoured walls assembled on the wind tunnel are

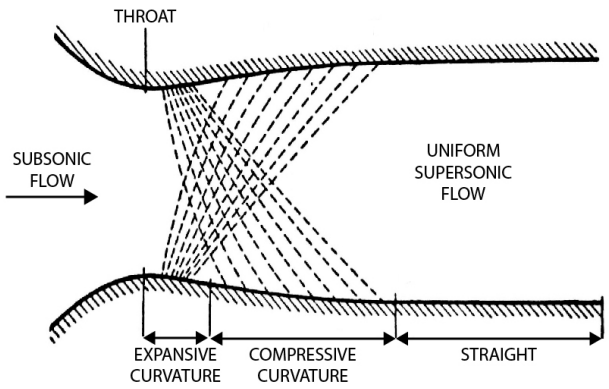

Figure 5.5: Typical arrangement for attaching the nozzle contours.

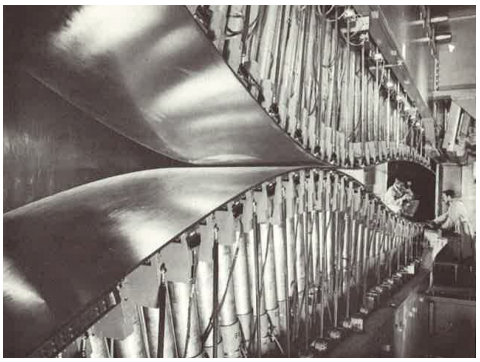

Figure 5.6: Flexible contour nozzle [259].

the most used solution. Another simple design option is the one-sided nozzle made of just one nozzle contour and a straight wall that replaces the centreline of the corresponding two-sided nozzle. The use of the one-sided nozzle has several advantages, i.e. only one nozzle contour is machined and a single block is mechanically shifted with respect to the other to achieve a continuous variation of the Mach number [280]. On the other hand, the nozzle length for a given Mach number is twice as long as for a corresponding two-sided tunnel.

Figures 5.7 and 5.8 illustrate a Mach 4 one-sided nozzle that was considered during the initial stages of the wind tunnel design. The Mach number distribution is resolved with the inviscid simulation in Figure 5.7 whereas the k-ω Wilcox turbulence model is used to obtain the flow field shown in Figure 5.8. It can be observed that in both cases the one-sided nozzle develops a highly asymmetrical velocity profile which has led to the choice of a conventional symmetric nozzle for the current project.

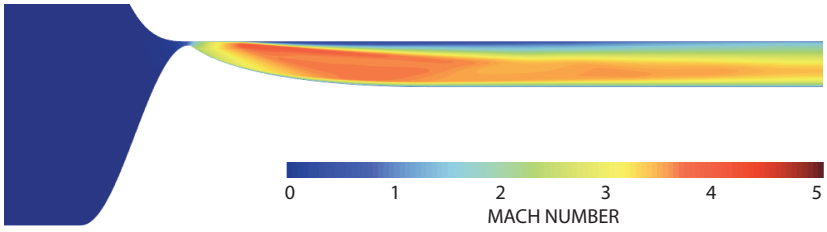

Figure 5.7: Inviscid simulation for a Mach 4 one-sided nozzle.

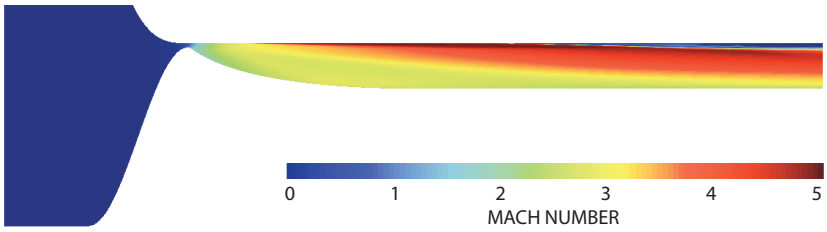

Figure 5.8: Simulation for a Mach 4 one-sided nozzle with the k-ω model.

5.3.1 Nozzle contour

The nozzle contour is influenced by several parameters including the length, height, and inflection angle [281]. For a nozzle with a fixed throat/test section area ratio, long nozzles with small inflection angles (less than approximately 12 degrees) provide the most uniform flow since the flow has the time to gradually relax towards equilibrium. However, in high-enthalpy facilities, long nozzles have the drawback to produce large losses. Short nozzles are characterised by a large inflection angle and a small wall radius of curvature at the throat, making accurate machining difficult. This kind of nozzle is preferred since the size, cost, and wind tunnel starting time is minimised, but the effects of non-equilibrium are aggravated and flow separation is more likely to occur [282]. In general, a nozzle slightly longer than the minimum is safer and less prone to produce an oscillatory flow [283].

The easiest way to obtain an initial contour is to scale an existing nozzle contour to reflect the area ratio, nozzle length and nozzle-exit diameter [281]. However, if this information is not available, analytical methods exist to generate a theoretical nozzle contour for a desired Mach number, even though they are often complicated to be implemented. Busemann's nozzle design procedure assumes an initial curve and finds the terminal curve able to provide uniform flow in the test section [284]. The accuracy of this method increases proportionally with the number of points that divide the volume which contains the expansion waves, thus in the limit of an infinitely fine mesh the method converges to the exact solution. The inaccuracies due to the assumptions have been estimated by Stever [263] to be small enough that the nozzle profile can be designed with this method.

Puckett's and Foelsch's methods start from the inflection point of the nozzle assuming uniform flow and work backwards terminating when the test section is built [283, 285]. The latter method has been preferred because it generates a nozzle profile with more accuracy [286]. Methods developed by Friedrichs [287] and later by Nilson [288] tailored the governing equations in terms of the stream function and velocity potential as independent variables. Beckwith & Moore [289] used the Method of Characteristics (MOC) to obtain the continuous expansion from a uniform flow to a radial flow, and the Foelsch equations for the transition from radial flow to the uniform flow at the end of the nozzle.

The MOC is the most famous approach to design a nozzle contour, developed by the mathematicians Jaques Saloman Hadamard in 1903 [290], but initially successfully implemented by Ludwig Prandtl and Adolf Busemann in 1929 [291, 292]. This approach, detailed in Appendix A, has been found particularly convenient because the variation of the fluid properties in supersonic flows occur across the Mach lines, called characteristics, which are inclined at the Mach angle to the local velocity vector.

The application of MOC to the design of a supersonic nozzle consists of generating a grid of points where the value of the flow properties of the stream function are determined,

bounded by the wall contour made of infinitesimally small segments. Although the characteristics are curved, if the points are close one another, a fine grid of straight lines can be obtained, referred as characteristics net. The accuracy of the computed solution increases proportionally with the number of points that divide the entire area into smaller parts [285]. Additionally, in symmetric nozzles the centreline is treated as a solid boundary so that only one half of the characteristics net is calculated [292].

The shape of the sonic line depends on the profile of the subsonic inlet, i.e. a larger radius of curvature generates a flatter sonic line with centred and divergent waves at the throat, whereas no centred Mach lines occur if the sonic line is curved [292]. However, a straight sonic line is an idealisation and the Mach line at the throat is always an arc of a circle on which the Mach number is constant. Nevertheless, the supersonic portion of the nozzle is independent of the conditions upstream of the sonic line and the flow in the test section is not influenced by the choice of the inlet [293]. There is no rigorous analytic method available for the design of the subsonic portion of the nozzle, and only some general rules of thumb have been outlined. As reported by Gaffney [294], the design of the subsonic portion upstream of the nozzle throat is constructed by extending the curve used for the supersonic expansion to the subsonic side. Following this idea, a scaled sinusoidal curve from Giuni [261] has been used and a polynomial interpolation was applied at the throat in order to obtain a smoother profile from the subsonic inlet to the expansion section.

5.3.2 Boundary layer correction

A nozzle designed purely by the MOC without boundary layer corrections does not deliver a uniform flow in the test section [188]. An accurate estimation of boundary layer correction due to viscous and dissipative effects present at the walls needs to be included once the desired inviscid Mach number nozzle is obtained with the MOC. Although theoretical methods have been suggested for the calculation of boundary layer growth, the application of boundary layer corrections is complicated and often no correction is applied [53].

Cain et al. [282] reported that for high Reynolds number flows, which occur when the boundary layer developing on the nozzle walls is thin compared with the test section height, the MOC can be used to accurately calculate the inviscid core flow before applying the displacement effect of the boundary layer along the walls. However, this method degrades in accuracy as the relative thickness of the boundary layer increases. According to Tucker [295], for a nozzle with a test section Mach number lower than 4, the assumption of negligible heat transfer rate through the walls and thin boundary layer can be used, whereas Liepman [280] restricted the range up to Mach 3. Therefore, in low Mach number nozzles, where boundary layers are thin, the flow characteristics are closely approximated by the inviscid contour as assumed by the MOC and many nozzles have been satisfactorily designed with no vis-

cous corrections [280, 281]. For higher Mach numbers the boundary layer is sensitive to heat transfer through the walls and an inaccurate estimation of the boundary layer growth may cause a considerably divergence from the assumption of perfect gas, particularly for hypersonic nozzles, in which the boundary layer may exceed 10% of the nozzle height.

The growth of the boundary layer along the axial direction is a function of the Reynolds number, nozzle length, and Mach number, and causes a decrease in the cross-sectional area available for the flow, losses in velocity and momentum, and the reduction of the exit Mach number. To include these effects, it is desirable to shift out the ordinates of the ideal nozzle contour at each point of the nozzle by the amount equal to the local boundary layer displacement thickness, δ^*, as illustrated in Figure 5.9 [296, 297]. This quantity corresponds to the distance through which the wall of a channel carrying a perfect flow would have to be displaced in order to produce the same mass flow reduction caused by the boundary layer.

The rate of growth of the boundary layer downstream of the throat has been demonstrated to be approximately constant [298, 299]. Sivells [300] more conservatively stated that the growth is approximately linear from the inflection point to the test section. To determine the boundary layer growth along the nozzle, a zero boundary layer thickness at the throat is usually assumed [259]. However, the boundary layer at the throat may be different from zero and, in this case, the actual throat is located slightly downstream of the geometrical one [300]. With the assumption of zero thickness at the throat, the growth of the boundary layer on the surface would be higher because of the smaller Reynolds number associated with the boundary layer development [299]. In addition, the throat area would be overestimated leading to a greater test section area and consequently a higher Mach number in the working section. On the other hand, experimental evidence shows that this assumption is true at Mach number higher than 3 [301].

The calculation of the compressible turbulent boundary layer has been examined by various authors with thermally insulated walls [302–306]. All these methods express the boundary layer momentum thickness, θ, in the form:

$$\theta = f\,(M)\,X{Re_X}^N \tag{5.9}$$

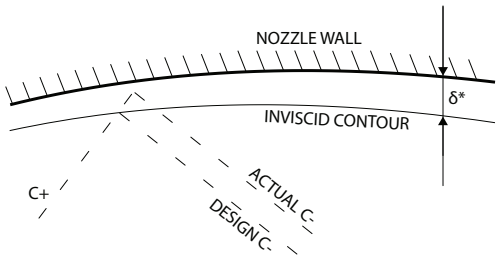

Figure 5.9: Boundary layer effect on the nozzle wall.

with X equivalent to the flat plate length expressed in Equation 5.10 and F= $f\,(M)$.

$$X = F^{-1} \int_0^x F\,dx \tag{5.10}$$

Tucker [295] presented a procedure for an approximate calculation of boundary layer growth in compressible flows for a range of Mach numbers from 0.1 to 10. This method starts from the momentum equation for compressible turbulent boundary layers with the assumption of perfect gas, and constant pressure and temperature at any section normal to the wall. The flow properties are calculated with a reference temperature defined as T_{am}= $0.5\,(T_W + T_\infty)$, where T_W is the temperature at the wall and T_∞ in the free-stream, respectively. This procedure provides a quick estimation of the boundary layer properties with sufficient accuracy [299, 307] by using Equations 5.11 to 5.13.

$$\delta^* = \left[E_2 K \frac{dx}{dM} x^{-1/7} \left(I_2 - I_1\right) + \delta_1 E_2 F_1 \right] \tag{5.11}$$

$$f = \frac{\theta}{\delta} \tag{5.12}$$

$$g = \frac{\delta^*}{\delta} \tag{5.13}$$

The subscripts 1 and 2 denote the throat and test section, respectively. The parameter K is defined as K= $0.0218\big(\mu_\infty \sqrt{T_\infty}/P_\infty\big)^{1/7}$, the quantities f, g, E, F, and I, are tabulated in reference [295] depending on the value of the velocity profile parameter N. The suitable choice of N in Equation 5.14 has been found controversial. Tucker [295] expressed N= ${2.2Re_{am}}^{1/14}$, Rogers & Davis [299] multiplied it by a factor of $(1 + 0.1M^2)^{1/7}$ whereas Ruptash [308] uses 2.6 as the numerical coefficient. Additionally Wilson [309] recommended to take N= 7 for all Reynolds numbers.

$$\frac{U}{U_\infty} = \left(\frac{y}{\delta}\right)^{1/N} \tag{5.14}$$

By using Equations 5.9 and 5.10 Tucker's method reduces to:

$$\theta = 0.0153 \left(1 + \frac{M^2}{10}\right)^{-5/7} X {Re_X}^{-1/7} \tag{5.15}$$

with the function F defined as:

$$F = \left(\frac{dI}{dM}\right)^{7/6} \tag{5.16}$$

The method proposed by Rogers & Davis [299] provides an approximate boundary layer thickness downstream of the nozzle similar to that on a flat plate for wind tunnels with

rectangular cross-section and adiabatic walls with Equation 5.17:

$$\delta = 0.0153 x f^{-1} \left(1 + 0.1M^2\right)^{-5/7} {Re_X}^{-1/7} \tag{5.17}$$

where the parameter f= θ/δ is tabulated as a function of the Mach number and N [295]. When N= 7, the term $f\ \left(1 + 0.1M^2\right)^{5/7}$ is approximately 0.1 and Equation 5.17 can be simplified to the form:

$$\delta = 0.153 x {Re_X}^{-1/7} \tag{5.18}$$

Stratford & Beavers [310] compared several methods and proposed an average expression for θ, δ, and δ^* by using N= 7:

$$\theta = 0.022\left(1 + 0.16M^2\right)^{-0.6} X {Re_X}^{-1/6} \tag{5.19}$$

in which X is defined by Equation 5.10, whereas F and Re_X are defined as follows:

$$F = \left[\frac{M}{(1 + M^2/5)}\right]^4 \tag{5.20}$$

$$Re_X = \frac{a_0}{\nu_0} X M \left(1 + \frac{M^2}{5}\right)^{\omega - 3} \tag{5.21}$$

The exponent in the viscosity-temperature relation, ω, is usually taken as 0.75, except for very high temperature flows where 0.5 is preferred. Stratford & Beavers [310] observed that using the $1/7^{th}$ power law for the velocity profile, the boundary layer thickness, δ, is 10% lower than for incompressible flow at Mach 4 and 10% higher at Mach 10. As a consequence, an alternative approach was proposed, assuming zero variation of δ with the Mach number so that δ is calculated in the same way as for incompressible flows, and δ^* and θ can be easily derived from θ/δ and δ^*/δ. For a free-stream $Re_X \propto 10^6$:

$$\delta = 0.37 X {Re_X}^{-1/5} \tag{5.22}$$

$$\theta = 0.036\left(1 + \frac{M^2}{10}\right)^{-0.7} X {Re_X}^{-1/5} \tag{5.23}$$

$$\delta^* = 0.046\left(1 + 0.8M^2\right)^{0.44} X {Re_X}^{-1/5} \tag{5.24}$$

In the present study, two-dimensional nozzles that develop test section Mach numbers of 2 and 4 have been generated by an in-house version of MOC method implemented in MATLAB following the procedure outlined by Ibrahim [311]. The different approaches to calculate the boundary layer displacement thickness described above are applied to the wind

tunnel nozzles and compared in Tables 5.3 and 5.4. Compared to the other methods, Tucker's method considerably underpredicts the boundary layer thickness. On the other hand, only experimental data can estimate the actual boundary layer profile. As previously mentioned, with an inflow Mach number smaller than 4, the inviscid nozzle contour designed the MOC without the displacement effect of the boundary layer along the walls can be used. The need to have parallel walls to compare similar studies on shock trains with an isolator of constant cross-sectional area has led to the choice to not include boundary layer correction. Figure 5.10 shows the Mach 2 and Mach 4 nozzles with parallel test section walls used for the current wind tunnel.

Method	$\delta\ [mm]$	$\delta^*\ [mm]$	$\delta^*/h\ [\%]$	$\theta\ [mm]$
Tucker [295]	0.57	0.15	0.57	0.05
Stratford & Beavers [310]	1.87	0.43	1.61	0.14
Rogers & Davis [299]	1.77	0.48	1.77	0.15

Table 5.3: Comparison of methods for the estimation of the boundary layer for a Mach 2 nozzle.

Method	$\delta\ [mm]$	$\delta^*\ [mm]$	$\delta^*/h\ [\%]$	$\theta\ [mm]$
Tucker [295]	2.88	1.37	5.05	0.16
Stratford & Beavers [310]	3.68	1.45	5.33	0.18
Rogers & Davis [299]	3.66	1.74	6.41	0.20

Table 5.4: Comparison of methods for the estimation of the boundary layer for a Mach 4 nozzle.

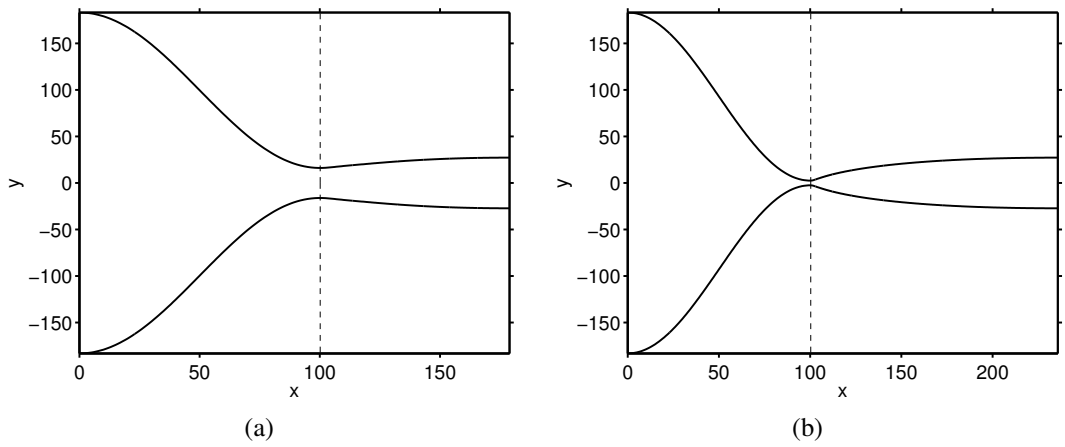

Figure 5.10: Inviscid nozzle contour designed with the MOC for the current wind tunnel facility (all dimensions in mm): a) Mach 2; b) Mach 4.

5.4 Test section

The particular flow structure investigated in this study, has led to the integration of the wind tunnel and the test model, i.e. the channel downstream of the nozzle is the working area. Experimental data have shown that the maximum pressure rise across the shock train can be achieved when the shock train and the isolator are of the same length. For a constant area duct, Sullins [18] found that the shock train pressure rise reaches up to 95% of the normal shock strength with a duct length of 10 to 20 duct heights, whereas for Neumann & Lustwerk [60] this length is between 8 to 12 tube diameters for Mach numbers from 1.8 to 4.2. In approximately the same Mach number range, Sun et al. [67] were able to capture the entire shock train system using a test section with a length-to-height ratio of 18.75.

Ikui et al. [73] observed that the length of the shock train varies in the range of 4 to 15 tube diameters for Mach numbers from 1.33 to 2.79, so they used a 60 mm square test section and 800 mm long, which gives a length-to-height ratio of 13.3. For Mach numbers between 2 and 2.85, Sullins [18] used a length-to-height ratio of 28.45 in a 22.76 $inches$ long isolator facility with a working area height of 0.8 $inches$. For the Mach 2.3 experimental and numerical analysis carried out by Kawatsu et al. [92] a square test section of 30 mm and 290 mm long, and length-to-height ratio of 9.67, was sufficient. An even lower value of the length-to-height ratio of 4.31 was employed by Bement et al. [19] in a 17.24 $inches$ long isolator with a heigh of 4.00 $inches$.

Most applications have parallel side walls or a rectangular cross-section, therefore, the present investigation focuses on this topic. The comparison with previous wind tunnels, and thus the requirement of a long test section, has led to the choice of a length-to-height ratio L/D_{eq} of 10.48, with test section dimensions 101.60 mm $\times$ 54.42 mm (width $\times$ height) and length of 742.95 mm. Additionally, the modularity of the wind tunnel allows to study the shock train behaviour in a divergent duct of up to 10 degrees by means of replaceable blocks. Small divergence or constant area ducts produce higher efficiencies of shock compression because, in this condition, there exists a positive velocity gradient in the subsonic flow downstream of the shock compression region which stabilises the boundary layer and reduces separation. [56, 97] According to Walther et al. [98], the use of divergence angles of 1 to 2 degrees on both the duct walls of the combustor inlet is effective in mitigating the steep static pressure rise downstream of the fuel supply point and counteracts the thermal blockage by heat addition. The small level of divergence is meant to counteract the boundary layer growth so that the effective fluidic cross-section remains constant.

The most significant studies in constant area ducts are summarised in Table 5.5 and Figure 5.11. Several wind tunnels have been designed for the study of shock train characteristics with the ratio between length and height of the test section as a driving parameter. However, for test sections with a circular cross-section the diameter substitutes the duct height. In

	M	$L\,[mm]$	$H\,[mm]$	$W\,[mm]$	$D\,[mm]$	$D_{eq}[mm]$	L/D_{eq}
Baurle [122] [*]	2.5	609.60	25.40	50.80	-	33.87	18
Bement [19]	1.94	437.90	101.6	104.65	-	103.10	4.25
Dutton [190]	1.6-2.45	40.64	5.08	7.62	-	6.10	6.67
Emami [41]	4	654.05-169.67	58.42	50.8	-	54.34	3.12-12.04
Handa [79]	1.7	35	10	20	-	13.33	2.63
Huang [23] [*]	2	960	80	80	-	80	12
Ikui [62, 73, 76]	1.33-2.79	800-840	15-60	60	-	24-60	13.33-35
Kawatsu [92]	1.8-2.3	290	30	30	-	30	9.67
Koike [48]	2	430	80	80	-	80	5.38
Koo [186] [*]	4.9	242.32	25.40	50.80	-	33.87	7.16
Lin [99]	1.8-2.2	641.35-654.05	38.10	101.60	-	55.42	11.57-11.80
	1.8-2.2	644.65	-	-	70.10	70.10	9.20
Merkli [59]	3	190.33-761.33	19.1	9.5	-	12.69	15-60
Om [55]	1.28-1.48	241.30	-	-	51.90	51.90	4.65
Ostras [69]	3.80	358.16-1929.18	-	-	81.40	81.40	4.40-23.70
Sridhar [100] [*]	2	300	30	30	-	30	10
Sugiyama [83]	1.67-1.9	1030	-	-	50	50	20.60
Sullins [18]	2-2.85	578.10	20.32	50.80	-	29.03	19.92
Sun [67]	2-4	1500	80	80	-	80	18.75
Yamauchi [9]	2.5	290	30	30	-	30	9.67
Waltrup [107]	1.53-2.72	16.75-22.74	-	-	2.75	2.75	6.09-8.27
Wang [111]	1.5-2	300	30	45	-	36	8.33
Weiss [58]	1.5	160	8	15	-	10.43	15.33
Current design	2-4	742.95	54.43	101.60	-	70.88	10.48

Table 5.5: Review of wind tunnels designed for shock train investigation. M: Mach number; L: duct length; H: rectangular duct height; W: rectangular duct width; D: circular duct diameter; D_{eq}: equivalent diameter; L/D_{eq}: length-to-equivalent diameter ratio; [*]: numerical studies.

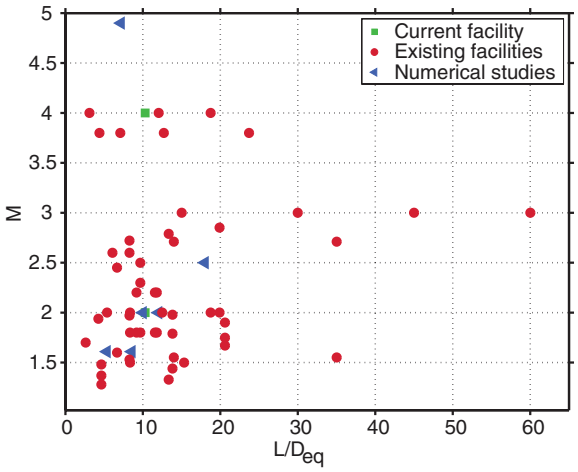

Figure 5.11: Comparison of previous works of length-to-equivalent diameter ratio with Mach number.

order to compare facilities of different cross-sectional shapes, all lengths are divided by the equivalent diameter of the duct, D_{eq}. Most studies have been conducted in the Mach number range between 1.5 and 3 and length-to-equivalent diameter ratio between 5 and 20.

5.4.1 Windows

Optical analysis of the flow requires the ability to observe the flow, and the test section windows must be chosen to be as wide as possible. Glass has been found to be the most suitable material to fulfil this purpose whereas plastics do not have the desired optical properties [259]. Additionally, for schlieren systems, the glass should have flat surfaces, a homogeneous structure and must be free of internal imperfections such as dust and bubbles. Two glass windows of $558.8\ mm$ width are mounted on both sides of the test section to attain full optical access to the flowfield. These glasses were part of the original design of the wind tunnel and were installed into a frame which can be easily removed in order to facilitate access to the test section [261].

The particular features of the flow phenomena investigated in this project requires optical access also from the upper wall, allowing the installation of high speed cameras and to perform experimental techniques including oil flow visualisation, PIV, and PSP. As illustrated in Figure 5.12, two rectangular windows of toughened glass with a thickness of $15\ mm$ are chosen to split the visual field into two parts. The relatively small dimensions makes the problem of the glass strength not too restrictive but the procedure suggested by Pope & Goin [259] was followed to determine a thickness:

$$th = \sqrt{\frac{6M_{max}}{S_{max}}} \tag{5.25}$$

where M_{max} is the maximum moment and S_{max} the maximum allowable stress which occurs

Figure 5.12: Wind tunnel windows.

at the centre of the window. For glass, S_{max} is $6500\ psi$ and using a safety factor of 10 becomes $650\ psi$. The maximum moment M_{max} is then calculated by Equation 5.26, in which P is the pressure, s the length of the short side, and B a coefficient plotted in Figure 5.13 that depends on the ratio of the long side to the short side, l/s, and the Poisson's ratio.

$$M_{max} = BPs^2 \tag{5.26}$$

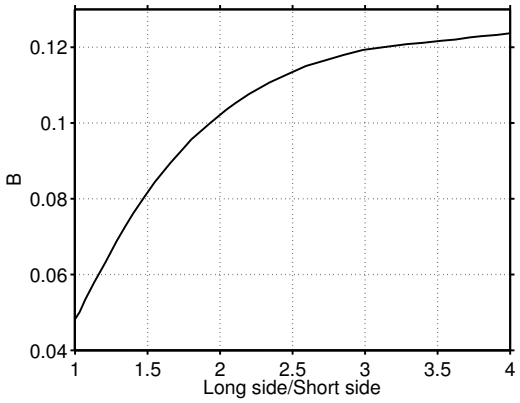

Figure 5.13: Rectangular plate momentum factor B [259].

5.5 Diffuser

During the wind tunnel starting phase, the air flows through the wind tunnel up to a critical point that causes a normal shock to form at the nozzle throat, choking the flow. As the power and thus the ratio of the stagnation pressure to diffuser exit pressure is increased, the normal shock gradually moves downstream of the nozzle travelling through the test section. Once the pressure ratio is increased enough that the normal shock is positioned in the diffuser, the wind tunnel is considered fully started. The diffuser guarantees the establishment of

supersonic flow in the working area once the normal shock wave stabilises downstream of a section with the minimum cross-sectional area, called second throat [312]. The function of the diffuser is therefore to convert the kinetic energy downstream of the working section into pressure energy with minimum energy dissipation [262].

For steady operation of a supersonic wind tunnel, the diffuser throat area must be large enough to permit the passage of the mass flow in a stream tube having an area that corresponds to that at the entrance of the diffuser. It should be larger than the nozzle throat area, but smaller than the test section. For each Mach number, the definition of the Mach number downstream of the shock in Equation 5.27 is substituted into the expression of the area ratio between two points in Equation 5.28, leading to Equation 5.29 that defines the minimum diffuser area based on the test section. Thus, the area of the second throat, A_2^*, can be obtained once the test section, A, is fixed for a desired Mach number, M, as illustrated in Figure 5.14. Equation 5.29 is then divided by Equation 5.30 to obtain the ratio of the second throat area to the nozzle throat area, in Equation 5.31.

$$M_2{}^2 = \frac{0.5\,(\gamma-1) + M_1{}^2}{2\gamma M_1{}^2/\,(\gamma-1) - 1} \tag{5.27}$$

$$\frac{A_2}{A_1} = \frac{M_2}{M_1}\left[\frac{1+0.5\,(\gamma-1)\,M_2{}^2}{1+0.5\,(\gamma-1)\,M_1{}^2}\right]^{\frac{\gamma+1}{2(\gamma-1)}} \tag{5.28}$$

$$\frac{A_2^*}{A} = \frac{(5+M^2)^{1/2}(7M^2-1)^{5/2}}{216M^6} \tag{5.29}$$

$$\frac{A}{A^*} = \frac{1}{M}\left[\frac{2}{\gamma+1}\left(1+\frac{\gamma-1}{2}M^2\right)\right]^{\frac{\gamma+1}{2(\gamma-1)}} \tag{5.30}$$

$$\frac{A_2^*}{A_1^*} = \frac{P_{0_1}}{P_2} \tag{5.31}$$

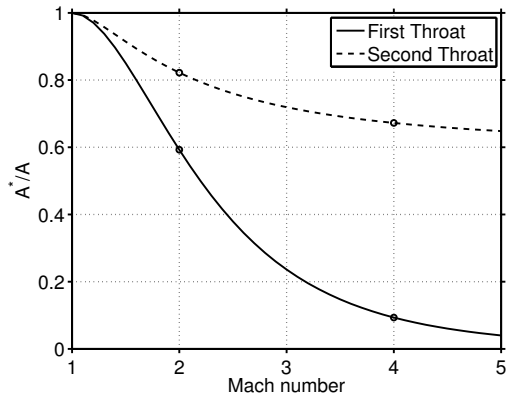

Figure 5.14: Area ratio of first and second throats with the Mach number.

The diffuser efficiency depends on a number of parameters and several studies have attempted to optimise the leading variables including the angle of divergence between the test section and the diffuser throat, and the length of the second throat. Similarly to the nozzle design, diffusers can be either fixed or adjustable. Fixed diffusers are cheaper, but undesirable if the wind tunnel is designed to deliver a wide range of Mach numbers. In spite of the higher costs, adjustable diffusers allow the maximum recovery. The angle of convergence is usually chosen up to 30 degrees, whereas the divergence section downstream of the second throat should not exceed 6 degrees to avoid boundary layer separation [259].

However, no conclusive optimal configuration has been found since the diffuser is usually designed on the basis of previous studies. This component was already available from the original wind tunnel design [261]. The necessary adjustments have been done balancing the mechanical construction requirements and the need to keep the wall convergence angle relatively small to minimise energy losses.

5.5.1 Flow blockage

Usually aerodynamics tests are performed on a scaled test model positioned in the test section that represents part of or an entire vehicle from the automotive and aerospace sectors. Equation 5.31 implies that losses in the total pressure due to the shock waves which occur on the test model placed in the test section require a second throat larger than that of a clear wind tunnel, confirmed by actual wind tunnel operation [259]. Therefore, the size of the test model must be smaller than the maximum size necessary for the wind tunnel to start.

When the wind tunnel is started, the shock wave establishes just after the throat so that the test model is immersed in a subsonic flow. At the axial location where the cross-sectional area of the model, A_m, has the larger value, the relative cross-sectional area of the test section, A-A_m, is the minimum and the Mach number cannot exceed 1, with A the area of the geometrical test section. The test model size should allow the shock wave to pass through this area and then stabilise behind the test model. If the shock is not able to pass across the test model during the starting process of the wind tunnel, the wind tunnel is said to be choked. Theoretically, A-A_m should be the same as the second throat area, however experimental data for Mach numbers greater than 2 recommend that the size of the test model is smaller, as illustrated in Figure 5.15. Additionally, the shape of the test model influences the maximum dimensions of the test model. Pope [259] reported that wind tunnels have started with a sharp model with sizes bigger than the theoretical value, whereas in the case of a blunt model the model size should be further reduced. In Figure 5.15 the black dots have been calculated for the flow inside the current wind tunnel taking into account the boundary layer. The effective area, A_{eff}, is the test section area minus the larger value of the boundary layer displacement thickness calculated in Section 5.3.2. Although as mentioned in Section 5.4

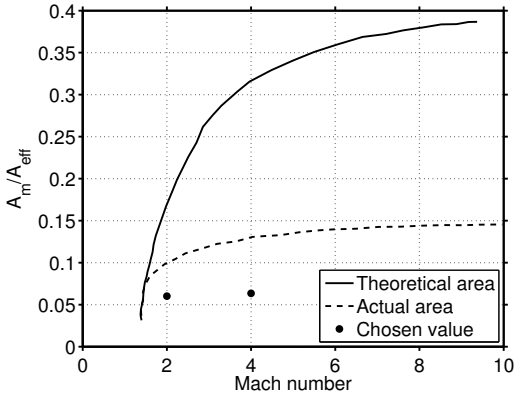

Figure 5.15: Maximum model diameter in function of the Mach number for blunt nose models [259].

there is no test model to be placed into the test section, the calculation of the flow blockage due to the presence of a physical body in the test section was necessary for the design of the Pitot rake, in Appendix B.

5.5.2 Variable throat diffuser

In real air-breathing engines, the shock train is generated by the combined effect of the injection and heat release upstream of the fuel injector ports and extends into the combustion chamber [24]. As the back pressure is increased, the position of the shock wave moves upstream. Once the shock is forced to reach the point of minimum area, the shock Mach number approaches its lowest value and the associated losses are minimised [34]. Since the early studies on supersonic combustion, it was realised that this behaviour can be duplicated in a throttled non-reacting flow [110]. In experimental testing, the shock wave can be located to a certain position by adjusting the static pressure at the end of the test section [79]. The pressure rise and the shock train propagation upstream are reproduced by means of blockage modulation to simulate the isolator performance from normal starting to a choked state [44].

Several designs have been proposed to achieve this purpose, but in all cases a device is used to control the pressure in the working section by changing the back pressure value. Kawatsu et al. [92] generated and controlled the shock train system with a butterfly valve downstream of the test section. Similarly, a control valve attached at the exit of the test section allowed Yamauchi et al. [80] to move the shock train within a prescribed range by manually adjusting the readings of the wall pressure taps upstream and downstream of the location where the shock front is placed. Emami [41] accomplished the reproduction of back pressure variation using a variable-area throttling mechanism attached to the end of the isolator. With the same idea, a protruding ramp hinged along its front edge located in the downstream portion of the test section was used by Hutzel et al. [175]. To create a variable second throat, Bruce & Babinsky [313] mounted an elliptical cam in the diffuser, Ostras &

Penzin [69] used a flat plate, whereas Fischer et al. [61,119] placed a movable double wedge at the end of the isolator. The simplicity of the latter devices has led to the design of a quick and accurate blockage system installed at the end of the test section to modify the second throat cross-sectional area. As shown in Figure 5.16, a movable flap allows the control of the flow in the test section. The throttle plate in the diffuser is initially positioned horizontally allowing the supersonic flow to establish in the test section. The angle of rotation is selected by means of an handle that gradually pivots the plate about a hinge.

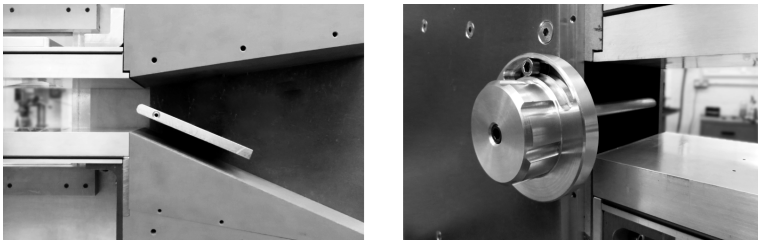

Figure 5.16: Throttle device.

5.5.3 Opening valve

Another vital component of the wind tunnel is the valve placed between the test section and the vacuum tank that acts as the main switch of the wind tunnel. To operate the tunnel, a pressure difference across the upstream and downstream is required. When the desired vacuum pressure is reached, the valve is opened, and air is drawn from outside the tunnel into the vacuum chamber establishing supersonic flow in the test section.

The minimum pressure reached by the vacuum pump determines the initial pressure of the tank which, together with the velocity needed to draw the air into the tunnel, affects the time required by flow to establish in the test section, and consequently the time between two subsequent runs. To maximise the run time, the valve should open as quickly as possible. However, tunnel leaks reduce the test time by acting as an additional inlet and make it difficult to reach low pressures. A ball valve, connected to the diffuser with a rectangle-to-round transition section, is opened by a pneumatic spring return actuator with opening time of $0.5\ s$.

5.6 Numerical validation of the nozzle contour

A CFD-coupled methodology with the inclusion of the interaction between the core flow and the boundary layer has been introduced in the process of optimisation in support of the MOC [314, 315]. Although the only accurate way to validate the mathematical model is the collection of experimental data [262], a CFD solver is used in the design stage to determine the final nozzle contour.

5.6.1 Validation case 1 of nozzle contour

The numerical code is firstly applied to the two-dimensional sharp-edged-throat supersonic nozzle designed by Mbuyamba [316] with the MOC. The geometry and flow conditions are reported in Table 5.6. In the approach by Mbuyamba [316], the 2D RANS equations were closed by the k-ε turbulence model whereas the k-ω Wilcox model was used in the current study. The comparison of the velocity contours in Figure 5.17 shows an excellent agreement. The computed gas velocity distribution with the numerical approach used by Mbuyamba [316], on the top, and that applied in the current study, on the bottom, do not show visible differences. The flow is well established downstream of the nozzle and the boundary layer develops on the duct walls in the same way as the MOC nozzle of Mbuyamba [316].

Since only the supersonic portion of the nozzle is designed with the MOC and is independent of the conditions upstream of the sonic line [293], the inlet contour used in the current wind tunnel was attached upstream of the throat to allow the flow to establish. Figure 5.18 illustrates the distribution of the computed flow properties averaged at each length-wise station where the axial coordinate x= 0 corresponds to the throat. The simulation is two-dimensional and the flow properties are not constant in the y-direction and therefore cannot be compared to the quasi one-dimensional isentropic equations. According to the quasi one-dimensional theory, the flow properties are uniform at each cross-section. This assumption is valid only if the nozzle is infinitely long, i.e. the nozzle divergence angle is infinitely small [317]. Nozzles designed using the method of characteristics, such as the ones in this

M	$T_0[K]$	$P_0[MPa]$	$P[MPa]$	$P_b[kPa]$	$h^*[mm]$	$L[mm]$
3	416.67	2	1.06	0.05	2.7	150

Table 5.6: Boundary and geometry conditions of the computational domain of the MOC nozzle designed by Mbuyamba [316].

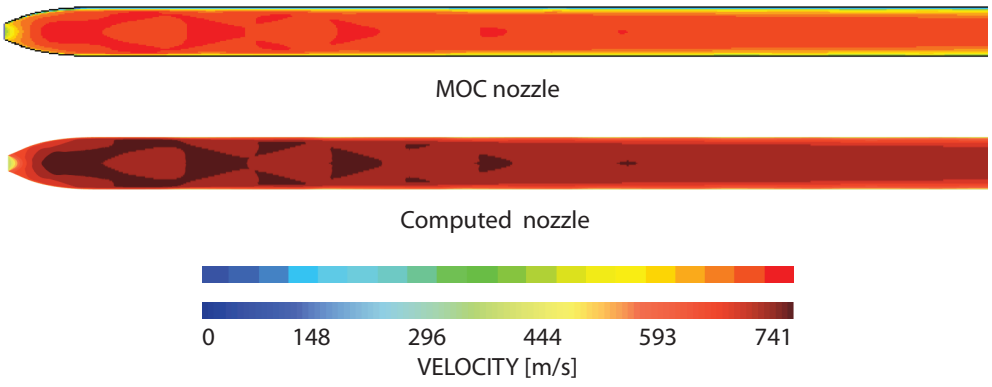

Figure 5.17: Comparison of the gas velocity contours for a MOC nozzle from Mbuyamba [316] (top) and the computed κ-ω Wilcox turbulence model (bottom).

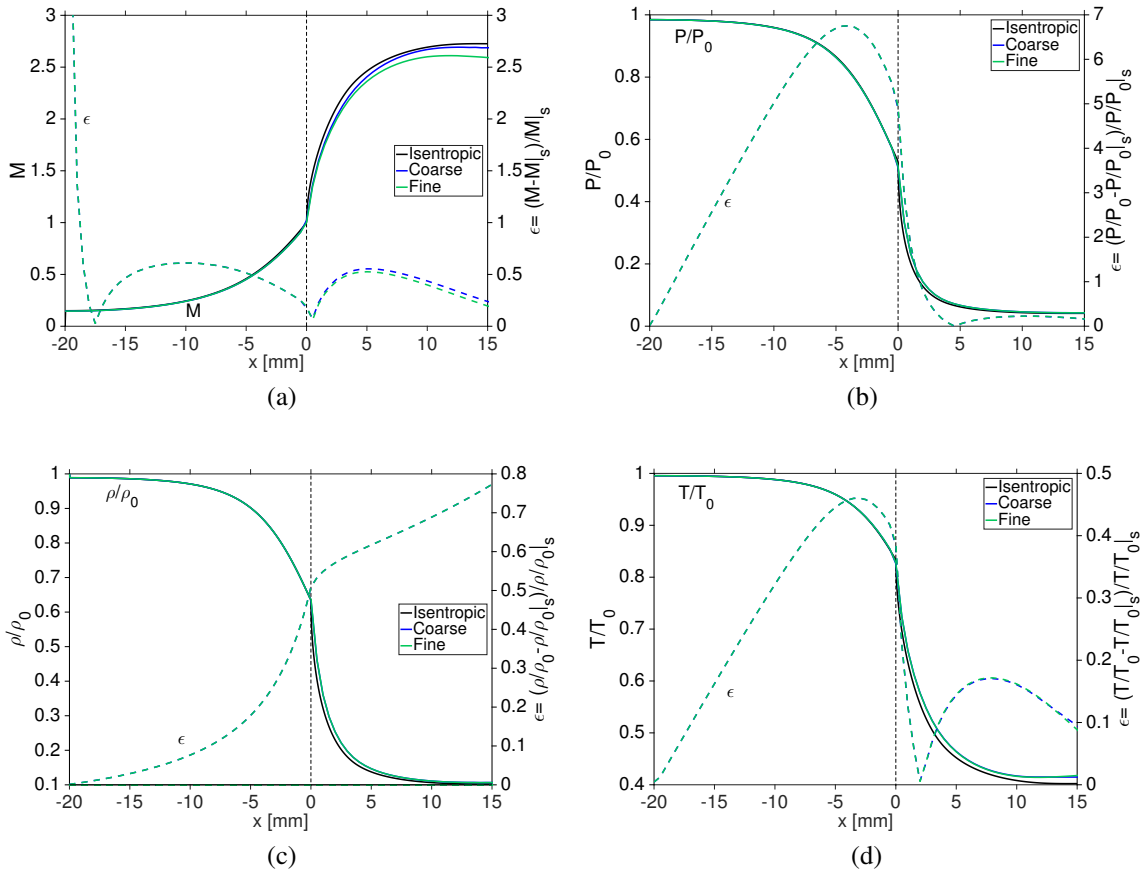

Figure 5.18: Distribution of the computed flow properties averaged at each length-wise station for the Mach 3 nozzle of Mbuyamba [316]: a) Mach number; b) Pressure ratio; c) Density ratio; d) Temperature ratio.

project, have an angle that breaks this assumption. As a consequence, the two-dimensional effects become important and the flow properties are non-uniform at each cross-section, as visible from Figure 5.17. This does not affect the quality of the flow in the core flow, in particular in the diamond area downstream of the nozzle (see Figure A.1).

As expected, the nozzle converts the slow moving gas flow into high velocity, low pressure, low density, and low temperature gas. From Figure 5.18 it can be observed that in the subsonic part of the nozzle, ahead of the throat, the coarse and the fine grids do not differ from the isentropic solution. Downstream of the throat the difference between the coarse and fine grid is insignificant in terms of pressure and density distribution. Compared with the finest grid, with the coarse grid the temperature, and consequently the Mach number, slightly deviate from the isentropic solution at the end of the nozzle. Overall, all the flow properties are well reproduced and the coarse grid is sufficiently accurate to resolve the flow field. This is also evident from the relative error, $\epsilon = \mid (\phi - \phi_S) \mid / \phi_S$, of the computed flow variable, ϕ, to the isentropic value, ϕ_S. From Figure 5.18(a) to Figure 5.18(d), ϕ equals M, P/P_0, ρ/ρ_0, and T/T_0, respectively.

5.6.2 Validation case 2 of nozzle contour

In this section an experimental configuration is presented and replicated providing an additional validation of the numerical approach used for the supersonic nozzle designed for the indraft wind tunnel. An experimental campaign was conducted in the indraft supersonic wind tunnel at Nagoya University. The schematic of the experimental setup is illustrated in Figure 5.19. The topic of the experiments focused on the laser energy deposition on external aerodynamics, and in particular on a diamond wing, which is not related to shock trains in internal flows. On the other hand, the facility has many analogies with the one described in this chapter providing a ground for comparison.

Referring to Figure 5.19, the facility is composed of a settling chamber, a converging-diverging de Laval nozzle, a test section, a diffuser, an isolation pneumatic butterfly valve, a vacuum pump, and vacuum chamber [318]. Once the valve is opened, the air travels from the left to the right, entering the inlet at atmospheric pressure and discharging into a vacuum tank of 11.5 m^3 volume. The effective run time is 5 sec. The test section is of square cross-sectional area with dimensions 80 mm $\times$ 80 mm and 100 mm long. The description of the geometry and flow conditions is reported in Table 5.7.

The Laval nozzle was designed by Sekiya [320] with the method of characteristics to deliver uniform flow at a Mach number M= 2 in the test section. In the design stage two-dimensional numerical simulation was used to verify the development of the boundary layer along the walls. To guarantee a constant effective area in the entire test section, a boundary

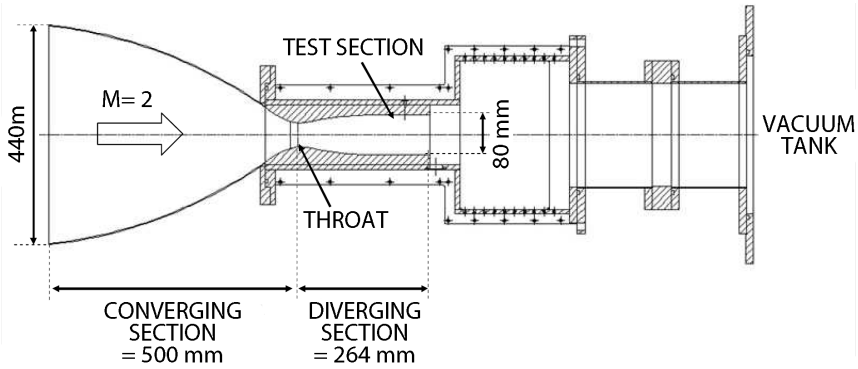

Figure 5.19: Schematic of the in-draft supersonic wind tunnel at Nagoya University [320].

M	M_P^*	M_S^*	$P_0[kPa]$	$P[kPa]$	$T[K]$	$H[mm]$	$W[mm]$	$L[mm]$	$time[s]$
2	1.92	1.89	100	13.8	167	80	80	100	5

Table 5.7: Wind tunnel flow conditions at Nagoya university. The subscripts 0 refers to the total condition [318–320].

layer correction method was applied by shifting out the ordinates of the ideal nozzle contour. The boundary layer was considered linearly growing on the upper and lower walls from the subsonic portion ahead of the nozzle throat to a thickness of 1.5 mm at the test section end.

Figure 5.20 illustrates the comparison of the Mach number between the nozzle designed with the method of characteristics and the computed flow by using the 2D RANS equations closed by the k-ω Wilcox turbulence model. The computed flow field accurately reproduces the Mach number contour obtained by Sekiya [320]. The flow that establishes at the end of the nozzle is uniform outside the boundary layer and a Mach number equal to 2 is achieved in the test section.

The flow properties distribution averaged at each length-wise location and the relative error to the isentropic equations, ϵ, are illustrated in Figure 5.21. Two grids of different sizes show that the solution is grid independent. All the flow properties match with the isentropic equations with a small discrepancy downstream of the nozzle, in the test section, due to the presence of the boundary layer. The only remarkable effect of the boundary layer appears between the turbulent solution and the inviscid solution in the temperature distribution, in Figure 5.21(d). This discrepancy clearly emerges analysing the relative error, ϵ.

Figure 5.21(a) shows that the correction on the nozzle profile to counteract the boundary layer leads to a nozzle that, according to the isentropic equations, delivers a Mach number greater than 2. The k-ω Wilcox model confirms that with the boundary layer correction the nozzle effectively delivers a uniform flow with a constant Mach number of approximately 2 along the x-axis. On the other hand, using a Pitot rake in a 30 mm $\times$ 30 mm square in the test section core flow an effective Mach number M_P^*= 1.92 was measured [319]. With the schlieren photography of the test section in the presence of the test model of a wing profile, in Figure 5.22(a), the angle of the oblique shock was measured, which allowed to determine the Mach number M_S^*= 1.89. The experimental methods confirm that the flow Mach number in the test section is approximately 1.9 while, the analytical method used by Sekiya [320] and the numerical approach estimate a higher Mach number.

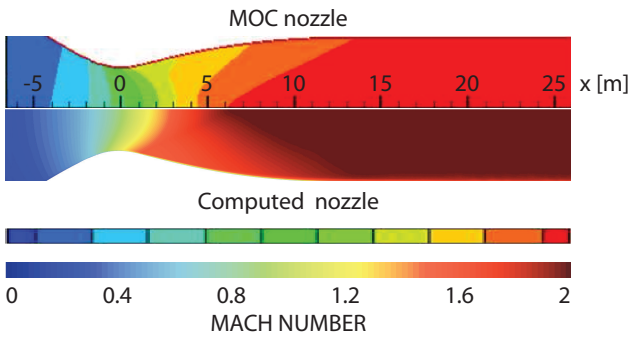

Figure 5.20: Comparison of the numerical simulation of the Mach 2 nozzle (top) and the computed flow with the current numerical approach (bottom).

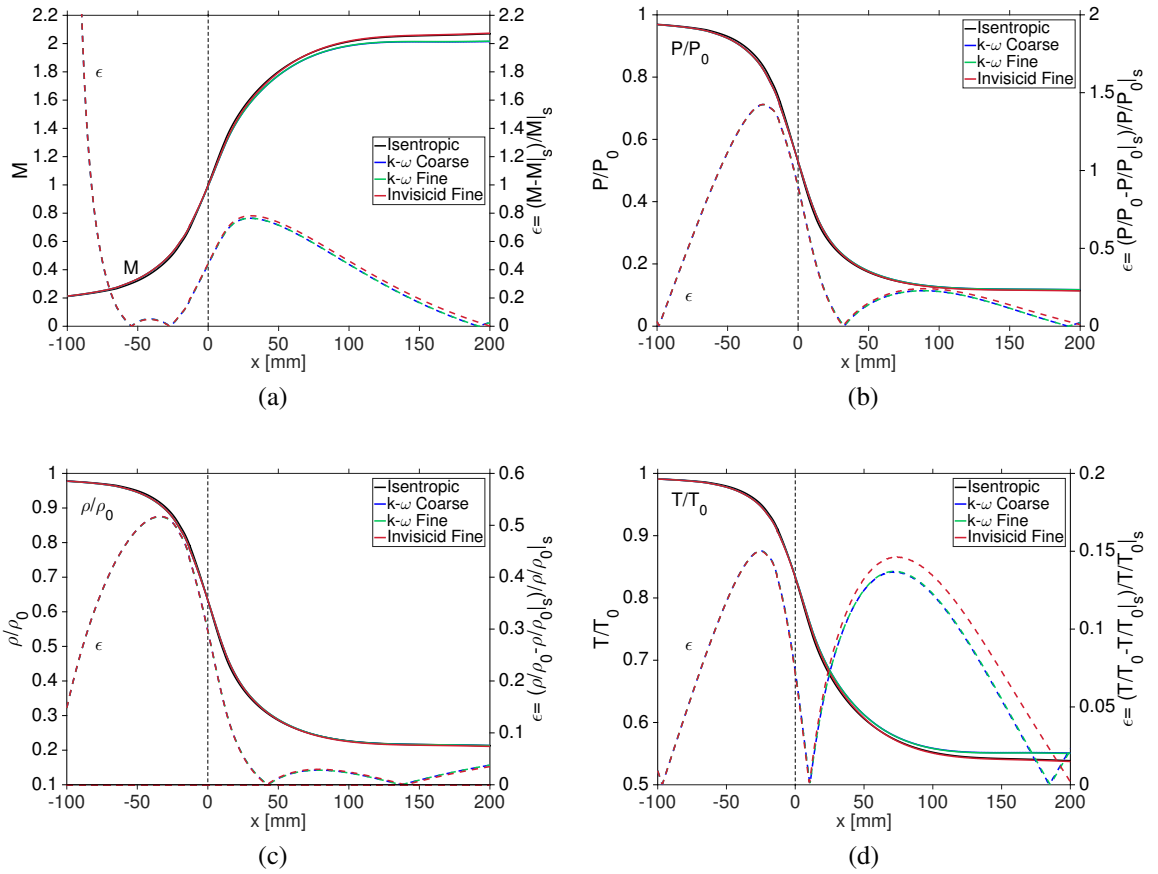

Figure 5.21: Distribution of the computed flow properties averaged at each length-wise station for the Mach 2 nozzle of Sekiya [320]: a) Mach number; b) Pressure ratio; c) Density ratio; d) Temperature ratio.

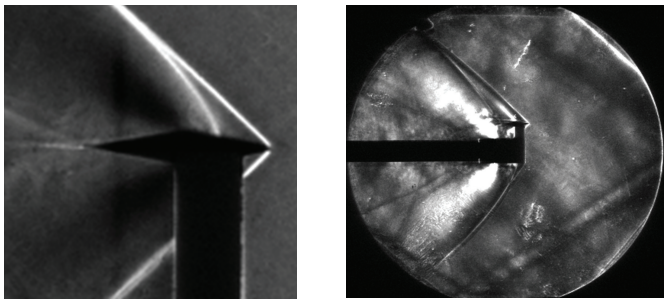

Figure 5.22: a) Wing profile; b) Diamond area of uniform flow created by the nozzle.

It is interesting to notice, in Figure 5.22(b), that the test model is placed in the diamond area where the gas flow is uniform. All the oblique waves that originate upstream perfectly cancel out. Consequently, this wind tunnel nozzle has been successfully designed since it provides the flow in the test section with the desired characteristics.

5.6.3 Nozzle contour of the indraft wind tunnel

For the current study, the inviscid nozzle contour designed with the MOC was imported into STAR-CCM+ to generate the mesh as a domain for running the simulations. As displayed in Figure 5.23, a polyhedral mesh has been used with a refinement in the nozzle and in proximity of the wall in order to locate the first cell at y^+ <1 in the entire domain, in Figure 5.24(a). Two grids composed of 21390 and 485689 cells were compared to analyse the effect of grid sensitivity. As Figure 5.24(b) illustrates, the Mach number distribution of the nozzle does not exhibit significant differences between the two grids. The origin of the x-axis is taken at the throat, as shown in Figure 5.25.

Different turbulence models to close the RANS equations can be used. The κ-ω Wilcox model has been reported to be more suitable for supersonic aerothermodynamic applications [179, 281, 294]. To check the accuracy of the turbulence model, the κ-ω Wilcox model is compared with the standard κ-ε model. The boundary conditions imposed are an inlet ambient pressure, outlet pressure of $0.001\ mbar$, total temperature of $300\ K$, adiabatic wall and symmetry with respect to the centreline.

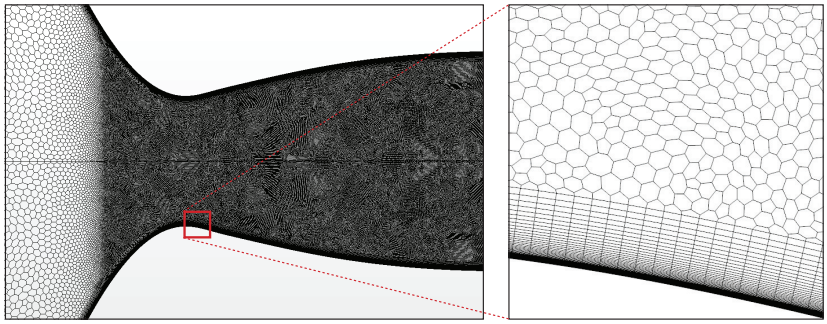

Figure 5.23: Mesh grid in the Mach 2 nozzle.

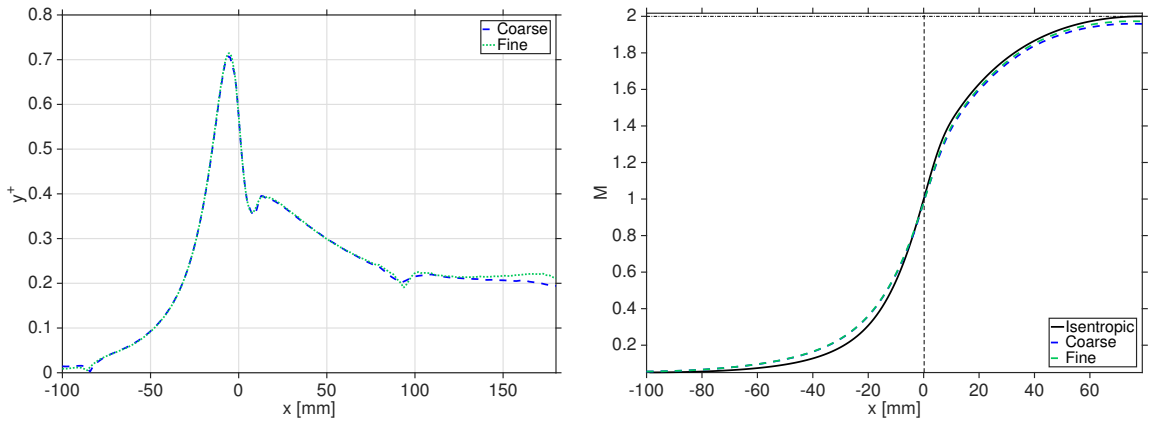

(a) (b)

Figure 5.24: Effect of grid resolution: a) y^+ distribution along the Mach 2 nozzle; b) Mach number distribution averaged at each length-wise station.

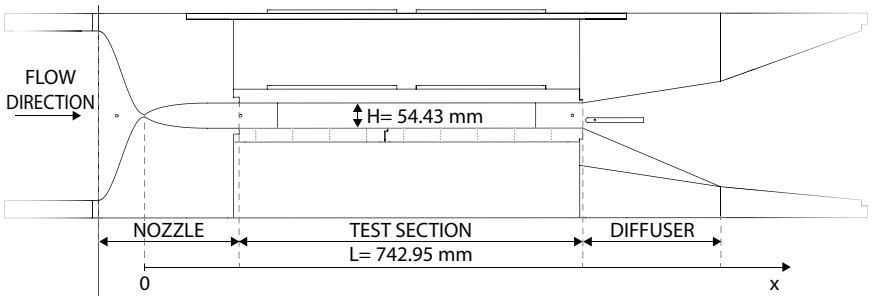

Figure 5.25: Schematic of the wind tunnel.

Figure 5.26 illustrates the distribution of the flow properties averaged at each length-wise station for the Mach 2 nozzle and the relative error to the isentropic solution, ϵ. It can be observed that all the flow properties are independent of the turbulence model and, in particular, are well described by the inviscid model. This result was expected since the mathematical equations for isentropic flows do not take into account turbulence effects and, as discussed in Section 5.3, except in proximity of the wall, the inviscid equations accurately describe the core flow. This is confirmed by Figure 5.27 which illustrates that the numerical

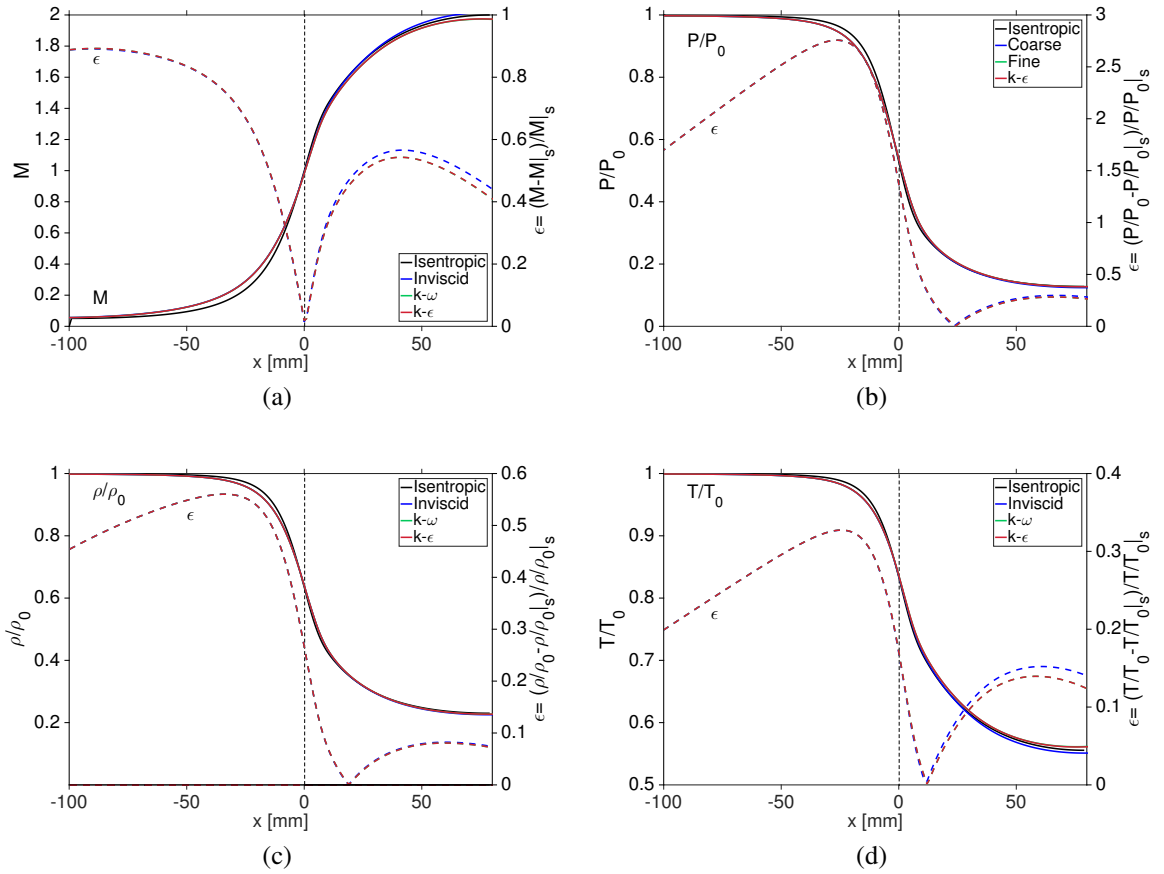

Figure 5.26: Centreline distribution of the flow properties for the Mach 2 nozzle: a) Mach number; b) Pressure ratio; c) Density ratio; d) Temperature ratio.

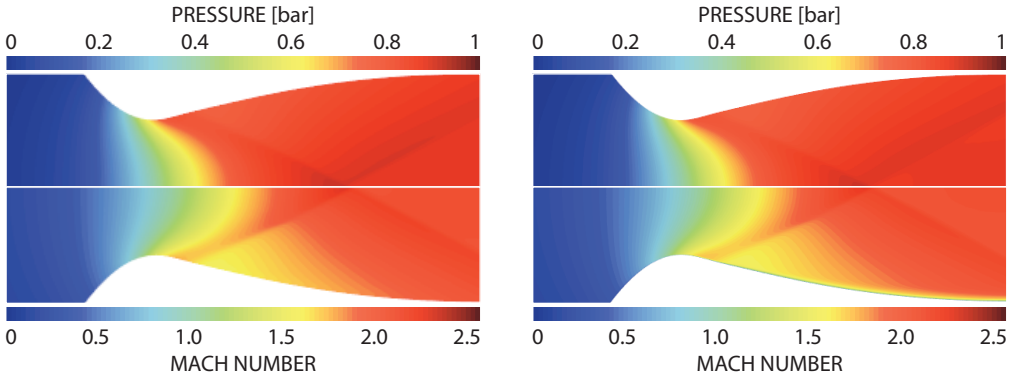

Figure 5.27: Mach number and pressure distribution for the Mach 2 nozzle: a) Inviscid; b) κ-ω model.

distribution of the flow properties in the inviscid case and with the κ-ω turbulence model are very similar. Results with the κ-ε model are analogous to those of the κ-ω model.

The distribution of the flow properties averaged at each length-wise station and the relative error, ϵ, for the Mach 4 nozzle are shown in Figure 5.28. In this case the pressure and

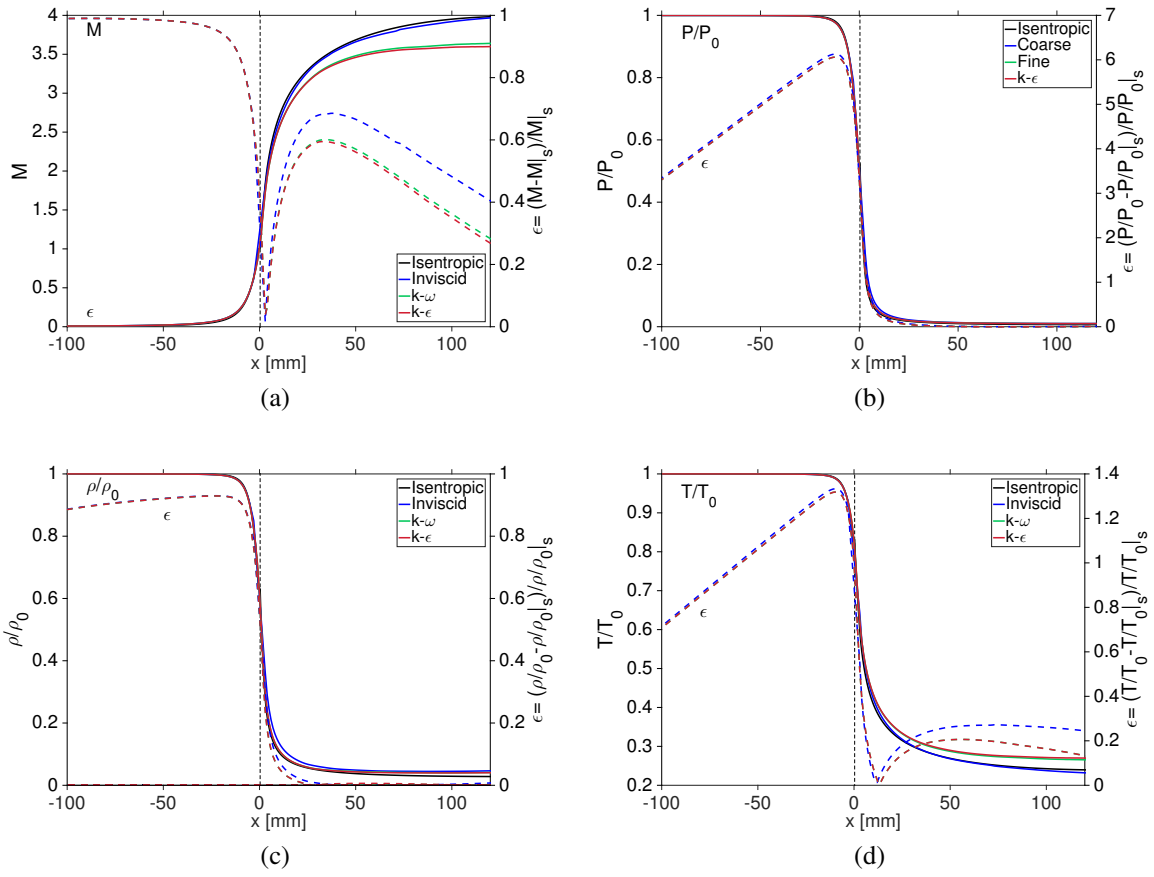

Figure 5.28: Distribution of the flow properties averaged at each length-wise station for the Mach 4 nozzle: a) Mach number; b) Pressure ratio; c) Density ratio; d) Temperature ratio.

density profiles match the isentropic equations independent of the turbulence model. However, both the κ-ω Wilcox and the κ-ε models present a discrepancy with the inviscid solution in terms of temperature, and in particular in the Mach number. This discrepancy arises from the inclusion of the viscous effects. Although the flow properties with the inviscid model match the isentropic equations, the development of the boundary layer on the wall strongly affects the core flow. It is clear that, if the viscous effects are taken into account, the Mach 4 nozzle delivers an averaged Mach number lower than that designed with the MOC because the flow does not properly establish. These observations find a confirmation in the numerical distribution of pressure and Mach number in Figure 5.29. Compared to the Mach 2 nozzle, the computed flow field demonstrates that the Mach 4 nozzle does not deliver a uniform flow at the end of the nozzle where the walls become parallel. The reason of this is not clear as the two nozzles were generated from the same code. In any case, the collection of experimental velocity profiles will allow to establish the flow characteristics in the wind tunnel.

Since only the Mach 2 nozzle is considered to be adequately designed, the calculation of the boundary layer for this Mach number is reported in Table 5.8. Additionally, the nozzle coordinates are tabulated in Table 5.9. Although the Mach number distribution along the nozzle, in Figure 5.24(b), did not exhibit significant differences between the coarse and the fine grids, the coarse mesh does not accurately refine the boundary layer. The boundary layer is considerably thicker than that resolved with the fine grid. Compared to the analytical

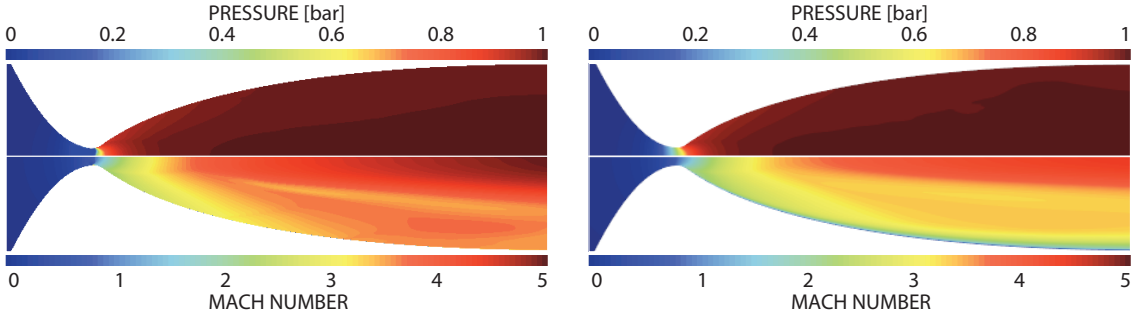

Figure 5.29: Mach number and pressure distribution for the Mach 4 nozzle: a) Inviscid; b) κ-ω model.

Method	$\delta\ [mm]$	$\delta^*\ [mm]$	$\delta^*/h\ [\%]$	$\theta\ [mm]$
κ-ω coarse	3.39	0.49	1.8	0.16
κ-ω fine	2.73	0.39	1.43	0.16
κ-ε fine	2.4	0.24	0.88	0.17

Table 5.8: Comparison of methods for the estimation of the boundary layer displacement thickness at Mach 2.

$x\ [mm]$	$y\ [mm]$	$x\ [mm]$	$y\ [mm]$
-100	183	8.37	17.8
-95	182	12.1	18.7
-90	179	15.8	19.6
-85	174	20.1	20.6
-80	167	24.9	21.6
-75	159	28.3	22.3
-70	149	31.3	22.9
-65	138	34.1	23.4
-60	125	36.8	23.9
-55	113	39.4	24.3
-50	99.7	42	24.7
-45	86.6	44.7	25.1
-40	73.8	47.4	25.4
-35	61.7	50.1	25.7
-30	50.6	52.8	26
-25	40.6	55.7	26.3
-20	32.1	58.6	26.5
-15	25.2	61.6	26.7
-10.3	20.4	64.6	26.9
-6.53	17.9	67.8	27
-2.8	16.5	71.1	27.1
0.921	16.2	74.4	27.2
4.65	16.8	77.9	27.2

Table 5.9: Nozzle coordinates for Mach 2.

models described in Section 5.3.2, the numerical simulations predict a larger boundary layer thickness. In addition, respect to the κ-ε model, the κ-ω model predicts a thicker boundary layer. Since at the moment no experimental data are available, nothing can be said about the accuracy of the analytical models or the numerical approach employed for this study. Again, the experimental velocity profile at the end of the nozzle will allow to determine the actual boundary layer for the nozzles designed for the current wind tunnel with the Pitot rake designed and detailed in Appendix B.

5.7 Experimental starting of the wind tunnel

This section provides the details about the experimental conditions recorded during the first attempts to run the wind tunnel with the Mach 2 nozzle. The pressure was recorded in the settling chamber, in the test section downstream of the nozzle, and in the pipe downstream of the opening vale.

Once the ball valve is opened, the air start flowing in the wind tunnel and the pressure in vacuum tank start rising. To monitor the wind tunnel starting process, pressure data were recorded for 12 seconds, as illustrated in Figure 5.30. The flow required 3 second to settle in the wind tunnel giving a time window to collect data between 3 to 10 seconds after which the

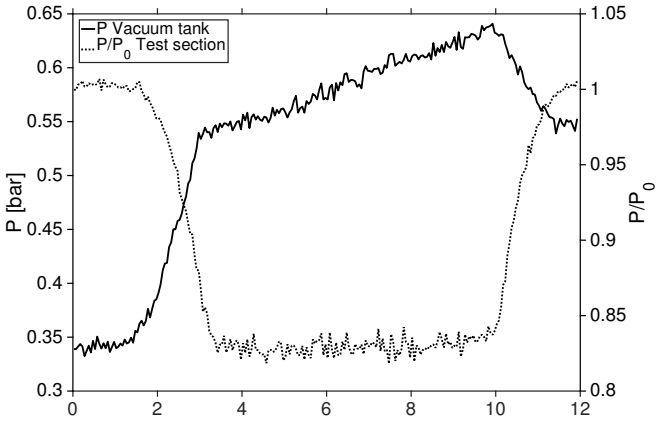

Figure 5.30: Experimental pressure variation in the wind tunnel with the Mach 2 nozzle.

valve was closed. It can be observed that the minimum vacuum level reached by the vacuum tank is around 0.35 bar and by the time the flow has settled in the wind tunnel the pressure has reached the value of approximately 0.6 bar. The pressure difference across the upstream and downstream ends required to operate the tunnel is not sufficient for the supersonic flow to establish in the wind tunnel. This is confirmed by the pressure ratio in the test section that reaches the value P/P_0= 0.83 in the time interval between 4 to 9 seconds. From the equations of compressible isentropic flows of a perfect gas, the pressure ratio required to reach the supersonic range must be smaller than 0.53.

In the measured condition, the average velocity achieved in the test section was approximately 165 m/s, leading to a Mach number of 0.48. The reasons behind this failure are under investigation but have been identified to be mainly caused by the presence of leakages in the entire pipeline.

5.8 Conclusions

A wind tunnel with a test section area of 101.60 mm $\times$ 54.42 mm and 742.95 mm long has been designed with the purpose of reproducing the compressibility effects developed by shock trains inside a high-speed engine intake. The Method of Characteristics, with no correction for viscous and dissipative effects at the walls, is used to design the nozzle contour for Mach 2 and 4. Theoretical methods to take into account the boundary layer growth have been analysed and compared with numerical simulation. The choice to not include boundary layer effects is due to the high level of integration between the facility and the model under investigation, i.e. the necessity to have parallel walls as a baseline case for the comparison with previous studies. Additionally, in nozzles with test section Mach numbers lower than 4 with thin boundary layers, the flow properties are satisfactorily approximated by the inviscid

contour and many nozzles designed with no viscous corrections perform adequately.

The peculiarity of the flow structure investigated in the current project requires a narrow duct as the test section. To replicate changes in the back pressure, a movable flap is installed at the end of the test section.

To provide an initial estimation of the wind tunnel characteristics the designed nozzle flows were simulated. The numerical approach was firstly applied to two configurations with a Mach 3 and a Mach 2 nozzle, demonstrating that the acquired computational methodology with the κ-ω turbulence model is suited for solving the supersonic nozzle flows. The computed flow field in the Mach 2 nozzle showed that a uniform flow settles at the end of the nozzle. The computed boundary layer thickness was estimated to be larger than that obtained with the analytical models. The simulated Mach 4 nozzle flow showed that the core flow is not uniform and large transverse uniformities are present.

Lastly, preliminary experimental tests have been performed to run the tunnel. The reasons that have prevented the correct operation of the wind tunnel have been identified to be caused by the leaks in the entire pipeline. The collection of experimental data is necessary and further tests will provide precious information in support of the analytical and numerical tools employed for the design of the current wind tunnel.

6 | Numerical simulation of compressible internal flows

BEFORE any measurements can be discussed, the reliability of the solution needs to be confirmed. The quality of the solution depends on a number of variables, but mainly on the size of the grid cells as well as their distribution in the computational domain. Therefore, in the first part of this chapter the sensitivity of the solution to different variables is analysed on two test cases. In the second part, the results of the shock train that are generated in the current wind tunnel configuration are presented and analysed.

6.1 Validation case 1

To validate the numerical approach that will be applied to study the shock train in the wind tunnel, the case for M= 2 of the experimental data collected by Sun et al. [65, 67, 71] in a square duct has been replicated. The cross-section and length of the test section are $80 \times 80\ mm^2$ and 1500 mm, with a length-to-equivalent diameter ratio L/D_{eq} of 18.75. Along with experiments, the authors performed a numerical investigation with a computational domain of 11 times the height starting from L/D_{eq}= 7. To match the experimental conditions of the flow confinement, δ/h= 0.25, a velocity profile given by the $1/7^{th}$ power law was imposed at the inlet. The geometry and flow conditions are reported in Table 6.1. The numerical approach solved the two-dimensional RANS equations closed by the algebraic Baldwin-Lomax turbulence model. The laminar viscosity for the air was calculated using the Sutherland's law. To correct the near-wall behaviour for zero pressure gradient boundary

M	$T_0[K]$	$P_0[kPa]$	$P[kPa]$	$P_b[kPa]$	$H\ [mm]$	$W\ [mm]$	$L\ [mm]$	$Re\ [m]$	δ/h
2	300	196	25.05	92.2	80	80	880	2.5×10^7	0.25
4	300	499	3.29	36.9	80	80	880	3.6×10^7	0.35

Table 6.1: Boundary and geometry conditions of the computational domain of the validation model [71]. The subscript 0 refers to the total condition and P_b is the back pressure.

layers the Van-Driest damping factor was used.

Figure 6.1 illustrates the comparison between the experimental and numerical results obtained by Sun et al. [67] for inlet Mach numbers of 2 and 4. According to the authors, the computed results agreed well with the experimental data even though the Boussinesq approximation, which is implicit in the algebraic model used, limits an accurate description of separated flows. The static pressure distributions along the duct obtained by Sun et al. [67] by numerical simulation and experiment are shown in Figure 6.2. Two values of the back pressure, P_b= 96.6 kPa (case A) and P_b= 92.2 kPa (case B), are compared for an inlet Mach number of 2. It can be observed that the experimental pressure data at the wall of case B were well replicated with the numerical simulation. For case A, although the location of the first shock wave matches the experimental data, the pressure distribution is not well-resolved. It is important to take into account the poor accuracy of the numerical results obtained by Sun et al. [67, 71] when the discrepancies with the current numerical code are analysed.

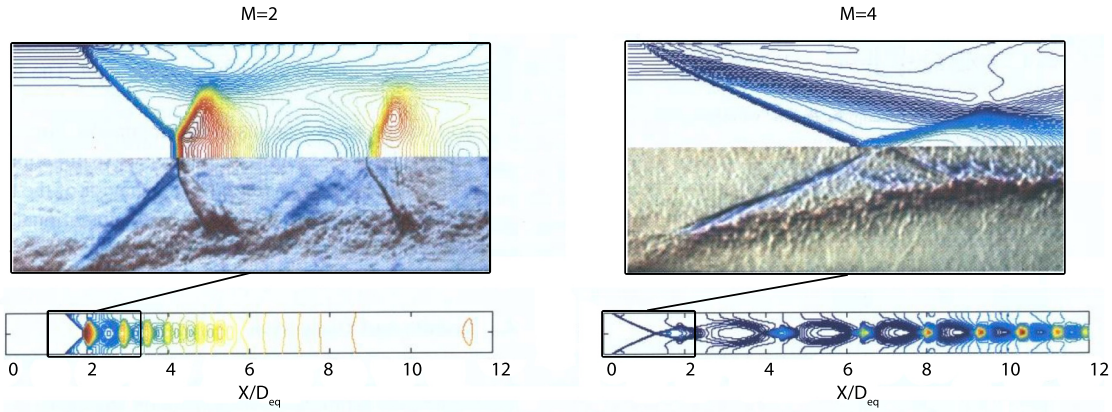

Figure 6.1: Schlieren photography and CFD density contours: a) M= 2; b) M= 4 [67].

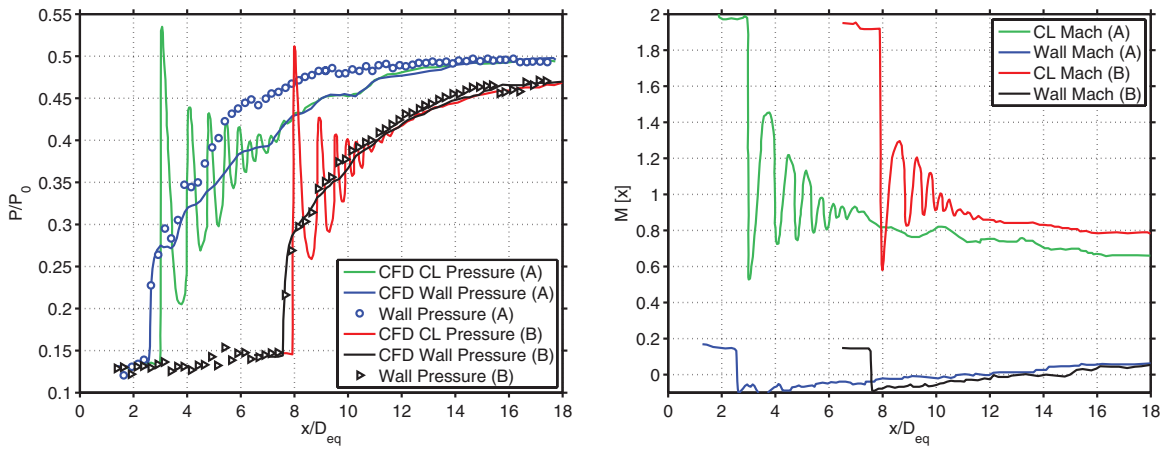

(a) (b)

Figure 6.2: Static pressure and centreline Mach number distribution for different back pressures [67].

Additionally, the only experimental data available are from the pressure tapping at the wall, whereas centreline pressure and Mach number distributions are executed with computation only. Thus, only the wall pressure distributions are considered reliable to make comparisons.

6.1.1 Description of numerical setup

Numerical simulations were carried out solving two- and three-dimensional coupled implicit Reynolds-averaged Navier-Stokes (RANS) equations in STAR-CCM+. The k-ω Wilcox was used in most of the cases, due to its stability and the capability to satisfactorily solve the shock train characteristics. The RANS equations are discretised using a cell-centred finite volume method. Inviscid and viscous fluxes are evaluated using Liou's AUSM+ flux-vector splitting scheme based on the upwind concept and second-order central differences, respectively. The temporal term is discretised with a second-order accuracy interpolation scheme.

The experimental configuration and flow conditions for a Mach 2 shock train are described in Table 6.1. The working fluid is treated as an ideal gas. The viscosity and thermal conductivity are evaluated using Sutherland's law. Adiabatic and no-slip boundary conditions are imposed on the walls along the duct. Initial conditions are set with an inviscid normal shock at the exit of the computational domain. Stagnation conditions are imposed at the inlet with uniform flow properties. At the outlet boundary the flow variables, except for the pressure, are extrapolated from the adjacent cell value using reconstruction gradients. The back pressure was determined from the experimental pressure profile of Sun et al. [67] and assumed to be constant at the exit plane with a value of P_b= 92.2 kPa.

The computational domain is simply formed of a rectangular block. Due to the symmetry of the problem, half of the region of the flow field is computed in the two-dimensional case, and one quarter in the three-dimensional case. Figure 6.3 shows the structure of the numerical grid employed, where y/D_{eq}= 0 corresponds to the wall and y/D_{eq}= 0.5 is the centreline of the duct. The grid is composed of structured quadrilateral cells and the grid points are

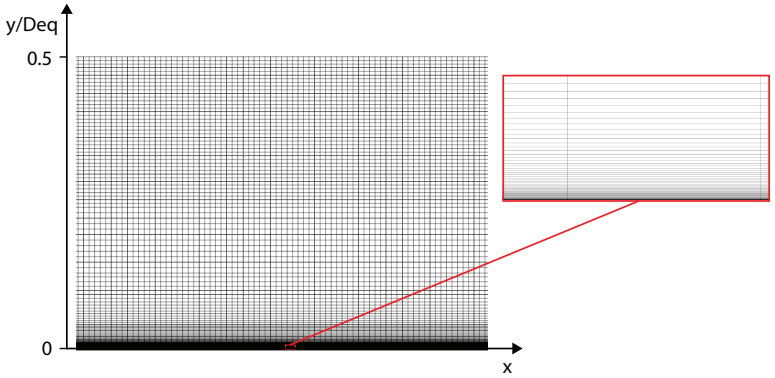

Figure 6.3: Portion of the half duct numerical grid employed in the 2D computational domain.

clustered towards the wall to resolve the behaviour of the boundary layer. Refinements are necessary in the regions where the gradients are known to be relevant and the thickness of the closest cell to the wall is important for the accuracy of the results.

6.1.2 Effect of grid resolution

The flow confinement at the inlet of the computational domain plays a fundamental role on the location of the shock train. The sensitivity of the computational length will be examined in Section 6.1.3, whereas in this section L/D_{eq}= 23 has been used to allow the boundary layer to develop. To compare the results with those of Sun et al. [67], only a portion of duct with length L/D_{eq}= 11 was taken to process the data, with the inlet located at δ/h= 0.25.

To conduct a grid independence study, a coarse grid that meets the criteria of convergence is used as a starting point to gradually increase the number of cells in the computational domain. When the solution does not change with an increasing number of cells it is said to be grid independent. Another factor that has to be considered is the computational time, i.e. the time that a numerical simulation needs to drop the residuals below a certain level, that depends on the size of the domain and number of cells. While few cells may cause poor results because important flow characteristics are not captured, in most cases a complete grid independence would lead to such a high number of cells that the achieved accuracy is not justified by the increased computational cost. More preferably, the relative error with respect to the finest grid is calculated to evaluate the quality of the coarser grid. As tabulated in Table 6.2, seven grids are employed to find the optimal combination between these two requirements. Only with the coarser grid, the maximum value of wall y^+ is greater than 1, whereas from Grid 2 the value of wall y^+ is smaller than unity in the entire domain, providing a good resolution of the boundary layer gradients.

Grid	**Size**	y^+
1	368 × 62	0.33–1.67
2	921 × 116	0.021–0.45
3	2454 × 154	0.018–0.42
4	4601 × 276	0.016–0.40
5	6134 × 314	0.013–0.38
6	9200 × 350	0.004–0.37
7	12268 × 452	0.003–0.36

Table 6.2: Number of cells in different grids.

Due to the presence of viscous effects, the boundary layer exists at the wall. In internal supersonic flows, in response to the presence of a back pressure rise, the flow interacts with the boundary layer forming the shock train. The initial shock creates an adverse pressure gradient on the incoming boundary layer on the duct walls, which in turn may cause the boundary layer to separate. As Figure 6.4 illustrates, the flow is decelerated to subsonic velocity behind the first normal shock wave, NS, in the core flow. The pressure rise is transmitted upstream through the boundary layer region, causing a thickening of the boundary layer itself. The growth of the boundary layer deflects the streamline forming an oblique shock, FOS. Since the flow remains supersonic behind the first oblique shock, a rear oblique shock wave, ROS, forms behind it. The two oblique shocks converge into the triple point, TP, and combine with the initial normal shock into a λ shock structure, λS. At the point of bifurcation, a shear layer, SL, develops as it can be observed in the form of slip lines. The thickening of the boundary layer reduces the effective area of the core flow, so that the subsonic flow behind the rear oblique shock wave, ROS, is accelerated again to supersonic speeds. At this point the supersonic flow interacts with the thick boundary layer and the same process is repeated several times up to a terminal shock after which the flow is subsonic in the entire cross-section. In the central part of the duct, in the region confined between the slip lines, the stronger deceleration through the normal shock produces a misalignment with the outer parts where the flow passes through the two oblique shocks. This explains the existence of the slip lines, which are narrow surfaces of finite thickness that separate the gas flow that is decelerated by the normal shock to that passing through the λ shock.

The comparison of the solution obtained with two different grids, in Figure 6.5, shows that even though the general behaviour of the shock train is outlined in both cases, a very coarse grid fails to capture the fine structures such as the slip lines. Additionally, the shock train resolved by the coarse grid is shorter and formed by a smaller number of shock waves. The two axes in Figure 6.5 illustrate the axial shift in the shock train between the solution of the current code and that obtained by Sun et al. [67]. The reference location L_0/D_{eq} identifies the location where the flow confinement δ/h is equal to 0.25.

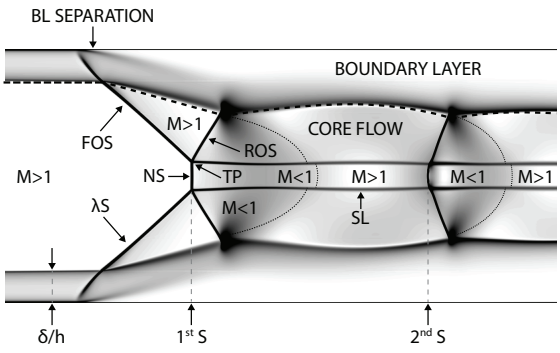

Figure 6.4: Schematic of the shock wave/boundary layer interaction in shock train.

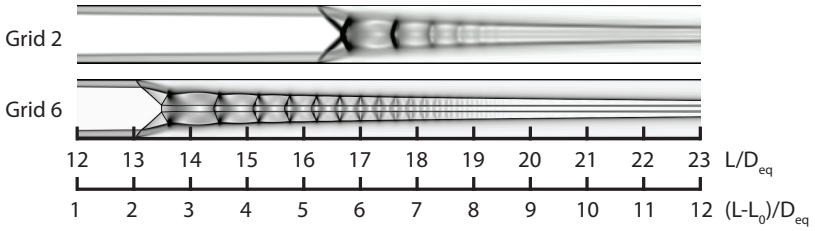

Figure 6.5: Numerical schlieren with different grid resolution.

The differences between Grid 2 and Grid 6 distinctively emerge from Figure 6.6 where pressure and Mach number profiles with different grid sizes are compared. The figures on the left hand side show the flow properties distributions plotted at the actual location of the numerical domain, whereas the plots in the right hand column have been shifted by the location of the initial shock wave so that they start at the same location. It is clear that the location of the shock train varies from one simulation to the next. The wall static pressure monotonically increases due to the diffusing effect of the boundary layer. On the other hand, the peaks in the centreline pressure plot identify the individual waves composing the shock train which are gradually damped along the duct. This trend matches both the experimental and numerical results obtained by Kawatsu et al. [92].

It is observed that, as the grid resolution increases, the shock train moves upstream towards the inlet and increases in length. This is caused by the fact that a coarse grid is not adequate to accurately resolve the flow. Fine grids better match the experimental data because the representation of the flow field is more accurate. Since the back pressure is prescribed as a boundary condition, the pressure at the end of the shock train converges towards the experimental value. These results agree with all cases in the literature. An interesting finding was reported by Carroll et al. [68] observing that a grid refinement in the transverse direction causes the shock train to move towards the exit plane.

Figure 6.7 illustrates the relative error with respect to the finest grid. The experimental wall pressure and the computed wall pressure profiles are shifted for the pressure rise of the finest grid. As the grid is refined, the difference between two subsequent plots gradually decreases and both Grid 6 and Grid 7 match the experimental data with sufficient accuracy. The location of the shock train tends to stabilise at a fixed axial coordinate, as illustrated in Figure 6.8(a). The difference between Grid 6 and Grid 7 is not significant and the relative error is less than 1.2%. This means that a further refinement of the grid would lead to a very small difference compared with the results achieved with Grid 7.

The magnitude of the pressure peaks of the first and second shocks, respectively peak 1^{st} shock and peak 2^{nd} shock, as well as the pressure recovery behind 1^{st} shock are reported in Figure 6.8(b). From Grid 4 to Grid 7 the variation in magnitude of the first and second shock is very small, as it is evident also from the pressure profiles in Figure 6.6(b). As a consequence, the results with a finer grid are expected to be very close to Grid 7 which is

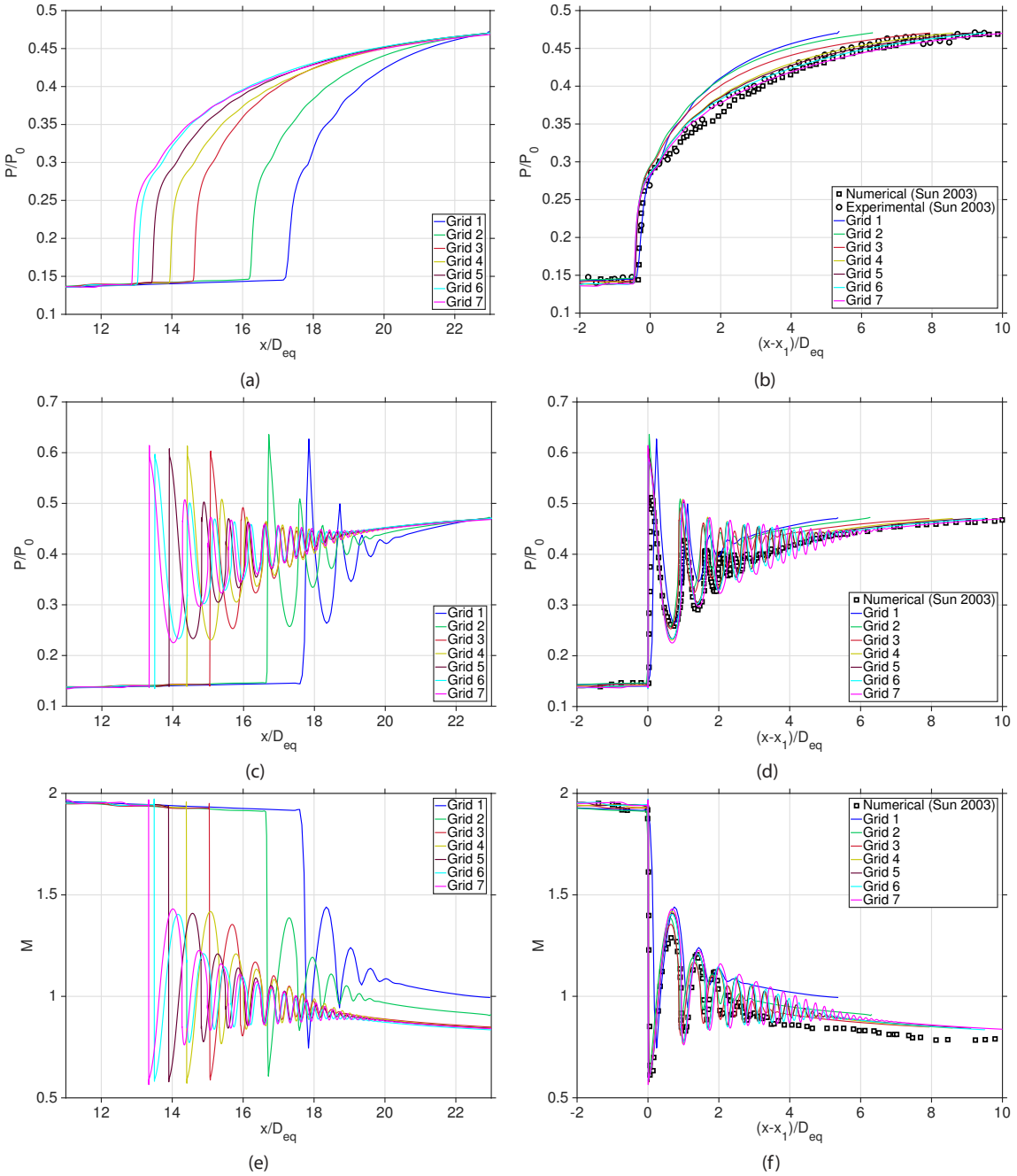

Figure 6.6: Effect of grid size on the accuracy of pressure and Mach number distributions. a) - b) Wall static pressure; c) - d) Centreline static pressure; e) - f) Centreline Mach number.

adequate to achieve grid-independent results. In such flows, where the ratio of the thickness of the boundary layer to the duct height is a key parameter in determining the shock train characteristics, an error of only a few percent in resolving the boundary layer can result in a considerable divergence from the experiments. Taking into account both the accuracy of the grid with the computational cost, Grid 6 is used to perform the simulations reported in this work unless specified otherwise.

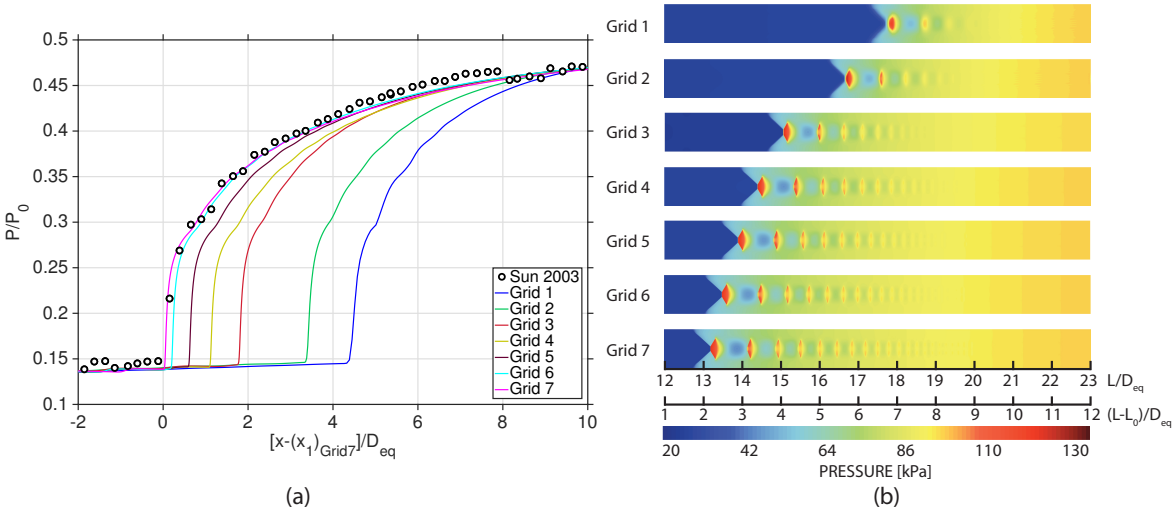

Figure 6.7: Effect of grid resolution on pressure. a) Wall pressure; b) Numerical contour.

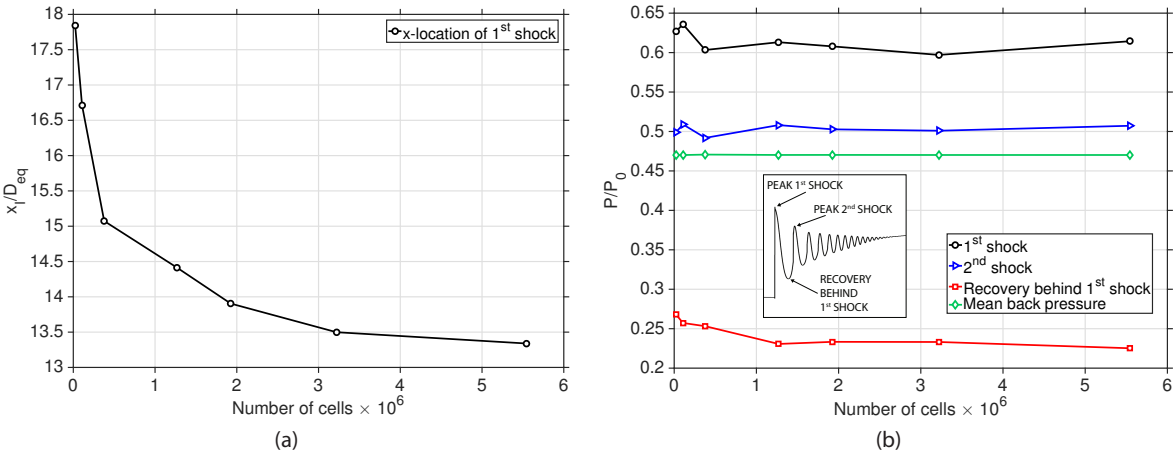

Figure 6.8: Variation with grid resolution of: a) Axial coordinate of the leading shock wave; b) Value of pressure of different parts of the shock train.

6.1.3 Influence of duct length

Sun et al. [67, 71] validated their numerical approach using the experimental data and imposing a boundary layer profile at the computational inlet. However, instead of imposing an analytical velocity profile, in the current study the boundary layer was left to develop along the duct wall as it occurs naturally in the experiments. To do so, a longer computational domain was necessary to investigate the effect of the boundary layer development. Grid 4 was used to perform the sensitivity of the results to the duct length because, except for small variations in the subtle flow features, this grid adequately captures the overall shock train structure. Five values of length-to-height ratio, L/D_{eq}, are compared in Figure 6.9 where case A, B, C, D, and E correspond to L/D_{eq} of 11, 18.75, 23, 25.75, and 30, respectively.

Without a boundary layer at the inlet of the computational domain the shock train begins downstream in the duct as case A in Figure 6.9 shows, in agreement with Huang et al. [23].

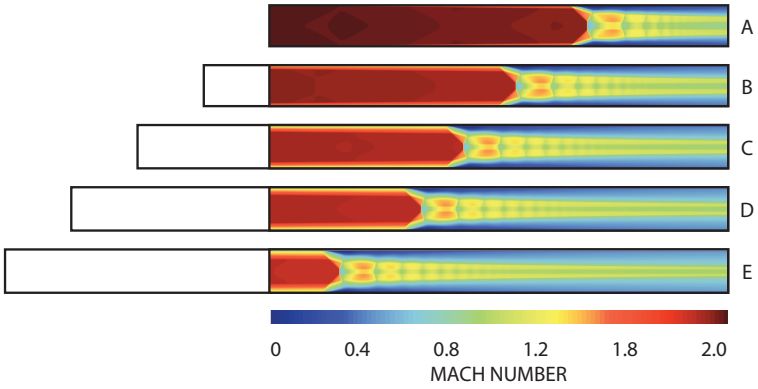

Figure 6.9: Mach number contour for different duct length.

Increasing the duct length, the boundary layer develops and thickens ahead of the shock train, as reported in Table 6.3. The viscous effects near the wall reduce the flow speed and the duct effective area. In a narrow channel, typical of this kind of flows, the ratio of boundary layer thickness ahead of the shock train to the duct height is one of the dominant variables which influences the position and length of the shock train [56, 58, 59]. Morgan et al. [54] stated that the flow confinement, more than the pressure ratio, is the key parameter in determining the location of the initial shock. Figure 6.9 illustrates that as the boundary layer ahead of the shock train increases in thickness, the shock train requires a smaller duct length to establish so that the shock train is pushed upstream, similarly to what obtained by Sun et al. [71].

The distribution of the pressure and Mach number in Figure 6.10 shows that the viscous effects increase the static pressure and reduce the velocity of the flow ahead of the shock train. A longer shock train is composed of more shock waves but the shape of the shock train is similar in all cases as well as the strength of the first shock.

From Figure 6.10(b) it can be observed that, as the duct length increases, the Mach number ahead of the shock train decreases considerably below 2. As a consequence the flow conditions ahead of the shock train are different from those of Sun et al. [67] and no meaningful comparison can be accomplished. Therefore, for the cases with a long duct, a greater inlet Mach number is used to ensure a Mach 2 shock train. An iterative process of grid refinement and duct length analysis has led to the choice of using a computational domain of L/D_{eq}= 23 for the current study. With a fine grid this length allows the boundary layer to develop and establish the flow as the reference study [67].

Case	**A**	**B**	**C**	**D**	**E**
$\boldsymbol{L/D_{eq}}$	11	18.75	23	25.75	30
$\boldsymbol{\delta/h}$	0.17	0.28	0.33	0.37	0.41

Table 6.3: Boundary layer thickness ahead of the front shock.

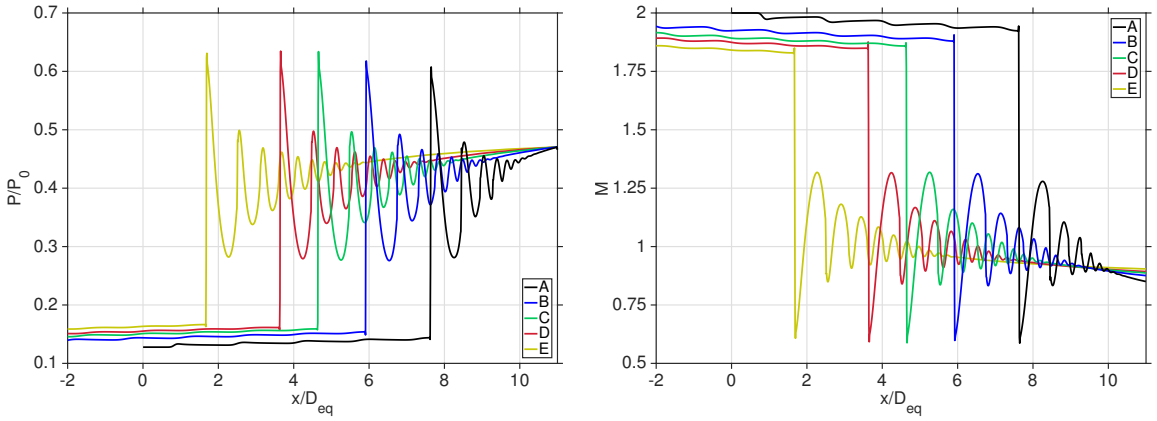

(a) (b)

Figure 6.10: Comparison of centreline flow quantities with different length of the computational domain. a) Static pressure; b) Mach number.

6.1.4 Effect of initial boundary layer

In this section the boundary layer profile is imposed at the inlet of a computational domain of length L/D_{eq}= 11 with an inlet Mach number of 2 and flow conditions described in Table 6.1. The imposition of the boundary layer required to run an initial simulation to extract the flow properties at a specific axial location that are then applied at the inlet of another simulation as a fixed boundary condition. The numerical contours shown in Figure 6.11 are obtained with Grid 6 and illustrate that by imposing a boundary layer profile at the inlet of computational domain the shock train establishes in the same manner as with the case in which the boundary layer naturally develops along the duct walls.

Figure 6.12(a) illustrates the velocity profile at the inlet of the computational domain. The boundary layer thickness is approximately δ/h= 0.25 but the velocity profile exhibits a change in gradient and does not overlap with the $1/7^{th}$ power law of the reference paper by Sun et al. [67]. On the other hand, the profile in Figure 6.12(b) agrees well with theory. For reference, the blue lines represent the linear relationship in the viscous sublayer and the logarithmic law in the log layer. The values of the von Karman constant κ= 0.40 and the log law constant C= 5.2 are taken from Morgan et al. [54].

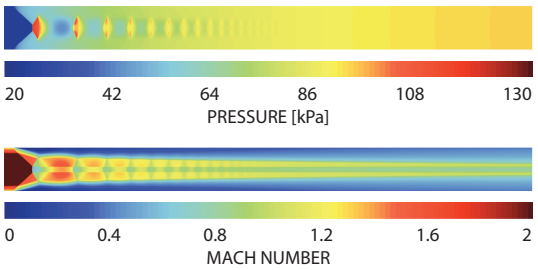

Figure 6.11: Pressure and Mach number contour.

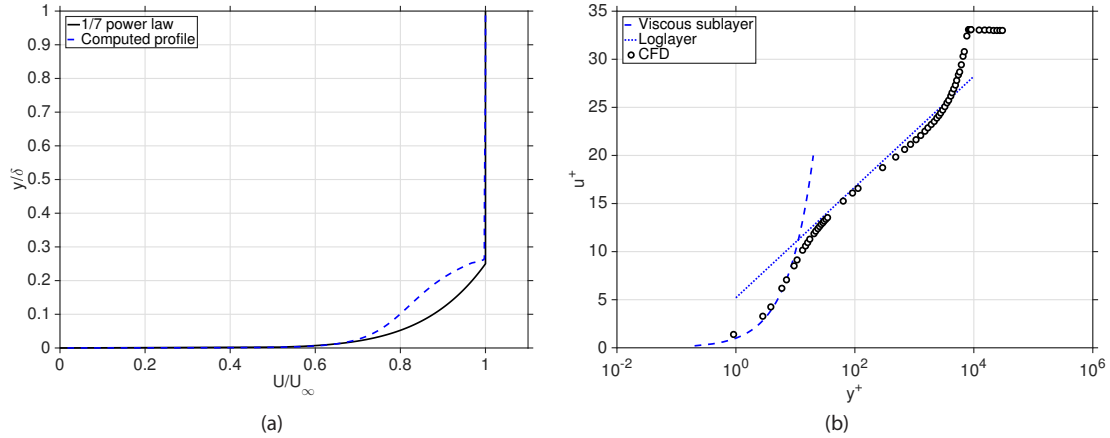

Figure 6.12: a) Velocity profile; b) y^+-u^+ plot.

The divergence of the computed velocity profile with the analytical formula in Figure 6.12(a) is due to the fact that the $1/7^{th}$ power law is an ideal model and in reality the velocity profile does not follow this trend, particularly in internal compressible flows. In order to investigate this discrepancy further, the numerical setup described in Section 6.3.1.1 was applied to the case described by Hoeger et al. [321]. Hoeger et al. [321] performed a two-dimensional numerical study in an isolator of square cross-sectional area with an inlet Mach number of 1.8 using the k-ω Menter SST turbulence model. The flow conditions are reported in Table 6.4. Figure 6.13 illustrates the numerical contours obtained using the same grid structure specified by Hoeger et al. [321]. The two grids, referred as medium and fine grid, are composed of 50000 and 100000 cells, respectively. In Figure 6.14(a), the velocity profile just ahead of the shock train equals that obtained by Hoeger et al. [321] except for the region at the edge of the boundary layer. Despite this small discrepancy Figure 6.14(b) shows an excellent agreement with the predicted profile.

M	$T_0[K]$	$P_0[kPa]$	$P[kPa]$	$P_b[kPa]$	$H\ [in]$	$W\ [in]$	$L\ [in]$
1.8	232.9	120.66	25.05	50	2.5	2.5	24

Table 6.4: Boundary and geometry conditions of the computational domain of Hoeger et al. [321]. The subscript 0 refers to the total condition and P_b is the back pressure.

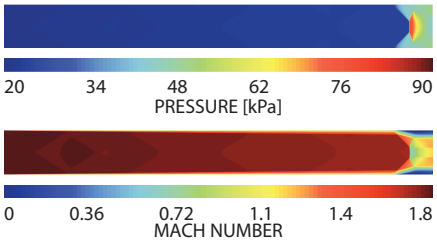

Figure 6.13: Pressure and Mach number contours with fine grid.

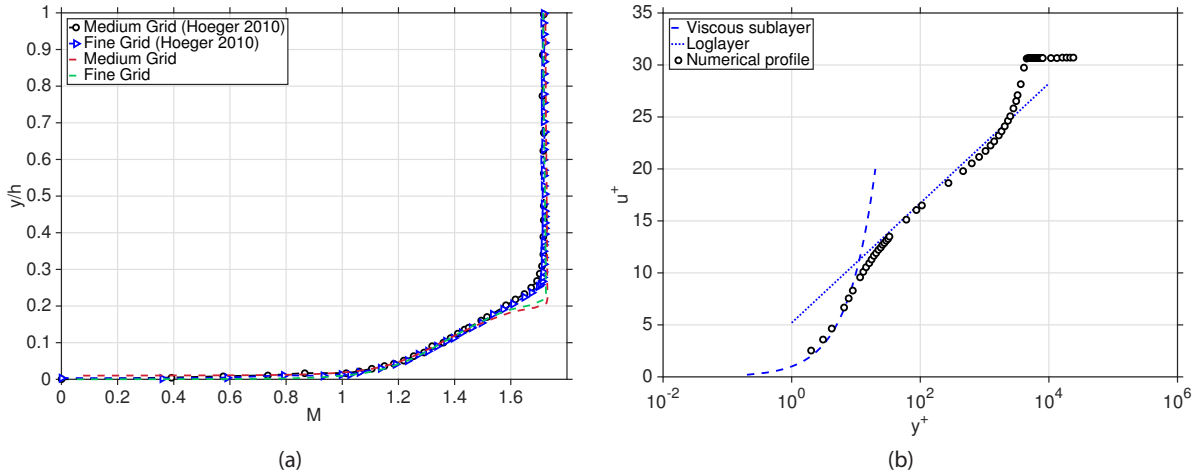

Figure 6.14: a) Velocity profile; b) y^+-u^+ plot.

6.1.5 Effect of turbulence model

The influence of using three different turbulence models is investigated. Figure 6.15 illustrates the magnitude of the density gradient with the k-ω Wilcox, k-ω Menter SST, and k-ε realisable models available on STAR-CCM+ [194]. Compared to the k-ω Wilcox model, the k-ω Menter SST and k-ε realisable models in Figure 6.16 show several differences. Firstly, the close up in Figures 6.16(b) and 6.16(c) show that the leading shock wave is not normal at the centre of the duct. The front shock has a χ shape, although in the k-ε case, in Figure 6.16(c), a slip line at the centreline is visible.

It is interesting to note that, in the k-ω Menter SST case, in Figure 6.16(b), a weak slip line is present just behind the first shock wave. A second shock occurs and is linked to the rear legs of the oblique shocks at the edge of the boundary layer. This latter shock is normal in a small portion at the centreline of the duct and decelerates the flow to subsonic conditions, as visible also from the centreline pressure and Mach number profiles, in Figures 6.17(c) and 6.17(e), respectively. The pressure distribution in Figure 6.17(c) illustrates that with the k-ω Menter SST the initial pressure rise is not composed of a single peak. The corresponding

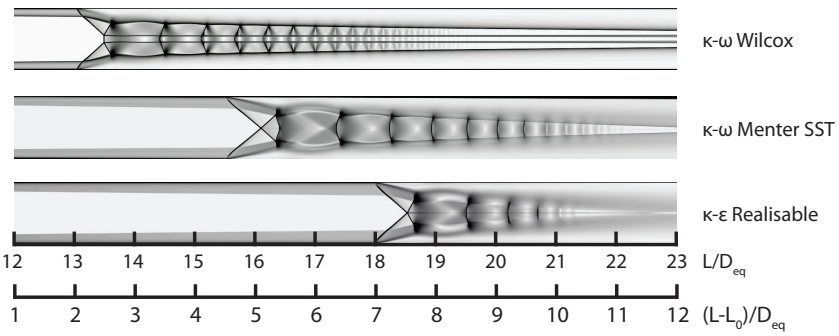

Figure 6.15: Numerical schlieren with different turbulence model.

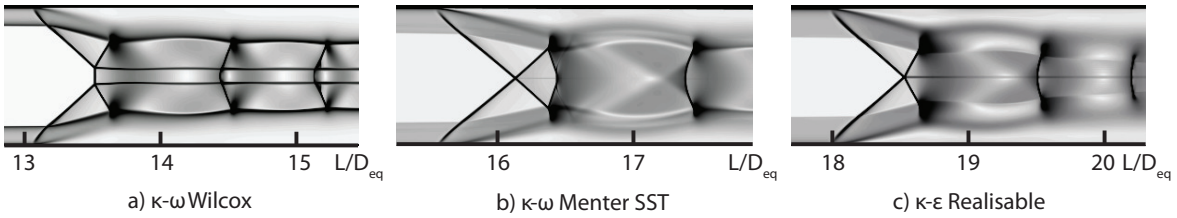

Figure 6.16: Close up of numerical schlieren at the first shock with different turbulence model.

plots of the Mach number, in Figure 6.17(e), illustrate that the flow passing through the χ shock is decelerated but remains in the supersonic range. The flow is further decelerated to subsonic speed through the normal shock, in Figure 6.17(f). This corresponds to the steep pressure rise in the first peak of the centreline pressure, in Figure 6.17(d).

From Figure 6.17(e), in the k-ω Menter SST and k-ε cases, the Mach number distribution through the entire shock train remains mostly above 1, with a value at the end of the shock train in the supersonic range. From the pressure distributions, both the wall and centreline pressure converge to the value of the back pressure imposed as the boundary condition. The wall pressure in the k-ω Menter SST model is underpredicted, as visible in Figure 6.17(b). Although the k-ε model locates the shock train several L/D_{eq} downstream in the duct, it does a better job of predicting the shock train structure. While the amplitude of the shocks is overpredicted, the spacing between consecutive shock is quite accurate although discrepancies are present. The k-ε realisable model captures the relative distance between the first three shocks quite accurately compared against the centreline properties obtained with k-ω Wilcox, but the latter shocks in the shock train structure are very weak. The considerably shorter shock train length may also be a contributing factor. The k-ω Menter SST model predicts a slightly longer shock train but it fails to properly axially locate the several shock waves of the shock train system. The absence of a normal portion of the leading shock at the centreline contributes to the failure in capturing the subsonic flow following the first shock and consequently the entire structure of the shock train is affected.

This investigation shows the high sensitivity of the shock train to the solving equations. The establishment of the shock train in the duct mainly depends on the way the boundary layer develops on the walls, and hence a model capable to accurately reproduce the subtle features close to the solid boundary plays a fundamental role. Although the three turbulence models employed are two-equation models, only the k-ω Wilcox fulfils this requirement. The k-ω Wilcox closely matches the reference data by Sun et al. [67] of the entire shock train in terms of flow properties, location of the shock train, distance between shocks, and shock strength. There is considerable evidence in the literature that the k-ω model is more computationally robust than the k-ε model for the description of turbulent flows close to a solid boundary [322]. The k-ω Menter SST includes the k-ε model in the far-field through a blending function. This demonstrates the inability of the k-ε to describe the shock train

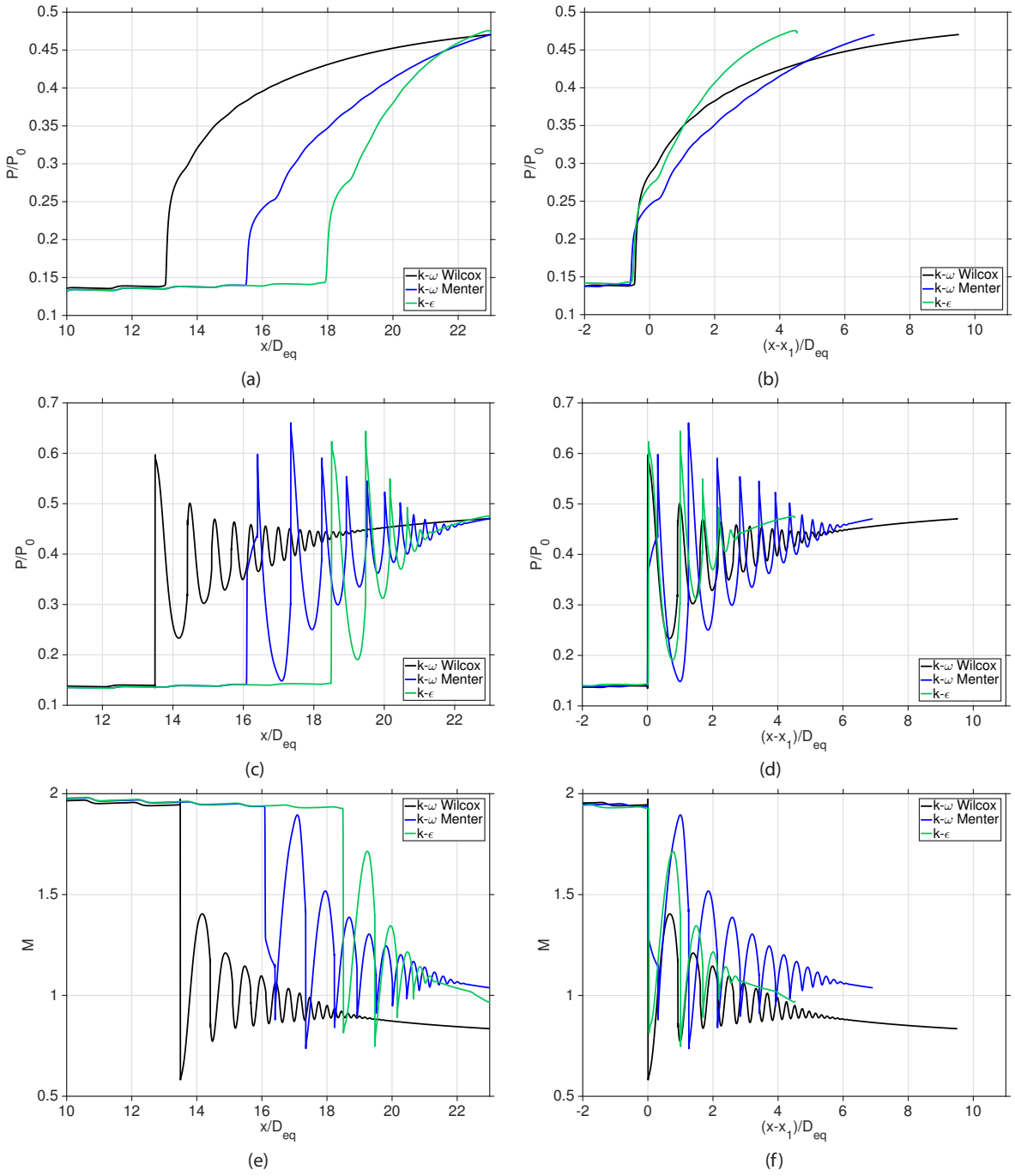

Figure 6.17: Effect of turbulence model on the accuracy of pressure and Mach number distributions. a) - b) Wall static pressure; c) - d) Centreline static pressure; e) - f) Centreline Mach number.

characteristics even in the core flow. It should be noted that the use of a commercial code does not allow flexibility and control on the code implementation. It has been reported that sometimes the choice of the model closure coefficients is problem-dependent [323, 324]. On the other hand, the k-ω Wilcox model confirms to be the most suitable for describing the shock train behaviour in internal ducts.

6.1.6 Effect of sidewalls

Two-dimensional simulations have the advantage of being efficient since the inclusion of the third dimension costs additional computational time. However, the presence of the sidewalls cannot be neglected in the current study since the duct aspect ratio is unity. Grid 4 is used to generate the two-dimensional computational domain whereas the same grid structure is applied to the three-dimensional domain with the addition of the third dimension. Due to the symmetry of the duct, one quarter of the experimental geometry is simulated in the three-dimensional case with a grid composed of 28 millions of cells.

As visible from Figure 6.18 the location of the shock train in the 3D case occurs with an apparent thin boundary layer. In reality, compared to the 2D case, in 3D the shock train occurs upstream because of the effect of the boundary layer on the side walls and the corners. In the 2D case, the boundary layer develops only on the top and bottom walls of the test section, but in the 3D case the boundary layer on the side walls and the corners must be considered. Since the duct is of square cross-sectional area, the boundary layer on the side walls affects the flow in the same extent as the top and bottom walls. With the inclusion of the boundary layer from all the walls, the flow confinement reaches approximately the same value as in the 2D case. This demonstrates that the flow confinement plays the greatest role in determining the location of the initial shock, in agreement with the literature [54, 99].

Figure 6.19 illustrates the numerical schlieren and the Mach number contour at the duct centreline on different cross-sections that are reported in Figure 6.20. The location x_1 identifies the cross-section corresponding to the initial pressure rise and the subsequent planes are spaced of L/D_{eq}= 1 apart. The results show a boundary layer separation region at the corners that extends along the entire duct. The separated region tends to enlarge downstream of the leading shock, from x_1 to x_3, but gradually reduces from x_4. Additionally, from x_5 the flow structure shows little changes which mean that the last shocks are very weak and the shock train is terminated at approximately x_6. As previously mentioned, experimental studies have shown that the shock train changes its structure between symmetric and asymmetric while it oscillates in the axial direction. To replicate this asymmetry, the full cross-sectional area

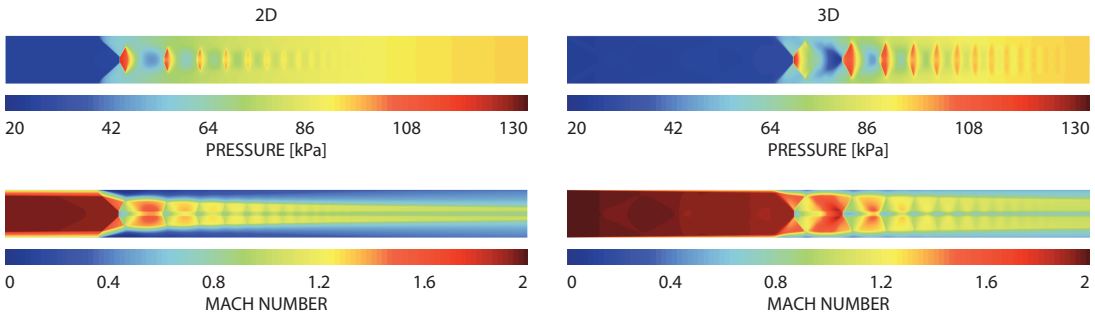

Figure 6.18: Pressure and Mach number contour in the 3D domain.

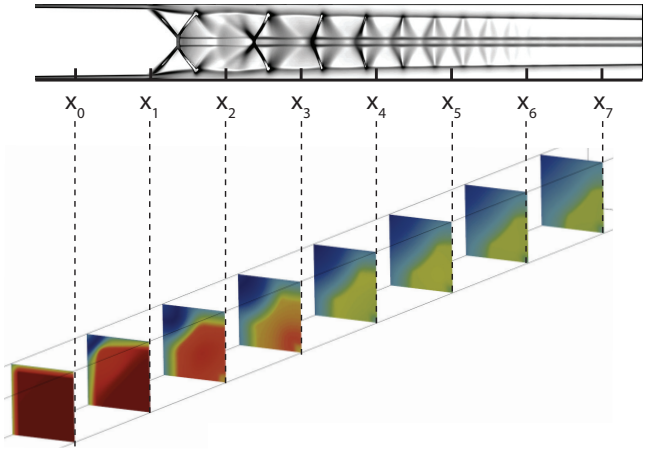

Figure 6.19: Numerical schlieren (top) and Mach number contour (bottom) at different axial locations.

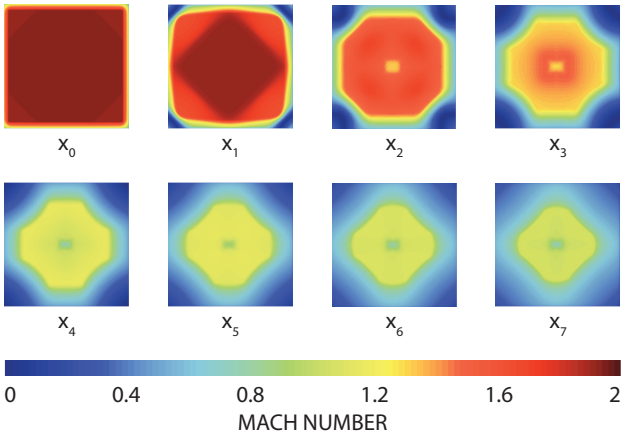

Figure 6.20: Mach number contour at different cross-sections.

should be used as a computational domain, as successfully obtained by Kawatsu et al. [92]. However, a common practice consists of using one quarter of the full geometry because of the reduced computational costs [100]. In this study the decision to use one quarter of the duct was dictated by the limits in computational resources.

Figure 6.21 compares the Mach number and pressure profiles obtained with the 2D and 3D simulations. The plots are shifted to a common origin beginning at the wall static pressure rise. The pressure profiles, in Figure 6.21(a), illustrates a small difference between the two cases. The wall static pressure in the 3D case does not monotonically grow as it occurs in the 2D case. The presence of a corrugated profile has been previously observed in three-dimensional simulations, and depends on the back pressure and the surface roughness [99, 122]. The centreline pressure shows that the shape of the shock train is similar in the two cases and, in particular, the first shock wave is captured with the same strength. On the other hand, the flow behind the first shock is decelerated more strongly in 3D, as the deeper trough illustrates. The reason of such a difference is due to the thinner boundary layer behind the leading shock which allows the flow to expand more in the subsonic region. This is believed

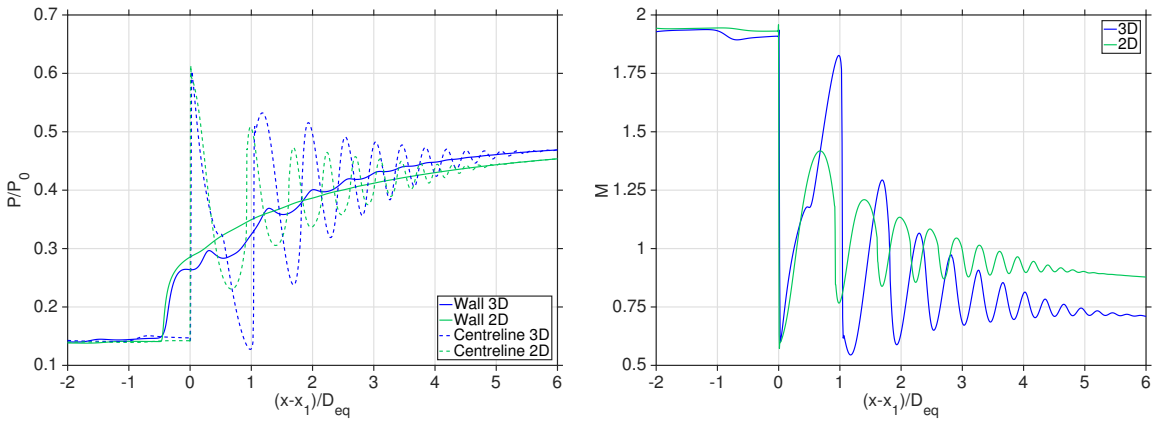

(a) (b)

Figure 6.21: Mach number and pressure distribution with 2D and 3D domain: a) Static pressure; b) Mach number.

to cause the non-perfect matching of the subsequent shock waves composing the shock train. As previously explained, the first shock is responsible for determining the shape of the entire shock train structure. The same trend is visible from the Mach number profile in Figure 6.21(b): since the flow conditions of the incoming flow ahead of the shock train are the same in both cases, the strength of the leading shock matches excellently. However, behind the leading shock the subsequent shocks differ. It emerges that with 3D simulation at the end of the shock train the flow is decelerated to a lower Mach number.

The lack of experimental data cannot confirm the real pressure and Mach number variation through the shock train. Therefore, taking into account the limitation, two-dimensional simulations are still useful for the qualitative understanding of the mechanism of formation of the shock train in long ducts. Furthermore, using a full computational domain would highlight the asymmetry of the flow field but it is not believed that this would cause a drastic change in the location and shape of the shock train.

6.1.7 Influence of back pressure

The shock train structure is sensitive to the back pressure [93, 94]. In this section, except for the back pressure, the same experimental configuration and flow conditions for a Mach 2 shock train described in Table 6.1 are investigated. The back pressure values of P_b= 96, 92, and 77 kPa tested by Sugiyama et al. [65] are replicated. The boundary layer thickness ahead of the shock train changes in the three cases, as reported in Table 6.5. A back pressure decrease corresponds to an increase of the boundary layer thickness and the separation at the wall tends to become larger. The authors estimated the boundary layer thickness with schlieren photography therefore the small difference between the reference data, in Table 6.5, and the computed results lays in the range of experimental uncertainty.

Case	$P_b[kPa]$	δ/h [65]	δ/h computed
A	96	0.15	0.17
B	92	0.25	0.26
C	77	0.35	0.36

Table 6.5: Flow confinement depending on the back pressure.

Figure 6.22 compares the experimental data of Sugiyama et al. [65] and numerical schlieren obtained with the current simulations. The shape of the shock train and the distance between the first and second shocks are correctly replicated in all the cases. The numerical distribution of pressure and Mach number are illustrated in Figure 6.23. All three simulations predict the entire shock train downstream compared to the experiment. The simulations in this section were performed with Grid 5 which is accurate enough for illustrating the relative differences in the three cases. Additionally, as Handa et al. [79] reported, the oscillations of the shock train in the experiment make it difficult to accurately compare the experimental and calculated Mach number contours.

As the pressure ratio between the two extremities of the duct increases, the pressure rise propagates upstream and the entire shock structure moves towards the inlet, in agreement with the numerical results obtained by Huang et al. [23]. This behaviour is similar to what happens in real supersonic air-breathing engines, since when the pressure ratio increases over a certain level, the shock wave structure is expelled outside the inlet [17]. It can be observed that, in case C in Figure 6.23, the shock train is not completely terminated at the outlet of the computational domain and the flow behind the last shock is supersonic. This is an important result to consider in the design of vehicles which require a subsonic flow for combustion.

As the back pressure, P_b, decreases, the first shock is weakened because of the viscous effects that decelerate the flow as it travels along the duct. In Figure 6.23(b), all the plots start at the same initial conditions, but with a lower value of the back pressure the flow passes across shock waves of weaker intensity. This is visible from the first trough and the first peak in the Mach number profile, and extends to the subsequent portion of the shock train. Moreover, case B appears to be composed of a larger number of shock waves in comparison with case A, but nothing can be said about case C. It can be supposed that the weaker intensity

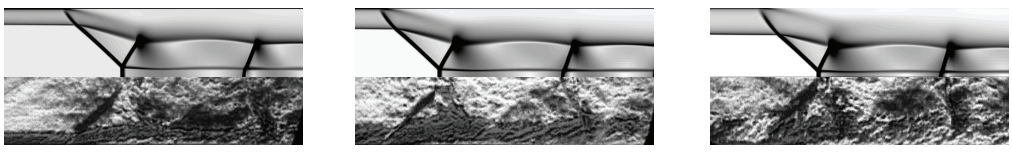

Figure 6.22: Numerical and experimental schlieren for different values of back pressure.

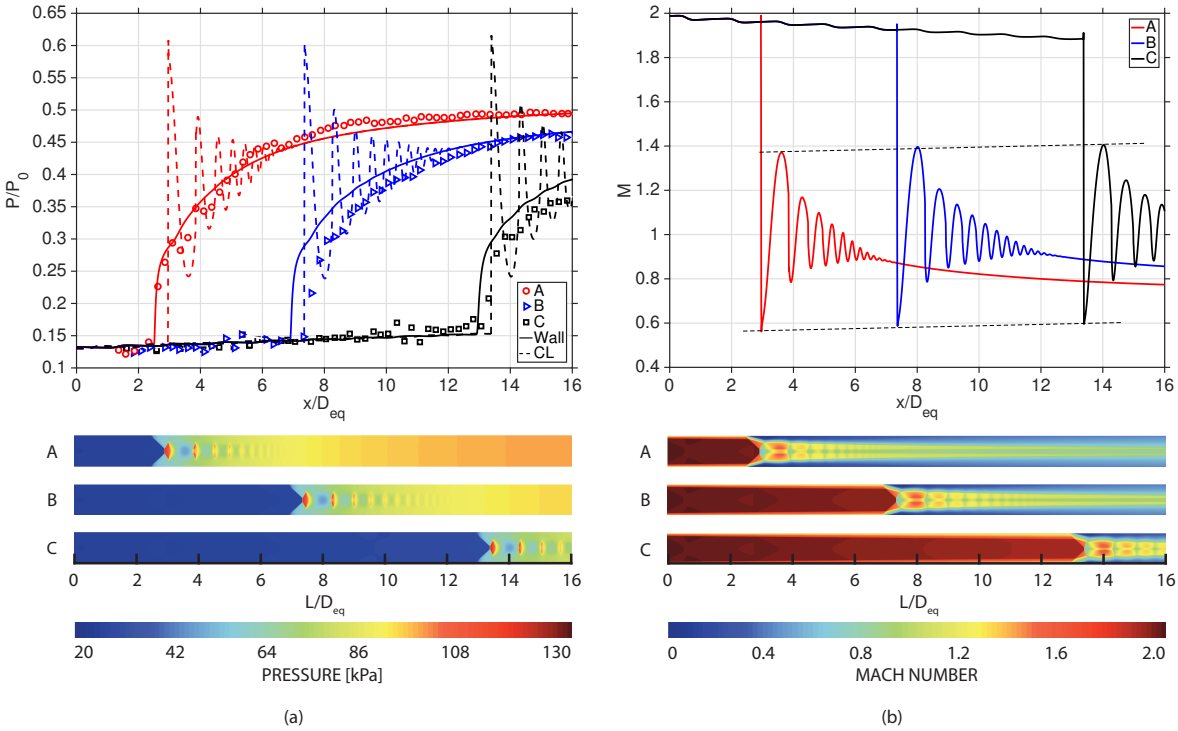

Figure 6.23: Computed flow properties profiles for different values of back pressure: a) Static pressure; b) Centreline Mach number.

of the shock waves in the shock train structure is compensated by a greater number of shocks.

In any case, the pressure rise through the shock train is always smaller than that through an inviscid normal shock. The three pressure profiles in Figure 6.23(a) reach 84%, 79%, and 67% of a normal shock wave respectively for case A, B, and C, in agreement with the general behaviour of the shock train. As a consequence, a pressure rise closer to a normal shock is more effective in decelerating the flow to subsonic speeds. As the back pressure increases the several shock waves in the shock train effectively reduce the flow speed to the subsonic range reducing the risk of having a supersonic flow in the combustion chamber.

6.1.8 Transient simulation: back pressure variation

In this section the effect of changing the back pressure is analysed with unsteady simulations by applying a function in time instead of a constant value. The steady state solution gives an averaged position of the shock train in the duct. However, in real air-breathing engines, the shock train behaviour is inherently unsteady and the entire structure is subject to fluctuations due to the longitudinal combustion instabilities [94, 325].

The pressure rise and the shock train propagation induced by unsteady combustion are reproduced by means of sinusoidal pressure oscillations at the exit plane with Equation 6.1,

$$P(t) = P^* \left[1 + \varepsilon \sin(\omega t)\right] \tag{6.1}$$

P^* is the value of the back pressure applied in the steady case and the oscillation amplitude coefficient, ε, is varied between 0.01 and 0.1. These values are used to model different flow conditions subject to back pressure changes in an air-breathing engine. In fact, if the back pressure is too large, the shock system is not able to compensate the pressure rise and propagates upstream until it is disgorged from the inlet.

6.1.8.1 Effect of time step

The suitable time step in unsteady simulations is related to the dimensions of the grid cells, therefore the optimum time step changes for grids of different resolution. Although Grid 2 provides a solution of limited accuracy, it requires a considerably smaller amount of computational resources compared to the finer grids. As previously discussed in Section 6.1.2, excluding the very coarse grid, no substantial differences are observed in the shape of the first shock wave. Since the strength of the first shock affects the entire shock train structure, the leading shock is used as a reference to detect the axial shock train movement in the duct and the change in magnitude during a period. Based on this observation, Grid 2 is considered suitable to perform the analysis of the shock train in the presence of a back pressure forcing.

Different time steps are set based on the characteristic time, T_c, defined as L/U_∞, where L is the length of the computational domain and U_∞ the freestream velocity. The time step size ΔT_1= 0.1 T_c is used as the baseline case and three further refinements were taken halving the previous time step, i.e. ΔT_2= 0.05 T_c, ΔT_3= 0.025 T_c, and ΔT_4= 0.0125 T_c. The temporal term has been discretised with a second-order accuracy interpolation scheme.

To investigate the effect of the time step on the numerical solution, in the baseline case the periodic wave is applied with an amplitude ε= 0.1 and frequency f= 2 Hz. An amplitude of approximately 10% of the steady value is representative of the variation in back pressure analysed in Section 6.1.7. The value of the frequency is chosen to replicate similar flow conditions that can be established in the current wind tunnel.

Figure 6.24 shows the time history of the movement of the leading shock in the axial direction. The axial position is normalised by its values at the rest point before any downstream pressure forcing is imposed. After the first cycle, the oscillatory motion is settled down and all remaining oscillations occur between the same minimum and maximum positions, x^- and x^+, respectively. The collapsed curve in Figure 6.25 is obtained from four consecutive oscillation periods and shows that the solution is independent of the time step.

During the cyclic motion, the shock train travels back and forth from its initial position, x^*. To an increase in the back pressure the shock train responds by moving upstream towards the inlet of the computational domain, whereas a decrease in the back pressure forces the shock train to move towards the outlet. The temporal evolution of the Mach number is illustrated in Figure 6.26 consistently to what already discussed in Section 6.1.7. With the

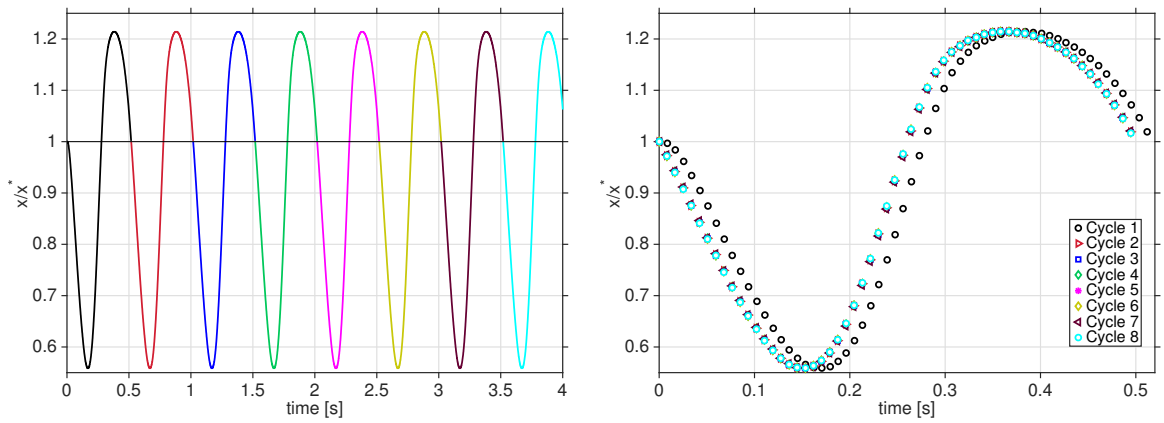

(a) (b)

Figure 6.24: Time history of the position of the leading shock in the axial direction with ΔT_2. a) Different forcing periods with time; b) Collapsed curve of different forcing periods.

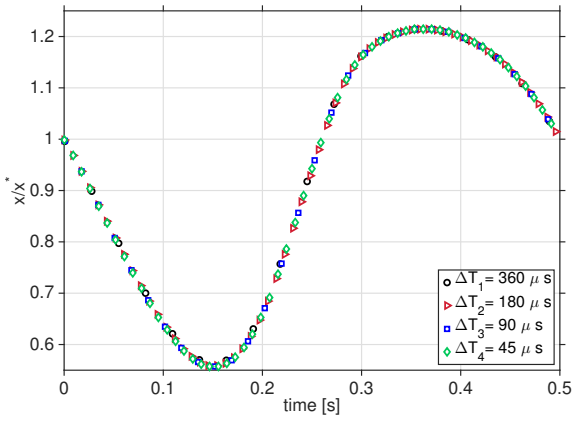

Figure 6.25: Collapsed curve of the normalized location of the leading shock in the axial direction with different time steps.

same inlet conditions, when the back pressure increases the shock train is subject to a larger pressure ratio between the two extremities of the duct. The higher back pressure pushes the shock train towards the inlet whereas when the back pressure is released, the shock train is subject to a lower back pressure and thus it establishes closer to the duct outlet.

Figure 6.27 shows that, although the forcing imposed at the exit plane is symmetrical, the motion of the shock train does not match the same trend of the back pressure. Firstly, the distance covered in the upstream portion of the cycle is double that covered in the downstream portion. This means that the shock train moves faster downstream than upstream since the time to move in both directions is the same. The response of the shock train when subject to a periodic back pressure variation shows the presence of non-linear phenomena, in agreement with previous numerical and experimental findings [93–95]. Secondly, the extremes of the shock train position, x^- and x^+, occur at different time instants compared with the corresponding extremes in the back pressure, P^+ and P^-, respectively. When the back

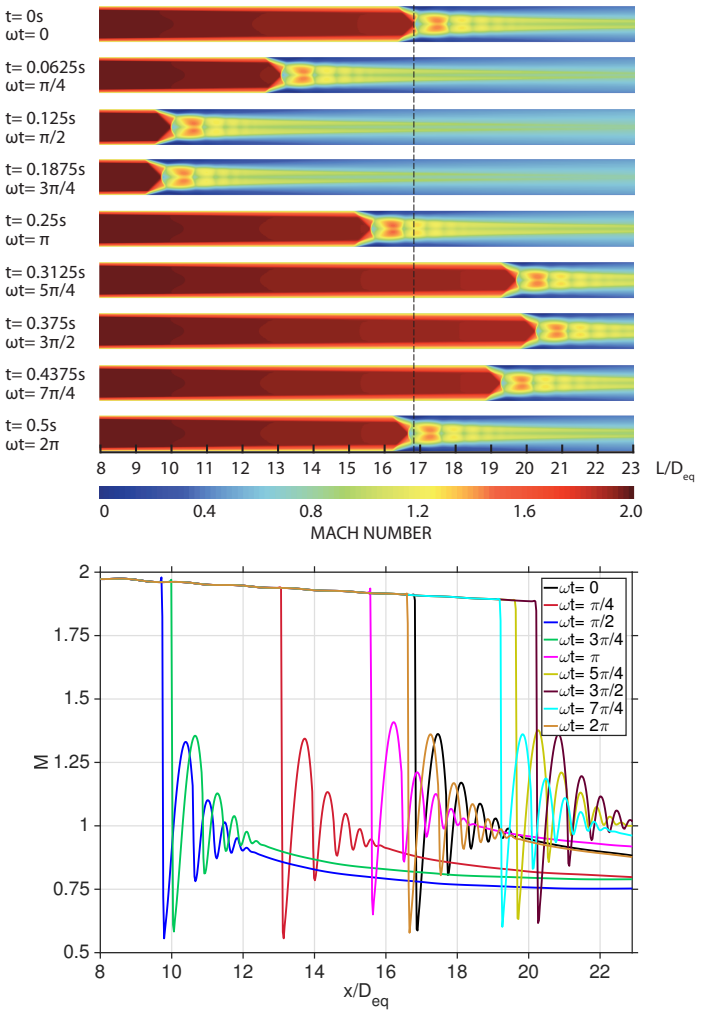

Figure 6.26: Temporal evolution of the computed contour (top) and centreline profile (bottom) of the Mach number with Grid 2 and time step ΔT_2.

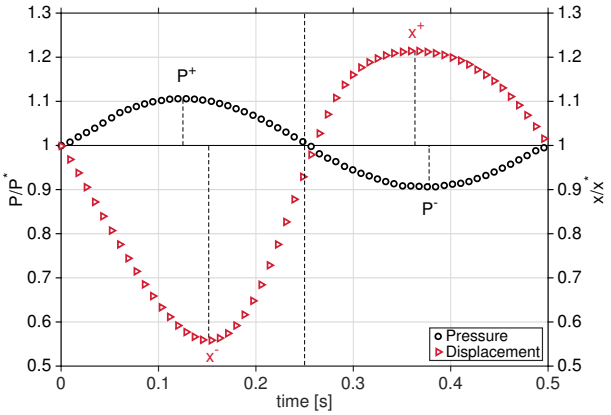

Figure 6.27: Plot of normalised forcing pressure and location variation of the leading shock.

pressure increases, the minimum shock train position occurs with a delay of approximately 26.5 ms after the maximum back pressure value. The delay of the minimum shock train

position, x^-, from the maximum back pressure value, P^+, shows that the flow responds to an external change with a time delay. More interestingly, x^+ is reached approximately 14.5 ms before the minimum back pressure value, due to the presence of a thicker boundary layer downstream that greatly influences the entire shock train when it travels towards the outlet.

Figure 6.28 shows the Mach number behind the leading shock for different cycles. The Mach number behind the first shock wave is characterised by a large oscillation due to the forcing and a small oscillation due to the unstable nature of the flow. With an increase in back pressure the shock train responds with a decrease in the flow speed behind the leading shock meaning that the first shock is stronger and the flow is more strongly decelerated. On the contrary, when the back pressure is decreased, the first shock becomes weaker and the flow speed behind the leading shock higher. It has been reported that, according to the acoustic theory and small-perturbation models, the velocity variation of the flow is of the same frequency but altered phase of the sinusoidal back pressure variation [93].

The hysteresis effect is considerably pronounced in Figure 6.28. In the first half of the cycle, when the back pressure is increased, the variation of the Mach number exhibits a smooth wave behaviour. At the time instant t= 0.25 s the Mach number reaches the maximum but

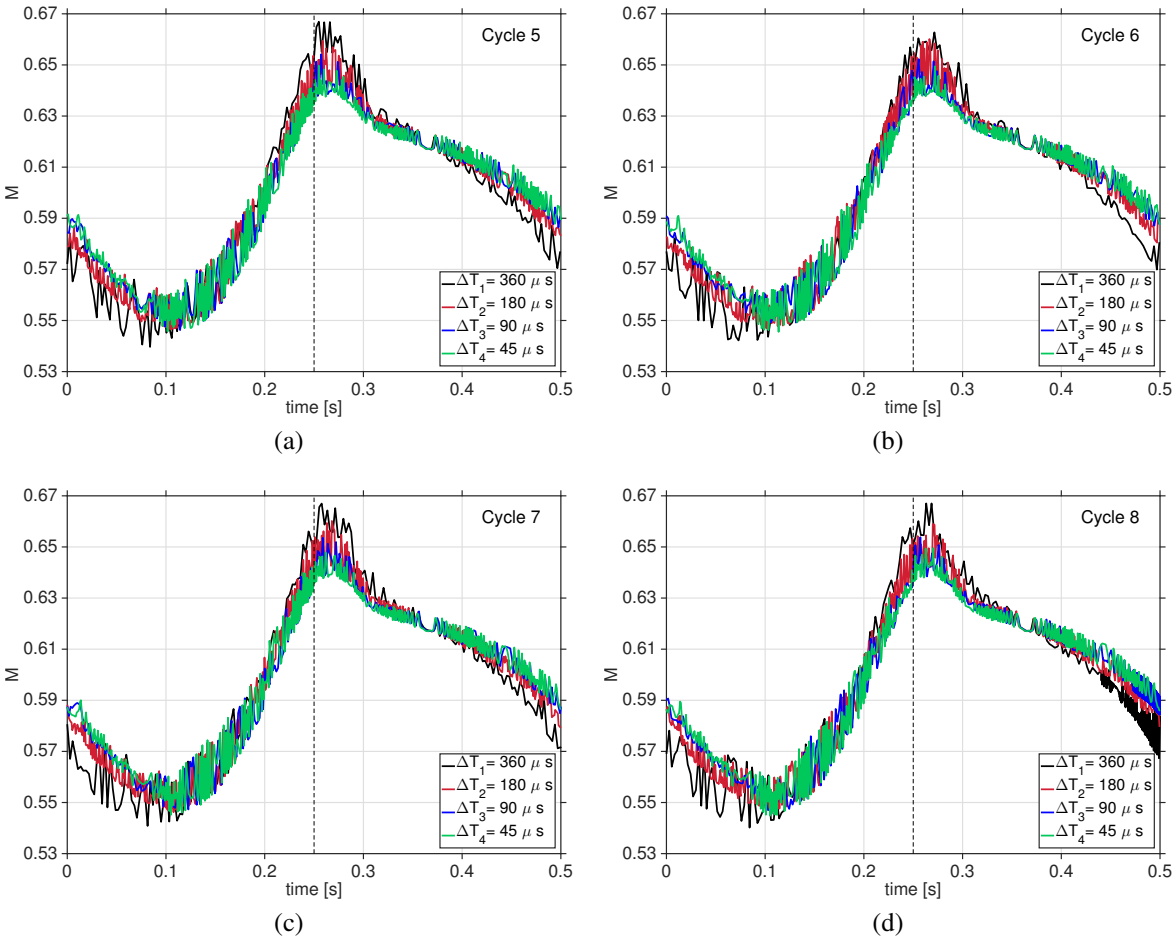

Figure 6.28: Time history of the Mach number behind the leading shock during different cycles.

the second half of the cycle is no longer characterised by a sinusoidal wave. Additionally, the plot obtained with ΔT_1 shows small differences compared with the ones with smaller time steps. Therefore, the time step ΔT_2 is used for the subsequent cases.

6.1.8.2 Effect of numerical grid on the time step

In unsteady simulations, the time step is strongly related to the dimensions of the grid cells since it is pertinent to truncation errors of the unsteady terms [326]. In this section the solutions using Grid 2, Grid 4, and Grid 6 are compared for each time step, i.e. ΔT_1, ΔT_2, and ΔT_3. Despite the effort to use non-dimensional parameters and to minimise the influence of the shock train location, differences between the various grids are expected because subtle flow structures are resolved only with a very fine grid (see Section 6.1.2).

Figure 6.29(a) shows that by increasing the grid size with the time step ΔT_1, the displacement of the leading shock from its initial position decreases considerably. Moreover, by using Grid 6 the position of the leading shock during a back pressure cycle does not reproduce the sinusoidal variation. On the other hand, by using a smaller time step, ΔT_2 in

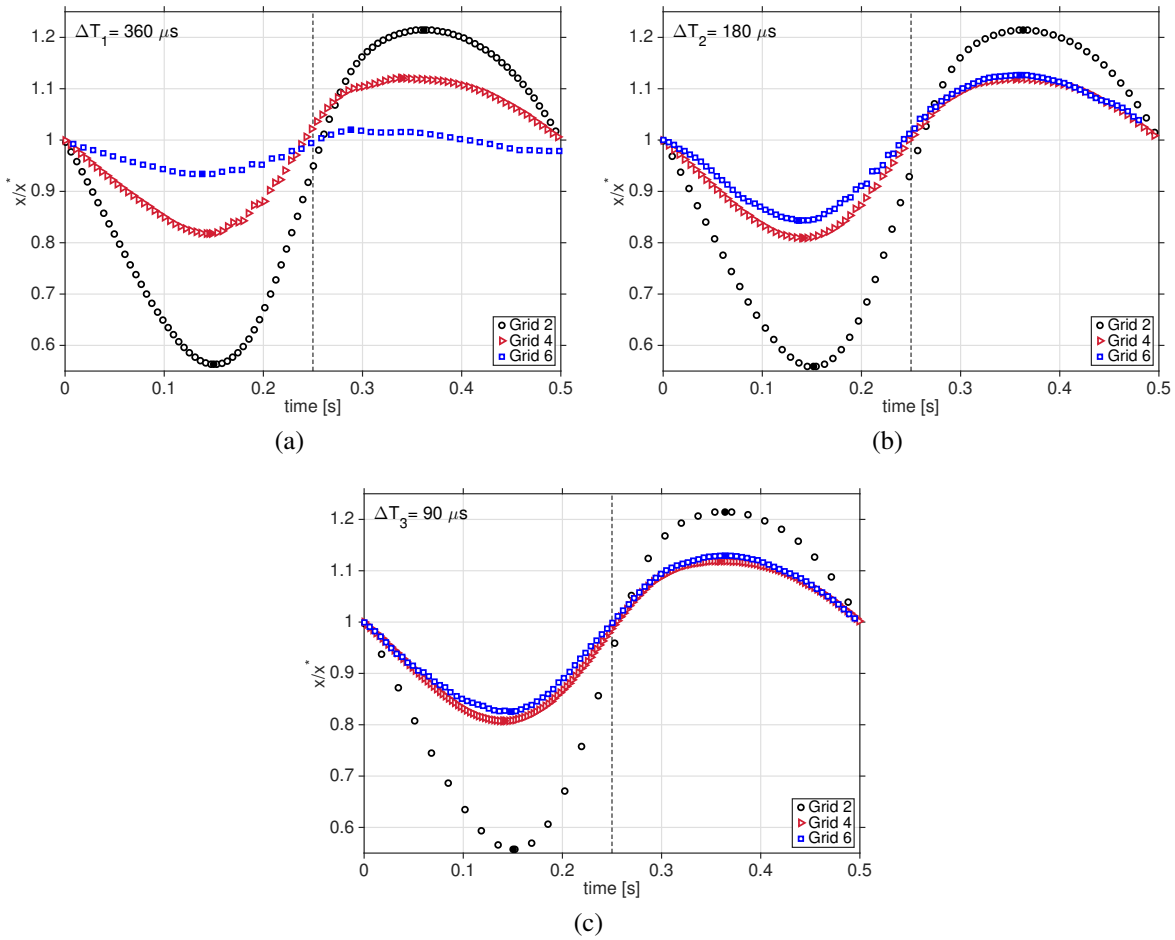

Figure 6.29: Position of the leading shock in the axial direction with different grid size and time step. a) ΔT_1; b) ΔT_2; c) ΔT_3.

Figure 6.29(b) and ΔT_3 in Figure 6.29(c), the solution increases in accuracy and the variation in the position of the first shock during a period exhibits a sinusoidal behaviour with all the grids. The difference in the displacement of the leading shock from its initial position obtained with Grid 4 and Grid 6 becomes gradually smaller. In particular, with ΔT_3, the solution obtained with Grid 4 and Grid 6 are overlapping. Small discrepancies arise from the dependence of the solution on the grid size. The reason of the remarkable divergence of the oscillation obtained with Grid 2 is caused by the large variations in the outlet velocity profile and boundary layer thickness that are not accurately resolved with a coarse grid. As the number of cells becomes larger, the flow field is replicated at a more detailed level. As a consequence, the dimension of the grid confirms to be strongly related to the time step. The time step ΔT_1 is not adequate to resolve the flow with fine grids which require a smaller time step. For Grid 4 the time step ΔT_2 is adequate but Grid 6 requires ΔT_3 or a finer time step.

In conclusions, from all the grids employed it emerges that the furthest upstream and downstream axial position reached by the shock train in the duct are different. The response of the shock train to an increase in the back pressure always leads to a movement upstream towards the inlet of greater magnitude compared to the movement towards the outlet caused by a decrease in the back pressure. The influence of a pressure increase compared to a pressure drop does not depend on neither the grid size nor the time step. Based on this finding Grid 2 is chosen to analyse the effect of different conditions due to changes in the back pressure. As previously explained, the accuracy of the solution obtained with Grid 2 is limited but adequate to identify the essential features of the shock train response to an external forcing requiring lower computational resources compared to the finer grids.

6.1.8.3 Variation of back pressure

The asymmetric response of the leading shock position in the axial direction is investigated further in this section. The forcing pressure wave was applied either with an initial pressure increase, $P(+)$, or a pressure decrease, $P(-)$. In Figure 6.30, $P(-)$ has been reversed in order to make the two plots comparable.

Whether the pressure is first increased or decreased the time history of the shock train position exhibits the same trend. Since the forcing has the same amplitude, the leading shock reaches the same minimum and maximum positions but the two paths do not completely overlap, as Figure 6.30(a) illustrates. On the other hand, the Mach number in Figure 6.30(b) shows that the strength of the leading shock varies with the same trend. This confirms that non-linear phenomena due to the interactions between the shock waves with the boundary layer are present and play a key role in determining the time history of the shock train position along the duct. These effects, however, do not affect the change in the speed, consistently with the fact the velocity, and hence the Mach number, varies in the same way as the pressure, but with altered phase angle.

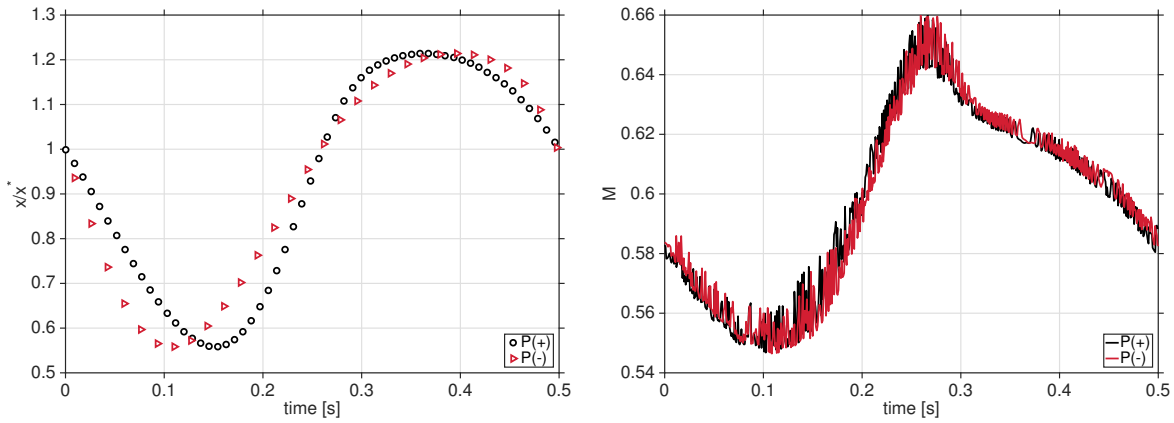

(a) (b)

Figure 6.30: a) Position of the leading shock in the axial direction; b) Mach number behind the leading shock in the shock train.

6.1.8.4 Forcing oscillation amplitude

The engine of a high-speed air-breathing vehicle requires different combustion conditions during the various phases of the flight envelope. As a consequence, the flow structures which form at the inlet and inside the isolator are subject to transient conditions. The disturbances induced by changes in the combustion develop an oscillatory behaviour of the flow. Large oscillation amplitudes may cause the shock train to be expelled out of the inlet. Small oscillations of the order of a few percent of the mean pressure value characterise the dynamics of the combustion process in the engine.

In Figure 6.31 the effect of the oscillation amplitude with ε= 0.01, 0.05, and 0.1 are presented. When an oscillation amplitude of ε= 0.2 was applied, the shock train was disgorged out of the inlet. As the oscillation amplitude increases the difference between the

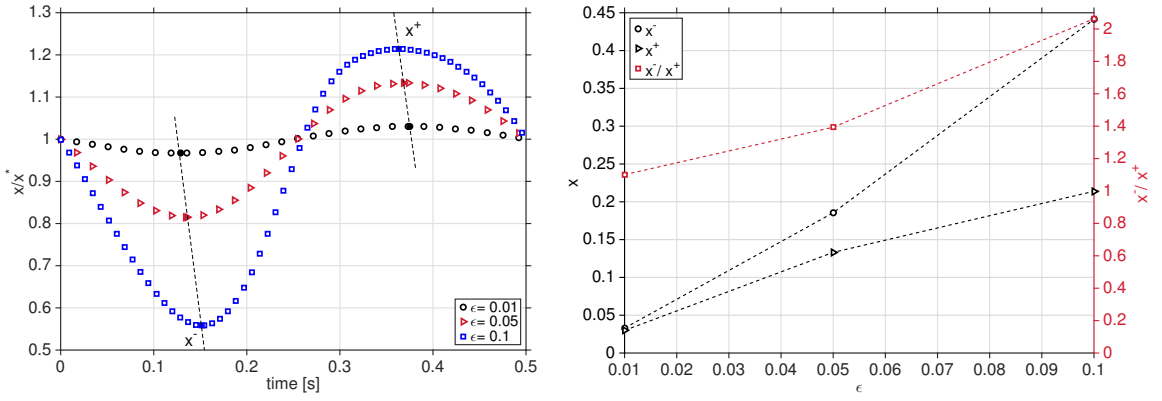

(a) (b)

Figure 6.31: a) Position of the leading shock in the axial direction; b) Variation of the position extremes in function of the oscillation amplitude.

maximum and minimum positions of the leading shock in the axial direction becomes more pronounced, in agreement with previous numerical studies [94]. Figure 6.31(b) shows that with a small oscillation amplitude, the ratio of the minimum to the maximum displacement, x^-/x^+, is approximately unity. Increasing ε, the displacement of the minimum and maximum from the mean position, x^- and x^+, proportionally increases. With ε= 0.1 the ratio of the minimum to the maximum displacement, x^-/x^+, reaches the value of approximately 2.

Figure 6.31(a) illustrates that, for each ε, x^- and x^+ are located along lines with negative slope. As ε increases, x^- is gradually delayed whereas x^+ occurs earlier in time. This means that, compared to a small oscillation amplitude, with a large oscillation amplitude, the shock train covers a wider distance of the duct but takes more time to reach the furthest upstream axial position. After t= 0.25 s, when the back pressure is decreased, the shock train reaches the furthest downstream axial position earlier with increasing value of ε. This can be explained from the time history of the Mach number of the leading shock wave, in Figure 6.32. With a small value of ε, the leading shock responds with a small change in magnitude which is comparable to the oscillation inherent of the shock train unsteadiness. After the first quarter of the cycle, the back pressure starts to decrease from its maximum

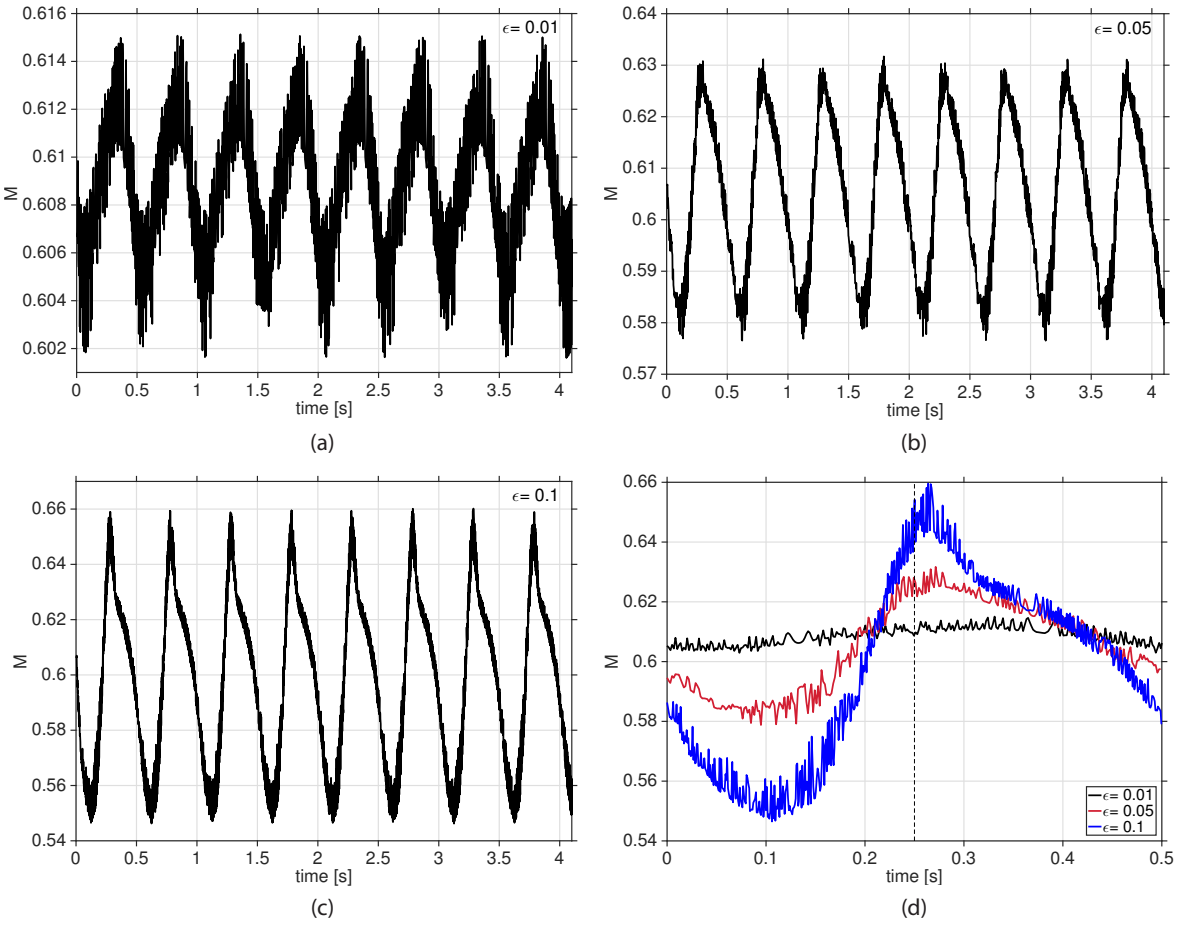

Figure 6.32: Mach number behind the leading shock for different forcing amplitudes.

value with a gradient in the Mach number that is higher for larger oscillation amplitudes, so that the shock train is subject to a greater acceleration. With a small oscillation amplitude the leading shock Mach number exhibits a less pronounced maximum value, and the time history of the response resembles more a sinusoidal wave.

Finally, all curves in Figure 6.32(d) return to the mean value at the time instants of approximately t= 0.21 s and t= 0.42 s, which are considerably later than the maximum and minimum of the back pressure cycle.

6.1.8.5 Effect of forcing frequency

Figure 6.33 shows the effect of different forcing frequencies with the same oscillation amplitude. The x-axis is normalised to the period of the forcing wave. As Figure 6.33(a) illustrates, a decrease in the forcing frequency leads to a larger difference between x^- and x^+, in agreement with what has been observed by previous studies [95, 327]. In the first half of the cycle, the minimum and maximum Mach number of the leading shock, M^- and M^+ in Figure 6.33(b), act in the opposite way compared to x^- and x^+. As the forcing frequency increases, x^- tends to be delayed whereas M^- occurs earlier in time compared to low forcing frequencies. While for f= 2 Hz the minimum Mach number, M^-, occurs at approximately 1/4 of the x-axis, for f= 20 Hz the minimum Mach number is close to the mean value at the beginning of the period. Different behaviour is exhibited in the second part of the pressure cycle. Compared to low forcing frequencies, both x^+ and M^+ occur with an increasing time delay as the oscillating frequency assumes larger values. After the first half of the pressure cycle the shock train position does not recover to its initial value. Indeed, the shock train returns to its initial position with a greater delay as the forcing frequency increases.

It in interesting to note that the variation in the forcing frequency affects also the mag-

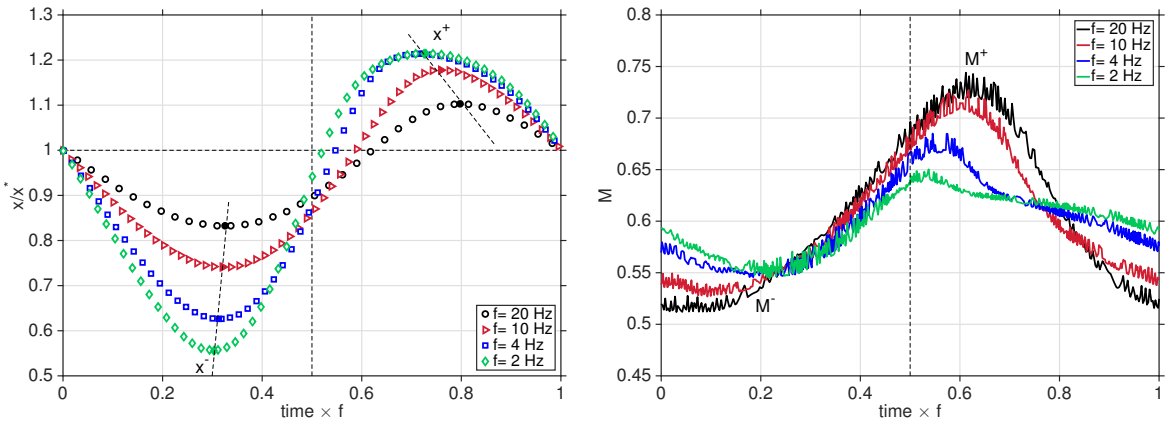

Figure 6.33: a) Position of the leading shock in the axial direction; b) Mach number behind the leading shock in the shock train.

nitude of the leading shock, in Figure 6.33(b). It is observed that for small frequencies the extremities of the Mach number profile are closer to the mean position. Additionally, the mean value itself changes, decreasing with higher frequencies. This may be caused by the establishment of additional mechanisms in the flow once a certain frequency in reached.

Therefore, high forcing frequencies reduce the axial movement of the leading shock but increase the range of Mach number values during a period. The interaction between the shock waves with the viscous effects introduce in the flow additional mechanisms that seem to be accentuated with higher frequencies in the oscillation of the back pressure. This is believed to be the reason of the change of the time instant when the leading shock returns to the initial location. Figure 6.34 summarises the effect of the oscillation frequency and amplitude on the position of the leading shock. The non-linear phenomena are exhibited in the asymmetrical variation of the position of the leading shock with different oscillation frequency.

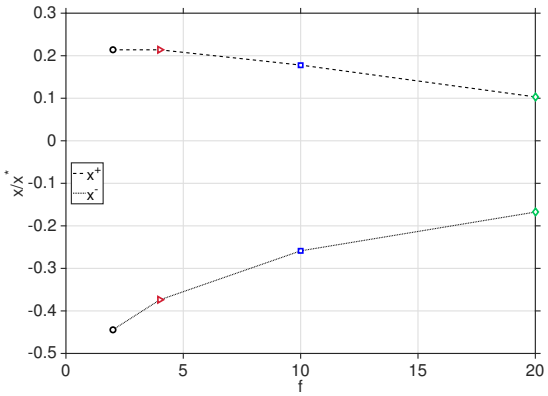

Figure 6.34: Effect of the oscillation frequency and amplitude on the position of the leading shock.

6.1.8.6 Step function of back pressure

To investigate further the response of the shock train to a pressure change, sudden pressure variations are applied with a step function with a step time of $1s$. This time is sufficient to allow the shock train to recover from the steep change in the back pressure. The flow conditions are the same described in Table 6.1 except for the back pressure. An initial value of P^*= 90 kPa is used.

Figure 6.35 illustrates the time history of the back pressure forcing and the position of the leading shock in the axial direction normalised to the corresponding initial values. Referring to Figure 6.35(a), the initial back pressure was increased with a step ΔP_1= ΔP_2= 5 kPa. The back pressure was then dropped with a step ΔP_3= 20 kPa and then raised again of ΔP_4= 20 kPa. In this way the maximum and minimum values of the back pressure, P^+ and P^-, are $\pm$10 kPa. The normalised displacement of the leading shock wave is shown in Figure 6.35(b). It emerges that although ΔP_1 is equal to ΔP_2, the displacement of the shock

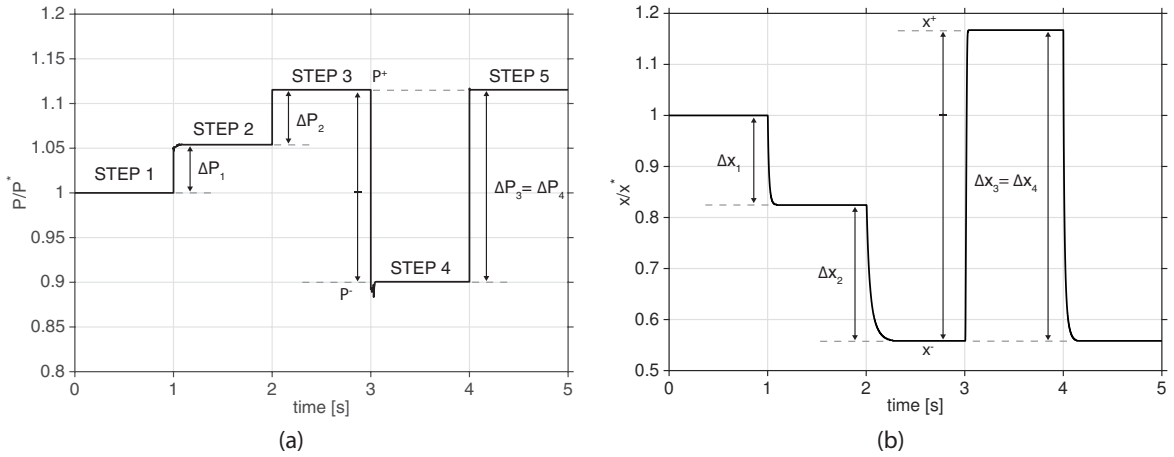

Figure 6.35: a) Time history of the back pressure forcing with a step function; b) Position of the leading shock in the axial direction.

train Δx_2 is greater than Δx_1. Similar to what was observed with a sinusoidal back pressure forcing, an increase of pressure affects the shock train in a more accentuated manner than a pressure decrease. The maximum and minimum displacement to the initial location, x^+ and x^-, are different. The minimum displacement, x^- is considerably larger. In this case there are no hysteresis effects since the flow is completely settled before the next step time. The greater the value of P^+, the further the shock train is moved upstream in the duct.

Figure 6.36 illustrates that at the beginning of each step time the Mach number is subject to a steep change before settling down. Additionally, with a pressure rise the Mach number behind the leading shock exhibits a sudden but small drop. On the contrary, a pressure drop more strongly influences the shock train. Although the pressure drop ΔP_3 and the pressure rise ΔP_4 are of the same absolute value, the Mach number behind the leading shock shows a larger steep change when subject to a pressure drop. This confirms the previous findings that shock waves/boundary layer interactions lead to a different response of the shock train to a variation of the back pressure.

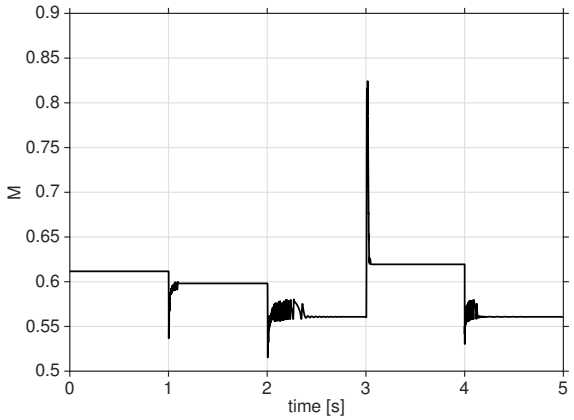

Figure 6.36: Mach number behind the leading shock in the shock train with a back pressure variation with a step function.

6.1.9 Effect of back pressure with Mach 4 flow

The effect of the back pressure is investigated with two-dimensional RANS equations and an inlet Mach number of 4. The flow conditions are reported in Table 6.6 and the schlieren pictures are shown in Figure 6.37. It can be observed that in this case the first shock is present in the χ shape and the shock train is asymmetric in all cases. Several studies reported that the shock train is characterised by an inherent asymmetric structure, as already discussed in Chapter 2. Numerical simulations are not capable of replicating the asymmetric behaviour, even with unsteady Navier-Stokes equations [52, 92]. Sridhar et al. [100] numerically matched the experimental data in terms of pressure profile and the position of the leading shock. The small differences due to the imposition of uniform boundary conditions were negligible. In a similar way the simulations presented in this section have been performed on half of the duct height and consequently the flow is symmetric.

The comparison of the experimental schlieren photography obtained by Sugiyama et al. [65] is illustrated in Figure 6.38. Only cases B and C have been reproduced since the exact boundary layer thickness that develops ahead of the shock train in case A was not replicable. Although the back pressure of case A is only 2 kPa greater than that of case B there is a substantial difference in the experimental boundary layer thickness. In numerical simulations such a small difference in back pressure is not sufficient to generate the flow conditions experimentally tested in case A. In fact, increasing the back pressure from 37 kPa to 39 kPa, the movement of the shock train towards the inlet and the reduction of the boundary layer thickness ahead of the leading shock are difficult to be perceived.

It is interesting to note that, in Figure 6.38, the intersection point of the χ shape in the leading shock of the shock train is not in the centre of the duct but it can be in the upper or

Case	$P_b[kPa]$	δ/h [65]	δ/h **computed**
A	39	0.28	-
B	37	0.39	0.33
C	22	0.47	0.40

Table 6.6: Flow confinement depending on the back pressure with a Mach 4 shock train.

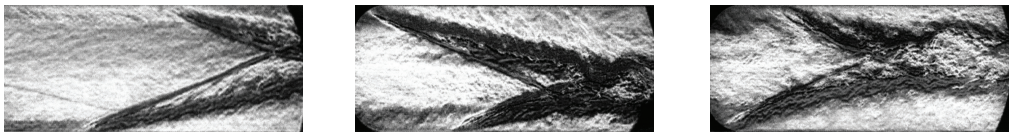

A B C

Figure 6.37: Experimental schlieren for different back pressure values with a Mach 4 shock train [65].

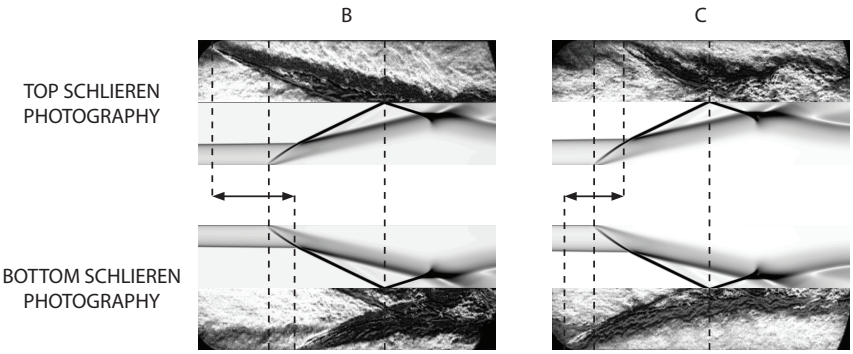

Figure 6.38: Numerical and experimental schlieren of the Mach 4 shock train for different values of back pressure.

lower half. This results in an asymmetrical configuration with the two oblique portions of the leading shock of different length. In case B, the oblique shock in the upper half of the duct is longer than the oblique shock in the lower half. The opposite occurs in case C. However, in both cases, the numerical schlieren resolves the first shock with the oblique portion of a length between the longer and the shorter observed in experiments.

Results of the numerical simulation of pressure and Mach number are illustrated in Figure 6.39. As Sugiyama et al. [65] reported, the location of the shock train did not stay at a specific location during the experiment but moved upstream with time, and therefore the wall pressure data were time-averaged. Compared to Mach 2, the pressure at the wall in a Mach 4 flow increases more linearly. The flow passing through the first shock is decelerated

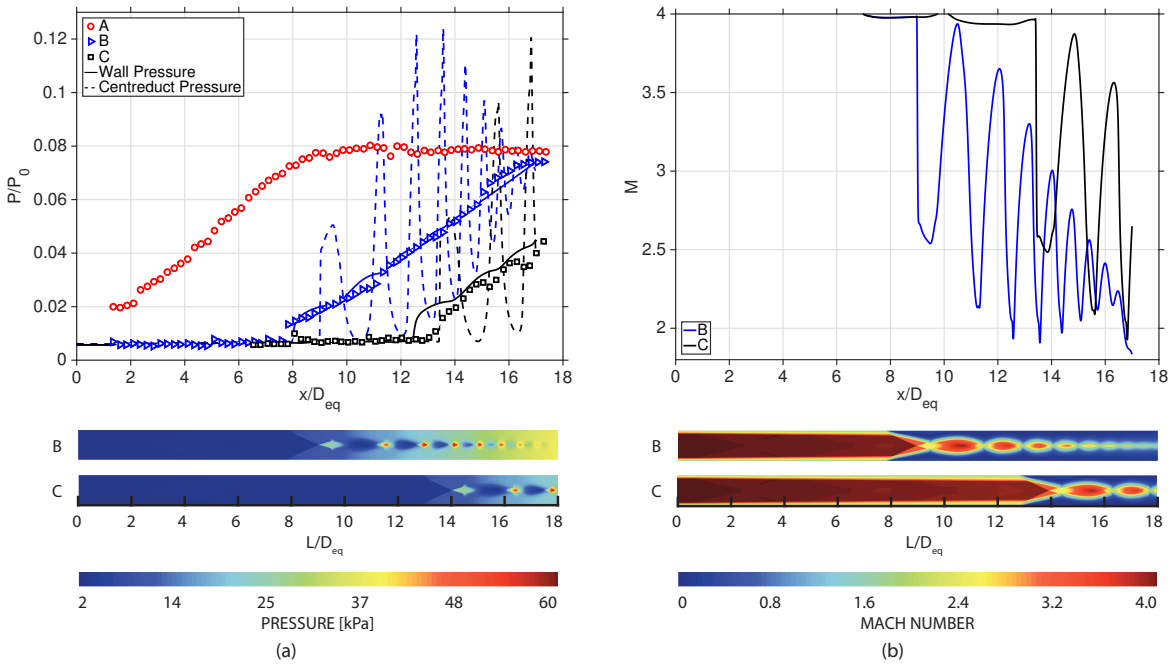

Figure 6.39: Computed flow properties profiles with a Mach 4 shock train for different values of back pressure: a) Static pressure; b) Centreline Mach number.

but stays supersonic at the centreline, as Figure 6.39(b) illustrates. The drops and increases identify the shocks composing the shock train that gradually decelerate the flow, which remain supersonic at the end of the structure. To conclude, for a Mach 4 flow that enters the isolator the aircraft must be able to sustain a supersonic combustion as it occurs in scramjets.

6.2 Validation case 2

For the validation of the numerical code the test case described by Carroll et al. [328–330] was also chosen for comparison. The flow conditions are detailed in Table 6.7 and the schematic of the two-dimensional supersonic wind tunnel is shown in Figure 6.40.

The experimental duct was initially designed with a constant cross-section but the flow visualisation detected an oscillatory movement of the shock train location with an amplitude of the order of the boundary layer thickness [331]. In order to remove these oscillations, the test section was modified by providing a zero pressure gradient in the test section for a fully started wind tunnel. A diverging angle of 0.13 degrees on the upper and lower walls was applied from the nozzle exit. The numerical computation of a shock train in a slightly divergent duct is easier compared to a duct with constant cross-sectional area because such a geometry plays an efficient role in the stabilisation of the shock system. The difficulty in a constant area duct is due to the fact that the only thing that maintains the shock train at a fixed position is the deformation of the boundary layer as a consequence of the interactions with the shock wave.

M	$T_0[K]$	$P_0[kPa]$	$P[kPa]$	$P_b[kPa]$	$H\,[mm]$	$W\,[mm]$	$L\,[mm]$	$Re\,[m]$	δ/h
1.61	295	206	51.11	107	32.06	76.20	753.80	3×10^7	0.32

Table 6.7: Boundary and geometry conditions of the computational domain of the validation model [68]. The subscript 0 refers to the total condition and P_b is the back pressure.

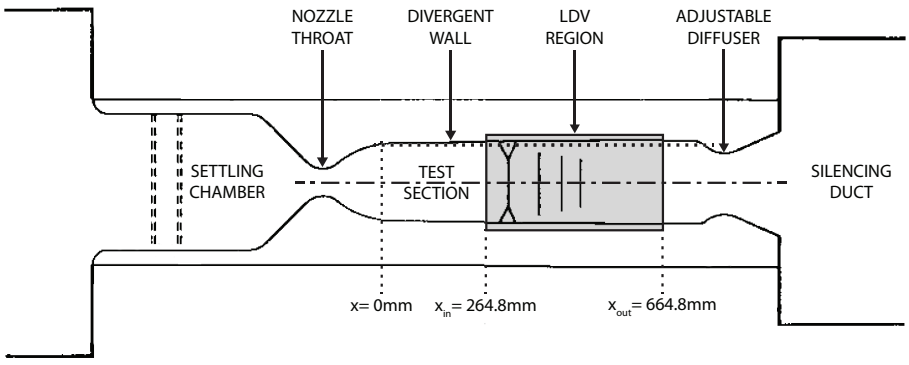

Figure 6.40: Schematic of the experimental facility used by Carroll et al. [328].

The structures of the shock train are illustrated by means of schlieren photography in Figure 6.41 together with the Mach number contour. The Mach number was computed from the Laser Doppler Velocimetry (LDV) measurement of velocity with the assumption of constant stagnation temperature along the centreline of the adiabatic flow whereas the static temperature distribution in the boundary layer was obtained using an appropriate recovery factor [329]. As stated by Carroll & Dutton [329] the complexity of the LDV measurements and data reduction prevented an accurate estimation of the experimental errors. The combined effect of several mutually interacting error sources from the experimental rig and the data acquisition system has to be considered in a critical manner when numerical results are discussed. Figure 6.41 shows a discrepancy between the two methodologies employed. The density changes in the schlieren photograph detect five shock waves that compose the shock train with axial location indicated by x_n. On the contrary, the LDV Mach number contour only captures the first two shocks. For this reason only the quantitative data about the first two shock waves are considered to be reliable.

The experimental data of Carroll et al. [329] are shown in Figure 6.42 along with the nu-

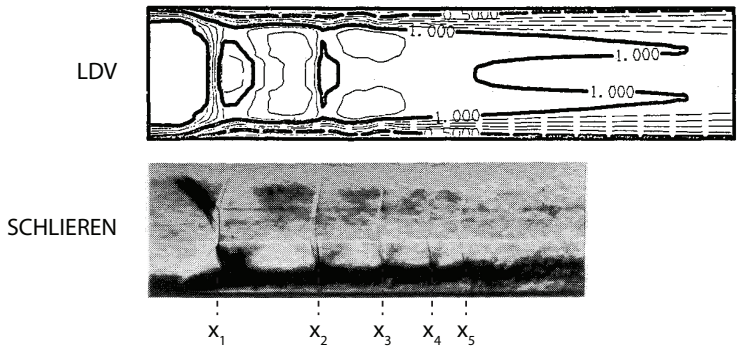

Figure 6.41: Mach number contour computed from LDV (top) and schlieren photography (bottom) by Carroll et al. [329].

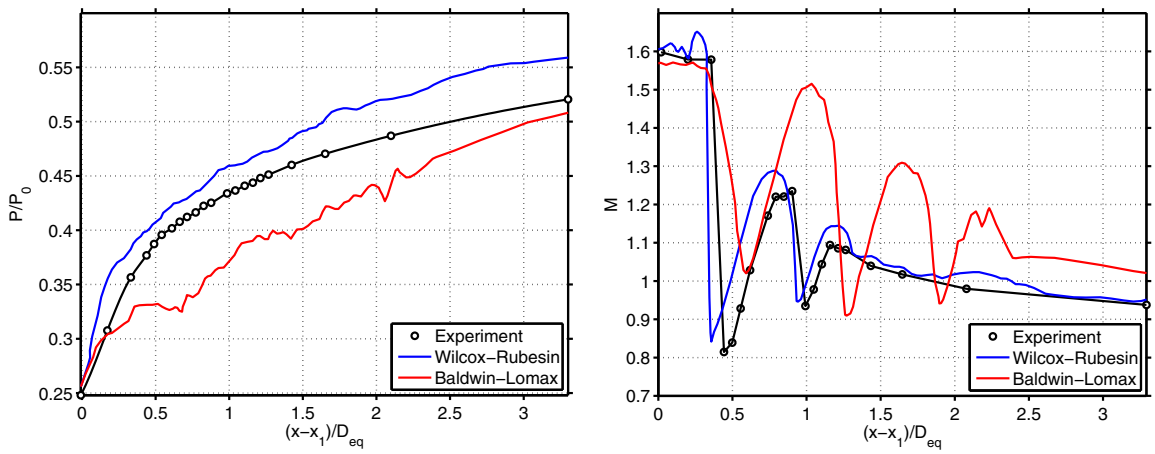

Figure 6.42: Flow properties distribution shifted for common pressure rise and normalised to the equivalent diameter [68]. a) Wall static pressure; b) Centreline Mach number.

merical wall pressure and Mach number distributions computed from same authors [68]. The static pressure was measured along the centreline of the upper and lower test section walls by means of pressure taps. The numerical results were obtained with the RANS equations and compare the Baldwin-Lomax with the k-ω Wilcox-Rubesin turbulence model. Both turbulence models barely capture the general features of the shock train and fail to provide accurate quantitative data. The Baldwin-Lomax model underpredicts the pressure distribution at the wall and captures more shock waves in the shock train with larger spacing between the shocks. The Mach number remains above unity after the first shock and at the end of the shock train the flow is still supersonic. The Wilcox-Rubesin model shows a more rapid pressure rise and the pressure at the exit plane does not match the experimental value. The reason for this is that the pressure was risen above the value experimentally observed in order to stabilise the shock train in the duct. Additionally, although the flow structures remained the same as the grid was refined, a complete grid independent result was not achieved. While a refinement in the streamwise direction had little influence, in the transverse direction a greater number of cells causes the shock train to move towards the exit plane [68].

The reason for such a substantial discrepancy was ascribed to the effect of the sidewall boundary layer. Compared to the square duct used in Section 6.1, in this case the experiments were run in a duct with an aspect ratio of 2.4. The authors considered the central part of the duct two-dimensional but the effect of the fairly thick boundary layer that develops on the walls cannot be neglected. Morgan et al. [54] more recently attempted to apply three-dimensional LES to the experimental configuration of Carroll et al. [328–330] described above. As Figure 6.43 illustrates the shock train is captured with greater accuracy in terms of number of shock waves. On the other hand, the location of the shock train in the duct was not correctly predicted with any of the grids tested, as it emerges from Figures 6.43(a) and 6.43(c). This because they did not accurately replicate the same problem. The wall divergence angle was neglected thus a rectangular test section of constant cross-sectional area was used and the Reynolds number was one order of magnitude lower than the experiment.

6.2.1 Description of numerical setup

For this test case a rectangular block and a divergent duct of length L= 753.80 mm are used as computational domains. The two geometries are built with the same grid resolution and the different number of cells is due to the slight change in the two configurations. Only half of the flow field is modelled with symmetry at the centreline of the duct.

Two-dimensional RANS equations are solved with the k-ω Wilcox model. The same type of boundary conditions described in Section 6.3.1.1 are used with values changed accordingly to this specific problem. The length of the duct is representative of the experimental duct extension and guarantees the development of the boundary layer. To match the experi-

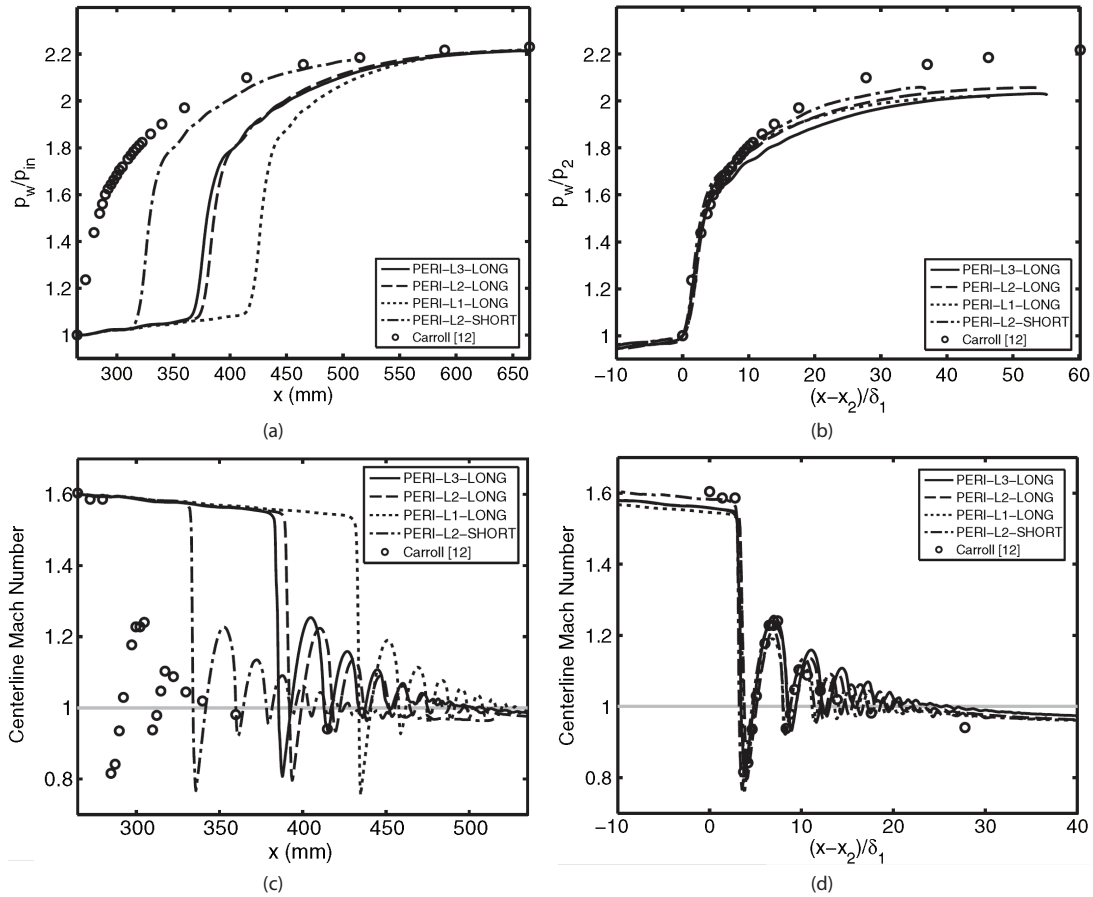

Figure 6.43: Wall static pressure and centreline Mach number distribution normalised to the flow confinement ratio [54]. a)-c) Physical streamwise coordinates; b)-d) Coordinates shifted by location of initial shock.

mental inflow Mach number of 1.61 just upstream of the shock train, a higher computational Mach number is imposed at the inlet. Since the experimental duct starts diverging at the end of the nozzle, the nozzle exit Mach number of 1.63 is used to calculate the flow properties in the case of diverging duct [329]. For the constant area case, a higher inlet Mach number is required and a value of 1.75 was used. In both cases the undisturbed confinement level ahead of the shock train, δ/h, is approximately 0.32. The back pressure, determined from the experimental results, was assumed constant at the exit plane with a value of P_b= 107 kPa.

6.2.2 Effect of grid resolution

Grid sensitivity is carried out on the divergent duct and Table 6.8 summarises the details of the various grids used. As previously observed by Carroll et al. [68], due to the high dependence of the solution on the grid resolution, a refinement in the transverse direction has the effect to move the shock train towards the exit plane.

The computed flow obtained with Grid 3, in Figure 6.44, illustrates the excellent agree-

Grid	N_x	N_y	Size	y^+
1	3016	116	0.32×10^6	0.13–2.9
2	3770	155	1.09×10^6	0.014–0.83
3	8376	255	3.24×10^6	0.008–0.54

Table 6.8: Number of cells in different grids.

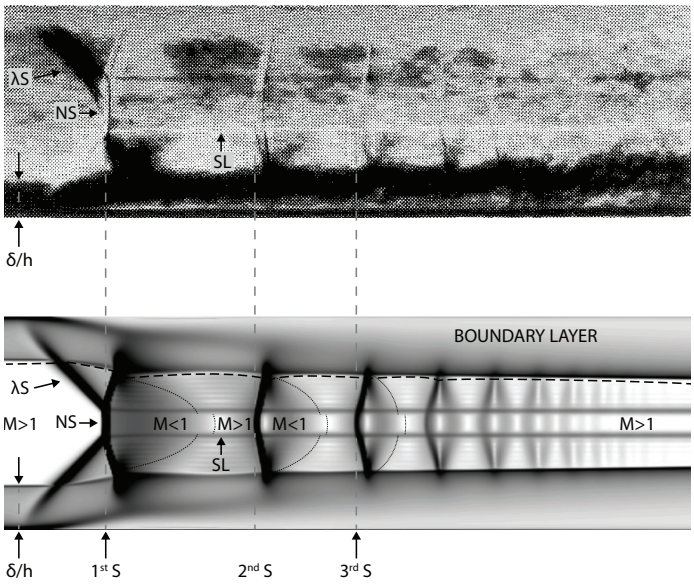

Figure 6.44: Comparison of the shock train: experimental schlieren photography by Carroll et al. [329] and numerical density gradient magnitude obtained with the current numerical approach with Grid 3.

ment with experiment in the shape and spacing between subsequent shocks in the shock train relative to the initial shock. Despite the limited resolution of the schlieren photograph, all the main shock train features are visible and are similar to that described in Section 6.1.2. The shock train is composed of several shocks which are captured by the numerical simulation. The first shock wave, $1^{st}S$, is normal at the centre of the duct and indicated as NS which, due to the thickening of the boundary layer, bifurcates into a λ shock structure, λS. The slip lines, SL, generated at the bifurcation point of the first shock and extended through the entire shock train, is barely visible in the schlieren image, but it is well-defined in the computation. In proximity of the centreline, in the region confined between the slip lines, the flow is subject to a series of normal shock waves. The flow is decelerated to subsonic speeds behind the first shock and then, due to the thickening of the boundary layer, accelerates again to supersonic speeds forming a second shock wave. This process occurs several times leading to the structure made of a series of shock waves.

Figure 6.45 illustrates the computed pressure and Mach number profiles for different grid

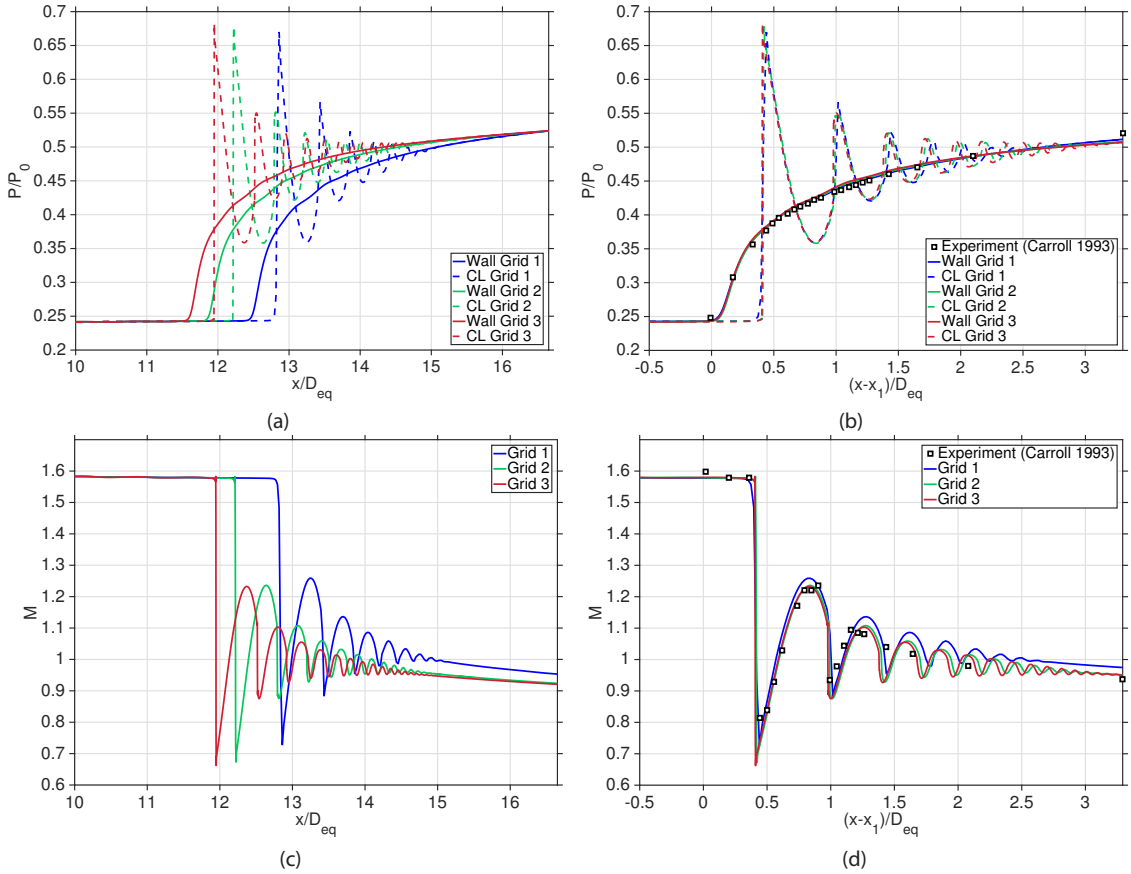

Figure 6.45: Effect of the grid size on the accuracy of pressure and Mach number distributions. a) - b) Static pressure; c) - d) Centreline Mach number.

sizes. The figures on the left hand side are plotted at the physical location of the numerical domain. In analogy with the results discussed in Section 6.1.2, as the grid size increases, the location of the shock train on the axial axis moves upstream towards the inlet. However, as the grid is refined, the shock train tends to settle at a fixed axial coordinate. This confirms the high sensitivity of the shock train to the grid resolution.

The plots on the right hand side of Figure 6.45 have been shifted to a common origin beginning at the wall pressure rise. There is good agreement between the predicted profile and the measured shock train wall pressure. All the grids employed show the same flow configuration and an almost perfect overlap is observed in the plots. Furthermore, except for Grid 1, a larger number of the shock waves composing the shock train is resolved with the finer grids. As previously mentioned, fine grids better match the experimental data because the flow structures, such as the boundary layer, are resolved in more details. On the other hand, only the first and second shocks of the shock train are detected from the LDA measurements, therefore only these two waves are taken as reference for comparison. Overall, with the grids employed the arrangement of the several shock wave in the shock train do not exhibit significant variations and in this sense the solution is grid independent.

6.2.3 Effect of duct geometry

In the literature several studies have reported the significant impact of the isolator geometry on the shock train structure. In this section the effect of a small divergence angle on the walls of the test section is investigated. As concluded in Section 6.2.2, Grid 2 captures the overall shock train structure with sufficient accuracy but requires less computational resources than Grid 3. Therefore, Grid 2 is used in both the divergent and the constant area cases.

Figure 6.46 compares the computed results of the shock train that develops in a channel of constant and divergent area. The inlet boundary conditions are different in the two cases. While for the divergent duct the experimental flow conditions are replicated, in the constant cross-sectional area case the effective area decreases. As a consequence of the reduction in the effective area, the incoming flow is decelerated and the flow conditions ahead of the shock train would be different to those in the divergent duct. For this reason, in order to have the same flow conditions ahead of the shock train, and thus making possible a comparison, in the constant area case the inflow Mach number is increased to 1.75.

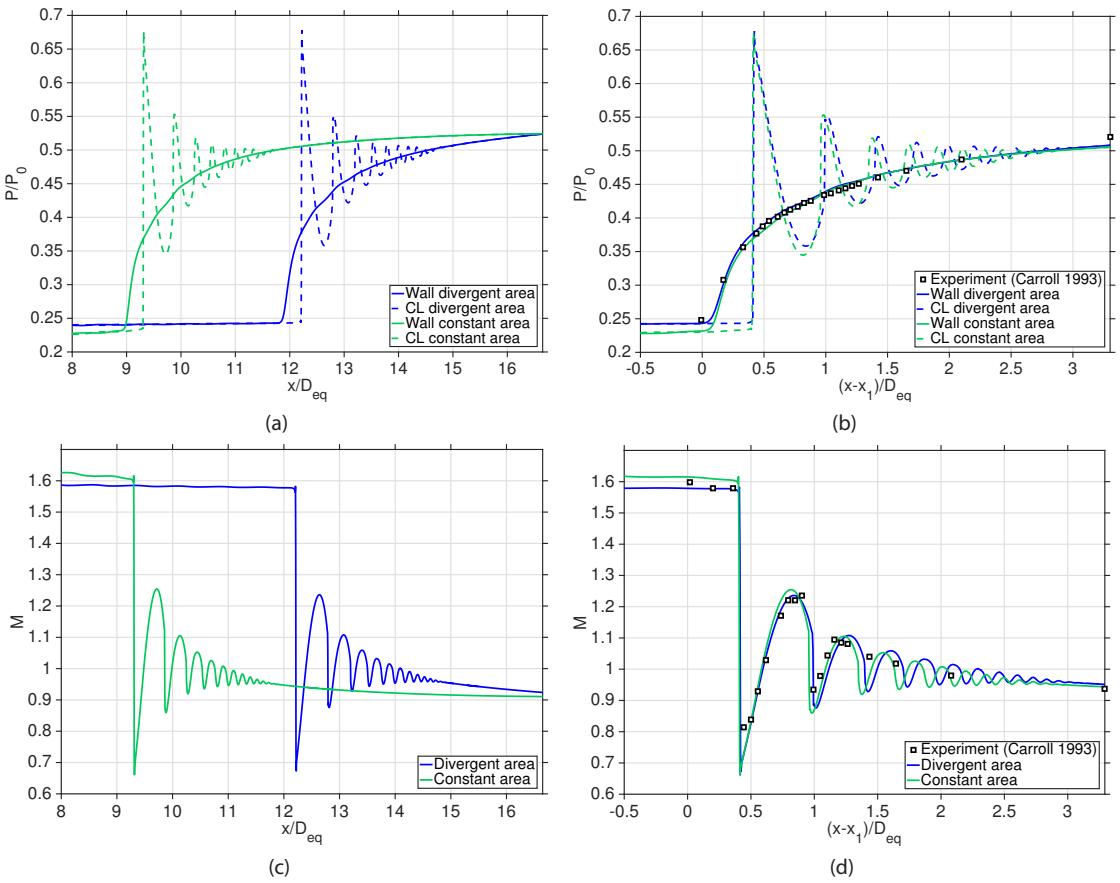

Figure 6.46: Comparison of flow quantities with different domain geometry with Grid 2: a) Static pressure at the physical axial coordinates; b) Static pressure at shifted coordinates by location of initial shock; c) Mach number at the physical axial coordinates; d) Mach number at shifted coordinates by location of initial shock.

According to Huang et al. [23], increasing the wall divergence angle from 0 deg to 1 deg, the shock train in a Mach 2 flow changes from the oblique to the normal shock configuration. However, if the angle is further increased to 1.5 deg the boundary layer separation on the walls becomes more serious and the shock train exhibits the oblique shock structure observed in the constant area case. In the experiments performed by Carroll et al. [328–330] described in Section 6.2 the divergent angle is considerably small and such a change in configuration is not observed. Only a small difference in the shock structure can be detected from the collapsed plots in Figure 6.46. The profiles of the centreline pressure and Mach number in the two cases show a perfect overlap of the first shock. On the other hand, the magnitude of the subsequent shocks present little discrepancies with a more relaxed spacing between the various shocks in the diverging duct case.

While the change in the shape of the shock train is minimal, the influence of the small divergence angle is visible in the plots of Figures 6.46(b) and 6.46(d). The diverging duct was designed to achieve a zero-pressure gradient on the wall, thus mitigating the effect of the boundary layer. The effective cross-sectional area remains approximately constant along the entire test section. On the contrary, in the constant area duct the thickening of the boundary layer decreases the central inviscid flow area. It is evident that a shock train is influenced by the geometry of the duct. With the same flow conditions ahead of the shock train, the divergent duct has the effect to locate the shock train towards the exit of the duct, in agreement with what was observed by Kawatsu et al. [92].

The computed density gradient, in Figure 6.47, displays the actual axial location of the shock train in the two duct geometries. The numerical contours confirm that the shock train structure remains unchanged in the two cases. The same flow elements are similar in both cases, with the slip lines visible at the centre of the duct. The distance between the slip lines is similar in the two cases, proving that the normal portion of the leading shock is of the same extension.

It can be concluded that a shock train of the same intensity does not exhibit modified structure when changing from a channel of constant to divergent cross-section. However, even minimal variations in the slope of the duct walls has a strong influence on the location of the shock train in the duct.

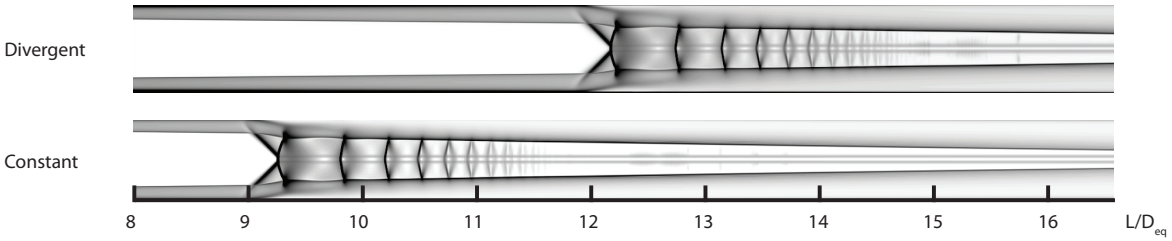

Figure 6.47: Numerical density gradient magnitude showing the effect of different duct geometry.

6.3 Shock train in indraft supersonic wind tunnel

This section presents the numerical results of the shock train that forms inside the indraft wind tunnel. In the first part, steady turbulent simulations of the full wind tunnel are performed with different back plate angles. The second part treats the shock train in more details so that only the portion of the test section is used as computational domain. The effect of a back pressure change is analysed in the transient case.

6.3.1 Wind tunnel working conditions

6.3.1.1 Description of numerical setup

Two- and three-dimensional RANS equations were solved with the k-ω Wilcox model and the same numerical code described in Section 6.3.1.1. Ideal gas is used as the working fluid with viscosity and thermal conductivity evaluated using Sutherland's law. Ambient and vacuum boundary conditions are set at the inlet and outlet of the wind tunnel, respectively. Adiabatic and no-slip boundary conditions are imposed on the wall.

The geometrical symmetry with respect to the centreline allows to simulate only half of the flow field as illustrated in Figure 6.48. The grid is composed of polyhedral elements with clustered cells in proximity of the wall to resolve the boundary layer. Compared to the structured grid employed in the validation cases, for the simulation of the wind tunnel the use an unstructured grid guarantees a better representation of the geometrical contour where curved profiles are present. The nozzle contour is responsible of the establishment of a uniform flow in the test section and requires a grid structure that faithfully follows the wall profile. To verify any dependence to the grid structure, a structured grid was also employed. By using tetrahedral cells, the total number of cells and the number of iteration required to converge increase. However, since the converged solution is the same, only the results obtained with the unstructured grid are illustrated in the following sections.

Figure 6.48: Numerical 3D domain of the wind tunnel.

6.3.1.2 Effect of grid resolution

The effect of the grid size is assessed in this section on the wind tunnel domain with the back plate in the horizontal position. The size of the four grids employed in the two-dimensional case are detailed in Table 6.9.

Figure 6.49 illustrates the Mach number and pressure at the centreline of the wind tunnel. The plots on the right hand side have been shifted to a common origin beginning at the wall pressure rise. As previously observed in the validation cases, a finer grid allows a more detailed description of the flow features. A higher grid resolution better captures the various waves composing the shock train. From the centreline pressure profile, several shock waves

Grid 1	Grid 2	Grid 3	Grid 4
72394	117670	350110	526794

Table 6.9: Number of cells in different two-dimensional grids.

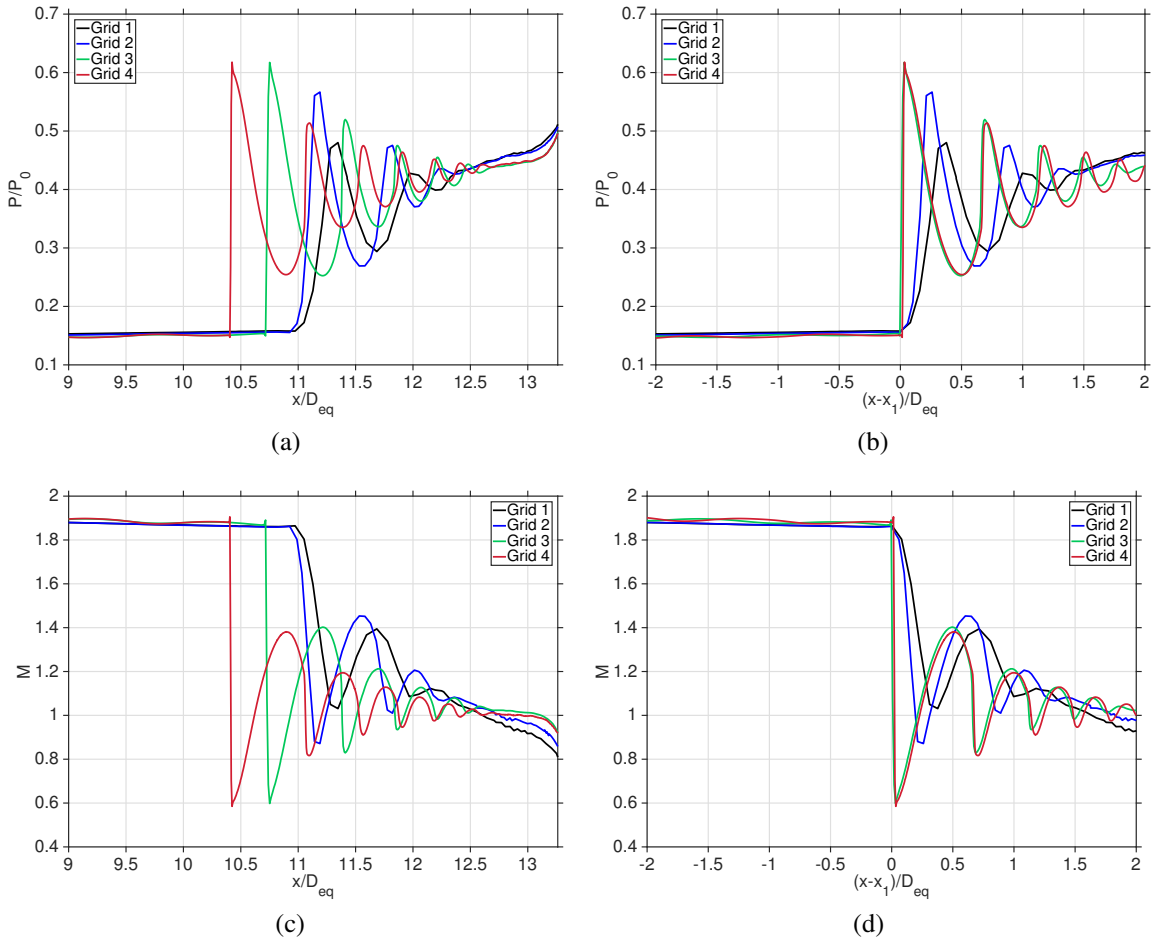

Figure 6.49: Effect of the grid size on the accuracy of pressure and Mach number in the wind tunnel centreline with a two-dimensional domain. a) - b) Static pressure; c) - d) Centreline Mach number.

are clearly visible with Grid 3 and Grid 4 whereas Grid 1 and Grid 2 resolve only the first two shocks. The magnitude of the density gradient for Grid 4, in Figure 6.50, shows that a normal shock train forms in the wind tunnel test section. Consistently with what already discussed in Sections 6.1.2 and 6.2.2, the location of the shock train is sensitive to the grid size. As the grid is refined, the shock train tends to occur towards the inlet and the difference between two subsequent plots gradually decreases. In particular, Figures 6.49(b) and 6.49(d) show that the centreline pressure and Mach number obtained with Grid 3 and Grid 4 overlap. With a further grid refinement the shock train would occur slightly upstream of the shock train location achieved with Grid 4. However, the shape and number of shocks in the shock train would remain unchanged, and consequently in this sense Grid 4 provides a grid independent solution. For the finest grid, the Mach number profile in Figure 6.49(c) illustrates that the shock train that forms in the wind tunnel with a Mach 2 nozzle occurs at approximately L/D_{eq}= 10.4.

The wall pressure profile on the top and bottom walls of the wind tunnel, in Figure 6.51, shows that the shock train is symmetric with respect to the duct centreline except at the end of the test section where the influence of the back plate becomes more relevant. An asymmetry in the boundary layer profiles is generated in the proximity of the back plate but this disturbance remains confined in a small portion of the duct and the information does not travel upstream.

The results of the grid sensitivity performed in the three-dimensional case is illustrated in Figure 6.52. To generate the three-dimensional domain the same grid structure used in the

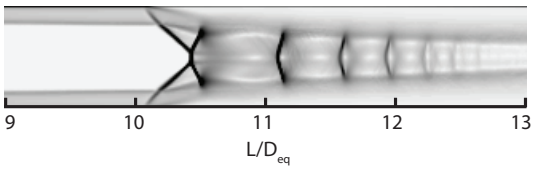

Figure 6.50: Numerical density gradient magnitude with Grid 4.

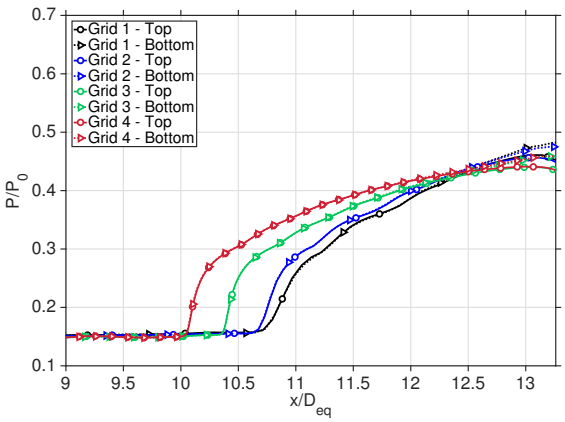

Figure 6.51: Effect of the grid size on the accuracy of pressure on the wind tunnel walls.

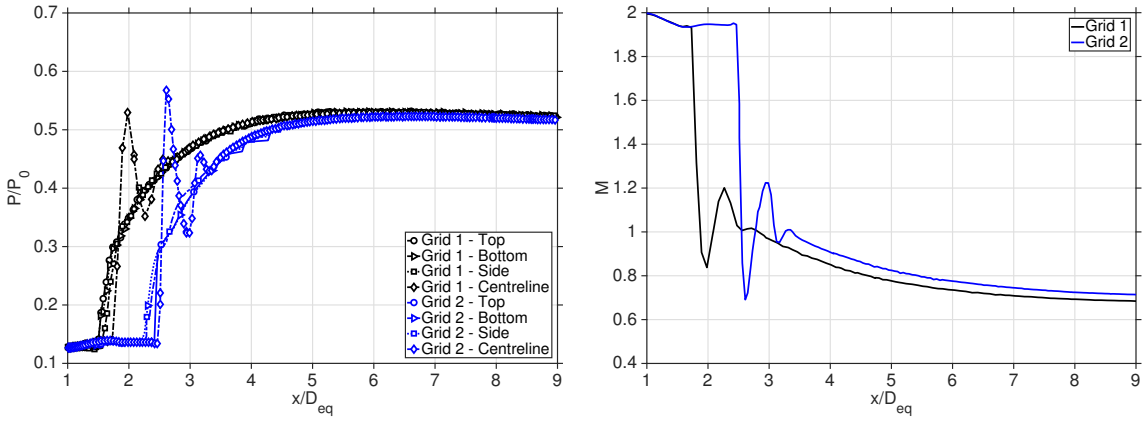

(a) (b)

Figure 6.52: Effect of the grid size on the accuracy of pressure and Mach number in the wind tunnel centreline with a three-dimensional domain. a) - b) Static pressure; c) - d) Centreline Mach number.

two-dimensional simulations is employed. Only Grid_{3D} 1 and Grid_{3D} 2, composed of 1.96 and 4.32 millions of cells, respectively, have been used because of the large computational resources required to generate the finer grids. Figure 6.52(a) compares the two grids in terms of static pressure on the top, bottom, and side walls along with the distribution of the pressure in the centre of the duct, whereas Figure 6.52(b) shows the Mach number in the centre of the duct. Although Grid_{3D} 1 and Grid_{3D} 2 are too coarse to highlight valuable information on the characteristic of the shock train, they are useful when compared to the two-dimensional case. From the comparison between the 2D and the 3D cases a remarkable difference in locating the shock train emerges. In the 2D case the shock train is located at the end of the test section, but by adding the third dimension the shock train occurs just after the end of the nozzle. Additionally, the difference in the axial direction between two subsequent grids is amplified in the three-dimensional case. While in 2D, the difference in the axial direction between Grid 1 and Grid 2 was about $\Delta L/D_{eq}$= 0.16, in 3D it becomes $\Delta L/D_{eq}$= 0.63.

6.3.1.3 Effect of back pressure and side walls

The effect of the back pressure is studied in this section together with the effect of the side walls. Two values of the back pressure are obtained by changing the angle of the back plate. The back plate angle is set at the initial value in the horizontal position at 0 deg and then increased to 10 deg.

Figure 6.53 represents the Mach number and pressure at the centreline of the wind tunnel whereas the wall pressure is illustrated in Figure 6.54. In both figures the column on the left-hand side shows the results for the two-dimensional domain and the column on right-hand side displays the three-dimensional case. As already mentioned in Section 6.3.1.2, some differences emerge in the characteristics of the shock train by including the side wall effects.

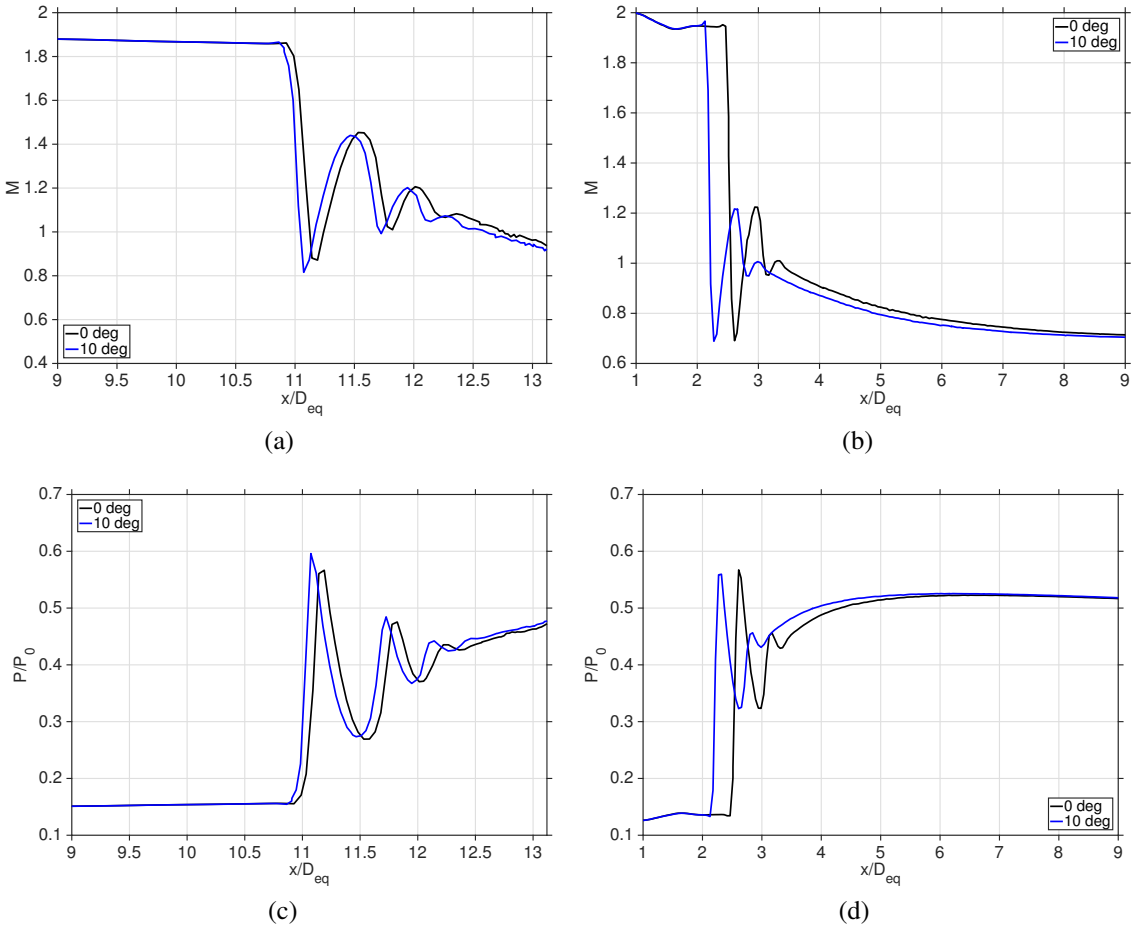

Figure 6.53: Centreline distribution in the test section: a) 2D Mach number; b) 3D Mach number ; c) 2D pressure; d) 3D pressure.

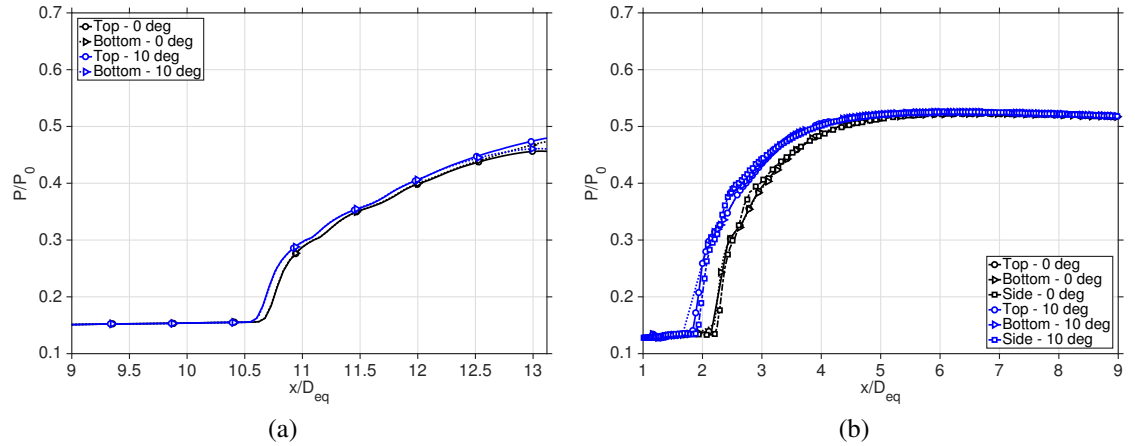

Figure 6.54: Wall pressure distribution in the test section: a) 2D; b) 3D.

From the Mach number profile, in Figures 6.53(a) and 6.53(b), it is evident that in the 3D case the first shock of the shock train is stronger and decelerates the flow to a lower

Mach number. This impacts the entire shock structure and the flow Mach number at the end of the test section is approximately 0.7 whereas is almost sonic in the 2D case. While the two-dimensional wall pressure monotonically increases, in the 3D case both the centreline and wall pressure profiles reach a maximum value behind the shock train. After this point the pressure decreases towards the outlet. The same trend is observed in the wall static pressure collected by Sullins [18] in a rectangular duct with aspect ratio of 2.5 as Figure 6.55 shows. None of the wall pressure profiles of the validation Case 1 in Section 6.1.7 nor the experimental data from the validation Case 2 in Section 6.2 exhibit this trend. The mechanism that creates this particular feature seems mostly related to the overall geometrical configuration rather than the effect of the side walls. In fact, in the shock train studied by Sun et al. [71] there is a large influence of the side wall effects since the duct aspect ratio is 1, but the wall pressure monotonically increases. On the other hand, the aspect ratio of the test section of the current wind tunnel and those of Carroll et al. [328–330] and Sullins [18] are in the range 1.9-2.5.

Figure 6.54 shows that there is little difference between the upper and lower walls of the test section. In the 3D case the side wall effects are included. The presence of the back plate does not interfere on the development of the shock train. This is an important result about the design of the wind tunnel demonstrating that the back plate mechanism does not alter the flow in the test section. The flow field in the test section, in Figure 6.56, also confirms the limitations of the numerical simulations since possible asymmetries are not computed, in agreement with the literature [52, 92].

Compared to the 2D case, another difference that emerges in 3D is the greater effect of the back plate angle. In 3D, the change in the back plate angle causes a greater displacement in the shock train along the axial direction. However, in both the 2D and 3D cases the variation in the back plate angle is not converted into a remarkable pressure variation and the flow seems to be only slightly influenced. From this analysis it is believed that the back

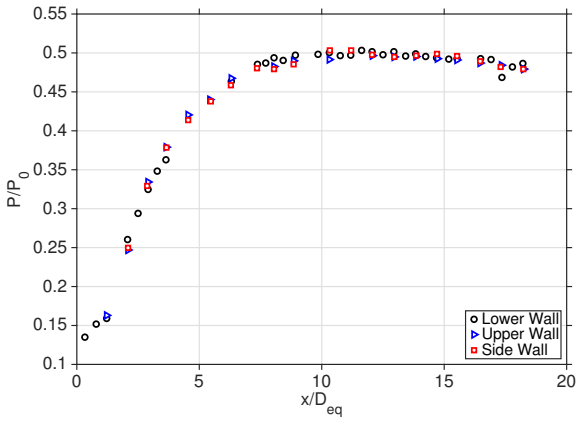

Figure 6.55: Static pressure distribution through a Mach 2 shock train collected on the upper, lower, and side walls of a rectangular duct of cross-sectional area of $H = 0.8\ in$ by $W = 2\ in$ [18].

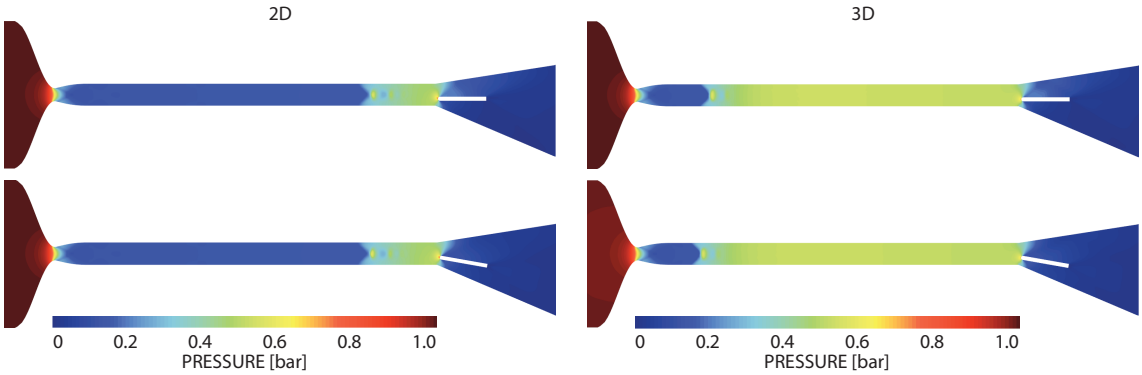

Figure 6.56: Two-dimensional and three-dimensional pressure distribution in the shock train with back plate angle at 0 deg and 10 deg.

plate mechanism in this configuration is not efficient in controlling the shock train. For this reason the back pressure variation is analysed in the next section with the computational domain formed only by the nozzle and the test section, at the end of which a sinusoidal wave is applied. This choice has the advantage of reducing the size of the computational domain allowing a greater refinement of the grid in the test section. Additionally, the results are aimed to lay the basis for a potential change in design of the back pressure mechanism.

6.3.2 Shock train with a back pressure variation

This section explores the effects that a periodic back pressure variation has on the shock train in the wind tunnel in order to replicate the rotation of the back plate. This aims to reproduce the pressure fluctuations that occur during the flight conditions in the combustion chamber of an air-breathing aircraft. In this case the numerical domain is composed of the nozzle and the test section only. Additionally, since these two components of the wind tunnel present a symmetry with respect to the centreline, only half of the domain is computed allowing the use of a finer grid. The grid size is assessed in the steady case with the back pressure extrapolated at the end of the test section from the numerical results presented in the Section 6.3.1.3.

6.3.2.1 Effect of grid resolution

The analysis of the grid size serves to determine the proper numerical domain to run the unsteady simulations. Four grids are increasingly refined with size detailed in Table 6.10.

The sensibility to the grid size presents several analogies to what has already been described in Section 6.1.2. Figure 6.57 compares the numerical results obtained with the various grids. As the grid size increases, finer flow structures are resolved and the flow field is described more accurately. This has a large impact on the development of the boundary

Grid	Size	y^+
1	44571	0.028–0.27
2	375367	0.015–0.25
3	906855	0.009–0.22
4	1306285	0.008–0.20

Table 6.10: Number of cells of the different grids employed.

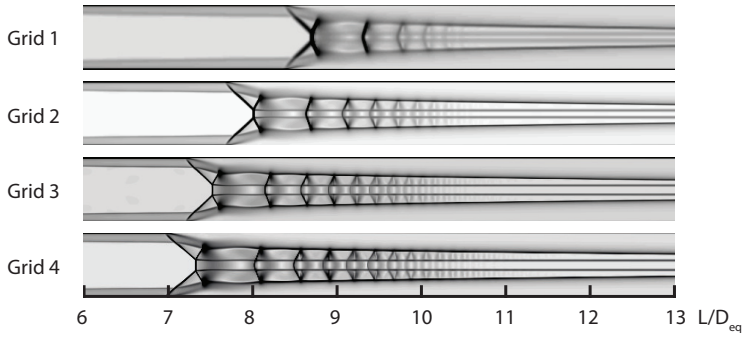

Figure 6.57: Numerical schlieren with different grid size.

layer that deeply contributes in determining the location of the shock train in the duct. It is evident that from Grid 2 the flow structures are better resolved. The slip lines that have been experimentally observed in this type of flow configuration are not present with Grid 1. On the other hand, the computed contours of the density gradients in all cases adequately resolve the first shock wave, composed of two λ shocks close to the wall that merge forming a normal shock at the centre of the duct.

The pressure and Mach number profiles are illustrated in Figure 6.58. The figures on the left column highlight the relative axial location with different grids. The increase in the grid resolution causes a shift of the shock train towards the inlet. However, the profiles of the centreline pressure and Mach number on the right column, which are collapsed to a common origin corresponding to the wall pressure rise, do not exhibit significant differences using the different grids. As noted in Section 6.1.2, over a certain grid size, there is no substantial change in the shock train structure. In this case, excluding Grid 1, no appreciable dissimilarity is visible among the grids in capturing the first shock wave, and the subsequent shocks composing the shock train are well captured in the four cases. Towards the end of the shock train the centreline pressure and Mach number profiles obtained with Grid 2 to Grid 4 differ by the amount of peaks that identify the waves composing the shock train. However, both the pressure and Mach number profiles tend to the same value with all the grids. Based on these observations Grid 4 can be considered suitable for a grid-independent study.

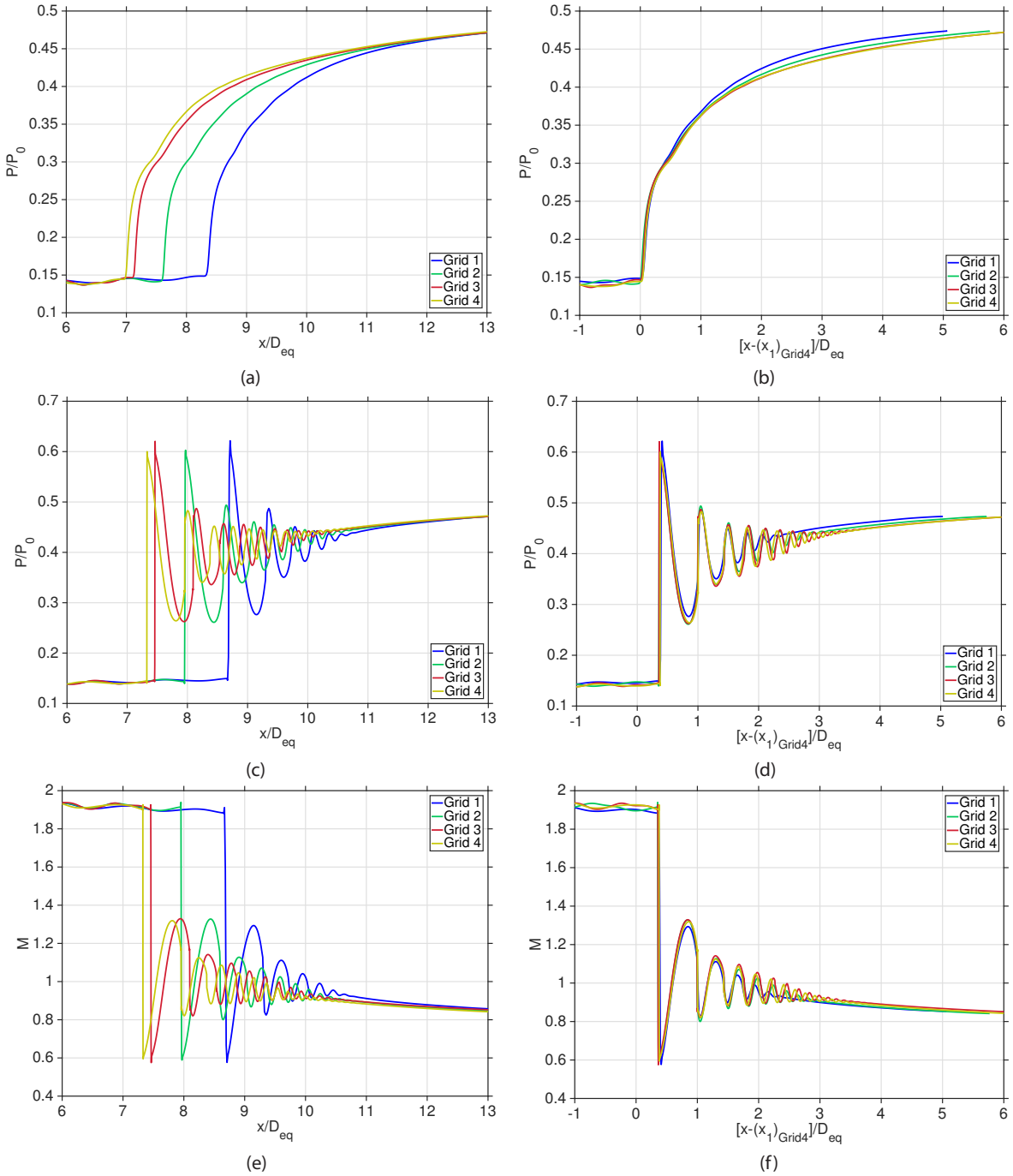

Figure 6.58: Effect of the grid size on the shock train that forms in the wind tunnel. a) - b) Wall static pressure; c) - d) Centreline static pressure; e) - f) Centreline Mach number.

6.3.2.2 Effect of time step

In this section the back pressure change is analysed using unsteady simulations by applying a sinusoidal function in time. The pressure cycle is repeated with a frequency, f, and varies around its mean value, P^*, with a maximum amplitude $P^+ = \varepsilon P^*$, where ε is the oscillation amplitude coefficient. The temporal term has been discretised with a second-order accuracy interpolation scheme.

The effect of the time step on the numerical solution is firstly investigated on Grid 1 because it provides a solution with sufficient accuracy but requires less computational resources compared to the finer grids. A periodic wave of amplitude ε= 0.1 and frequency f= 2 Hz is imposed at the exit plane. The characteristic time, T_c, defined as the ratio of the length of the test section to the velocity at the centreline of the test section when the wind tunnel is fully started, is used to determine the optimum time step. The baseline case is performed with ΔT_1= 0.1 T_c and two further refinements were taken by halving the previous time step, i.e. ΔT_2= 0.05 T_c and ΔT_3= 0.025 T_c.

Figure 6.59(a) shows the movement of the leading shock of the shock train in the axial direction during a back pressure cycle. The time history from four consecutive oscillation periods is collapsed into one curve in order to compare the effect of the time step. All the curves perfectly overlap with each other showing that for Grid 1 the solution using ΔT_1 is independent of the time step.

In Figure 6.59(b) the forcing pressure and the change in the location of the leading shock are plotted together and normalised with their corresponding initial value. It is observed that the response of the shock train in the wind tunnel to a sinusoidal forcing back pressure behaves in a similar manner to the test case described in Section 6.1.8. The forcing imposed at the exit plane is symmetrical with respect to the initial value and reaches a minimum and a maximum, P^- and P^+, respectively. The distance covered by the shock train around the initial position, x^*, changes depending on whether the shock train moves in the upstream or downstream portion of the duct. In agreement to the findings discussed in Section 6.1.8.1, in the first half of the pressure cycle, the flow responds to an external change with a time delay. The shock train reaches the further upstream position in the duct after the maximum peak in the back pressure. On the contrary, the complicated flow structure that establishes downstream of the shock train affects the response of the shock train to the change in the

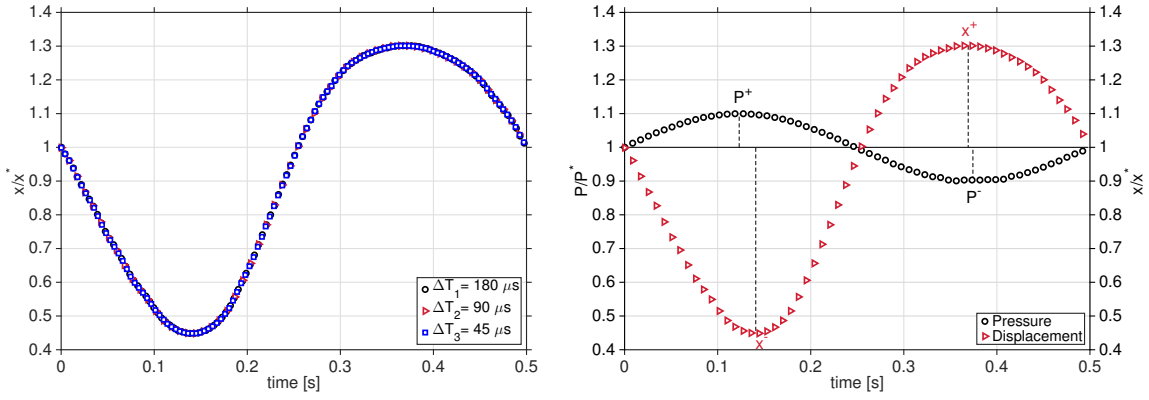

(a) (b)

Figure 6.59: a) Collapsed curve of the normalized location of the leading shock in the axial direction with different time steps; b) Plot of normalised forcing pressure and location variation of the leading shock with ΔT_1.

external forcing. In the second half of the pressure cycle, the furthest downstream position is reached few microseconds before the minimum back pressure value.

Figure 6.60 shows the time history of the Mach number behind the first shock wave. The first three figures illustrate that the movement of the shock train follows the same trend using different time steps. The small oscillations due to the unstable nature of the flow may vary in the three cases but the magnitude remains constant. The large oscillation due to the forcing follows a periodic pattern with frequency f= 2 Hz independently of the time step, as the overlapped curves in Figure 6.60(d) illustrate.

Compared to the case analysed in Section 6.1.8.1, in this case the large oscillation due to the forcing is quite small compared to the small oscillation inherent of the shock train, and consequently the hysteresis effect is not considerably pronounced. The maximum Mach number is reached at the time instant t= 0.25 s that corresponds to the time instant when the back pressure has completed half of the cycle.

To investigate the effect of the grid resolution on the time step, in Figure 6.61, Grid 1 to Grid 3 are compared using the same time step. Figures 6.61(a) and 6.61(b) show that the position of the first shock during a cycle of the back pressure follows a sinusoidal variation

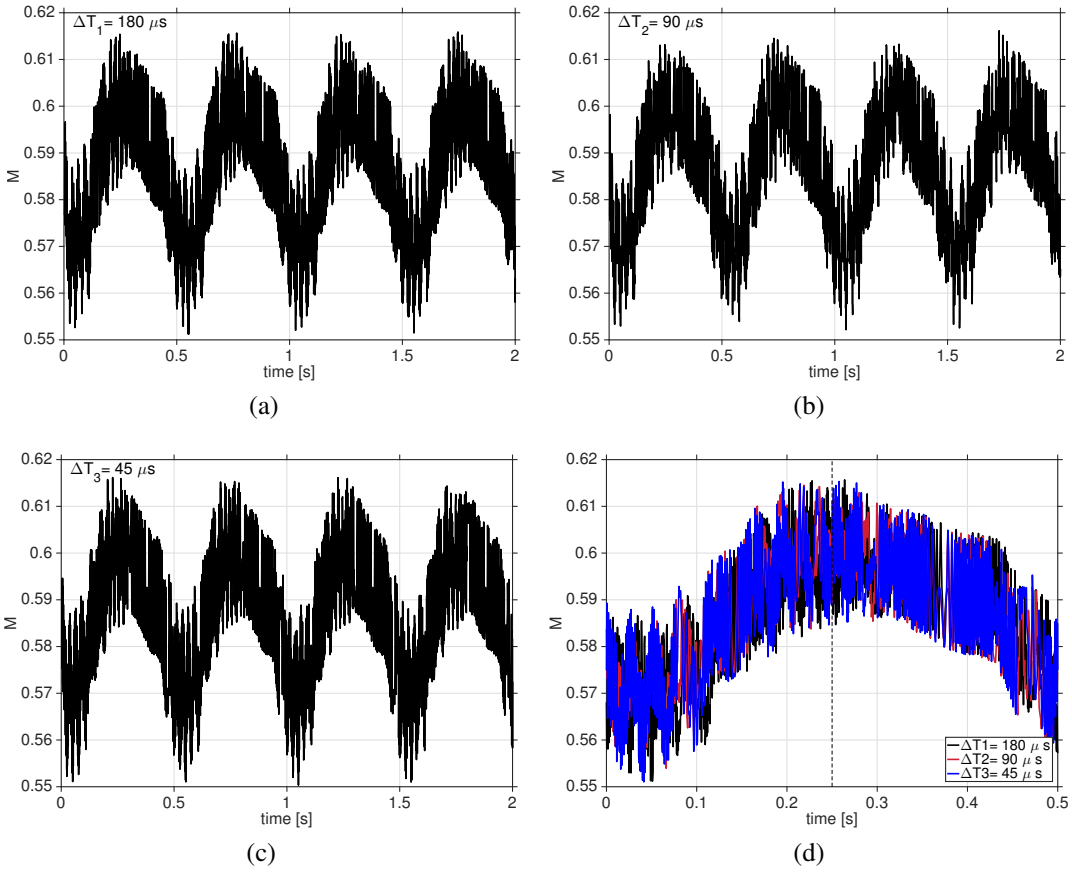

Figure 6.60: Mach number behind the leading shock in the shock train using different time steps. a) ΔT_1; b) ΔT_2; c) ΔT_3; d) Comparison of different time steps.

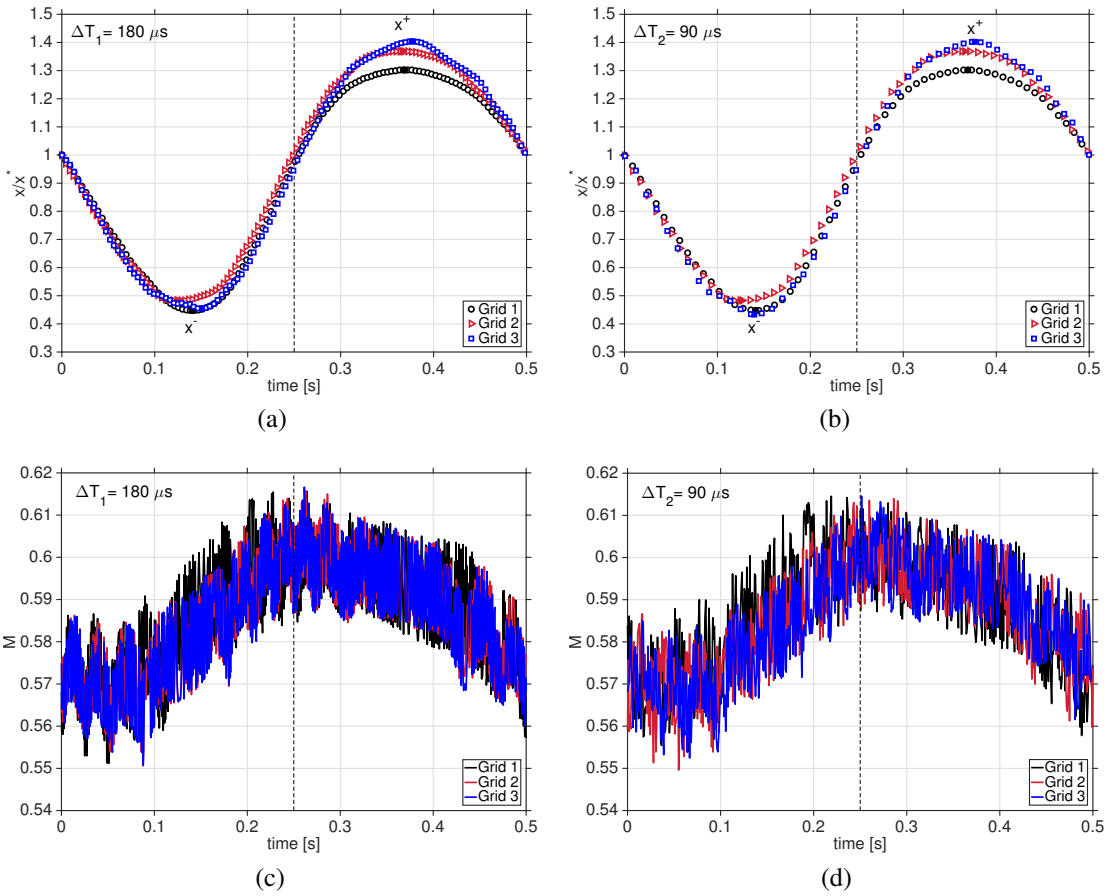

Figure 6.61: Effect of grid on the solution with different time steps: a) Position of the leading shock in the axial direction with ΔT_1; b) Position of the leading shock in the axial direction with ΔT_2; c) Mach number behind the leading shock in the shock train with ΔT_1; d) Mach number behind the leading shock in the shock trainwith ΔT_2.

with stretched peak values. The minimum displacement from the mean position, x^-, is always larger than the maximum displacement, x^+, independently of the grid size. With the time step ΔT_1, in Figure 6.61(a), the differences in the movement of the leading shock are due to the effect of the grid size. As explained in Section 6.3.2.1 the location of the shock train on the duct is related to the capability of the grid to resolve the boundary layer which, in turn, exhibits its effect on the shock train axial displacement in transient simulations. The difference between two grids tends to become smaller with increasing number of cells so a further refinement is expected to lead to a solution similar to that obtained with the finest grid. Moreover, if a smaller time step is used, in Figure 6.61(b), no change occurs in capturing the movement of the shock train comparing the corresponding grid in Figure 6.61(a). The variation of the Mach number behind the leading shock, in Figures 6.61(c) and 6.61(d), shows that the same trend and amplitude in the plot is exhibited using the various grids.

Overall a periodic variation of the back pressure influences the shock train in a similar manner to what was described in the flow configuration of Sun et al. [67, 71]. The same

behaviour is observed leading to the conclusion that the viscous effects on the wall influence the shock train. This is an intrinsic behaviour of the shock train in internal flows and does not depend on the channel configuration nor on the setup of the numerical approach.

6.3.3 Response of the shock train to back pressure variations

The oscillatory behaviour of the shock train under the effect of disturbances induced by changes in the combustion chamber are replicated and discussed in this section. Since the combustion conditions inside an air-breathing engine may change remarkably during the various phases of the flight envelope, different back pressure amplitudes and frequencies are examined. The RANS equations are solved using Grid 2 because, as concluded in Section 6.3.2.1, except for the shock location, no differences in the shock train structure are present compared to a finer grid. The time step ΔT_2 is used because has proved to be the optimal time step for Grid 2.

The effect of different forcing frequencies with oscillation amplitude ε= 0.1 is illustrated in Figure 6.62. The x-axis is normalised to the period of the forcing wave. With analogy to what was observed in Section 6.1.8.5, the difference between minimum and maximum displacement, x^- and x^+, becomes larger with decreasing forcing frequency. On the other hand, as the forcing frequency increases, the time instant when the shock train returns to its initial position, x^*, is delayed. With f= 20 Hz and f= 100 Hz, after the first half of the pressure cycle, the shock train position does not recover to its initial value but it is still travelling back from the furthest upstream axial position.

Figure 6.63 shows the effect of the oscillation frequency on the Mach number behind the leading shock. The behaviour of the shock train in the indraft wind tunnel are consistent with results discussed in Section 6.1.8.5. Independently of the back pressure oscillation frequency, in Figure 6.63(f), the maximum value of the Mach number occurs when the shock train returns to its initial position from the furthest upstream position. Moreover, the variation

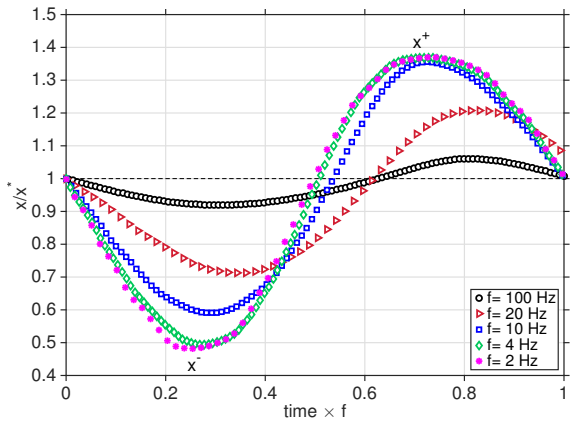

Figure 6.62: Position of the leading shock in the axial direction with different forcing frequencies.

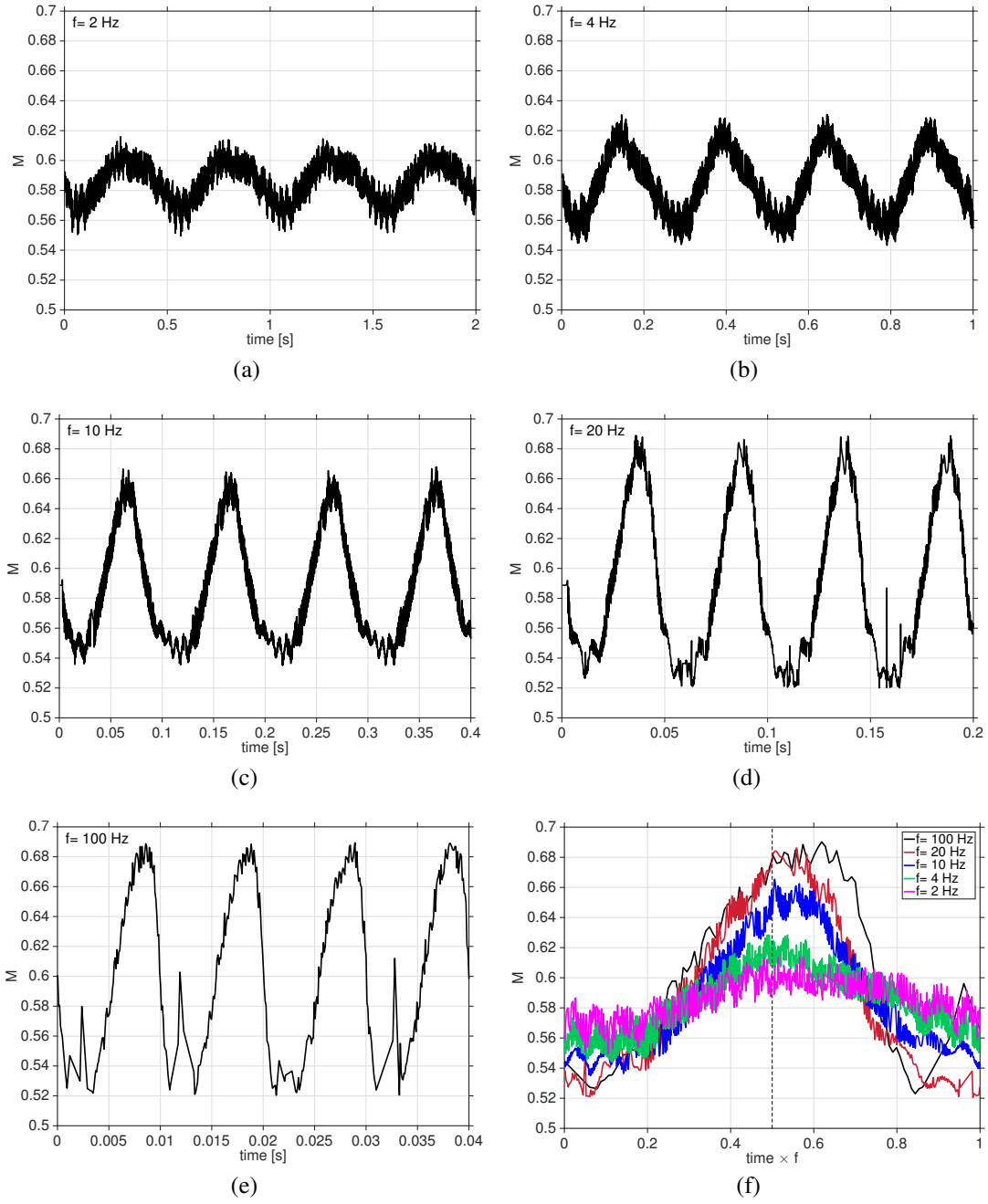

Figure 6.63: Mach number behind the leading shock in the shock train. a) $f = 2\ Hz$; b) $f = 4\ Hz$; c) $f = 10\ Hz$; d) $f = 20\ Hz$; e) $f = 100\ Hz$; f) Comparison of different forcing frequencies.

in the forcing frequency affects the strength of the shock train. For small frequencies the extremities of the Mach number profile are closer to the initial value, when the leading shock is at its initial position. As f increases, the maximum Mach number behind the leading shock increases, meaning that the strength of the leading shock is reduced. Also the minimum value decreases with higher frequencies and, therefore the leading shock is stronger. In summary, during a period, at high forcing frequencies the axial movement of the leading shock is reduced but the variation in strength is increased.

Figure 6.64 illustrates that the position of the leading shock in the axial direction is affected by the oscillation amplitude, ε. As expected the minimum and maximum displacement, x^- and x^+, are different increasing the oscillation amplitude from ε= 0.01, in Figure 6.64(a), to ε= 0.2, in Figure 6.64(b). However, while with large oscillation amplitudes the displacement of the shock train towards the inlet is larger than the displacement in the downstream direction, with small amplitudes the trend is inverted. The shock train subject to a forcing with an oscillation amplitude ε= 0.1, in Figure 6.62, to ε= 0.2, in Figure 6.64(b), behaves in similar manner as the case described in Section 6.1.8.4. As Figure 6.64(b) shows, the maximum displacement in the upstream direction, x^-, is larger than the displacement in the downstream direction, x^+. Additionally, at frequencies $f \leq 10\ Hz$, the shock train is expelled outside the inlet. In an air-breathing engine, this situation would cause inlet unstart. The same behaviour is expected also with a finer grid since Figures 6.61 illustrated that the minimum and maximum displacement of the leading shock are the same as those of Gird 2.

Figure 6.64(a) shows that when the oscillation amplitude is decreased of an order of magnitude, that is ε= 0.01, the furthest downstream position, x^+, becomes larger than the furthest upstream position, x^-, and this is enhanced with decreasing forcing frequency. In fact, for f= 100 Hz the difference between the minimum and maximum displacement is small but becomes remarkable at low frequencies. This suggests that, when the shock train is subject to a periodic forcing with low frequencies, the interactions between the shock waves with the boundary layer establish additional mechanisms that cause the asymmetry in the shock train movement. Conversely, at high frequencies the external disturbance dominates. This is true as long as the oscillation amplitude is restricted in a small portion of the duct. When the oscillation amplitude increases, the shock train covers a large portion of the duct and the shock wave/boundary layer interaction are no longer local. The large changes in the boundary layer profile along the duct greatly influence the flow field, in agreement with previous studies [63].

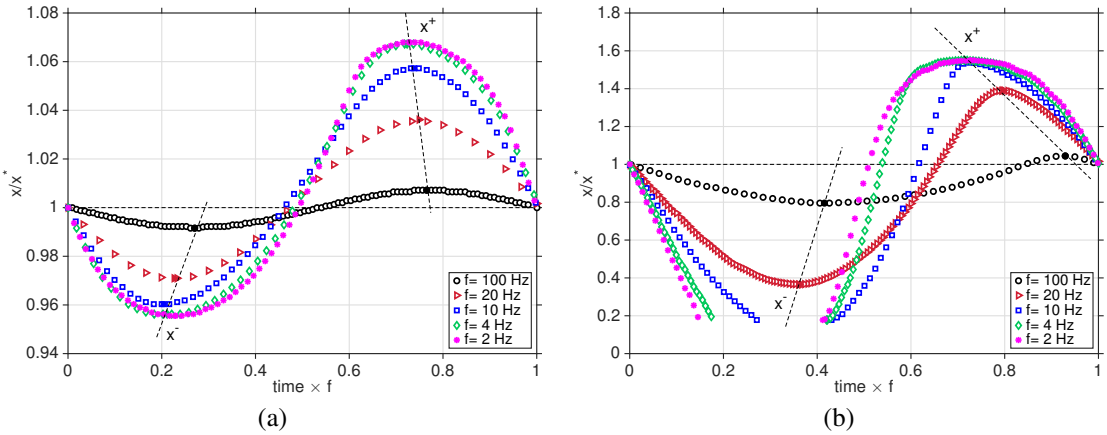

Figure 6.64: Position of the leading shock in the axial direction with different forcing frequencies: a) ϵ= 0.01; b) ϵ= 0.2.

From the comparison between Figures 6.64(a) and 6.64(b) it emerges that, as the oscillation amplitude increases, the movement of the shock train deviates from the sinusoidal variation. While for ε= 0.01 all the plots return to the initial value at approximately half of the pressure cycle, for ε= 0.2 the shock train movement is completely changed. With all frequencies the shock train returns to the initial position with a time delay. With a high forcing frequency, f= 100 Hz, the shock train moves around its mean position with a periodic path but the time required to cover the upstream part of the duct is considerably longer than the time employed to reach the furthest downstream position.

Figure 6.65 shows the effect of the oscillation amplitude. As the oscillation amplitude increases the difference between the maximum and minimum positions of the leading shock in the axial direction becomes more pronounced. This trend is exacerbated at high values of the oscillation frequency. In Figure 6.65(b), as ε becomes larger, x^- is delayed whereas the variation of the furthest downstream position with the various oscillation amplitudes occurs gradually earlier on the time. This provides an additional confirmation of the sensitivity of the shock train to changes in the back pressure and, in particular, to a back pressure increase.

Figure 6.66 summarises the movement of the shock train when both the oscillation frequency and amplitude of the back pressure are varied. The values of the furthest upstream position, x^-, for ε= 0.2 and oscillation frequencies smaller than f= 20 Hz are not calculated since no information can be obtained. In these cases the back pressure reaches a value that the shock train is not able to sustain. The shock train travels towards the upstream direction and is expelled outside the inlet. The flow is disrupted but recovers once the back pressure is released. The asymmetrical variation of the leading shock position with different oscillation frequency shows that the interaction between shock waves with the boundary layer generate a complicated response of the shock train to a sinusoidal forcing. The shock displacement in the upstream and downstream directions decreases as the forcing frequency increases.

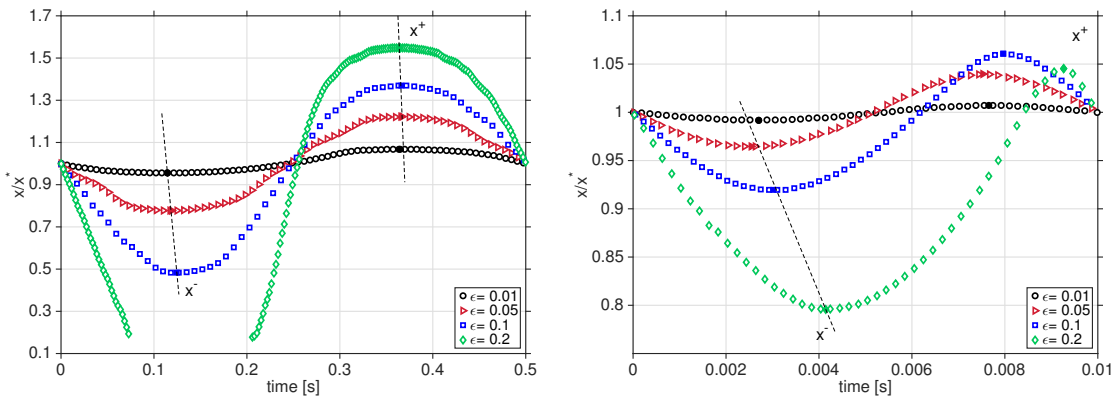

(a) (b)

Figure 6.65: Position of the leading shock in the axial direction with different forcing amplitudes: a) f= 2 Hz; b) f= 100 Hz.

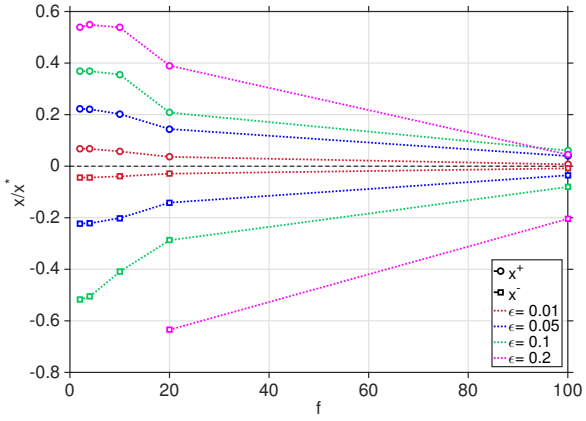

Figure 6.66: Effect of the oscillation frequency and amplitude on the position of the leading shock.

By using a finer grid the results are expected to be similar to those described above. The displacement of the leading shock around its mean position is approximately the same for Grid 2 and Gird 3. However, since with finer grids the shock train occurs at an axial coordinate located towards the inlet it might happen that the shock train is expelled outside the inlet at a frequency higher than f= 10 Hz.

6.3.4 Analytical description of shock trains

The three different configurations of the shock train previously analysed are compared against the empirical correlation defined by Billig [110] with Equation 2.10. This model has been demonstrated to best reproduce the pressure rise for the shock train in a narrow rectangular channel at moderate Mach numbers [58]. Figure 6.67 confirms that this analytical model is capable to adequately predict the pressure rise along the duct wall. The deviation between the numerical and theoretical data can be explained by the fact that this model is formulated under assumptions that limit its accuracy. Moreover, the dependence on the grid size of the numerical data are believed to prevent the accurate calculation of the boundary layer profiles.

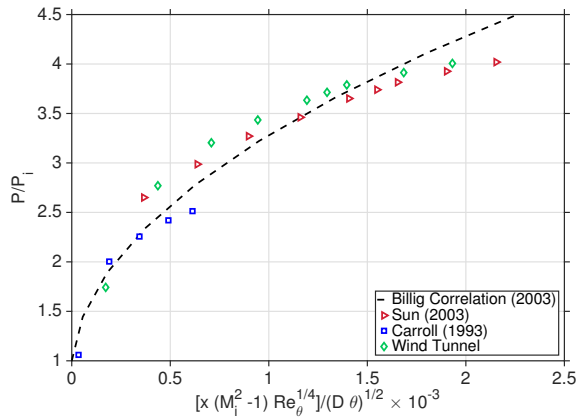

Figure 6.67: Comparison of Billig correlation with numerical data.

From Figure 6.67 it emerges that the shock train in the configuration of Sun et al. [67] and of the present wind tunnel exhibit a similar pressure rise along the duct. Additionally, in both cases the shock train is extended of approximately the same length. The case by Carroll et al. [329] instead generates a shorter shock train and a smaller pressure ratio. This is in agreement with the numerical findings since the shock train described by Carroll et al. [329] occurs at a lower Mach number and is composed of a smaller number of shock waves compared to the other two cases.

6.4 Conclusions

The selection and validation of a test case is necessary to achieve the goal of applying a numerical scheme and turbulence model able to capture the shock train behaviour. Two experimental cases have been studied and validated in order to create a model and provide with knowledge for the main study of this project. Both the geometries, a square cross-sectional area and a divergent duct, replicate the isolator configurations of air-breathing aircraft.

Sensitivity cases to different grid resolution, turbulence models, duct configuration, and back pressure values have been tested. The k-ω Wilcox turbulence model is best suited to describe supersonic internal flows such as the shock train. The grid analysis has shown that the location of the shock train in the duct is strongly dependent on the grid size. As the grid resolution increases, the shock train moves upstream towards the inlet but the difference between grids become gradually smaller because the flow is more accurately resolved. Therefore, a grid with a higher number of cells is expected to give results very close to the finest grid employed. The difficulties in achieving completely grid-independent results reflect the characteristic of supersonic internal flows of being extremely complicated to be studied. The ratio of the thickness of the boundary layer to the duct height has demonstrated to be the key parameter in determining the shock train properties. The shock train establishment in the duct is caused by the interaction with the boundary layer and occurs after a determined length in the duct. A small error in resolving the boundary layer drastically changes the shape of the leading shock, which influences the subsequent portion of the shock train.

The coupling between the shock train movement with back pressure oscillations has been analysed. It can be concluded that, under a sinusoidal forcing, the shock train executes a motion around its mean position that deviates from a perfect sinusoidal profile with variation in oscillation amplitude, frequency, and whether the pressure is first increased or decreased. With large oscillation amplitudes the shock train is greatly influenced by a pressure increase rather than a pressure drop, but the opposite is observed at small oscillation amplitudes. Additional complications occur with the variation of the forcing frequency, but the shock

displacement around its mean position decreases as the forcing frequency increases. A similar behaviour is observed in the two cases analysed, leading to the conclusion that the shock train in internal flows is influenced by the viscous effects on the wall.

The validation of the current numerical approach indicates that acquired computational methodology can be utilised in solving the shock train flow field inside isolators in general, and more specifically is suitable for the current experimental configuration.

7 | Conclusions and future work

7.1 Conclusions

THE main findings of this project are divided into two categories: the design and manufacturing of a supersonic wind tunnel for internal flow investigations along with the development and implementation of experimental methodologies applicable to the current setup, and the numerical investigation on shock trains that form in long ducts.

7.1.1 Design of an indraft supersonic wind tunnel

The initial part of the current project was dedicated to the design of an indraft supersonic wind tunnel for the study of the shock train characteristics. Using the structure of an existing facility, the new design was carried out keeping in mind the concepts of simplicity, flexibility for a wide range of experimental configurations, safety, cost, and sufficient run time.

Two supersonic nozzle contours delivering test section Mach numbers $M = 2$ and $M = 4$ were designed with the Method of Characteristics. A preliminary estimation of the boundary layer thickness developing in the test section was determined with the aid of analytical methods and numerical simulation. All the analytical methods were found to underestimate the boundary layer thickness when compared to the CFD results. Since the flow structure investigated replicates the compressibility effects developed by shock trains inside the isolator, a baseline case with parallel walls was necessary for the comparison with previous studies. As a consequence, boundary layer corrections were not included.

The numerical validation of an experimental wind tunnel with a Mach 2 nozzle revealed that a small wall divergence equal to the local boundary layer displacement thickness has beneficial effects on the stability of the boundary layer. The effective area remains approximately constant in the entire test section guaranteeing a uniform and constant Mach number.

The design of the supersonic nozzle was supported by numerical simulations giving a satisfactory overview of the flow that develops along the Mach 2 nozzle. The flow properties were found independent of the turbulence model used to close the two-dimensional RANS equations and, except in proximity of the wall, the inviscid equations accurately described the core flow. This outcome finds confirmation in the literature since many wind tunnel nozzles

were designed with no viscous corrections with test section Mach numbers lower than 4.

The computed flow field of the Mach 4 nozzle showed that the core flow is not uniform and large transverse variations are present. With the inclusion of the viscous effects, the Mach 4 nozzle delivers an averaged Mach number lower than that designed with the MOC. The discrepancy between the two nozzle profiles remain unclear because the nozzles were generated from the same code. Additionally, two test cases of similar configurations were validated leading to the definition of a satisfactory numerical approach to be used for the analysis of supersonic nozzles. The collection of experimental data will allow to establish the actual flow velocity profiles in the test section.

A new system for the regulation of the pressure ratio at the two ends of the test section has been constructed. Numerical simulation demonstrated that the presence of the back plate does not interfere on the development of the shock train. However, the rotation of the back plate angle did not produce a remarkable pressure variation and the entire shock train was scarcely influenced. It is believed that the back plate mechanism in the present configuration is not efficient in controlling the shock train and a potential change in the design of the back pressure mechanism is recommended.

Preliminary experimental tests performed to run the wind tunnel have shown the inability of the pipeline system to establish the required pressure difference across the tunnel to obtain a supersonic flow in the test section. The reasons that prevented the correct operation of the wind tunnel have been identified in the presence of leakages between the vacuum vessel and the wind tunnel.

In addition to the wind tunnel facility, the setup of flow diagnostic techniques were implemented. A full pressure sensitive paint system was developed. Several commercial polymer-based paint and in-house ruthenium-based compounds were calibrated in a specifically designed calibration chamber under controlled conditions that replicate as close as possible the wind tunnel conditions. Paints have been selected as potentially optimal to be applied to the wind tunnel tests, however only experimental data would confirm the efficacy of these PSP formulations to study the shock train.

7.1.2 Numerical simulation of compressible internal flows

The formation of shock trains in long ducts, driven by the presence of the viscous effects on the walls, is an extremely complex process that is not fully understood. Different approaches, including analytical, experimental and numerical tools, have been developed but discrepancies are still present. This is because of the inadequacy of the state-of-the art diagnostics in resolving this type of flows and the difficulties in collecting important flow variables.

Two experimental cases on shock train in internal ducts have been studied and validated to build up confidence in the numerical procedure to further examine the effects of different

parameters that characterise the shock trains. The majority of simulations performed in this work used the assumption of two-dimensional flow, which is not completely accurate for describing internal flows where the three-dimensional effects from the shock wave/boundary layer interactions play a key role in determining the structure of the shock train. However, such a simplification is necessary to balance accuracy with computational resources.

Simulations showed to be effective in capturing the large-scale features of the shock train. Computed non-dimensional wall pressure distributions were in good agreement with experimental data. It is observed that the location of the shock train strongly varies with the grid size. Fine grids more accurately resolve the flow field, i.e. the shock train moves upstream towards the inlet and is composed of a greater number of shock waves.

The choice of the numerical approach have demonstrated to be crucial in the development of the boundary layer. The main difficulty of this work was to determine the setup capable to accurately resolve the boundary layer on the duct wall. The k-ω Wilcox turbulence model provided quite accurate results over a wide range of pressure ratios for such a complex flow field. In supersonic internal flows, in absence of any geometrical change, the establishment of the shock train system occurs purely as a consequence of the flow conditions within or at the two ends of the duct. This means that the ratio of the back pressure to the inlet pressure, and the way the boundary layer develops on the duct walls are parameters of the highest importance.

To reproduce the pressure fluctuations that occur during the flight conditions in the combustion chamber of an air-breathing aircraft, a periodic back pressure variation was applied in transient simulations. The results presented in the current investigation on the behaviour of shock trains reveal a similarity with the studies performed by other researchers. The analysis of the shock train movement under a sinusoidal back pressure forcing showed that the shock train executes a motion around its mean position that deviates from a perfect sinusoidal profile with variation in oscillation amplitude, frequency, and whether the pressure is first increased or decreased. With large oscillation amplitudes the shock train is greatly influenced by a pressure increase rather than a pressure drop, but the opposite was observed at small oscillation amplitudes. Overall, it was observed that the shock train displacement around its mean position decreases as the forcing frequency increases.

Most of the work done served as a baseline investigation for the understanding of the shock train that develops in the designed indraft wind tunnel. A fundamental insight about the physical behaviour of the interaction between the shock waves with the boundary layer in internal ducts can be achieved only with the combination of the numerical findings with experimental data. Therefore, an experimental campaign is recommended for further investigations.

In summary, this study has fulfilled the main objectives:

- A wind tunnel capable to study the shock train in different flow and geometrical configurations was designed and manufactured.
- A pressure sensitive paint system to measure transient shock wave phenomena has been implemented and compounds have been identified as suitable for investigating the shock train behaviour.
- The flow phenomena that characterise the shock train have been numerically investigated comparing several validation cases of similar configuration.
- The shock train that develops inside the rectangular cross-sectional area duct in the indraft wind tunnel at a flow Mach number of 2 has been numerically investigated providing valuable findings for experimental comparison.
- The sensitivity of the shock train to variations in the geometrical configuration and flow properties has been analysed over a wide range of different scenarios.
- The effect of a back pressure periodic forcing on the flow behaviour was examined with transient simulation by changing the frequency and amplitude of the oscillation forcing.

7.2 Future work

In this section a summary of the improvements and recommendation for the problems and limitations detected in this project is carried out.

- The characterisation of the wind tunnel is necessary for the collection of the velocity profiles in the test section providing a validation of the computed flow field. This includes the confirmation of the vacuum level achievable in the vacuum vessel to determine the wind tunnel working conditions.
- Experimental confirmation of the efficiency of the back pressure controlling device is essential to corroborate transient simulations. Potential improvement of the current mechanism to achieve a remarkable back pressure variation is suggested. A calibration of the back pressure system is anyway needed.
- The Mach number range tested in this project is rather limited. Only one value was successfully analysed. Three wind tunnel nozzles were proposed during the initial stages of the design process. It would be beneficial to investigate the behaviour of the shock train when the Mach number is increased.
- The collection of experimental data in support of the numerical findings achieved in this investigation will provide an in-depth understanding of mechanism governing the shock train formation in internal ducts.

- The confirmation of the suitability of the calibrated pressure sensitive paints to the shock train that forms in the wind tunnel is necessary. Pressure and temperature sensitive paints are indispensable tools to map the duct walls. These measurements would provide high-resolution distribution of the surface pressure and also show an indication of imminent separation prior to that detected by the pressure measurements. This would reveal important information about the transient nature of this phenomenon.

- The numerical simulations performed in this project were limited by the computational power and software available. This restricted the use of the turbulence models and also limited the choice of solving parameters. Future work on the topic should also consider to extend this finding to the three-dimensional case.

- The numerical results showed a symmetrical flow field. The need to reduce computational resources has led to the choice to take advantage of the geometry symmetries. To explore the asymmetric boundary layer development reported in the literature, the full geometry should be used as a computational domain with transient simulation.

- Once the wind tunnel has been characterised, boundary layer techniques may be applied to explore the effect on the shock train. This would counteract the negative effects associated with a pressure rise that in air-breathing inlets may lead to the engine unstart.

Bibliography

[1] *Istituto della Enciclopedia Italiana Treccani*, (1925).

[2] Fry, R.S., "A Century of Ramjet Propulsion Technology Evolution," *Journal of Propulsion and Power* **20(1)**, 27–58, (2004).

[3] Crocco, L., "Instruction and research in jet propulsion," *Journal of American Rocket Society* **80**, 32–43, (1950).

[4] Frank S.K., James L.H., "Hypersonic transport technology," *Acta Astronautica* **4(1-2)**, 181–199, (1977).

[5] Timnat, Y.M., "Recent developments in ramjets, ducted rockets and scramjets," *Progress in Aerospace Sciences* **27(3)**, 201–235, (1990).

[6] McClinton, C.R., "X-43-Scramjet Power Breaks the Hypersonic Barrier: Dryden Lectureship in Research for 2006," *44th AIAA Aerospace Sciences Meeting and Exhibit*, (2006).

[7] Segal, C., "The Scramjet Engine: Processes and Characteristics," *Cambridge University Press*, Cambridge, (2009).

[8] McLafferty, G., "Theoretical Pressure Recovery Through a Normal Shock in a Duct with Initial Boundary Layer," *Journal of the Aeronautical Sciences* **20(3)**, 169–174, (1953).

[9] Yamauchi, H., Choi, B., Kouchi, T., Masuya, G., "Mechanism of Mixing Enhanced by Pseudo-Shock Wave," *AIAA paper 2009-25*, (2009).

[10] Gibbs-Smith, C.H., "Aviation: an historical survey from its origins to the end of World War II," *H.M.S.O.*, London, (2009).

[11] Taylor, M.J.H., Taylor, J.W.R., Gunston, B., "Jane's encyclopedia of aviation," *Jane's*, London, (1980).

[12] Gunston, B., "Chronicle of aviation," *Chronicle Communications*, London (1960).

[13] Gibbs-Smith, C.H., "The aeroplane: a historical survey of its origins and development," *H.M.S.O.*, London, (1960).

[14] Ferri, A., Nucci, L.M., "Preliminary investigation of a new type of supersonic inlet," *NACA-TN-2286*, (1951).

[15] Swithenbank, J., "Hypersonic air-breathing propulsion," *Progress in Aerospace Sciences* **8**, 229–294, (1967).

[16] Sullins, G.A., "Demonstration of mode transition in a scramjet combustor," *Journal of Propulsion and Power* **9(4)**, 515–520, (1993).

[17] Curran, E.T., Heiser, W.H., Pratt, D.T., "Fluid phenomena in scramjet combustion systems," *Annual Review of Fluid Mechanics* **28**, 323–360, (1996).

[18] Sullins, G., "Experimental Results of Shock Trains in Rectangular Ducts," *AIAA paper 92-5103*, (1992).

[19] Bement, D.A., Stevens, J.R., Thompson, M.W., "Measured operating characteristics of a rectangular combustor/inlet isolator," *AIAA/SAE/ASME/ASEE 26th Joint Propulsion Conference* **90-2221**, (1990).

[20] Billig, F.S., Corda, S., Pandolfini, P.P., "Design Techniques for Dual Mode Ram Scramjet Combustors," *AGARD 75th symposium of hypersonic combined cycle propulsion, Madrid* **23**, 1–20, (1990).

[21] Smart, M.K., "Scramjets," *Advances on Propulsion Technology for High-Speed Aircraft* **9**, 1–38, (2008).

[22] Smart, M.K., "How much compression should a scramjet inlet do?," *AIAA Paper* **50(3)**, 610–619, (2012).

[23] Huang, W., Wang, Z., Pourkashanian, M., Ma, L., Ingham, D.B., Luo, S., Lei, J., Liu, L., "Numerical investigation on the shock wave transition in a three-dimensional scramjet isolator," *Acta Astronautica* **68(11-12)**, 1669–1675, (2011).

[24] Billig, F.S., "Combustion processes in supersonic flow," *Journal of Propulsion and Power* **4(3)**, 209–216, (1988).

[25] Hunt, J.L., Rausch, V.L., "Airbreathing hypersonic systems focus at NASA Langley Research Center," *AIAA paper 98-1641*, (1989).

[26] Bertin, J.J., Cummings, R.M., "Fifty years of hypersonics: where we've been, where we're going," *Progress in Aerospace Sciences* **39(6-7)**, 511–536, (2003).

[27] Ferri, A., "Review of scramjet propulsion technology," *Journal of Aircraft* **5(1)**, 3–10, (1968).

[28] Lewis, M.J., "Designing hypersonic inlets for bow shock location control," *Journal of Propulsion and Power* **9(4)**, 313–321, (1993).

[29] Heiser, W.H., Pratt, D.T., "Hypersonic airbreathing propulsion," *American Institute of Aeronautics and Astronautics*, Washington, D.C., (1994).

[30] Van Wie, D.M., "Internal flowfield characteristics of a scramjet inlet at Mach 10," *Journal of Propulsion and Power* **12(1)**, 158–164, (1996).

[31] Raj, N.O.P., Venkatasubbaiah, K., "A new approach for the design of hypersonic scramjet inlets," *Physics of Fluids* **24(8)**, 1–15, (2012).

[32] Qin, B., Chang, J., Jiao, X., Bao, W., Yu, D., "Numerical investigation of the impact of asymmetric fuel injection on shock train characteristics," *Acta Astronautica* **105(1)**, 66–74, (2014).

[33] Gaitonde, D.V., "Progress in shock wave/boundary layer interactions," *Progress in Aerospace Sciences* **72**, 80–99, (2015).

[34] Kantrowitz, A., Donaldson, C. P., "Preliminary Investigation of Supersonic Diffusers," *Langley Aeronautical, Laboratory, National Advisory Committee for Aeronautics*, (1945).

[35] Wang, W., Guo, R., "Numerical study of unsteady starting characteristics of a hypersonic inlet," *Chinese Journal of Aeronautics* **26(3)**, 563–571, (2013).

[36] Do, H., Im, S., Mungal, M.G., Cappelli, M.A., "Visualizing supersonic inlet duct unstart using planar laser Rayleigh scattering," *Experiments in Fluids* **50(6)**, 1651–1657, (2010).

[37] Do, H., Im, S., Mungal, M.G., Cappelli, M.A., "The influence of boundary layers on supersonic inlet flow unstart induced by mass injection," *Experiments in Fluids* **51(3)**, 679–691, (2011).

[38] Wagner, J.L., Yuceil, K.B., Clemens, N.T., Dolling, D.S., "Experimental investigation of unstart in an inlet/isolator model in Mach 5 flow," *AIAA Journal* **47(6)**, 1528–1542, (2009).

[39] Wagner, J.L., Yuceil, K.B., Clemens, N.T., "Velocimetry measurements of unstart in an inlet isolator model in Mach 5 flow," *AIAA Journal* **48(9)**, 1875–1888, (2009).

[40] Tao, C., Daren, Y., Juntao, C., Wen, B., "Topological geometry interpretation of supersonic inlet start/unstart based on catastrophe theory," *Journal of Aircraft* **45(4)**, 1464–1468, (2008).

[41] Emami, S., Trexler, C.A., Auslender, A.H., Weidner, J.P., "Experimental Investigation of Inlet-Combustor Isolators for a Dual-Mode Scramjet at a Mach Number of 4," *NASA Technical Paper 3502*, (1995).

[42] Che-Idris, A., Saad, M.R., Zare-Behtash, H., Kontis, K., "Performance analysis of a scramjet inlet-isolator using experimental & numerical methods," *28th Congress of the International Council of the Aeronautical Sciences, Brisbane, Australia* **4**, 2907–2915, (2012).

[43] Nair, M.T., Naresh, K., Saxena, S.K., "Computational analysis of inlet aerodynamics for a hypersonic research vehicle," *Journal of Propulsion and Power* **21(2)**, 286–291, (2005).

[44] Chen, Z., Shihe, Y., Yangzhu, Z., Yu, W., Qinghu, Z., Pengcheng, Q., "Investigation on flows in a supersonic isolator with an adjustable cowl convergence angle," *Experimental Thermal and Fluid Science* **52**, 182–190, (2014).

[45] Saha, S., Chakraborty, D., "Hypersonic intake starting characteristics-A CFD validation study," *Defence Science Journal* **62(3)**, 147–152, (2012).

[46] Tan, H.J., Guo, R.W., "Experimental study of the unstable-unstarted condition of a hypersonic inlet at Mach 6," *Journal of Propulsion and Power* **23(4)**, 783–788, (2007).

[47] Soltani, M.R., Farahani, M., "Experimental investigation of effects of Mach number on the flow instability in a supersonic inlet," *Experimental Techniques* **37(3)**, 46–54, (2013).

[48] Koike, S., Osawa, J., Nakakita, K., Kato, H., Kameda, M., "Simultaneous pressure and velocity field measurement of pseudo-shock-wave using PSP and PIV," *AIAA paper 21012-1190*, (2012).

[49] Crocco, L., "High Speed Aerodynamics and Jet Propulsion," *Princeton University Press* **3**, Princeton, (1958).

[50] Matsuo, K., Miyazato, Y., Kim, H.D., "Shock train and pseudo-shock phenomena in internal gas flows," *Progress in Aerospace Sciences* **35**, 33–100, (1999).

[51] Squire, L.C., "Interaction of swept and unswept normal shock waves with boundary layers," *AIAA Journal* **34(10)**, 2099–2101, (1996).

[52] Gawehn, T., Gülhan, A., Al-Hasan, N.S., Schnerr, G.H., "Experimental and numerical analysis of the structure of pseudo-shock systems in laval nozzles with parallel side walls," *Shock Waves* **20**, 297–306, (2010).

[53] Om, D., Childs, M.E., "Multiple Transonic Shock-Wave/Turbulent Boundary-Layer Interactions in a Circular Duct," *AIAA Journal* **23(10)**, 1506–1511, (1985).

[54] Morgan, B., Duraisamy, K., Lele, S.K., "Large-Eddy Simulations of a Normal Shock Train in a Constant-Area Isolator," *AIAA Journal* **52(3)**, 539–558, (2014).

[55] Om, D., Childs, M.E., Viegas, J.R., "Transonic Shock-Wave/Turbulent Boundary-Layer Interactions in a Circular Duct," *AIAA Journal* **23(5)**, 707–714, (1985).

[56] Lustwerk, F., "The Influence of Boundary Layer on the 'Normal' Shock Configuration," *Massachusetts Institute of Technology, Guided Missiles Program*, (1950).

[57] Babinsky, H., Harvey, J.K., "Shock Wave-Boundary-Layer Interactions," *Cambridge University Press*, Cambridge (2011).

[58] Weiss, A., Grzona, A., Olivier, H., "Behavior of shock trains in a diverging duct," *Experiments in Fluids* **49(2)**, 355–365, (2010).

[59] Merkli, K., "Pressure Recovery in Rectangular Constant Area Supersonic Diffusers," *AIAA Journal* **14(2)**, 168–172, (1976).

[60] Neumann, E.P., Lustwerk, F., "High-Efficiency Supersonic Diffusers," *Journal of the Aerospace Sciences* **18(6)**, 369–374, (1951).

[61] Fischer, C., Olivier, H., "Experimental Investigation of the Internal Flow Field of a Scramjet Engine," *AIAA paper 2009-7369*, 1657–1667, (2009).

[62] Ikui, T., Magai, M., Matsuo, K., "The Mechanism Of Pseudo-Shock Waves," *Bulletin of the JSME* **17(108)**, 731–739, (1974).

[63] Sajben, M., Donovan, J.F., Morris, M.J., "Experimental investigation of terminal shock sensors for mixed-compression inlets," *Journal of Propulsion and Power* **8(1)**, 168–174, (1992).

[64] Lukasiewicz, J., "Diffusers for Supersonic Wind Tunnels," *Journal of the Aeronautical Sciences* **20(9)**, 617–626, (1953).

[65] Sugiyama, H., Minato, R., Mizobata, K., Tojo, A., Muto, Y., "Study on shock wave and turbulent boundary layer interactions in a square duct at Mach 2 and 4," *Journal of Thermal Science* **15(1)**, 37–42, (2006).

[66] Hataue, I., "Computational study of the shock-wavey/boundary-layer interaction in a duct," *Fluid Dynamics Research* **5(3)**, 217–234, (1989).

[67] Sun, L. Sugiyama, H., Mizobata, K., Minato, R., Tojo, A., "Numerical and experimental investigations on Mach 2 and 4 pseudo-shock waves in a square duct," *Transactions of the Japan Society for Aeronautical and Space Sciences* **47(156)**, 124–130, (2004).

[68] Carroll, B.F., Lopez-Fernandez, P.A., Dutton, J.C., "Computations and experiments for a multiple normal shock/boundary-layer interaction," *Journal of Propulsion and Power* **9(3)**, 405–411, (1993).

[69] Ostras, V.N., Penzin, V.I., "Experimental Study of Friction in a Channel with Pseudoshock," *Fluid Mechanics* **4(6)**, 32–38, (1975).

[70] Nagai, M., "Mechanism Of Pseudo-Shock Wave in Supersonic Jet," *Bulletin of the JSME* **26(212)**, 207–214, (1983).

[71] Sun, L.Q., Sugiyama, H., Mizobata, K., Fukuda, K., "Numerical and Experimental Investigations on the Mach 2 Pseudo-Shock Wave in a Square Duct," *Journal of Visualization* **6(4)**, 363–370, (2003).

[72] Mahoney, J.J., "Inlets for supersonic missiles," *American Institute of Aeronautics and Astronautics*, Washington, D.C., 55–66, (1990).

[73] Ikui, T., Magai, M., Matsuo, K., Sasaguchi, K., "Modified Diffusion Model of Pseudo-Shock Waves Considering Upstream Boundary Layers," *Bulletin of the JSME* **24(197)**, 1920–1927, (1981).

[74] Reinartz, B.U., Herrmann, C.D., Ballmann, J., "Performance Analysis of a Hypersonic Inlet Isolator Using Computation and Experiment," *Journal of Propulsion and Power* **19(5)**, 868–875, (2003).

[75] McLafferty, G.H., Krasnoff, E.L., Ranard, E.D., Rose, W.G., Vergara, R.D., "Investigation of Turbojet Inlet Design Parameters," *United Aircraft Corporation, Research Laboratories*, (1955).

[76] Ikui, T., Matsuo, K., Nagai, M., Honjo, M., "Oscillation Phenomena of Pseudo-Shock Waves," *Bulletin of the JSME* **17(112)**, 1278–1285, (1974).

[77] Matsuo, K., Mochizuki, H., Miyazato, Y., Gohya, M., "Oscillatory characteristics of a pseudo-shock wave in a rectangular straight duct," *JSME International Journal Series B* **36(2)**, 222–229, (1993).

[78] Kim, H.D., Matsuo, K., Kawagoe, S., Kinoshita, T., "Flow unsteadiness by weak normal shock wave/turbulent boundary layer interaction in internal flow," *JSME International Journal Series II* **34(4)**, 457–465, (1991).

[79] Handa, T. Mitsuharu, M.,Matsuo, K., "Three-Dimensional Normal Shock-Wave/Boundary-Layer Interaction in a Rectangular Duct," *AIAA Journal* **43(10)**, 2182–2187, (2005).

[80] Yamauchi, H., Choi, B., Takae, K., Kouchi, T., Masuya, G., "Flowfield characteristics of a transverse jet into supersonic flow with pseudo-shock wave," *Shock Waves* **22(6)**, 533–545, (2012).

[81] Yamane, R., Kondo, E., Tomita, Y., Sakae, N., "Vibration of pseudo-shock in straight duct, 1st Report, Fluctuation of static pressure," *Bulletin of the JSME* **27(229)**, 1385–1392, (1984).

[82] Yamane, R., Takahashi, M., Saito, H., "Vibration of pseudo-shock in straight duct, 2nd Report, Correlation of static pressure fluctuation," *Bulletin of the JSME* **27(229)**, 1393–1398, (1984).

[83] Sugiyama, H., "Locations And Oscillation Phenomena Of Pseudo-Shock Waves In A Straight Rectangular Duct," *JSME International Journal, Series B: Fluids and Thermal Engineering* **31(1)**, 9–15, (1988).

[84] Robinet, J.C., Casalis, G., "Shock Oscillations in Diffuser Modeled by a Selective Noise Amplification," *AIAA Journal* **37(4)**, 453–459, (1999).

[85] Su, W.Y., Zhang, K.Y., "Back-Pressure Effects on the Hypersonic Inlet-Isolator Pseudoshock Motions," *Journal of Propulsion and Power* **29(6)**, 1391–1399, (2013).

[86] Hsieh, T., Coakley, T.J., "Downstream Boundary Effects on the Frequency of Self-Excited Oscillations in Diffuser Flows," *AIAA Paper 87-0161*, (1987).

[87] Bogar, T.J., Sajben, M., Kroutil, J.C., "Characteristics frequencies of transonic diffuser flow oscillations," *AIAA Journal* **21(9)**, 1232–1240, (1983).

[88] Bogar, T.J., "Structure of self-excited oscillations in transonic diffuser flows," *AIAA Journal* **24(1)**, 54–61, (1986).

[89] Xiao, Q., Tsai, H.M., Papamoschou, D., "Numerical Investigation of Supersonic Nozzle Flow Separation," *AIAA Journal* **45(3)**, 532–541, (2007).

[90] Papamoschou, D., Zill, A., "Fundamental Investigation of Supersonic Nozzle Flow Separation," *AIAA paper 2004-1111*, (2004).

[91] Papamoschou, D., Johnson, A., "Unsteady Phenomena in Supersonic Nozzle Flow Separation," *AIAA paper 2006-3360*, (2006).

[92] Kawatsu, K., Koike, S., Kumasaka, T., Masuya, G., Takita, K., "Pseudo-Shock Wave Produced by Backpressure in Straight and Diverging Rectangular Ducts," *AIAA paper 2005-3285*, (2005).

[93] Hsieh, T., Wardlaw, A. B., Coakley, T., "Ramjet diffuser flowfield response to large-amplitude combustor pressure oscillations," *Journal of Propulsion and Power* **3(5)**, 472–477, (1987).

[94] Oh, J.Y., Ma, F., Hsieh, S.Y., Yang, V., "Interactions Between Shock and Acoustic Waves in a Supersonic Inlet Diffuser," *Journal of Propulsion and Power* **21(3)**, 486–495, (2005).

[95] Klomparens, R., Driscoll, J.F., Gamba, M., "Response of a shock train to downstream back pressure forcing," *AIAA paper 2016-0078*, (2016).

[96] Ikui, T., Matsuo, K., Mochizuki, H., Somekawa, K., "Pseudo-shock waves in a divergent channel," *Bulletin of the JSME* **23(175)**, 20–25, (1980).

[97] Neumann, E.P., Lustwerk, F., "Supersonic Diffusers for Wind Tunnels," *Journal of Applied Mechanics* **16(2)** , 195–202, (1949).

[98] Walther, R., Koschel, W., Sabelnikov, V., Korontsvit, Y., Ivanov, V., "Investigations into the Aerothermodynamic Characteristics of Scramjet Components," *International Society for Air Breathing Engines* **97-7085**, 463–473, (2008).

[99] Lin, K.C., Tam, C.J., Jackson, K.R., Eklund, D.R., Jackson, T.A., "Characterization of Shock Train Structures Inside Constant-Area Isolators of Model Scramjet Combustors," *AIAA paper 2006-0816*, 1442–1452, (2006).

[100] Sridhar, T., Chandrabose, G., Thanigaiarasu, S., "Numerical Investigation of Geometrical Influence On Isolator Performance," *IJTARME* **2**, 7–12, (2013).

[101] Green, J.E., "Interactions between shock waves and turbulent boundary layers," *Progress in Aerospace Sciences* **101**, 235–340, (1970).

[102] Cuffel, R.F., Back, L.H., "Flow and Heat Transfer Measurement in a Pseudo-Shock Region with Surface Cooling," *AIAA Journal* **14(12)**, 1716–1722, (1976).

[103] Inger, G.R., Lynch, F.T., Fancher, M.F., "Theoretical and experimental study of nonadiabatic transonic shock/boundary-layer interaction," *AIAA Journal* **23(10)**, 1476–1482, (1985).

[104] Castagna, A., "Experimental Research on the Transformation of Energy of a Gas Flowing in a Pipe," *Atti della Reale Accademia delle Scienze di Torino* **70**, 284–317, (1935).

[105] Tamaki, T., Tomita, T., Yamane, R., "Research on Pseudo-Shock (1st Report, λ-Type Pseudo-Shock)," *Bulletin of the JSME* **13(55)**, 191–226, (1970).

[106] Tamaki, T., Tomita, T., Yamane, R., "A Research on Pseudo-Shock (2nd Report, χ-Type Pseudo-Shock)," *Bulletin of the JSME* **14(74)**, 807–817, (1971).

[107] Waltrup, P.J., Billig, F.S., "Structure of Shock Waves in Cylindrical Ducts," *AIAA Journal* **11(10)**, 1404–1408, (1973).

[108] Waltrup, P.J., Billig, F.S., "Prediction of Precombustion Wall Pressure Distributions in Scramjet Engines," *AIAA Journal of Spacecraft and Rockets* **10(9)**, 620–622, (1973).

[109] Waltrup, P.J., Cameron, J.M., "Wall Shear and Boundary-Layer Measurements in Shock Separated Flow," *AIAA Journal* **12(6)**, 878–880, (1974).

[110] Billig, F.S., "Research on Supersonic Combustion," *AIAA Aerospace Sciences Meeting, Reno, NV*, (1992).

[111] Wang, C.P., Zhang, K.Y., Cheng, K.M., "Pressure Distribution Measurements in Scramjet Isolators under Asymmetric Supersonic Flow," *44th AIAA Aerospace Science Meeting and Exhibit*, (2006).

[112] Zimont, V.L., Ostras, V.N., "Calculation of pseudo-shocks in a cylindrical duct," *Fluid Mechanics Soviet Research* **5(2)**, 78–87, (1976).

[113] Shchetinkov, E.S., "Piecewise-one-dimensional models of supersonic combustion and pseudo-shock in a duct," *Combustion, Explosion and Shock Waves* **9(4)**, 409–417, (1973).

[114] Nagai, M., Yaga, M., "On the pseudo-shock wave relations," *In: Kral, L.D., Spina, E.F., Arakawa, C., Transitional and turbulent compressible flows, The American Society of Mechanical Engineers* **224**, 103–108, (1995).

[115] Matsuo, K., Miyazato, Y., Kim, H.D., "Mass averaging pseudo-shock model in a straight flow passage," *Proceedings of the Institution of Mechanical Engineers* **213(6)**, 365–375, (1999).

[116] Ortwerth, P.J., "Scramjet Vehicle Integration," *In: Scramjet Propulsion, Progress in Astronautics and Aeronautics*, Washington DC, Chapter 17, (2001).

[117] Tu, Q., Segal, C., "Isolator/Combustion Chamber Interactions During Supersonic Combustion," *Journal of Propulsion and Power* **26(1)**, 182–186, (2010).

[118] Auslender, A.H., "An Analytic Performance Investigation of Mechanically Back- Pressured Ramjet Data," *JANNAF 34th*, (1997).

[119] Fischer, C., Olivier, H., "Experimental investigation of wall and total temperature influence on a shock train," *AIAA Journal* **52(4)**, 757–766, (2014).

[120] White, M.E., Drummond, J.P., Kumar, A., "Evolution and Application of CFD Techniques for Scramjet Engine Analysis," *Journal of Propulsion and Power* **3(5)**, 423–439, (1987).

[121] Mousavi, S.M., Roohi, E., "Three dimensional investigation of the shock train structure in a convergent-divergent nozzle," *Acta Astronautica* **105(1)**, 117–127, (2014).

[122] Baurle, R.A., Middleton, T.F., Wilson, L.G., "Reynolds-Averaged Turbulence Model Assessment for a Highly Back-Pressured Isolator Flowfield," *JANNAF 45th Combustion Meeting Joint Subcommittee Meeting, Monterey, CA*, (2012).

[123] Greene, B.R., Clemens, N.T., Micka, D., "Control of shock boundary layer interaction using pulsed plasma jets," *51st AIAA Aerospace Sciences Meeting including the New Horizons Forum and Aerospace Exposition*, (2013).

[124] Im, S.K., Do, H., Godfrey Mungal, M., Cappelli, M.A., "Experimental study and plasma control of an unstarting supersonic flow," *6th AIAA Flow Control Conference*, (2012).

[125] Stanewsky, E., Smith, G.E.,"Adaptive wing and flow control technology," *Progress in Aerospace Sciences* **37(7)**, 583–667, (2001).

[126] Haack, S., Taylor, T., Cybyk, B., Foster, C., Alvi, F., "Experimental estimation of SparkJet efficiency," *AIAA paper 2011-3997*, 971–983, (2011).

[127] Prandtl, L., "Über Flüssigkeitsbewegung bei sehr kleiner Reibung," *Ludwig Prandtl Gesammelte Abhandlungen zur angewandten Mechanik, Hydro- und Aerodynamik*, 575–584, (1961).

[128] Ryu, K.J., Lim, S., Song, D.J., "A computational study of the effect of angles of attack on a double-cone type supersonic inlet with a bleeding system," *Computers & Fluids* **50(1)**, 72–80, (2011).

[129] Tindell, R. H., "Highly compact inlet diffuser technology," *Journal of Propulsion and Power* **4(6)**, 557–563, (1988).

[130] Kodera, M., Tomioka, S., Kanda, T., Mitani, T., Kobayashi, K., "Mach 6 test of a scramjet engine with boundary-layer bleeding and two-staged fuel injection," *AIAA paper 2003-7049*, (2003).

[131] Weise, A., "The separation of flow due to compressibility shock," *NACA Technical Memorandum* **1152**, (1947).

[132] Cohen, C.B., Valerino, A.S., "Investigation of operating pressure ratio of a supersonic wind tunnel utilizing distributed boundary-layer suction in test section," *NACA Research Memorandum E50H04*, (1950).

[133] Gefroh, D., Loth, E., Dutton, C., Hafenrichter, E., "Aeroelastically deflecting flaps for shock/boundary-layer interaction control," *Journal of Fluids and Structures* **17(7)**, 1001–1016, (2003).

[134] Anderson, J.D.J., "Airframe/Propulsion Integration of Supersonic Vehicles," *26th AIAA/SAE/ASME/ASEE Joint Proportion Conference, Orlando, Fl*, (1990).

[135] Harloff, G.J., Smith, G.E.,"Supersonic-inlet boundary-layer bleed flow," *AIAA Journal* **34(4)**, 778–785, (1996).

[136] Schulte, D., Henckels, A., Schell, I., "Boundary Layer Bleed in Hypersonic Inlets," *New Results in Numerical and Experimental Fluid Mechanics - Contributions to the 10th AG STAB/DGLR Symposium Braunschweig, Germany* **60**, 296–303, (1997).

[137] Kornilov, V.I., "Current state and prospects of researches on the control of turbulent boundary layer by air blowing," *Progress in Aerospace Sciences* **76**, 1–23, (2015).

[138] Paynter, G.C., Treiber, D.A., Kneeling, W.D., "Modeling supersonic inlet boundary-layer bleed roughness," *Journal of Propulsion and Power* **9(4)**, 622–627, (1993).

[139] Loth, E., "Smart Mesoflaps for Control of Shock Boundary-Layer Interactions," *AIAA paper 2000-2476*, (1988).

[140] McCormick, D.C., "Shock/boundary-layer interaction control with vortex generators and passive cavity," *AIAA Journal* **31(1)**, 91–96, (1993).

[141] Smith, A.N., Babinsky, H., Fulker, J., Ashill, P.R., "Shockwave/boundary-layer interaction control using streamwise slots in transonic flows," *Journal of Aircraft* **41(3)**, 540–546, (2004).

[142] Srinivasan, K.R., Loth, E., Dutton, C.J., "Aerodynamics of Recirculating Flow Control Devices for Normal Shock/Boundary-Layer Interactions," *AIAA Journal* **44(4)**, 751–763, (2006).

[143] Hafenrichter, E., Lee, Y., Dutton, J., Loth, E., "Normal Shock/Boundary-Layer Interaction Control Using Aeroelastic Mesoflaps," *Journal of Propulsion and Power* **19(3)**, 464–472, (2003).

[144] Holden, H., Babinsky, H., "Effect of microvortex generators on separated normal shock/boundary layer interactions," *Journal of Aircraft* **44(1)**, 170–174, (2007).

[145] Hadjadj, A., Dussauge, J.P., "Shock wave boundary layer interaction," *Shock Waves* **19**, 449–452, (2009).

[146] Saad, M.R., Zare-Behtash, H., Che Idris, A., Kontis, K., "Micro-ramps for hypersonic flow control," *Micromachines* **3**, 364–378, (2012). Shock Control Bumps," *Journal of Aircraft* **49(5)**, 1222–1233, (2012).

[147] Caraballo, E., Webb, N., Little, J., Kim, J.H., Samimy, M., "Supersonic Inlet Flow Control Using Plasma Actuators," *AIAA paper 2009-0724*, (2009).

[148] Babinsky, H., Li, Y., Ford, C.W.P., "Microramp Control of Supersonic Oblique Shock-Wave/Boundary-Layer Interactions," *AIAA Journal* **47(3)**, 668–675, (2009).

[149] Ogawa, H., Babinsky, H., Pätzold, M., Lutz, T., "Shock-Wave/Boundary-Layer Interaction Control Using Three-Dimensional Bumps for Transonic Wings," *AIAA Journal* **46(6)**, 1442–1452, (2008).

[150] Ashill, P.R., Fulkner, J.L., Shires, A., "A Novel Technique for Controlling Shock Strength of Laminar-Flow Aerofoil Sections," *Proceedings 1st European Forum on Laminar Flow Technology, Hamburg*, 175-183, (1992).

[151] Ogawa, H., Babinsky, H., "Shock/boundary-layer interaction control using three-dimensional bumps in supersonic engine inlets," *46th AIAA Aerospace Sciences Meeting and Exhibit, Reno, NV*, (2008).

[152] Bruce, P.J.K., Babinsky, H., "Experimental Study into the Flow Physics of Three-Dimensional Shock Control Bumps," *Journal of Aircraft* **49(5)**, 1222–1233, (2012).

[153] Lim, S., Koh, D.H., Kim, S.D., Song, D.J., "A computational study on the efficiency of boundary layer bleeding for the supersonic bump type inlet," *47th AIAA Aerospace Sciences Meeting including the New Horizons Forum and Aerospace Exposition*, (2009).

[154] Zhang, Y., Tan, H.J., Tian, F.C., Zhuang, Y., "Control of Incident Shock/Boundary-Layer Interaction by a Two-Dimensional Bump," *AIAA Journal* **52(4)**, 767–776, (2014).

[155] Leconte, J., "On the Influence of Musical Sounds on the Flame of a Jet of Coal-Gas," *Philosophical Magazine* **15**, 235–239, (1858).

[156] Sahoo, D., Annaswamy, A.M., Alvi, F., "Active Store Trajectory Control in Supersonic Cavities Using Microjets and Low-Order Modeling," *AIAA Journal* **45(3)**, 516–531, (2007).

[157] Kumar, V., Farrukh, A., "Efficient Control of Separation using Microjets," *AIAA paper 2005-4879*, (2005).

[158] Samimy, M., Kearney-Fisher, M., Kim, J., Sinha, A., "High speed and High Reynolds Number Jet Control Using Arc Filament Plasma Actuators for Noise Mitigation and for Flow and Noise Diagnostics," *J49th Aerospace Sciences Meeting, Orlando, FL*, (2011).

[159] Ali, M.Y., Solomon, J.T., Gustavsson, J., Kumar, R., Alvi, F.S., "Control of Resonant Flow Inside a Supersonic Cavity Using High Bandwidth Micro-Actuators," *AIAA paper 2010-1198*, (2010).

[160] Ukai, T., Zare-Behtash, H., Erdem, E., Kin Hing, L., Kontis, K., Obayashi, S., "Effectiveness of jet location on mixing characteristics inside a cavity in supersonic flow," *Experimental Thermal and Fluid Science* **52**, 59–67, (2014).

[161] Ukai, T., Zare-Behtash, H., Kin Hing, L., Kontis, K., Obayashi, S., "Effects of dual jets distance on mixing characteristics and flow path within a cavity in supersonic crossflow," *International Journal of Heat and Fluid Flow* **50**, 254–262, (2014).

[162] Zare-Behtash, H., Kin Hing, L., Kontis, K., Ukai, T., Obayashi, S., "Transverse jet-cavity interactions with the influence of an impinging shock," *International Journal of Heat and Fluid Flow* **53**, 146–155, (2015).

[163] Utkin, Y.G., Keshav, S., Kim, J.H., Kastner, J., Adamovich, I.V., Samimy, M., "Development and use of localized arc filament plasma actuators for high-speed flow control," *Journal of Physics D Applied Physics* **40(3)**, 685–694, (2003).

[164] Samimy, M., Kim, J.H., Kastner, J., Adamovich, I., Utkin, Y., "Active control of high-speed and high-Reynolds-number jets using plasma actuators," *Journal of Fluid Mechanics* **578**, 305–330, (2007).

[165] MacHeret, S.O., Shneider, M.N., Miles, R.B., "Magnetohydrodynamic Control of Hypersonic Flows and Scramjet Inlets Using Electron Beam Ionization," *AIAA Journal* **40(1)**, 74–81, (2002).

[166] Kalra, C.S., Zaidi, S., Miles, R.B., "Shock Wave Induced Turbulent Boundary Layer Separation Control with Plasma Actuators," *46th AIAA Aerospace Sciences Meeting and Exhibit*, (2008).

[167] Roupassov, D.V., Nikipelov, A.A., Nudnova, M.M., Starikovskii, A.Y., "Flow Separation Control by Plasma Actuator with Nanosecond Pulsed-Periodic Discharge," *AIAA Journal* **47(1)**, 168–185, (2009).

[168] Adelgren, R.G., Elliott, G.S., Crawford, J.B., Carter, C.D., Donbar, J.M., Grosjean, D.F., "Axisymmetric Jet Shear-Layer Excitation Induced by Laser Energy and Electric Arc Discharges," *AIAA Journal* **43(4)**, 776–791, (2005).

[169] Grossman, K.R., Cybyk, B.Z., Rigling, M.C., VanWie, D.M., "Characterization of sparkjet actuators for flow control," *42nd AIAA Aerospace Sciences Meeting and Exhibit, Reno, NV*, 3957–3964, (2004).

[170] Narayanaswamy, V., Raja, L.L., Clemens, N.T., "Control of a shock/boundary-layer interaction by using a pulsed-plasma jet actuator," *AIAA Journal* **50(1)**, 246–249, (2012).

[171] Velkoff, H., Ketchman, J., "Effect of an Electrostatic Field on Boundary Layer Transition," *AIAA Journal* **6(7)**, 1381–1383, (1968).

[172] Léger, L., Moreau, E., Artana, G., Touchard, G., "Influence of a DC corona discharge on the airflow along an inclined flat plate," *Journal of Electrostatics* **50–51**, 300–306, (2001).

[173] Opaits, D.F., Roupassov, D.V., Saddoughi, S.G., Starikovskaia, S.M., Zavialov, I.N., Starikovskii, A.Y., "Plasma Control of Boundary Layer Using Low-Temperature Non-Equilibrium Plasma of Gas Discharge," *AIAA paper 2005-1180*, (2005).

[174] Tan, H.J., Li, C.H., Zhang, Y., "Investigation of a Fluidic Shock Control Method for Hypersonic Inlets," *Journal of Propulsion and Power* **26(5)**, 1072–1083, (2010).

[175] Hutzel, J.R., Decker, D.D., Cobb, R.G., King, P.I., Veth, M.J., "Scramjet isolator shock train location techniques," *49th AIAA Aerospace Sciences Meeting including the New Horizons Forum and Aerospace Exposition, Orlando, Florida*, (2011).

[176] Le, D.B., Goyne, C.P., Krauss, R.H., "Shock Train Leading-edge detection in a dual-mode scramjet," *Journal of Propulsion and Power* **24(5)**, 1035–1041, (2008).

[177] Chang, J., Li, B., Bao, W., Yu, D., "Shock train leading-edge detection in an isolator using genetic algorithm," *Proceedings of the Institution of Mechanical Engineers, Part G. Journal of Aerospace Engineering* **226(11)**, 1424–1431, (2012).

[178] Hunter, L.G., Tripp, J.M., Howlett, D.G., "Supersonic inlet study using the Navier-Stokes equations," *Journal of Propulsion and Power* **2(2)**, 181–187, (1986).

[179] Chan, W.Y.K., Jacobs, P.A., Mee, D.J., "Suitability of the k-ε turbulence model for scramjet flowfield simulations," *International Journal for Numerical Methods in Fluids* **70(4)**, 493–514, (2012).

[180] Quaatz,J.F., Giglmaier, M., Hickel, S., Adams, N.A., "Large-eddy simulation of a pseudo-shock system in a Laval nozzle," *International Journal of Heat and Fluid Flow* **49**, 108–115, (2014).

[181] Ferri, A., "Hypersonic flight testing," *International Science and Technology* **28**, 64–76, (1964).

[182] Krishnan, L., Sandham, N.D., Steelant, J., "Shock-Wave/Boundary-Layer Interactions in a Model Scramjet Intake," *AIAA Journal* **47(7)**, 1680–1691, (2009).

[183] Lomax, H., Pulliam, T.H., Zingg, D.W., "Fundamentals of Computational Fluid Dynamics," *Springer*, Berlin, (2001).

[184] Minucci, M.A.S., Nagamatsu, H.T., "Investigation of a two-dimensional scramjet inlet, M_∞= 8-18 and T_0= 4100 K," *Journal of Propulsion and Power* **9(1)**, 139–145, (1993).

[185] Boon, S., Hillier, R., "Hypersonic Inlet Flow Analysis at Mach 5, 6 and 7," *44th AIAA Aerospace Sciences Meeting and Exhibit, Reno, NV* **1**, 161–172, (2006).

[186] Koo, H., Raman, V., "Large-Eddy Simulation of a Supersonic Inlet-Isolator," *AIAA Journal* **50(7)**, 1596–1613, (2012).

[187] Hunter, L.G., Couch, B.D., "A CFD Study of Precombustion Shock-Trains From Mach 3–6," *AIAA paper 90-2220*, (1990).

[188] Mittal, S., Yadav, S., "Computation of flows in supersonic wind-tunnels," *Computer Methods in Applied Mechanics and Engineering* **191(6–7)**, 611–634, (2001).

[189] Kumar, A., "Analysis Of The Scramjet Inlet Flow Field Using Two-Dimensional Navier-Stokes Equations," *NASA Contractor Reports*, (1982).

[190] Dutton, J.C., Carroll, B.F., "Numerical and Experimental Investigation of Multiple Shock Wave/Turbulent Boundary Layer Interactions in a Rectangular Duct," *UILU ENG 88-4015, Gas Dynamics Lab., University of Illinois*, (1988).

[191] Wilcox, D.C., "More advanced applications of the multiscale model for turbulent flows," *AIAA, Aerospace Sciences Meeting, 26th, Reno, NV*, (1988).

[192] Tian, Y., Yang, S., Le, J., "Numerical study on effect of air throttling on combustion mode formation and transition in a dual-mode scramjet combustor," *Aerospace Science and Technology* **52**, 173–180, (2016).

[193] Kamali, R., Mousavi, S.M., Binesh, A.B., "Three dimensional CFD investigation of shock train structure in a supersonic nozzle," *Acta Astronautica* **116**, 56–67, (2015).

[194] *CD-Adapco STAR-CCM+ documentation*, (2015).

[195] Schlichting, H. Gersten, K., "Boundary-Layer Theory," *Springer*, Berlin, (2000).

[196] Persen, L.N. , "Introduction to boundary layer theory," *Tapir*, Norway, (1972).

[197] Wilcox, D.C., "Turbulence Modeling for CFD," *DCW Industries, Inc.*, La Canada, California, (1998).

[198] White, F.M., "Viscous Fluid Flow," *McGraw-Hill*, New York, (2005).

[199] Pope, S.B., "Turbulent Flows," *Cambridge University Press*, Cambridge (2000).

[200] Anderson, J.D.Jr., "Hypersonic and High Temperature Gas Dynamics," *McGraw-Hill*, New York, (1989).

[201] Wilcox, D.C., "Reassessment of the scale-determining equation for advanced turbulence models," *AIAA Journal* **26(11)**, 1299–1310, (1988).

[202] *FLUENT documentation*, (2001).

[203] Barber, T.J., Cox, G.B., "Hypersonic vehicle propulsion - A computational fluid dynamics application case study," *Journal of Propulsion and Power* **5(4)**, 492–501, (1989).

[204] Baldwin, B., Lomax, H., "Thin-layer approximation and algebraic model for separated turbulent flows," *AIAA paper 78-257*, (1978).

[205] Visbal, M., Knight, D., "The Baldwin-Lomax Turbulence Model for Two-Dimensional Shock-Wave/Boundary-Layer Interactions," *AIAA Journal* **22(7)**, 921–928, (1984).

[206] Liou, M.S., Adamson Jr, T.C., "Interaction between a normal shock wave and a turbulent boundary layer at high transonic speeds. Part II: Wall shear stress," *Zeitschrift für angewandte Mathematik und Physik* **31(2)**, 227–246, (1980).

[207] Knight, D.D., "Calculation of Three-Dimensional Shock/Turbulent Boundary-Layer Interaction Generated by Sharp Fin," *AIAA Journal* **23(12)**, 1885–1891, (1985).

[208] Hsia, Y.C., "Full Navier-Stokes analysis of an axisymmetric scramjet inlet," *Journal of Propulsion and Power* **9(6)**, 827–833, (1993).

[209] York, B., Knight, D., "Calculation of two-dimensional turbulent boundary layers using the Baldwin-Lomax model," *AIAA Journal* **23(12)**, 1849–1850, (1985).

[210] Wilcox, D.C., "Formulation of the k-ω turbulence model revisited ," *AIAA Journal* **46(11)**, 2823–2838, (2008).

[211] Rienitz., J., "Optical inhomogeneities: schlieren and shadowgraph methods in the seventeenth and eighteenth centuries," *Endeavour* **21(2)**, 77–81, (1997).

[212] Rienitz., J., "Schlieren experiment 300 years ago," *Nature* **254(5498)**, 293–295, (1975).

[213] Settles, G.S., "Schlieren and shadowgraph techniques: visualizing phenomena in transport media," *Springer*, Berlin, (2001).

[214] Kleine, H., Grönig, H., Takayama, K., "Simultaneous Shadow, Schlieren and Interferometric Visualization of Compressible Flows," *Optics and Lasers in Engineering* **44(3-4)**, 170–189, (2006).

[215] Vasil'ev, L.A.," "Schlieren Methods," *Israel Program for Scientific Translations*, (1971).

[216] Bell, J.H., Schairer, E.T., Hand, L.A.,Mehta, R.D., "Surface Pressure Measurements Using Luminescent Coatings," *Annual Review of Fluid Mechanics* **33**, 155–206, (2001).

[217] Bell, J.H., McLachlan, B.G., "Pressure-sensitive paint in aerodynamic testing," *Experimental Thermal and Fluid Science* **10(4)**, 470–485, (1995).

[218] Liu, T., Sullivan, J.P., "Pressure and Temperature Sensitive Paints," *Springer*, Berlin, (2005).

[219] Peterson, J.I., Fitzgerald, R.V., "New technique of surface flow visualization based on oxygen quenching of fluorescence," *Review of Scientific Instruments* **51**, 670–671, (1980).

[220] Strozik, M., Majkut, M., Dykas, S., "Measuring System for Pressure Sensitive Paint (PSP) Calibration in the Range of Low Pressure Gains," *Modern Applied Science* **9(2)**, 116–122, (2015).

[221] Kavandi, J., Callis, J., Gouterman, M., Khalil, G., Wright, D., Green, E., Burns, D., McLachlan, B., "Luminescent barometry in wind tunnels," *Review of Scientific Instruments* **61(11)**, 3340–3347, (1990).

[222] Gregory, J.W., Asai, K., Kameda, M., Liu, T., Sullivan, J.P., "A Review of Pressure-Sensitive Paint for High Speed and Unsteady Aerodynamics," *Proceedings of the Institution of Mechanical Engineers, Part G, Journal of Aerospace Engineering* **222(2)**, 249–290, (2008).

[223] Huang, C.Y., Gregory, J.W., Sullivan, J.P., "Flow visualization and pressure measurement in micronozzles," *Journal of Visualization* **10**, 123–130, (2007).

[224] Klein, C., Engler, R.H., Henne, U., Sachs, W.E., "Application of pressure-sensitive paint for determination of the pressure field and calculation of the forces and moments of models in a wind tunnel," *Experiments in Fluids* **39(2)**, 475–483, (2005).

[225] Zare-Behtash, H., Gongora-Orozco, N., Kontis, K., Holder, S.J., "Application of novel pressure-sensitive paint formulations for the surface flow mapping of high-speed jets," *Experimental Thermal and Fluid Science* **33(5)**, 852–864, (2009).

[226] Sakaue, H., "Anodized aluminum pressure sensitive paint for unsteady aerodynamic applications," *PhD thesis, Purdue University*, USA, (2003).

[227] Merienne, M.C., Coponet, D., Luyssen, J.M., "Transient Pressure-Sensitive-Paint Investigation in a Nozzle," *AIAA Journal* **50(7)**, 1453–1461, (2012).

[228] Liu, T., Campbell, B.T., Sullivan, J.P., "Fluorescent paint for measurement of heat transfer in shock-turbulent boundary layer interaction," *Experimental Thermal and Fluid Science* **10**, 101–112, (2011).

[229] Quinn, M.K., Yang, L., Kontis, K., "Pressure-Sensitive Paint: Effect of Substrate," *Sensors* **11(12)**, 11649–11663, (2011).

[230] Klein, C., Engler, R.H., Fonov, S.D., Trinks, O., "Pressure sensitive paint for oscillating pressure fields measurements," *ICIASF 99. 18th International Congress on Instrumentation in Aerospace Simulation Facilities* **15**, 1–4, (1999).

[231] Kameda, M., Tezuka, N., Hangai, T., Asai, K., Nakakita, K., Amao, Y., "Adsorptive pressure-sensitive coatings on porous anodized aluminium," *Measurement Science and Technology* **15**, 489–500, (2004).

[232] Asai, K., Amao, Y., Iijima, Y., Okura, I., Nishide, H., "Novel Pressure-Sensitive Paint for Cryogenic and Unsteady Wind-Tunnel Testing," *Journal of Thermophysics and Heat Transfer* **16(1)**, 109–115, (2002).

[233] Schairer, E.T., "Optimum thickness of pressure-sensitive paint for unsteady measurements," *AIAA Journal* **40(11)**, 2312–2318, (2011).

[234] Baron, A.E., Danielson, J.D.S., Gouterman, M., Wan, J.R., Callis, J.B., McLachlan, B., "Submillisecond response times of oxygen-quenched luminescent coatings," *Review of Scientific Instruments* **64(12)**, 3394–3402, (1993).

[235] Scroggin, A.M., Slamovich, E.B., Crafton, J.W., Lachendro, N., Sullivan, J.P., "Porous polymer/ceramic composites for luminescence-based temperature and pressure measurement," *Proceedings of the Materials Research Society Symposium* **560**, 347–352, (1999).

[236] Asai, K., Yorita, D., "Unsteady PSP Measurement in Low-Speed Flow - Overview of Recent Advancement at Tohoku University," *AIAA paper 2011-847*, (2011).

[237] Yang, L., Zare-Behtash, H., Erdem, E., Kontis, K., "Investigation of the double ramp in hypersonic flow using luminescent measurement systems," *Experimental Thermal and Fluid Science* **40**, 50–56, (2012).

[238] Merienne, M.C., Coponet, D., Luyssen, J.M., "Unsteady Pressure Field Investigation in a Nozzle by Using Anodized-Aluminum PSP Technique Under Supersonic Flow Conditions," *AIAA paper 2008-3946*, (2008).

[239] Sakaue, H., Morita, K., Iijima, Y., Sakamura, Y., "Response time scales of anodized-aluminum pressure-sensitive paints," *Sensors and Actuators A: Physical* **199(1)**, 74–79, (2013).

[240] Nakakita, K., Yamazaki, T., Asai, K., Teduka, N., Fuji, A., Kameda, M., "Pressure sensitive paint measurement in a hypersonic shock tunnel," *AIAA paper 2000-2523*, (2000).

[241] Egami, Y., Ueyama, J., Furukawa, S., Kameya, T., Matsuda, Y.,Yamaguchi, H., Niimi, T., "Development of fast response bi-luminophore pressure-sensitive paint by means of an inkjet printing technique," *Measurement Science and Technology* **26(6)**, (2015).

[242] Sakaue, H., Morita, K., Iijima, Y., Sakamura, Y., "Luminophore application method of anodized aluminum pressure sensitive paint as a fast responding global pressure sensor," *Review of Scientific Instruments* **76(8)**, 1–6, (2005).

[243] Kameda, M., Tabei, T., Nakakita, K., Sakaue, H., Asai, K., "Image Measurement of Unsteady Pressure Fluctuation by a Pressure-Sensitive Coating on Porous Anodized Aluminum," *Measurement Science and Technology* **16(12)**, 2517–2524, (2005).

[244] Schanze, K.S., Carroll, B.F., Korotkevitch, S, Morris, M.J., "Temperature dependence of pressure sensitive paints," *AIAA Journal* **35(2)**, 306–310, (1997).

[245] Raju, C., Viswanath, P.R., "Pressure-sensitive paint measurements in a blowdown wind tunnel," *Journal of Aircraft* **42(4)**, 908–915, (2005).

[246] *PSP Course notes, DLR Institute of Aerodynamics and Flow Technology, Göttingen, Germany*, (2015).

[247] Peng, D., Gregory, J.W., Crafton, J., Fonov, S., "Development of a Two Layer Dual-Luminophore Pressure Sensitive Paint for Unsteady Pressure Measurements," *AIAA paper 2010-4918*, (2010).

[248] Khalil, G.E., Coston, C., Crafton, J., Jones, G., Grenoble, S., Gouterman, M., Callis, J.B., Dalton, L.R., "Dual-luminophor pressure-sensitive paint I. Ratio of reference to sensor giving a small temperature dependency," *Sensors and Actuators, B: Chemical* **97**, 13–21, (2004).

[249] Goss, L., Jones, G., Crafton, J., Fonov, S., "Temperature Compensation for Temporal (Lifetime) Pressure Sensitive Paint Measurements," *AIAA paper 2005-1027*, (2005).

[250] Merienne, M.C., Le Sant, Y., "Reliable PSP Application and Data Processing at Low Speed Flow Conditions," *AIAA paper 2006-3632*, (2006).

[251] Mitsuo, K., Kurita, M., Nakakita, K., Fujii, K., Watanabe, S., Katagiri, S., Wada, Y., "Development of Bi-Luminophore Pressure-Sensitive Paint Systems," *22nd International Congress on Instrumentation in Aerospace Simulation Facilities*, (2007).

[252] Beck, W.H., Henne, U., Hirschen, C., "Application of the Pressure Sensitive Paint Technique to a Scramjet Nozzle Flow in the DLR Hypersonic Wind Tunnel," *14th Int Symp on Applications of Laser Techniques to Fluid Mechanics, Lisbon, Portugal*, (2008).

[253] Mochizuki, D., Tamura, S., Yasutake, H., Kataoka, T., Mitsuo, K., Wada, Y., "A photostable bi-luminophore pressure-sensitive paint measurement system developed with mesoporous silica nanoparticles," *Journal of Nanoscience and Nanotechnology* **13**, 2777–2781, (2013).

[254] Woodmansee, M., Dutton, J., "CFD Modeling of an Isolator Shock Train in a Scramjet Engine," *Experiments in Fluids* **24(2)**, 163–174, (1990).

[255] Gardner, A.D., Klein, C., Sachs, W.E., Henne, U., Mai, H., Richter, K., "Investigation of three-dimensional dynamic stall on an airfoil using fast-response pressure-sensitive paint," *Experiments in Fluids* **20(55)**, (2014).

[256] Gongora-Orozco, N., Zare-Behtash, H., Kontis, K., "Effects of filters on the performance and characteristics of pressure-sensitive paints," *Measurement Science and Technology* **20(7)**, 1–6, (2009).

[257] *Courtesy of NASA*.

[258] Mikhail, M.N., "Optimum Design of Wind Tunnel Contractions," *AIAA Journal* **17(5)**, 471–477, (1947).

[259] Pope, A., Goin, K.L., "High speed wind tunnel testing," *John Wiley & Sons*, New York, (1965).

[260] Wang, D., Zhao, W., Sugiyama, H., Tojo, A., "Study on Internal Supersonic Flows with Pseudo shock Wave Using Liquid Crystal Flow Visualization Method," *Chinese Journal of Aeronautics* **18(2)**, 102–107, (2005).

[261] Giuni, M., "Preliminary design of a transonic wind tunnel,", *MSc thesis, University of Glasgow & Politecnico di Milano*, Milano, (2010).

[262] Pankhurst, R.C., Holder, D.W., "Wind-tunnel technique : an account of experimental methods in low- and high-speed wind tunnels," *Sir Isaac Pitman & Sons, Ltd.*, London (1952).

[263] Stever, H.G., Rathbun, K.C., "Theoretical and Experimental Investigation of Condensation of Air in Hypersonic Wind Tunnels," *NACA-TN-2559*, (1951)

[264] Schmitz, M.C., Bissinger, N.C., "Design and Testing of a 2-D Fixed Geometry Hypersonic Intake," *AIAA paper 98-1529*, (1998).

[265] Mehta, R.D., "Detrimental Effects of Almost Immeasurably Small Freestream Nonuniformities Generated by Wind-Tunnel Screens," *AIAA Journal* **36(3)**, 379–386, (1998).

[266] Kohama, Y., Kobayashi, R., Ito, H., "Tohoku University low-turbulence wind tunnel," *AIAA paper 92-3913*, (1992).

[267] Kulkarni, V.,Sahoo, N., Chavan, S.D., "Simulation of honeycomb-screen combinations for turbulence management in a subsonic wind tunnel," *Journal of Wind Engineering and Industrial Aerodynamics* **99(1)**, 37–45, (2011).

[268] Scheiman, J., Brooks, J.D., "Comparison of experimental and theoretical turbulence reduction from screens, honeycomb, and honeycomb-screen combinations," *Journal of Aircraft* **18(8)**, 638–643, (1981).

[269] Li, C., Liu, Y., Cheung, J.C.K., "Wind tunnel test of honeycomb in improving flow quality," *Advanced Materials Research* **774–776**, 275–278, (2013).

[270] Mehta, R.D., Bradshaw, P., "Design Rules for Small Low-Speed Wind Tunnels," *The Aeronautical Journal - Royal Aeronautical Society* **73**, 443–449, (1979).

[271] Bradshaw, P., Pankhurst, R.C., "The Design of Low-Speed Wind Tunnels," *Progress in Aerospace Sciences* **1**, (1964).

[272] Farell, C.C., "Experiments on turbulence management using screens and honeycombs," *Journal of Fluids Engineering, Transactions of the ASME* **118(1)**, 26–32, (1996).

[273] Groth, J., Johansson, A.V., "Turbulence reduction by screens," *Journal of Fluid Mechanics* **197**, 139–155, (1988).

[274] Collar, A.R., "The effect of a gauze on the velocity distribution in a uniform duct," *A.R.C.R. & M. 1867*, (1939).

[275] Mehta, R.D., "A turbulent boundary layer perturbed by a screen," *AIAA Journal* **23(9)**, 1335–1342, (1985).

[276] Wieghardt, K.E.G., "On the Resistance of Screens," *Aeronautical Quarterly* **4**, 186–192, (1953).

[277] Hancock, P.E., "Plane multiple screens in non-uniform flow, with particular application to wind tunnel settling chamber screens," *European Journal of Mechanics - B/Fluids* **17(3)**, 357–369, (1998).

[278] Dryden, H.L., Schubauer,G.B., "The Use of Damping Screens for the Reduction of Wind Tunnel Turbulence," *Journal of the Aeronautical Sciences* **14(4)**, 221–228, (1947).

[279] Tan-Atichat, J., Nagib, H.M., Loehrke, R.I., "Interaction of free-stream turbulence with screens and grids: a balance between turbulence scales," *Journal of Fluid Mechanics* **114**, 501–528, (1982).

[280] Liepman, H.P., "An analytic design method for a two-dimensional asymmetric curved nozzle" *Air Research and Development Command U.S. Air Force Contract 460-31-14*, (1953).

[281] Chan, W.Y.K., Smart, M.K., Jacobs, P.A., "Flowpath design of an axisymmetric Mach 7.0 nozzle for T4," *UQ HIFiRE8 Technical Report 2013/01*, (2013).

[282] Cain, T.M., Huntington-Thresher, W.K.E., Mariott, P.G., "Final report on the centre-body nozzle design," *Fluid Gravity Engineering LTD*, (1994).

[283] Foelsch, K., "A New method of designing two-dimensional Laval nozzles for a parallel and uniform jet," *North American Aviation Report NA-46-235-2*, (1946).

[284] Crown, J.C., "Supersonic Nozzle Design," *NACA-TN-1651*, (1948).

[285] Puckett, A.E., "Supersonic Nozzle Design," *Journal of Applied mechanics* **13(4)**, 265–270, (1946).

[286] Stokes, G.M., "Description of a 2-Foot Hypersonic Facility at the Langley Research Center," *NASA TN D-1035*, (1961).

[287] Friedrichs, K.O., "On supersonic compressors and nozzles," *AMP report 82, AMG-NYU 77*, (1944).

[288] Nilson, E.N., "Design of an Inlet for a Two-Dimensional Supersonic Nozzle," *Journal of the Aeronautical Sciences* **22(10)**, 709–709, (1955).

[289] Beckwith, I.E., Moore, J.A., "An accurate and rapid method for the design of supersonic nozzles," *NACA-TN-3322*, (1955).

[290] Hadamard, J., "Leçons sur la propagation des ondes et les equations de l'hydrodynamique," *Hermann, Paris*, (1903).

[291] Anderson, J.D., "Modern compressible flow, with historical perspective," *McGraw-Hill*, New York, (1990).

[292] Al-Ajlouni, M., "An Automaic Method for Creating the Profile of Supersonic Convergent-Divergent Nozzle," *Jordan Journal of Mechanical and Industrial Engineering* **4(34)**, 404–411, (2010).

[293] Zebbiche, T., Youbi, Z., "Supersonic Two-Dimensional Minimum Length Nozzle Design at High Temperature. Application for Air," *Chinese Journal of Aeronautics* **20**, 29–39, (2007).

[294] Gaffney, R.L.J., "Design of Mach-4 and Mach-6 Nozzles for the NASA LaRC 8-Ft High Temperature Tunnel," *45th AIAA/ASME/SAE/ASEE Joint Propulsion Conference and Exhibit, Denver, CO*, (2009).

[295] Tucker, M., "Approximate Calculation of Turbulent Boundary-Layer Development in Compressible Flow," *NACA-TN-2337*, (1951).

[296] Butler, K., Cancel, D., Earley, B., Morin, S., Morrison, E., Sangenario, M., "Design and Construction of a Supersonic Wind Tunnel," *Bachelor thesis, Worcester Polytechnic Institute*, Worcester, UK, (2010).

[297] Yu, Y.N., "A Summary of Design Techniques for Axisymmetric Hypersonic Wind Tunnels," *Activity Reference, AGARD-AG-35*, (1958).

[298] McCabe, A., "Design of a Supersonic Nozzle," *Aeronautical Research Council Reports and Memoranda 3440*, London, (1964).

[299] Rogers, E.W.E., Davis, B.M., "A note on turbulent boundary layer allowances in supersonic nozzle design," *A.R.C.C.P. 333*, (1957).

[300] Sivells, J.C., "Design of Two-Dimensional Continuous-Curvature Supersonic Nozzles," *Journal of the Aeronautical Sciences* **22(10)**, 685–692, (1955).

[301] Baron, J.R., "Analytical Design of a Family of Supersonic Nozzles by the Friedrichs Method, Including Computation Tables and a Summary of Calibration Data," *M.I.T, WADC Technical Report 54-279*, (1954).

[302] Englert, E.W., "Estimation of compressible boundary-layer growth over insulated surfaces with pressure gradient," *NACA-TN-4022*, (1957).

[303] Reshotko, E., Tucker, M., "Approximate calculation of the compressible turbulent boundary layer with heat transfer and arbitrary pressure gradient," *NACA-TN-4154*, (1957).

[304] Michel, R., "Calcul pratique de la couche limite turbulente compressible. Principe et applications," *O.N.E.R.A. Note Technique 49*, (1959).

[305] Young, A.D., "The calculation of the profile drag of aerofoils and bodies of revolution at supersonic speeds," *College of Aeronautics Report 73*, (1953).

[306] Mager, A., "Transformation of the Compressible Turbulent Boundary Layer," *Journal of the Aerospace Sciences* **25(5)**, 305–311, (1958).

[307] Brinich, P.F., "Boundary-Layer Measurements in 3.84- by 10-Inch Supersonic Channel," *N.A.C.A. TN 2203*, (1950).

[308] Ruptash, J., "Supersonic wind tunnels - theory design and performance," *UTIA Review 5*, (1952).

[309] Wilson, R.E., "Turbulent Boundary Layer Growth with Favorable Static Pressure Gradient at Supersonic Speeds," *Proceedings of the 2nd Midwestern Conference on Fluid Mechanics, Ohio*, (1952).

[310] Stratford, B.S., Beavers, G.S., "The Calculation of the Compressible Turbulent Boundary Layer in an Arbitrary Pressure Gradient-A Correlation of certain previous Methods," *Aeronautical Research Council - Reports and Memoranda 3207*, (1961).

[311] Ibrahim, O.M., "Design of Supersonic Nozzle Using CFD," *PhD thesis, Sudan University for Science & Technology*, Khartoum, Sudan, (2012).

[312] Diggins, J.L., "Diffuser Investigations in a Supersonic Wind Tunnel," *NAVORD Report 1570*, (1951).

[313] Bruce, P.J.K., Babinsky, H., "Unsteady shock wave dynamics," *Journal of Fluid Mechanics* **603**, 463–473, (2008).

[314] Korte, J.J., Kumar, A., Singh, D.J., White, J.A., "CAN-DO, CFD-based aerodynamic nozzle design and optimization program for supersonic/hypersonic wind tunnels," *AIAA paper 92-4009*, (1992).

[315] Keeling, S.L., "A strategy for the optimal design of nozzle contours," *AIAA paper 93-2720*, (1993).

[316] Mbuyamba, J.B.M., "Calculation and Design of Supersonic Nozzles for Cold Gas Dynamic Spraying Using MATLAB and ANSYS Fluent," *MSc thesis, University of the Witwatersrand*, Johannesburg, (2013).

[317] Sarimurat, M.N., "Analytical Models for Flow Control in Subsonic and Supersonic Diffusing Flow Paths Using Steady Blowing and Suction," *PhD thesis, Syracuse University*, NY, USA, (2008).

[318] Osuka, T., Erdem, E., Hasegawa, N., Majima, R., Tamba, T., Yokota, S., Sasoh, A., Kontis, K., "Laser energy deposition effectiveness on shock-wave boundary-layer interactions over cylinder-flare combinations," *Physics of Fluids* **26**, 1–17, (2014).

[319] Sasoh, A., Iwakawa, A., Osuka, T., Majima, R., Tamba, T., Sakai, T., "Control of Shock Wave-Boundary Layer Interaction by Repetitive Laser Energy Depositions," *AIAA paper 2014-2369*, (2014).

[320] Sekiya, Y., "Design of an indraft supersonic wind tunnel," *MSc thesis, Nagoya University*, Nagoya, Japan, (2006).

[321] Hoeger, T., King, P., Decker, D., Jeffrey, D., Cox-Stouffer, S., "Response of a shock train to downstream back pressure forcing," *AIAA paper 2010-6556*, (2010).

[322] Speziale, C.G., Abid, R., Anderson, E.C., "Critical evaluation of two-equation models for near-wall turbulence," *AIAA Journal* **30(2)**, 324–331, (1992).

[323] Liou, M.S., Coakley, T.J., Bergmann, M.Y., "Numerical simulation of transonic flows in diffusers," *AIAA paper 81-1240*, (1981).

[324] Viegas, J.R., Horstman, C.C., "Comparison of Multiequation Turbulence Models for Several Shock Boundary-Layer Interaction Flows," *AIAA Journal* **17(8)**, 811–820, (1979).

[325] Clark, W.J., "Experimental Investigation of Pressure Oscillations in a Side Dump Ramjet Combustor," *Journal of Spacecraft* **19(1)**, 47–53, (1982).

[326] Wang, S., Ingham, D.B., Ma, L., Pourkashaniana, M., Tao, Z., "Turbulence modeling of deep dynamic stall at relatively low Reynolds number," *Journal of Fluids and Structures* **33**, 191–209, (2012).

[327] Culick, F.E.C., Rogers, T., "The Response of Normal Shocks in Diffusers," *AIAA Journal* **21(1)**, 1382–1390, (1983).

[328] Carroll, B.F., Dutton, J.C., "Turbulence phenomena in a multiple normal shock wave/turbulent boundary-layer interaction ," *AIAA Journal* **30(1)**, 43–48, (1992).

[329] Carroll, B.F., Dutton, J.C., "Multiple normal shock wave/turbulent boundary-layer interactions," *Journal of Propulsion and Power* **8(2)**, 441–448, (1992).

[330] Carroll, B.F., Dutton, J.C., "Characteristics of multiple shock wave/turbulent boundary-layer interactions in rectangular ducts," *Journal of Propulsion and Power* **6(2)**, 186–193, (1990).

[331] Carroll, B.F., Dutton, J.C., "A Numerical and Experimental Investigation of Multiple Shock Wave/Turbulent Boundary Layer Interactions in a Rectangular Duct," *Rept. UILU-ENG-88-4015, Department of Mechanical and Industrial Engineering, University of Illinois at Urbana-Champaign*, Urbana, IL, (1988).

[332] Emanuel, G.,"Theory of Shock Waves," *Handbook of Shock Waves, Academic Press*, New York, (2000).

Appendices

A | Nozzle method of characteristics

This section provides the details about the theory behind the Method of Characteristics (MOC) used to design the nozzle contours.

Referring to Figure A.1, the flow travels from left to right across a contraction which accelerates the subsonic flow until the sonic condition at the throat. Downstream of the throat, the flow is further accelerated in the expansion region 6-5-3-2-6 bounded by the throat (6-5), the characteristic (3-2), and the expansion portion of the nozzle wall (5-3). At point 3, the nozzle contour reaches the maximum value of the inflection angle, θ_{max}, which is one half of the Prandtl-Meyer angle of the desired flow. A nozzle designed with the maximum permissible expansion to produce the desired Mach number generates the shortest nozzle for a given initial rate of divergence. However, Puckett [285] recommended a conservative design procedure by using a value between 1/2 and 2/3 of θ_{max}. Also McCabe [298] advised to exceed the minimum nozzle length by about 30%. The selection of the area change in the divergent portion of the nozzle is particularly critical since the passage of a normal shock through the nozzle imposes a severe unfavourable pressure gradient on the boundary layer that may cause boundary layer separation. After point 3, the nozzle contour gradually flattens out in the compression region 3-2-1, bounded by the Mach lines 3-2 and 2-1, and the wall (3-1). The waves that are reflected from the wall in the expansion region, are neutralised in the compression region. At each point, the wall is bended with an angle that deflects each wave by an amount equal to its strength [284,285]. Once the last characteristic line (2-1) has

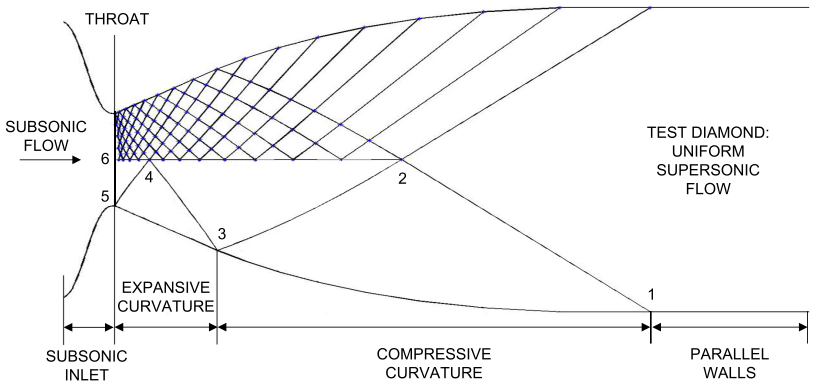

Figure A.1: Method of characteristics.

been cancelled, the walls become straight establishing a uniform and parallel flow with the desired Mach number inside a diamond-shape region.

The MOC allows the design of the ideal nozzle shape and determines the theoretical physical characteristics of the flow in the wind tunnel since the flow is assumed reversible and adiabatic, hence, isentropic with negligible dissipative frictional and viscous effects. Under these assumptions the governing partial differential equations (PDEs) can be solved with the aid of the characteristic theory. The two-dimensional hyperbolic equations become ordinary differential equations relating the dependent variables along preferred directions, called characteristic lines or Mach lines, in which the flow disturbances propagate [332]. For irrotational flows, the two-dimensional Euler equations in the x-y space can be expressed as a function of the velocity potential ϕ by Equation A.1, where $\partial\phi/\partial x$= u and $\partial\phi/\partial y$= v.

$$\left(1-\frac{u^2}{a^2}\right)\frac{\partial^2\phi}{\partial x^2}+\left(1-\frac{v^2}{a^2}\right)\frac{\partial^2\phi}{\partial y^2}-2\frac{uv}{a^2}\frac{\partial^2\phi}{\partial x\partial y}=0 \tag{A.1}$$

With a being the speed of sound.

The thermodynamic properties, such as P, T, ρ, and u, are continuous in the quadrilateral areas between the waves, but indeterminate across the characteristic lines so that changes in velocity and pressure through any wave can be computed. The expression $\partial^2\phi/\partial x\partial y$ is undetermined when its denominator is zero and by mathematical manipulation gives:

$$\left(1-\frac{u^2}{a^2}\right)\left(\frac{dy}{dx}\right)^2_{char}+2\frac{uv}{a^2}\left(\frac{dy}{dx}\right)_{char}+\left(1-\frac{v^2}{a^2}\right)=0 \tag{A.2}$$

Equation A.2 is a quadratic equation with the unknown $(dy/dx)_{char}$ representing the slope of the characteristic lines and has solution:

$$\left(\frac{dy}{dx}\right)_{char}=tan\left(\theta\mp\mu\right) \tag{A.3}$$

The physical meaning of Equation A.3 is illustrated in Figure A.2. Two characteristic lines

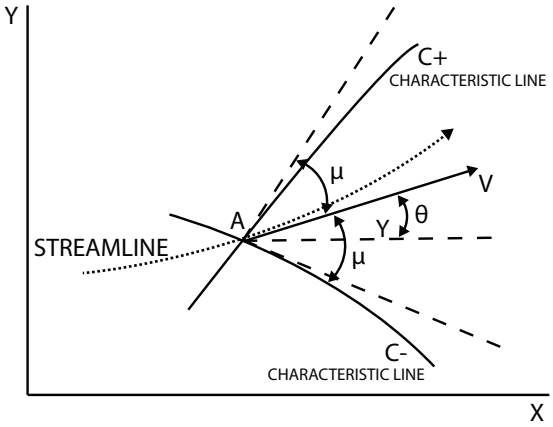

Figure A.2: Left and right characteristic line passing through a point A.

with slope $tan\,(\theta + \mu)$ and $tan\,(\theta - \mu)$ pass through a point A. For a streamline with a velocity V inclined at an angle θ with respect to the horizontal, one characteristic line, C_{-}, at the point A is inclined below the streamline direction by an angle μ. In a similar way, the other characteristic line, C_{+}, is inclined above the streamline direction by an angle μ.

B | Design of the Pitot rake

THE design of the Pitot rake for measuring the velocity profile in the test section of the wind tunnel is provided in Figure B.1. The Pitot rake can be adjusted along the y-directions, as visible in Figure B.2. Moreover, Figure B.2 illustrates the axial coordinate of the pressure taps for static pressure measurements. The first pressure tap is located at x_1= 240.21 mm and all the subsequent pressure taps are spaced 80 mm apart. The axial coordinate of the Pitot rake is at the same axial location of the second pressure tap, x_2.

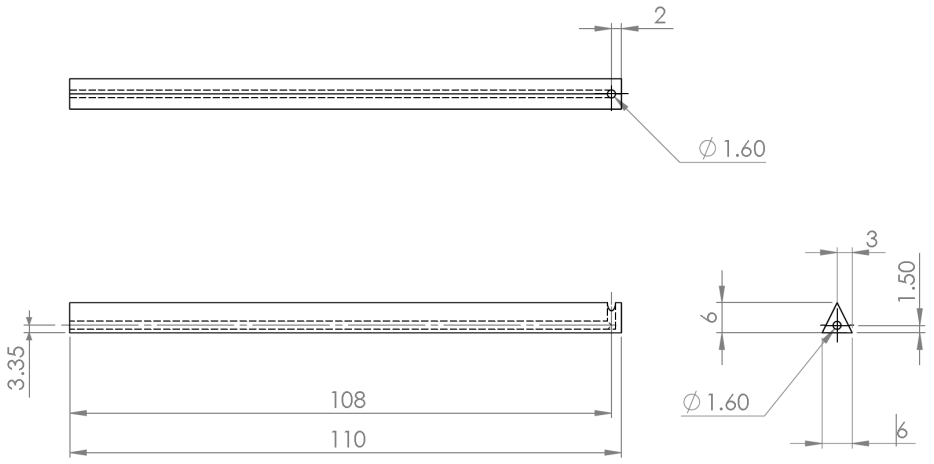

Figure B.1: Geometry of the Pitot rake (all dimensions in mm).

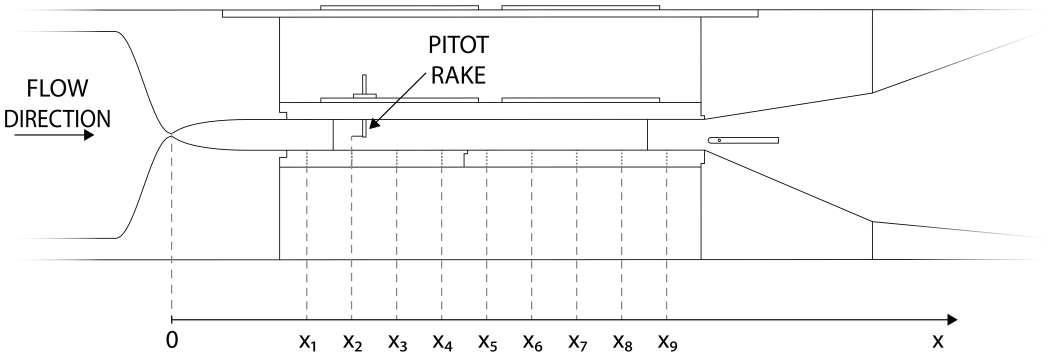

Figure B.2: Schematic of the wind tunnel with pressure taps locations.

C | List of Publications

Gnani, F., Lo, K.H., Zare-Behtash, H., Kontis, K., "Experimental Investigation on Shock Wave Diffraction over Sharp and Curved Splitters," *Acta Astronautica* **99**, 143–152, (2014).

Gnani, F., Zare-Behtash, H., Kontis, K., "Shock wave diffraction phenomena interacting with a supersonic co-flow," *21st International Shock Interaction Symposium (ISIS21), 3-8 August*, Riga, Latvia, (2014).

Gnani, F., Lo, K.H., Zare-Behtash, H., Kontis, K., "Shock Wave Diffraction Phenomena around Slotted Splitters," *Aerospace* **2(1)**, 1–16, (2015).

Gnani, F., Zare-Behtash, H., Kontis, K., "Indraft Supersonic Wind Tunnel for Shock Train Investigations," *30th International Symposium on Shock Waves (ISSW30), 19-24 July*, Tel-Aviv, Israel, (2015).

Gnani, F., Zare-Behtash, H., Kontis, K., "Pseudo-shock waves and their interactions in high-speed intakes," *Progress in Aerospace Sciences* **82**, 143–152, (2016).

Gnani, F., Zare-Behtash, H., Kontis, K., "Shock wave diffraction in the presence of a supersonic co-flow jet," *Shock Waves* **26(3)**, 253–262, (2016).

Gnani, F., Zare-Behtash, H., Kontis, K., "Shock Wave/Boundary Layer Interactions in Internal Flows," *22nd International Shock Interaction Symposium (ISIS22), 22-27 July*, Glasgow, UK, (2016).

F. Gnani, H. Zare-Behtash, C. White, K. Kontis, "Shock Train Structures in Rectangular Ducts," *31st International Symposium on Shock Waves (ISSW31), 14-29 July*, Nagoya, Japan, (2017).